From Detector Development to New Physics Searches: CMS HGCAL Validation and Search for Top-Philic Resonances Using Variable-Radius Jet Tagging

Dissertation zur Erlangung des Doktorgrades

an der Fakultät für Mathematik, Informatik und Naturwissenschaften

der Universität Hamburg

vorgelegt von

Gabriele Milella

Hamburg, 2025

Gutachter/innen der Dissertation:

Prof. Dr. Freya Blekman

Dr. Katja Krüger

Zusammensetzung der Prüfungskommission:

Prof. Dr. Freya Blekman

Dr. Andreas Hinzmann

Dr. Katja Krüger

Prof. Dr. Jochen Liske

Prof. Dr. Sven Olaf Moch

Vorsitzende/r der Prüfungskommission:

Prof. Dr. Jochen Liske

Datum der Disputation: 23.01.2026

Vorsitzender des Fach-Promotionsausschusses PHYSIK:

Prof. Dr. Wolfgang J. Parak

Leiter des Fachbereichs PHYSIK:

Prof. Dr. Markus Drescher

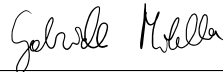Dekan der Fakultät MIN:

Prof. Dr.-Ing. Norbert Ritter

Declaration on oath

I hereby declare and affirm that this doctoral dissertation is my own work and that I have not used any aids and sources other than those indicated.

If electronic resources based on generative artificial intelligence (gAI) were used in the course of writing this dissertation, I confirm that my own work was the main and value-adding contribution and that complete documentation of all resources used is available in accordance with good scientific practice. I am responsible for any erroneous or distorted content, incorrect references, violations of data protection and copyright law or plagiarism that may have been generated by the gAI.

Hamburg, 28/10/2025

Ort, Datum | *Place, date*

Unterschrift | *Signature*

Abstract

This thesis presents two research works carried out within the Compact Muon Solenoid (CMS) experiment at the CERN Large Hadron Collider (LHC): the system validation of the scintillator section of the High Granularity Calorimeter (HG-CAL), and a search for a heavy resonance coupling to top quarks and produced in association with top quark pairs in proton–proton collisions at center-of-mass energies of 13 and 13.6 TeV.

For the High-Luminosity LHC (HL-LHC) phase, the endcap calorimeters of CMS will be replaced by the HGCAL, a high-precision sampling calorimeter designed to cope with the extreme radiation and pileup conditions expected at the HL-LHC. In regions where radiation levels remain moderate, the hadronic section employs scintillator tiles coupled to silicon photomultipliers (SiPM-on-tile) as active materials. Each HGCAL tilemodule, the basic detector unit of this region, accommodates up to 144 SiPM-on-tile channels read out by dedicated front-end electronics. The performance of several tilemodules was evaluated during test-beam campaigns at the DESY-II facility using 3 GeV electron beams. The measurements serve to validate the response and uniformity of the detector components and to confirm that they meet the design specifications for HL-LHC operation.

A search for a new heavy resonance that couples exclusively to top quarks and is produced in association with a top quark pair is presented. The analysis uses proton–proton collision data collected with the CMS detector at center-of-mass energies of 13 TeV (2016–2018) and 13.6 TeV (2022). The search targets the final state with two oppositely charged leptons from the W boson decays of the non-resonant top quarks, and two high-energy jets reconstructing the hadronically decaying resonant top quarks. In this scenario, the two top quarks from the resonance decay are expected to be highly Lorentz-boosted. Their hadronic decays are reconstructed using jets clustered with a variable-radius algorithm and identified with a dedicated top quark tagger based on a boosted decision tree (BDT). Events are selected in a final state containing opposite-sign leptons and b-tagged jets, and the resonance mass is reconstructed from pairs of tagged top jets. The analysis probes resonance masses between 500 GeV and 4 TeV and searches for local excesses in the reconstructed mass spectrum. The results are interpreted in the context of models with vector-like, scalar and pseudoscalar resonances produced in association with top quarks, representing the first such interpretation performed with CMS data.

5

Zusammenfassung

Diese Dissertation umfasst zwei Forschungsarbeiten, die im Rahmen des CMS-Experiments am Large Hadron Collider (LHC) des CERN durchgeführt wurden: die Systemvalidierung des Szintillatorteils des High Granularity Calorimeter (HGCAL) sowie die Suche nach einer schweren Resonanz, die an Top-Quarks koppelt und in Assoziation mit Top-Quark-Paaren in Proton-Proton-Kollisionen bei Schwerpunktsenergien von 13 und 13.6 TeV produziert wird.

Für die Phase des High-Luminosity LHC (HL-LHC) werden die Endkappen-Kalorimeter des CMS-Detektors durch das HGCAL ersetzt, ein hochpräzises Sampling-Kalorimeter, das entwickelt wurde, um den extremen Strahlungs- und Pileup-Bedingungen des HL-LHC standzuhalten. In Bereichen mit moderater Strahlungsbelastung verwendet der hadronische Teil Szintillatorkacheln, die mit Silizium-Photomultipliern (SiPM-on-Tile) als aktive Materialien gekoppelt sind. Jedes HGCAL-Tilemodul, die grundlegende Detektoreinheit dieser Region, enthält bis zu 144 SiPM-on-Tile-Kanäle, die von spezieller Front-End-Elektronik ausgelesen werden. Die Leistungsfähigkeit mehrerer Tilemodule wurde während Teststrahlkampagnen an der DESY-II-Anlage mit 3 GeV-Elektronenstrahlen untersucht. Die Messungen dienen zur Validierung der Antwort und Gleichmäßigkeit der Detektorkomponenten und bestätigen, dass diese die Konstruktionsspezifikationen für den HL-LHC-Betrieb erfüllen.

Im zweiten Teil der Arbeit wird eine Suche nach einer neuen schweren Resonanz vorgestellt, die ausschließlich an Top-Quarks koppelt und in Assoziation mit einem Top-Quark-Paar produziert wird. Die Analyse basiert auf Proton-Proton-Kollisionsdaten, die mit dem CMS-Detektor bei Schwerpunktsenergien von 13 TeV (2016–2018) und 13.6 TeV (2022) aufgezeichnet wurden. Die Suche richtet sich auf Endzustände mit zwei entgegengesetzt geladenen Leptonen aus den W-Boson-Zerfällen der nicht-resonanten Top-Quarks sowie zwei hochenergetischen Jets, die die hadronisch zerfallenden resonanten Top-Quarks rekonstruieren. In diesem Szenario werden die beiden Top-Quarks aus dem Resonanzzerfall erwartungsgemäß stark Lorentz-geboostet. Ihre hadronischen Zerfälle werden mit Jets rekonstruiert, die mit einem variablen Radius geclustert und mit einem speziellen, auf einem Boosted-Decision-Tree (BDT) basierenden Top-Quark-Tagger identifiziert werden. Ereignisse werden in einem Endzustand mit entgegengesetzt geladenen Leptonen und b-getaggten Jets ausgewählt, und die Resonanzmasse wird aus Paaren von getaggten Top-Jets rekonstruiert. Die Analyse untersucht Resonanzmassen zwischen 500 GeV und 4 TeV und sucht nach lokalen Überschüssen im rekonstruierten Massenspektrum. Die Ergebnisse werden im Rahmen von Modellen mit skalarer und pseudoskalarer Resonanz interpretiert, die in Assoziation mit Top-Quarks produziert werden, und stellen die erste derartige Interpretation mit CMS-Daten dar.

Individual contribution to the CMS Collaboration by the author

System validation of the scintillator section of CMS (HGCAL)

At the beginning of my doctoral project, I joined the CMS HGCAL group at DESY, Hamburg, where I contributed to the system validation of the scintillator section of the detector. My tasks included:

- participation in laboratory activities,

- participation in test beam activities at DESY,

- validation of the latest readout chip and DAQ system, including software installation for the new electronics,

- development of a new analysis template for test beam data analysis.

Results from the May 2024 test beam campaign are presented in Chapter 4. In the laboratory, I also participated in studies such as noise measurements on irradiated SiPMs, which are not included in this thesis. Some of these results were presented at several internal workshops and at international conferences, including the European Physical Society Conference on High Energy Physics (EPS-HEP) held in Hamburg in 2023 [1].

Hadronic top quark tagger with variable-size jets

I studied the performance of using variable-size jet clustering algorithms (HOTVR) instead of the fixed-size anti-k_T (AK8) jets, demonstrating that HOTVR can improve the sensitivity of searches for top-philic heavy vector bosons, particularly for low boson masses below 1 TeV. The CMS-recommended identification of hadronic top quarks in HOTVR jets relies on selection-based criteria on jet substructure observables, which are less sensitive than the machine learning–based taggers used for fixed-size jets. To address this limitation, I developed a new HOTVR-based top-quark tagger using a BDT classifier. My contributions included the training and validation of the BDT tagger and the integration of the resulting object into the CMS software framework. I presented this technique at several workshops and meetings, leading to a *Detector Performance* note [2], which was presented as a poster at the BOOST conference in Genova (2024). Chapter 6 summarizes these results.

Search for heavy top-philic resonance produced in association with top quarks

This search represents the first analysis in the opposite-sign dilepton channel and was initiated as part of this thesis project, for which I am the main analyzer. My contributions include:

- development and optimization of the analysis strategy,

- integration of the HOTVR algorithm into the CMS software framework,

- implementation of the data-driven background estimation,

- statistical interpretation of the results.

The analysis is currently in the unblinding stage: it refers to the final phase of an analysis, during which real collision data is examined for the first time in signal regions, such that the analysis strategy is fully validated before inspecting potential signal events. The target is to submit the results to *The European Physical Journal C* in fall 2026.

As part of this work, I generated the Monte Carlo signal samples using UFO-based theory models at $\sqrt{s}$ of 13 and 13.6 TeV. These samples have been validated and are now centrally available within the CMS Collaboration.

During the CMS internal review, my responsibilities included:

- presenting regular updates in the relevant working group meetings,

- writing and editing the analysis documentation and paper draft,

- preparing and delivering the preapproval presentation,

- managing communication with the review committee throughout the review process.

Preliminary results from this analysis were presented during my doctoral work at several internal CMS workshops and at the annual conference of the German Physical Society (DPG) in Karlsruhe, 2024. The expected results of the analysis are presented in Chapter 7.

Contents

Introduction

Particle physics aims to uncover the fundamental constituents of matter and the forces that mediate their interactions. The development of a unified theoretical framework to describe elementary particles and their interactions began in the mid-twentieth century and resulted in the formulation of the Standard Model (SM) of particle physics. The SM provides a precise description of the elementary building blocks of the universe and their fundamental interactions, and it has extensive experimental tests and validations over many orders of magnitude in energy.

The discovery of the Higgs boson in 2012 by the ATLAS [3] and CMS [4] experiments at the Large Hadron Collider (LHC) marked a milestone in high-energy physics, confirming the mechanism of spontaneous symmetry breaking predicted within the SM. More than a decade later, many parameters of the SM have been measured with high precision. Despite these remarkable successes, the SM is not a complete theory and fails to account for several experimental observations, motivating the development of various Beyond Standard Model (BSM) scenarios. Many proposed extensions of the SM predict the existence of a heavy resonance that couples preferentially or exclusively to top quarks. Such top-philic particles could help address some of the open questions of the SM and may provide understanding into BSM physics.

In this thesis, a search for such a heavy resonance is presented. The analysis uses data recorded by the Compact Muon Solenoid (CMS) experiment in proton-proton (p–p) collisions at center-of-mass energies, $\sqrt{s}$, of 13 TeV (2016–2018) and 13.6 TeV (2022). The search targets signal models in which the resonance couples exclusively to top quarks and is produced in association with a top quark pair. The studied final state is the opposite-sign dilepton channel, where the associated top quarks decay leptonically via a W boson into an electron or muon and the corresponding neutrino, while the top quarks originating from the resonance are reconstructed from their hadronic decays. The hadronically decaying top quarks are identified and reconstructed using a variable-radius jet clustering algorithm, exploiting jet substructure observables, and a dedicated Boosted Decision Tree (BDT)-based top quark tagging algorithm. For this purpose, the Heavy Object Tagger with Variable Radius (HOTVR) algorithm is employed for jet clustering, ensuring a stable selection efficiency over a wide range of top quark momenta. The BDT-based top tagger model is trained to distinguish between two jet classes: those originating from hadronic top quark decays and those arising from QCD multijet processes. The latter represents the dominant background contribution, which is modeled through a data-driven approach.

Different benchmark models, such as a top-philic Z', two-Higgs-doublet models, and axion-like particles (ALPs), are used to quantify the sensitivity of the

analysis. Since the analysis is currently under review within the CMS Collaboration, data in the invariant dijet-mass range from 400 GeV to more than 5 TeV remain blinded. This standard procedure prevents potential bias in the signal extraction. Consequently, the upper limits on new physics models' cross-section quoted in this thesis correspond to the expected results.

After the ongoing data-taking period at 13.6 TeV in 2025, the LHC is scheduled to undergo major upgrades to meet the requirements of the increased collision rate and $\sqrt{s}$ of 14 TeV foreseen for the High-Lumi-LHC (HL-LHC) phase, expected to start around 2028 and continue until around 2040. The higher interaction rates will lead to an increased number of collisions per bunch crossing, requiring new detector technologies and advanced reconstruction algorithms to disentangle rare signal events from the background. Moreover, the higher collision frequency leads to increased radiation levels and, consequently, greater damage to the detector components. This effect is particularly critical in the forward regions, close to the beam line.

Many detector components will be replaced with radiation-hard technologies to mitigate the effects of increased radiation damage. One such upgrade is the replacement of the CMS endcap calorimeters with the High Granularity Calorimeter (HGCAL). The HGCAL will use silicon sensors and scintillator tiles, read out by silicon photomultiplier (SiPM)s, as active detection elements depending on the detection region. It is designed to precisely measure particle showers over a broad dynamic range, providing spatial, energy, and timing information. The HGCAL is planned to be installed in the CMS detector by 2028 and is currently in the production phase, during which many of its components are being manufactured and assembled into the final detector modules. Reaching this stage has required extensive development and validation efforts. This thesis presents system-level validations and performance tests of the detector's scintillator section, performed during testbeam campaigns at DESY-II.

The thesis is structured in seven chapters:

- **Theoretical overview (Chapter 1)**
  This chapter provides an overview of the SM, with emphasis on spontaneous symmetry breaking and the known shortcomings of the theory. It also introduces several BSM scenarios that predict the existence of a heavy top-philic resonance.

- **The CMS experiment: physics and apparatus (Chapter 2)**
  This chapter describes the LHC accelerator and the CMS experiment. The main characteristics of the CMS detector are presented, with particular focus on the calorimetry system.

- **The upgrade of the CMS experiment (Chapter 3)**
  This chapter gives an overview of the planned CMS upgrades for the HL-LHC phase. The focus is on the HGCAL detector, with particular attention to the scintillator section and its associated readout electronics.

- **System validation of the scintillator section of the CMS HGCAL (Chapter 4)**
  This chapter summarizes the work carried out during the doctoral project on the system validation of the scintillator section of the HGCAL. Measuring

key characteristics of the system, such as the SiPM gain and the light yield of the scintillator tiles, is essential for verifying the detector design and expected performance, and preparing for the upcoming mass-production phase.

- **Physics object reconstruction (Chapter 5)**
  In this chapter, the algorithms used for the reconstruction and identification of the main physics objects employed in this analysis, tracks, vertices, electrons, muons, and jets, are described. Particular emphasis is placed on the jet reconstruction and heavy-flavour identification techniques.

- **Hadronic top quark tagger with variable-size jets (Chapter 6)**
  The variable-radius jet clustering algorithm with the BDT-based top quark tagger is presented in this chapter. It summarizes the work carried out during the doctoral project to train and evaluate the performance of the hadronic top quark tagger, including its validation in top quark–enriched and multijets QCD-enriched regions.

- **Search for heavy top-philic resonance produced in association with top quarks (Chapter 7)**
  The final chapter provides a detailed description of the analysis developed for the signal search. It presents the motivation, event selection criteria, and background estimation strategy. Finally, it describes the statistical procedure used for signal extraction and the determination of the expected upper limits on the cross section of the new physics models.

Chapter 1

Theoretical overview

Particle physics aims to understand the fundamental constituents of the Universe, known as elementary particles, and their interactions. The current theoretical framework describing the building blocks of Nature, supported by a large body of experimental results, is called the SM of particle physics. The SM has been successful in predicting the interactions of particles discovered experimentally, and has been validated by numerous precision tests across a wide range of energy scales.

This chapter presents a concise description of the model in Section 1.1, followed by an introduction to the physics of inelastic p–p collisions in particle colliders in Section 1.2. The core subject of the thesis is the search for physics BSM, therefore shortcomings of the SM are discussed in Section 1.3.

1.1 The Standard Model

The SM is a relativistic quantum field theory [5, 6, 7, 8] that describes the interaction of elementary particles via three of the fundamental forces: electromagnetic, weak, and strong interactions. Elementary particles in the SM are categorized by their spin into two groups: fermions and bosons. Fermions have half-integer spin and obey Fermi–Dirac statistics, and are grouped into quarks and leptons. Bosons have integer spin and obey Bose–Einstein statistics. The gauge bosons, photon (γ), W, Z, and gluon (g), mediate the fundamental interactions through their exchange between particles, whereas the scalar boson, the Higgs boson (H), gives mass to elementary particles via the Higgs mechanism rather than mediating a force. Figure 1.1 schematically summarizes the building blocks of the SM, showing the main properties of the fundamental particles, such as their masses, electric charges, and spins.

The fermions are grouped into pairs called families or *generations*:

- leptons: electrons and electron neutrinos (ν_e, e), muons and muon neutrinos (ν_μ, μ), and taus and tau neutrinos (ν_τ, τ)

- quarks: up and down quarks (u, d), charm and strange quarks (c, s), and bottom and top quarks (b, t)

Each particle has a corresponding charge–conjugate antiparticle with identical mass, giving a total of 12 leptons and 12 quarks. Only the first generation of
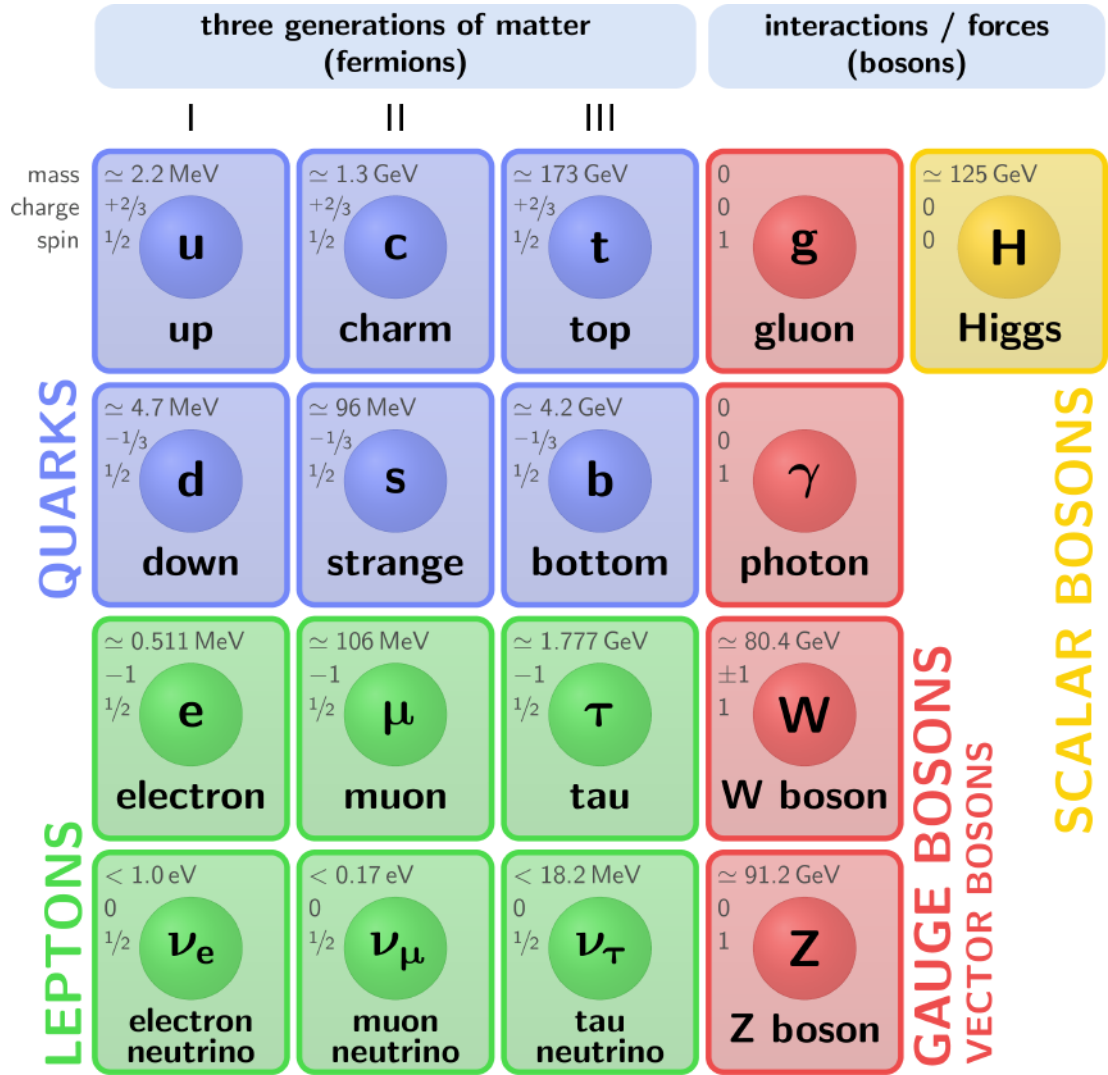
Figure 1.1: The SM of elementary particles [9].

quarks and leptons, i.e., electrons, form ordinary matter, such as atoms and atomic structures.

Regarding the particles that mediate interactions, the electromagnetic force is mediated by the photons, the weak force by the Z and $W^{\pm}$ bosons, and the strong force by the gluons. All of them are gauge vector bosons with spin-1. The graviton, the hypothetical mediator of the gravitational force, is not included in the SM, since gravity is about 10^{36} times weaker in coupling strength than the electromagnetic force, and its quantum field theory is not renormalizable, unlike the renormalizable interactions of the SM [10, 11]. In addition, the SM postulates a scalar particle, the Higgs boson (H) [12], which does not mediate any fundamental force but is associated with the Higgs field. This field provides a model to explain the masses of the particles that interact with it through its non-zero vacuum expectation value [8, 6].

All the particles of the Standard Model have been discovered over the course of the 20th and early 21st centuries. At the beginning of the 20th century, studies of the conduction of electricity through gases led to the discovery of the electron at the end of the 19th century by J. J. Thomson [13]. Searches for new particles were motivated by studies of atomic structure and quantum theory, leading to the discovery of the muon in cosmic-ray studies in 1936 at the California Institute of Technology [14], and the discoveries of the electron and muon neutrinos in experiments at the Hanford Site (1956 [15]) and at Brookhaven National Laboratory (1962 [16]), respectively. The tau lepton was discovered in 1975 at the Stanford Linear Accelerator Center [17], and its neutrino counterpart in 2001 at Fermilab [18].

Theories postulating the internal structure of protons and neutrons emerged in the mid-20th century, with the quark model proposed in 1964 [19] and experimental evidence for the up and down quarks obtained in deep inelastic scattering at SLAC in 1968–69 [20]. The strange quark was introduced in the quark model to explain kaon spectroscopy [19]. The charm quark was discovered in 1974 at SLAC and BNL [21, 22], while the bottom and top quarks were discovered at Fermilab in 1977 [23] and 1995 [24, 25], respectively.

The photon was introduced in 1905 by Einstein to explain the photoelectric effect [26]. The W and Z bosons were discovered at CERN in 1983 [27, 28], while the gluon was observed in 1979 at DESY [29]. Finally, the Higgs boson was discovered at CERN in 2012 [3, 4].

1.1.1 Particle interactions

The mathematical formalism describing the SM as a quantum field theory considers particles as excitations of relativistic quantum fields, $\psi(x)$, where x is a four-vector in space-time, $x_{\mu} = (x_t, x_x, x_y, x_z)^1$. The dynamics follow from the principle of least action, $\delta S = 0$, with the action defined as,

$$S = \int d^4x \ \mathcal{L}(x), \tag{1.1}$$

where $\mathcal{L}(x)$ is the Lagrangian density of the SM. Applying the Euler-Lagrange equations to this Lagrangian results in the corresponding equations of motion for

---

[1]In natural units $c = \hbar = 1$, so that time and spatial coordinates have the same dimension.

the fields.

The SM is a gauge theory, meaning that its Lagrangian density is invariant under continuous gauge transformations. By Noether's theorem [30], such symmetries imply the conservation of specific physical quantities. For example, for a free fermion field ψ, the non-interacting Dirac Lagrangian $\mathcal{L} = \bar{\psi}(i\gamma^\mu \partial_\mu - m)\psi$, where γ^μ are the Dirac gamma matrices, is invariant under a global $U(1)$ phase transformation $\psi(x) \to e^{i\alpha}\psi(x)$. By Noether's theorem, this invariance leads to the conserved current $j^\mu = \bar{\psi}\gamma^\mu\psi$ satisfying $\partial_\mu j^\mu = 0$, which corresponds to the conservation of electric charge.

In the case of the SM, the gauge transformations of the forces are *local*, namely the transformation parameters depend explicitly on the space-time point x. The SM is based on the gauge group

$$SU(3)_C \times SU(2)_L \times U(1)_Y, \tag{1.2}$$

which reflects the local symmetries of the Lagrangian. Imposing these gauge symmetries requires the introduction of corresponding gauge fields, which couple to the fermions and mediate the strong, weak, and electromagnetic interactions, respectively. These are mediated by gluons, $W^\pm$ and Z bosons, and the photon, respectively, where $SU(3)_C$ is the symmetry group underlying the strong interactions and modeled by the Quantum Chromo Dynamics (QCD) theory, and $SU(2)_L \times U(1)_Y$ to describe the weak and electromagnetic interaction in the unified electroweak (EWK) theory.

Strong interactions

After the discovery of the Δ^{++} particle [31], composed of three up quarks in the same spatial and spin state, a new quantum number, the *color* charge, was introduced to resolve the apparent violation of the Pauli exclusion principle [32, 33]. The color charge can take three values, conventionally referred to as blue, green, and red, and the theory describing the strong interactions of particles carrying color charge, namely quarks and gluons, is QCD. The symmetry group of QCD is $SU(3)_C$, and its Lagrangian density is

$$\mathcal{L}_{\text{QCD}} = \sum_{f=1}^{N_f} \bar{q}_f \left(i\gamma^\mu D_\mu - m_f \right) q_f - \frac{1}{4} G^a_{\mu\nu} G^{a\,\mu\nu} + \text{h.c.}, \quad q_f = \begin{pmatrix} q_f^{\text{red}} \\ q_f^{\text{green}} \\ q_f^{\text{blue}} \end{pmatrix}. \tag{1.3}$$

where q_f is the triplet of field describing a quark of flavor f, accounting for the three colors, $G^a_{\mu\nu}$ tensor describes eight gluons, namely $a = 1, .., 8$, representing the eight massless gluon fields, and D_μ is the QCD covariant derivative. Under $SU(3)_C$ gauge transformation, the color charge is conserved.

The first term of the $\mathcal{L}_{\text{QCD}}$ describes the interaction between quarks and gluons and arises from the requirement of local $SU(3)_C$ gauge invariance. The QCD covariant derivative is defined as

$$D_\mu = \partial_\mu + i g_s\, G^a_\mu(x)\, \lambda^a, \tag{1.4}$$

where g_s is the strong coupling constant, λ^a $(a = 1, \ldots, 8)$ are the generators of the $SU(3)$ group, and $G^a_\mu(x)$ denote the eight gluon gauge fields. The $SU(3)_C$ group is non-abelian, meaning that its commutation relation

$$[\lambda^a, \lambda^b] = 2i f^{abc} \lambda^c \tag{1.5}$$

defines the group structure, with f^{abc} being the totally antisymmetric structure constants of the group. The second term of $\mathcal{L}_{\mathrm{QCD}}$ follows directly from this non-abelian property, as the gluon field-strength tensor is given by

$$G^a_{\mu\nu} = \partial_\mu G^a_\nu - \partial_\nu G^a_\mu + g_s f^{abc} G^b_\mu G^c_\nu. \tag{1.6}$$

The last term, proportional to f^{abc}, implies that gluons carry color charge and therefore self-interact.

In nature, no color-charged particle can be isolated; therefore, free quarks cannot exist due to *color confinement*. The phenomenon can be understood qualitatively by approximating the QCD potential [34, 35] between two quarks as

$$V(r) = -\frac{4}{3}\frac{\alpha_s}{r} + k\,r, \quad \alpha_s = \frac{g_s}{4\pi} \tag{1.7}$$

where the first term is a Coulomb-like potential at short distances, α_s is the strong coupling constant, and k is the string tension, analogous to the harmonic oscillator. At large distances r between the quarks, the linear term dominates and the energy of the system grows until it becomes energetically favorable for a new quark-antiquark pair to emerge from the vacuum. This leads to a cascade effect of new particles, which are bound together in color-neutral singlets called hadrons. This process is referred to as *hadronization*, and the resulting cascades of particles are reconstructed as collimated *jets* in the context of p–p collision physics.

The resulting hadrons can be grouped into *mesons* and *baryons*, depending on the number of quark constituents. Mesons consist of a quark–antiquark pair, such as the $\pi^+(u\bar{d})$, while baryons are composed of three quarks, e.g., the proton $p(uud)$. These constituents are referred to as *valence quarks*. In addition, hadrons contain virtual quark–antiquark pairs, called *sea quarks*, as well as gluons. Together, valence quarks, sea quarks, and gluons are known as *partons*.

Electroweak interactions

Historically, electromagnetism was the first interaction to be formulated as a quantum field theory, namely quantum electrodynamics (QED) [36, 37]. In this theory, invariance under local phase rotations, represented by the $U(1)$ group, is postulated and typically written as

$$\psi(x) \rightarrow \psi'(x) = e^{iQ\alpha(x)}\,\psi(x)$$

where $\alpha(x)$ is a spacetime-dependent phase, and here Q denotes the electric charge, which is conserved in electromagnetic interactions.

On the other hand, weak interactions manifest as flavor–changing processes mediated by the charged $W^\pm$ bosons, for example in the muon decay $\mu^- \rightarrow e^- + \bar{\nu}_e + \nu_\mu$, and as neutral current processes mediated by the Z^0 boson, for example in elastic neutrino scattering, $\nu_\mu + e^- \rightarrow \nu_\mu + e^-$.

Electromagnetic and weak interactions are described by the unified EWK theory, first formulated by Glashow [38], Weinberg [36] and Salam [37]. The gauge

symmetry group of the EWK interactions is $SU(2)_L \times U(1)_Y$, where $SU(2)_L$ is referred to as the weak isospin group and $U(1)_Y$ as the weak hypercharge group.

A distinctive feature of the weak interaction is the violation of parity symmetry, first observed in the Wu experiment in 1957 [39], which studied the β decay of ^{60}Co. In the Glashow–Weinberg–Salam model, fermion fields are decomposed into left-handed and right-handed components. These correspond to the two possible chiral projections of a Dirac spinor, defined by the operators $P_{L,R} = \frac{1}{2}(1 \mp \gamma^5)$. The chirality is a Lorentz-invariant property, and it coincides with the helicity, i.e., the projection of the spin along the momentum direction, in the massless limit. The left-handed components of a fermion family form a doublet of isospin $SU(2)_L$, for instance

$$\begin{pmatrix} \nu_e \\ e^- \end{pmatrix}_L, \qquad \begin{pmatrix} u \\ d \end{pmatrix}_L. \tag{1.8}$$

for the first generation of leptons and quarks, respectively. Here, ν_{eL} and u_L have the third component of weak isospin $I_3 = +\frac{1}{2}$, while e_L and d_L have $I_3 = -\frac{1}{2}$. The right-handed components, in contrast, are singlet fields under $SU(2)_L$, such as e_R^-, u_R, and d_R. Right-handed neutrinos are not included in SM, as they do not participate in any interactions.

By requiring invariance under both local transformations, the electroweak Lagrangian density $\mathcal{L}_{\text{EWK}}$ is constructed as

$$\mathcal{L}_{\text{EWK}} = \sum_{\psi_L \in \text{doublets}} \bar{\psi}_L \, i\gamma^\mu D_\mu \psi_L + \sum_{\psi_R \in \text{singlets}} \bar{\psi}_R \, i\gamma^\mu D_\mu \psi_R - \frac{1}{4} W_{\mu\nu}^a W^{a\mu\nu} - \frac{1}{4} B_{\mu\nu} B^{\mu\nu},$$
$$\tag{1.9}$$

where ψ denotes the fermion fields, $W_{\mu\nu}^a$ is the $SU(2)_L$ field-strength tensor [2], while $B_{\mu\nu}$ is the $U(1)_Y$ field-strength tensor [3].

The electroweak covariant derivative is given by

$$D_\mu = \partial_\mu + ig\,W_\mu^a T^a + ig'\,Y\,B_\mu, \tag{1.10}$$

with

$$T^a = \frac{\sigma^a}{2} \quad \text{for } SU(2)_L \text{ doublets}, \qquad T^a = 0 \quad \text{for singlets},$$

where g and g' are the $SU(2)_L$ and $U(1)_Y$ gauge couplings, σ^a are the Pauli matrices, and Y is the hypercharge, defined as $Y = 2(q - I_3)$, with q the electric charge. A specific linear combination of the $SU(2)_L$ generator T_3 and Y, namely $Q = T_3 + Y$, generates a subgroup of $U(1)_{em}$, which corresponds to the electromagnetic charge that is conserved under these gauges.

The charged W bosons, carriers of the flavor–changing interactions, are obtained as linear combinations of the W_μ^1 and W_μ^2 fields,

$$W_\mu^\pm = \frac{1}{\sqrt{2}} \left(W_\mu^1 \mp i W_\mu^2 \right). \tag{1.11}$$

---

[2] $W_{\mu\nu}^a = \partial_\mu W_\nu^a - \partial_\nu W_\mu^a + g\,\epsilon^{abc} W_\mu^b W_\nu^c \qquad a = 1, 2, 3$

[3] $B_{\mu\nu} = \partial_\mu B_\nu - \partial_\nu B_\mu$

By performing a rotation of the neutral fields W_μ^3 and B_μ, the Z boson and the photon A_μ are obtained,

$$
\begin{pmatrix} Z_\mu \\ A_\mu \end{pmatrix} = \begin{pmatrix} \cos\theta_W & -\sin\theta_W \\ \sin\theta_W & \cos\theta_W \end{pmatrix} \begin{pmatrix} W_\mu^3 \\ B_\mu \end{pmatrix}, \tag{1.12}
$$

where θ_W is the Weinberg (weak mixing) angle.

The Weinberg angle is related to the gauge couplings g and g' as

$$
\tan\theta_W = \frac{g'}{g}, \qquad e = g\sin\theta_W = g'\cos\theta_W, \tag{1.13}
$$

with e the electromagnetic coupling constant. The Weinberg angle is determined experimentally as $\sin^2\theta_W \approx 0.23$ [6].

It is notable that the Lagrangian density in Equation 1.9 does not contain any term accounting for the masses of fermions or vector bosons, even though these masses have been experimentally observed and measured, as discussed in Section 1.1. Adding any boson's mass term to the Lagrangian density would break the $SU(2)_L$ gauge invariance. This apparent inconsistency of the theory is resolved by the mechanism of spontaneous symmetry breaking, proposed by Brout, Englert, and Higgs [40, 12].

1.1.2 Spontaneous symmetry breaking

The spontaneous symmetry breaking mechanism of the SM relies on introducing a self-interacting complex scalar field

$$
\phi(x) = \begin{pmatrix} \phi^+(x) \\ \phi^0(x) \end{pmatrix}, \tag{1.14}
$$

which is invariant under transformation in $SU(2)_L$ doublet with hypercharge $Y = \frac{1}{2}$. This field enters $\mathcal{L}_{\text{EWK}}$ through

$$
\mathcal{L}_\phi = (D_\mu\phi)^\dagger(D^\mu\phi) - V(\phi), \tag{1.15}
$$

describing its interaction with the gauge bosons, and with the covariant derivative of Equation 1.10. The scalar potential is taken as

$$
V(\phi) = \mu^2\,\phi^\dagger\phi + \lambda\,(\phi^\dagger\phi)^2, \qquad \lambda > 0, \ \ \mu^2 < 0, \tag{1.16}
$$

It depends only on $\phi^\dagger\phi$, so it is invariant under $SU(2)_L \times U(1)_Y$ transformations of ϕ. For $\mu^2 < 0$, the configuration $\phi = 0$ is unstable, and the minimum of the potential occurs for

$$
\phi^\dagger\phi = \frac{v^2}{2}, \qquad v = \sqrt{-\mu^2/\lambda}. \tag{1.17}
$$

The value of v is fixed by the Fermi coupling constant G_F[4], by

$$
v = (\sqrt{2}G_F)^{-\frac{1}{2}} = 246 \text{ GeV}, \tag{1.18}
$$

---

[4]It is calculated numerically from the rate of muon decays [6].

This vacuum expectation value (VEV) breaks the electroweak symmetry, since any specific choice of $\langle\phi\rangle$ is not invariant under the full $SU(2)_L \times U(1)_Y$ group. A convenient parametrization considering fluctuations around the minimum is obtained by fixing the so-called *unitary gauge*[5], where the scalar doublet takes the form

$$\phi(x) = \frac{1}{\sqrt{2}} \begin{pmatrix} 0 \\ v + H(x) \end{pmatrix}, \tag{1.19}$$

with $H(x)$ the Higgs boson field. In this gauge, the charged components are set to zero, while the neutral component acquires a non-zero VEV,

$$\langle\phi\rangle = \frac{1}{\sqrt{2}} \begin{pmatrix} 0 \\ v \end{pmatrix} \tag{1.20}$$

which breaks the gauge invariance $SU(2)_L \times U(1)_Y$, while keeping the subgroup $U(1)_{\text{em}}$ invariant. This makes it possible for the photon to remain massless while the electroweak gauge bosons gain mass.

Substituting ϕ in the form of Equation 1.19 into the kinetic term of $\mathcal{L}_\phi$ in Equation 1.15,

$$\begin{aligned}
\mathcal{L}_\phi \supset\ & m_W^2 \, W_\mu^+ W^{-\mu} \;+\; \frac{1}{2} m_Z^2 \, Z_\mu Z^\mu \\
&+ \frac{2m_W^2}{v} \, H \, W_\mu^+ W^{-\mu} \;+\; \frac{m_Z^2}{v} \, H \, Z_\mu Z^\mu \\
&+ \frac{m_W^2}{v^2} \, H^2 \, W_\mu^+ W^{-\mu} \;+\; \frac{m_Z^2}{2v^2} \, H^2 \, Z_\mu Z^\mu,
\end{aligned} \tag{1.21}$$

where the masses of the electroweak vector bosons are obtained,

$$m_W = \tfrac{1}{2} g v, \qquad m_Z = \tfrac{1}{2} v \sqrt{g^2 + g'^2}. \tag{1.22}$$

The ratio of the W and Z masses returns the Weinberg angle (see Equation 1.13,

$$\cos\theta_W = \frac{m_W}{m_Z}. \tag{1.23}$$

The masses m_W and m_Z were first precisely measured at LEP [41, 42]. The current world averages are [6]:

$$m_W = 80.379 \pm 0.012 \text{ GeV}, \qquad m_Z = 91.1876 \pm 0.0021 \text{ GeV}.$$

Besides generating the masses of the electroweak bosons, the expansion also produces interaction terms between the Higgs field and the W and Z bosons. In particular, Equation 1.21 contains trilinear couplings (HWW, HZZ), that are proportional to the squared masses, $g_{HWW} = 2m_W^2/v$ and $g_{HZZ} = m_Z^2/v$, and quartic couplings ($HHWW$, $HHZZ$).

---

[5]In other gauges, three massless scalar modes (Goldstone bosons) appear. These do not correspond to physical particles, but are absorbed to provide the longitudinal polarization states of the massive $W^\pm$ and Z bosons.

From the scalar potential term of the $\mathcal{L}_\phi$, the Higgs boson mass is defined as,

$$V(\phi) = \mu^2\,\phi^\dagger\phi + \lambda(\phi^\dagger\phi)^2 \;\Rightarrow\; m_H^2 = 2\,\lambda\,v^2. \tag{1.24}$$

Here λ is the Higgs self-coupling and is a free parameter of the SM, meaning that there is no *a priori* prediction of the Higgs boson mass. Experimentally, the Higgs boson mass was measured at CERN (2012) [4, 3]. The most up-to-date value [6, 43] is found to be

$$m_H = 125.11 \pm 0.11 \text{ GeV}. \tag{1.25}$$

Expanding the potential further around the minimum, trilinear and quadrilinear Higgs self-coupling can be found.

Following the same derivation, an additional term can be added to the Lagrangian density to describe the interactions between the Higgs boson and fermions, the so-called Yukawa Lagrangian,

$$\mathcal{L}_Y = -y_e \begin{pmatrix} \nu_e \\ e^- \end{pmatrix}_L^\dagger \phi\, e_R^- - y_u \begin{pmatrix} u \\ d \end{pmatrix}_L^\dagger \tilde{\phi}\, u_R - y_d \begin{pmatrix} u \\ d \end{pmatrix}_L^\dagger \phi\, d_R + \text{h.c.}, \tag{1.26}$$

for the first generation of fermions, where y_e, y_u, y_d are the Yukawa coupling constants, and $\tilde{\phi} = i\sigma^2\phi^*$ is the conjugate Higgs doublet. When the Higgs field acquires its vacuum expectation value, the Yukawa terms generate fermion masses

$$m_e = \frac{y_e v}{\sqrt{2}}, \qquad m_u = \frac{y_u v}{\sqrt{2}}, \qquad m_d = \frac{y_d v}{\sqrt{2}}. \tag{1.27}$$

The same structure extends to the other fermion generations, with independent Yukawa couplings y_f for each fermion f.

The quark mass eigenstates obtained from the Yukawa Lagrangian are not identical to the weak isospin eigenstates, and the mismatch between the weak eigenstates and the mass eigenstates is described by the Cabibbo–Kobayashi–Maskawa (CKM) matrix [44, 45]. This structure is required to account for the observed rates of flavor-changing weak decays. Explicitly, the relation between weak and mass eigenstates for down-type quarks can be written as

$$\begin{pmatrix} d' \\ s' \\ b' \end{pmatrix}_L = V_{\text{CKM}} \begin{pmatrix} d \\ s \\ b \end{pmatrix}_L, \tag{1.28}$$

where primed fields denote weak eigenstates.

The charged-current part of $\mathcal{L}_{\text{EWK}}$ can then be expressed in terms of the CKM matrix, which is a unitary 3×3 matrix. Its elements $V{ij}$ quantify the strength of flavor-changing transitions between quarks $i = (u, c, t)$ and $j = (d, s, b)$ mediated by the $W^\pm$ bosons. One of the possible parametrization of the is given by three mixing angles and one CP-violating phase, corresponding to four independent free parameters determined experimentally. Numerically, the matrix is approximately [6]

$$V_{\text{CKM}} \simeq \begin{pmatrix} |V_{ud}| & |V_{us}| & |V_{ub}| \\ |V_{cd}| & |V_{cs}| & |V_{cb}| \\ |V_{td}| & |V_{ts}| & |V_{tb}| \end{pmatrix} \simeq \begin{pmatrix} 0.974 & 0.226 & 0.0036 \\ 0.226 & 0.973 & 0.042 \\ 0.0086 & 0.041 & 0.999 \end{pmatrix}. \tag{1.29}$$

The values of the diagonal elements indicate that transitions within the same generation are strongly favored, for example, $u \to d$. The off-diagonal elements show how much the probability of flavor-changing transitions between different generations is suppressed.

Finally, the Higgs field is defined as a singlet under $SU(3)_c$, so it does not couple directly to gluons, consistently with the fact that gluons are massless.

1.2 The physics of p–p collisions and the energy scale

At particle colliders, elementary particles are produced and studied through inelastic scattering experiments. Given two colliding initial state particles with four-momenta P_1 and P_2, the $\sqrt{s}$ is defined as

$$\sqrt{s} = (P_1 + P_2), \tag{1.30}$$

which sets the energy scale of the interaction and must be sufficiently high to produce massive particles.

In the context of this work, p–p collision data are analyzed. Given a flux of particles, the number of interactions per unit flux is determined by the cross-section σ, expressed in barn [b], where $1\,\mathrm{b} \equiv 10^{-28}\,\mathrm{m}^2$. In quantum field theory, interaction probabilities are derived from S-matrix elements,

$$\mathcal{M}_{fi} = \langle f|S|i \rangle$$
$$S \propto \exp\!\Big[i \int d^4x \, \mathcal{L}_{\mathrm{int}}(x)\Big] \tag{1.31}$$

with i and f being the initial and final state, respectively.

The measurable cross-section follows from the squared amplitude of the matrix elements integrated over final-state phase space and normalized by the initial-state flux. Expanding S as a power expansion in the strong coupling constant α_s, the cross-section can be expressed as a

$$\sigma = \sigma^{(0)} + \alpha_s \, \sigma^{(1)} + \alpha_s^2 \, \sigma^{(2)} + \cdots . \tag{1.32}$$

The precision of the cross-section calculation is therefore intrinsically linked to the value of α_s. Truncating the series at the first term defines the leading order (LO), while including the next term corresponds to the next-to-leading order (NLO), and so on. Lower-order predictions generally suffer from large theoretical uncertainties due to missing corrections and a strong dependence on scale choices.

The strong coupling constant is not a fixed parameter but depends on the characteristic energy scale Q of the process, as described by the renormalization group equation,

$$\alpha_s(Q^2) = \frac{1}{\beta_0 \ln\!\big(Q^2/\Lambda_{\mathrm{QCD}}^2\big)}, \tag{1.33}$$

with β_0 being the first coefficient of the QCD β-function and Λ_{QCD} being the QCD scale parameter. From this relation, the *asymptotic freedom* condition

is visible: α_s becomes small at high energies, while it increases at low scales, reaching zero when the energy scale goes to infinity.

This implies that partons inside the protons can be treated as free at the energy scale of p–p collisions, and the interaction can be approximated as a collision between partons rather than between protons. The momentum of a parton is expressed as a fraction x of the parent hadron momentum, $p_{\text{parton}} = x\, p_{\text{hadron}}$, where x is the Bjorken scaling variable [46]. The probability of finding a parton of flavor f carrying momentum fraction x at a factorization scale μ_F is described by the parton distribution function (PDF), $\text{PDF}_f(x, \mu_F^2)$. The PDFs satisfy the momentum sum rule

$$\sum_f \int_0^1 x\,\text{PDF}_f(x, \mu_F^2)\, dx = 1\,,$$

ensuring that the total hadron momentum is carried and distributed by its partons.

By measuring PDFs at a given scale μ_F, their evolution to any other scale can be obtained by solving the DGLAP equations [47, 48, 49]. In the case of hadronic collisions, the factorization scale μ_F is introduced to separate the non-perturbative parton distribution functions from the perturbatively hard scattering. Different global analyses provide sets of PDF determinations to describe p–p collisions. In the context of this thesis, the NNPDF set [50] (version 3.1) is used, accessed through the `LHAPDF` library [51], and is shown in Figure 1.2 at a factorization scale of $\mu_F^2 = 10$ GeV^2 and $\mu_F^2 = 10^4$ GeV^2 a function of x. Figure 1.2 shows that at large x the valence quarks PDFs dominate, whereas at small x the gluon and sea quarks PDFs dominate.
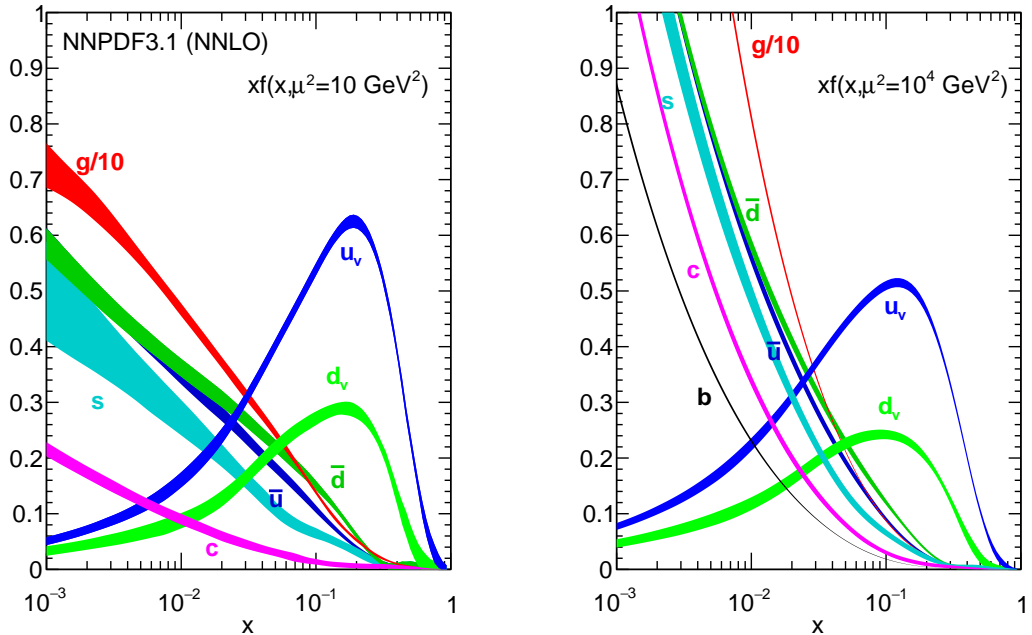

Figure 1.2: The NNPDF3.1 PDFs, evaluated at $\mu_F^2 = 10$ GeV^2 (left) and $\mu_F^2 = 10^4$ GeV^2 (right) [50, 51].

The scattering can thus be understood in terms of quasi-free partons, and the total cross-section can be written in terms of the partonic cross-sections $\hat{\sigma}(f_1 f_2 \rightarrow X)$ as

$$\sigma(pp \rightarrow X) = \sum_{f_1, f_2} \int dx_1 \, dx_2 \, \mathrm{PDF}_{f_1}(x_1, \mu_F^2) \, \mathrm{PDF}_{f_2}(x_2, \mu_F^2) \, \hat{\sigma}(f_1 f_2 \rightarrow X) , \quad (1.34)$$

where $\mathrm{PDF}_{f_i}(x_i, \mu_F^2)$ are the parton distribution functions (PDFs) of flavor f_i carrying momentum fraction x_i at scale μ_F^2.

At high energies, ultraviolet quantum fluctuations become relevant, corresponding to short-distance interactions. Their associated divergences are absorbed through the process of renormalization, which redefines the coupling and the fields. This introduces the renormalization scale μ_R, at which the strong coupling $\alpha_s(\mu_R)$ is defined. Neither μ_R nor μ_F is a physical parameter, and the total scattering cross-section is independent of them. At finite order in perturbation theory, however, a residual dependence remains, which is used to estimate the theoretical uncertainty. The standard procedure is to vary μ_R and μ_F simultaneously, and independently, within a prescribed range to define the theoretical uncertainty on cross-section predictions in QCD.

1.2.1 The top quark

As visible in Figure 1.1, the heaviest fundamental particle in the SM is the top quark, with a mass of $m_t = 172.56 \pm 0.31 \, \mathrm{GeV}$ [6]. The Yukawa coupling strength relative to the SM expectation (from Equation 1.26) is measured as [6]

$$Y_t = \frac{y_t}{y_t^{\mathrm{SM}}} = 1.16^{+0.24}_{-0.35}, \quad (1.35)$$

being around two orders of magnitude greater than any other Higgs-to-fermion coupling. Therefore, the physics of the top quark is a probe to understand the mechanism of EWK symmetry breaking, and at the same time a means to search for BSM physics. Many BSM models predict the existence of an extended Higgs sector, populated by charged Higgs and heavy Higgs bosons, for which the top coupling is predominant. Other models describe the existence of W' and Z' extensions of the SM, which couple preferentially to top quarks due to their mass. A detailed description of these BSM theories is given in Section 1.3, and searching for evidence for these theories is one of the main focuses of this thesis.

In p–p collisions, the dominant production mechanism of top quarks is top–antitop pair production ($t\bar{t}$), which occurs at LO through $q\bar{q}$ annihilation and gg fusion (together accounting for about 90% of the total at $\sqrt{s}$ of 13 TeV [52]), as shown in the Feynman diagrams of Figure 1.3. The production of $t\bar{t}$ pairs can also occur in association with additional quarks or gluons, usually light quarks (u, d, s, c) or gluons, which arise from initial-state radiation (ISR), emitted from the incoming partons before the hard scattering or final-state radiation (FSR), emitted from the outgoing partons after the hard scattering). Figure 1.4 shows these production mechanisms. In the context of this thesis and the search for new BSM particles, these associated processes constitute the main source of background for the analysis.
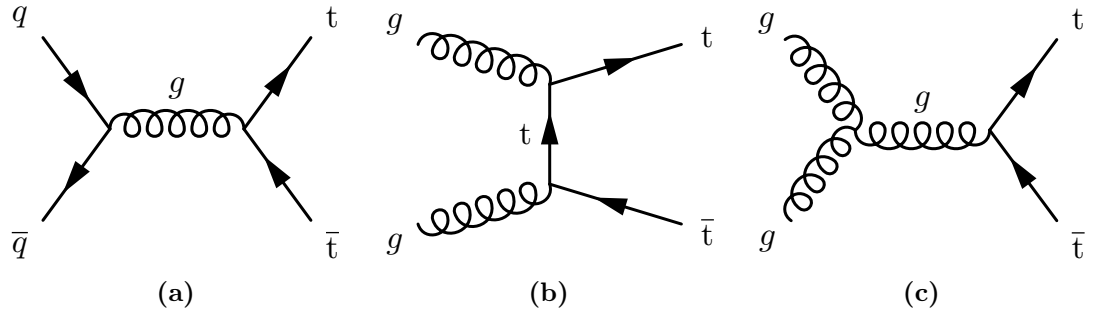
Figure 1.3: Feynman diagrams of $t\bar{t}$ production at LO: (a) quark fusion; (b,c) gluon fusion.
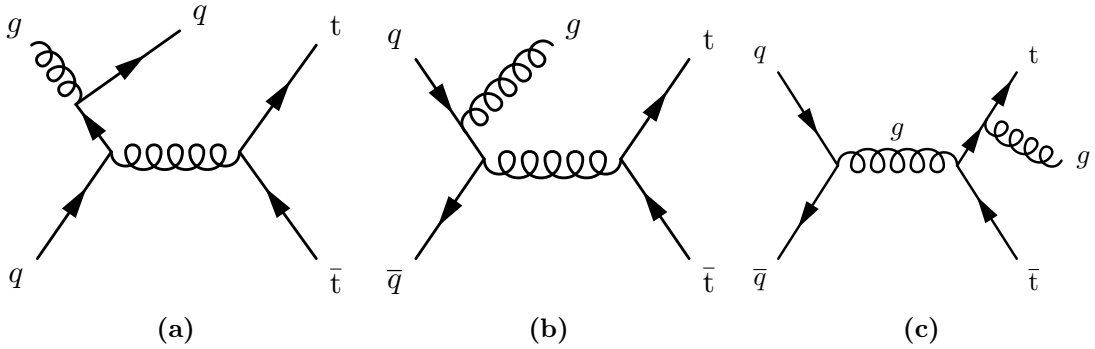

Figure 1.4: Feynman diagrams of $t\bar{t}$ production with additional radiation: (a) ISR; (b,c) FSR.

Another notable production mechanism is single top quark production, which occurs via the weak interaction and proceeds through three main channels: the s-channel ($q\bar{q}$ annihilation), the t-channel (gq fusion), and the tW channel, where a W boson appears in the final state. Figure 1.5 shows these production mechanisms.
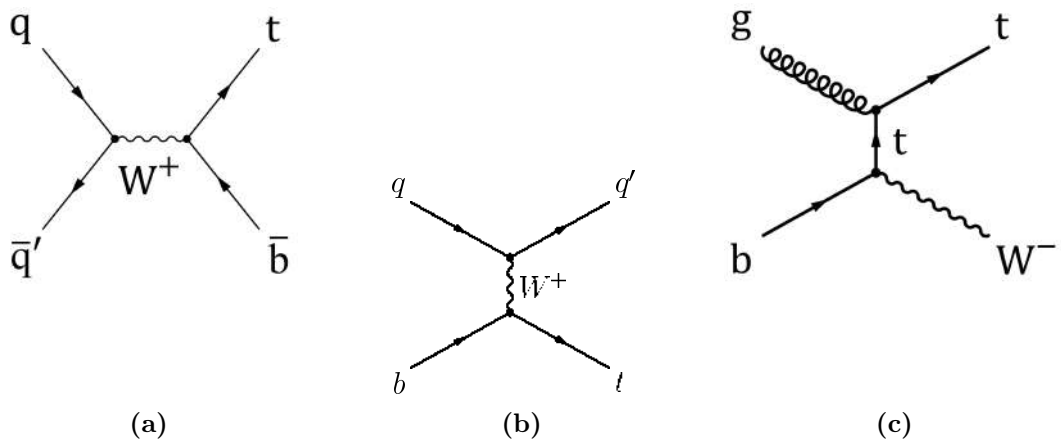
Figure 1.5: Feynman diagrams of single top quark production: (a) s-channel; (b) t-channel, (c) tW channel. The charge-conjugated processes lead to the production of single anti-top quarks, but not shown in the diagrams.

In addition to $t\bar{t}$ and single top production, the top quark can also be produced in association with one or more bosons. In the context of this thesis, a minor but non-negligible source of background in the search for four-top final states is given by $t\bar{t}Z$, $t\bar{t}W$, and $t\bar{t}H$ production. Figure 1.6 illustrates these processes.
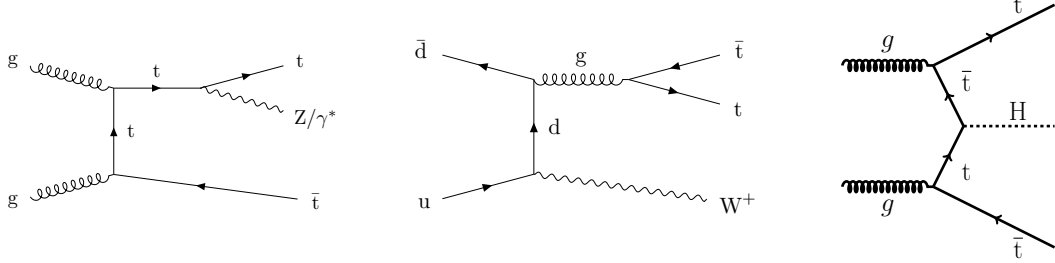

Figure 1.6: Feynman diagrams of $t\bar{t}$ production in association with Z (*left*), W (*center*), and H (*right*) bosons.

Moreover, the SM predicts the production of four top quarks ($t\bar{t}t\bar{t}$). Figure 1.7 shows the production mechanisms, which happen predominantly via gluon fusion, or via the exchange of a virtual Z/γ (b), or via the exchange of a virtual H. This process is extremely rare, with a cross-section at $\sqrt{s} = 13$ TeV of about 12 fb [53, 54], nearly three orders of magnitude smaller than the inclusive $t\bar{t}$ production. The $t\bar{t}t\bar{t}$ production is highly sensitive to potential contributions from BSM physics, and it is a promising channel to search for new phenomena.
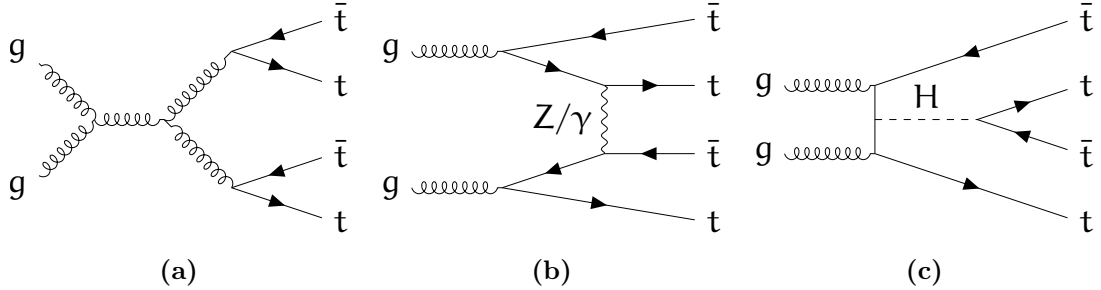

Figure 1.7: Feynman diagrams of $t\bar{t}t\bar{t}$ production: via gluon fusion (a), via the exchange of a virtual Z/γ (b), or via the exchange of a virtual H (c).

The favored decay channel of the top quark is the transition to a b quark via emission of a W boson, since the V_{tb} element of the CKM matrix (Equation 1.29 is close to unity[6], while $V_{ts}, V_{td} \ll V_{tb}$. The decay into an on-shell W boson is also kinematically allowed, given that $m_t > m_W$.

Because of its large mass, the top quark has a very short lifetime, $\tau_t \sim 5 \times 10^{-25}$ s [6], which is shorter than the typical hadronization timescale, $\tau_{\mathrm{had}} \sim 1/\Lambda_{\mathrm{QCD}} \sim 3 \times 10^{-24}$ s [6]. As a result, the top quark decays before it can hadronize or radiate significant soft gluons. This unique feature enables the top to retain information about its spin at the parton level, allowing the study of top-quark polarization and spin correlations through the angular distributions of its decay products. Given the top quark decay, three classes of $t\bar{t}$ final states can be identified, depending on the decay of the two W bosons:

---

[6] In this thesis it is assumed to be 1.

- **Fully hadronic:** both $W \to q\bar{q}'$, about 46% of events.

- **Semileptonic:** one $W \to q\bar{q}'$, the other $W \to \ell\nu_\ell$ with $\ell = e, \mu$, about 44% of events.

- **Dileptonic:** both $W \to \ell\nu_\ell$, about 10% of events.

In this thesis, semileptonic and dileptonic channels involving τ leptons are not considered, since hadronic τ decays require dedicated reconstruction techniques and their overall contribution is relatively small (about 7% for semileptonic $t\bar{t}$ and about 1% for dileptonic $t\bar{t}$). Extending this classification to four-top final states, the following channels are obtained:

- **Fully hadronic:** all four $W \to q\bar{q}'$, about 21% of events,

- **Semileptonic:** three $W \to q\bar{q}'$, one $W \to \ell\nu_\ell$, about 41% of events,

- **Dileptonic:** two $W \to q\bar{q}'$, two $W \to \ell\nu_\ell$, about 31% of events,

- **Trileptonic:** one $W \to q\bar{q}'$, three $W \to \ell\nu_\ell$, about 6% of events,

- **Tetraleptonic:** all four $W \to \ell\nu_\ell$, about 1% of events.

The analysis presented in this thesis focuses on the search for top-philic BSM resonance in four top quark final states in the dileptonic channel, which provides the cleanest signature and most efficient reconstruction compared to the fully hadronic channel, where large QCD backgrounds dominate. The focus is on opposite-sign dilepton events, which have a higher branching fraction and enable the identification of the non-resonant top quarks. This topology allows full kinematic and mass-resonance reconstruction of the hadronically decaying top quarks originating from the potential BSM resonance, unlike the same-sign dilepton selection.

1.3   Physics Beyond the Standard Model

The SM provides a precise and tested description of the interactions between fundamental particles, supported by a large number of experimental results. However, it is by construction not complete, and a more fundamental theory is required. In addition, some experimental observations cannot be explained within the SM. Notable shortcomings are

- **Gravity:** the most obvious omission in the SM is gravity. It is not included because it is much weaker than the other fundamental forces, but it becomes non-negligible at the Planck scale of about 10^{19} GeV. The existence of a massless spin-2 particle, the graviton, is postulated in the framework of quantum gravity [55].

- **Hierarchy problem:** the problem refers to the large difference in energy scales, between the experimentally measured Higgs boson mass of about 125 GeV and the Planck scale ($\sim 10^{19}$ GeV). Quantum corrections to the

Higgs mass, for example from top-quark loops, scale quadratically with the energy cutoff scale Λ,

$$\delta m_H^2 \sim -\frac{|y_t|^2}{8\pi^2}\Lambda^2. \tag{1.36}$$

where y_t is the top Yukawa coupling. If Λ is taken close to the Planck scale, these corrections are enormously larger than the physical Higgs mass, and an extreme fine-tuning is needed to keep $m_H \approx 125$ GeV, which is considered not "natural".

- **Flavor structure:** the SM contains three generations of fermions with identical gauge quantum numbers but vastly different masses. The model does not explain why exactly three generations exist, nor the pattern of the fermion masses and mixing angles observed in the quark and lepton sectors.

- **Baryon asymmetry:** there is a clear asymmetry between baryons and antibaryons, and therefore between matter and antimatter. This suggests that in the early universe, during the Big Bang, C and CP symmetries were violated, leading to the depletion of antimatter; otherwise, they would have constantly annihilated into photons. The observed baryon-to-photon ratio is $\simeq 6 \times 10^{-10}$ [56], which cannot be explained by the SM alone, as neither its predictions nor current experimental results account for this asymmetry.

- **Neutrino masses:** the Yukawa Lagrangian of Equation 1.26 assumes that neutrinos are massless. In contrast, there is clear experimental evidence for non-zero neutrino masses from the observation of neutrino oscillations [57, 58]. Neutrino oscillations arise because the flavor eigenstates of neutrinos are quantum superpositions of their mass eigenstates. To introduce neutrino masses, the SM must be extended by introducing additional terms, such as Majorana[7] or Dirac mass terms. A possible extension involves the existence of sterile neutrinos, which do not interact via the weak force and could mix with the active neutrinos, which may explain neutrino masses, baryon asymmetry, and dark matter.

- **Dark matter:** experimental results from astrophysical and cosmological observations of galaxy rotation curves [59], gravitational lensing [60], and the cosmic microwave background [56], provide evidence for the existence of dark matter: a new form of matter that interacts gravitationally but not via the electroweak or strong forces. At the level of elementary particles, dark matter could be explained by weakly interacting massive particles (WIMPs), but no such candidates are included in the SM.

- **Strong CP problem:** the SM allows a CP-violating term in the $\mathcal{L}_{\mathrm{QCD}}$, but experimental results on the neutron electric dipole moment constrain its coefficient to be unnaturally small, less than about 10^{-10} [61]. No natural explanation is given by the SM, while an extreme fine-tuning, known as the strong CP problem, is needed to explain why CP violation in the strong interaction is so suppressed.

---

[7]A Majorana neutrino is a fermion that is identical to its own antiparticle.

Various models have been proposed to address some of these shortcomings of the SM, which predict new particles and phenomena potentially observable at the TeV scale. In particular, searches for resonances decaying to $t\bar{t}$ pairs are well motivated, since many extensions of the SM predict such states. For example, in the Randall–Sundrum model [62] the presence of an extra spatial dimension leads to massive Kaluza–Klein [63] excitations that can couple strongly to top quarks. In compositeness models, where SM particles are not considered elementary, new excited states of fermions [64] and of the Higgs boson sector [65] can appear, some of which are expected to decay preferentially into $t\bar{t}$, if the resonance is massive enough.

Most experimental analyses consider models in which a $t\bar{t}$ resonance is produced via annihilation of a $q\bar{q}$ pair. However, if the resonance couples only weakly, or not at all, to light quarks, the production of the resonance in association with an additional $t\bar{t}$ pair provides an important channel to study and is the main focus of the analysis presented in this work.

In the context of the thesis and in the following, the model-independent production of a top-philic resonance is considered, assuming that it strongly couples to the top quark pair. The resonance could be either a vector, a scalar, or a pseudoscalar. General models are introduced that describe the associated production of new particles with $t\bar{t}$, which would be observable in p–p collisions as a heavy resonance decaying to $t\bar{t}$.

1.3.1 Top-philic heavy resonances in four top quarks final states

The benchmark models used in this analysis predict a new vector particle, denoted Z', as postulated in so-called top-philic models [66, 67]. These models assume a color-singlet vector particle of mass $m_{Z'}$, which couples only to the top quark with the following interaction Lagrangian

$$\mathcal{L}_{\text{top-philic}} = c_t\, t\gamma_\mu \left(\cos\theta P_L + \sin\theta P_R\right) t Z'^\mu + \text{h.c.}, \tag{1.37}$$

where

$$P_{L/R} = \frac{1 \mp \gamma_5}{2}, \qquad c_t = \sqrt{c_L^2 + c_R^2}, \qquad \tan\theta = \frac{c_R}{c_L}, \tag{1.38}$$

where c_t denotes the overall interaction strength, θ controls the relative coupling to left- and right-handed top quarks, and $\gamma^5 = i\gamma^0\gamma^1\gamma^2\gamma^3$ is defined in terms of the Dirac gamma matrices.

The decay width at LO is given by [66]

$$\Gamma(Z' \to t\bar{t}) = \frac{c_t^2\, m_{Z'}}{8\pi} \sqrt{1 - \frac{4m_t^2}{m_{Z'}^2}} \left[1 + \frac{m_t^2}{m_{Z'}^2}\left(3\sin^2\theta - 1\right)\right], \tag{1.39}$$

which can be approximated to

$$\Gamma(Z' \to t\bar{t}) \simeq \frac{c_t^2\, m_{Z'}}{8\pi}, \qquad \text{for } m_t \ll m_{Z'}. \tag{1.40}$$

In p–p collisions, the production mechanism of Z' in association with a $t\bar{t}$ pair targeted for the thesis work is via strong force from gg fusion, and is shown in Figure 1.8.
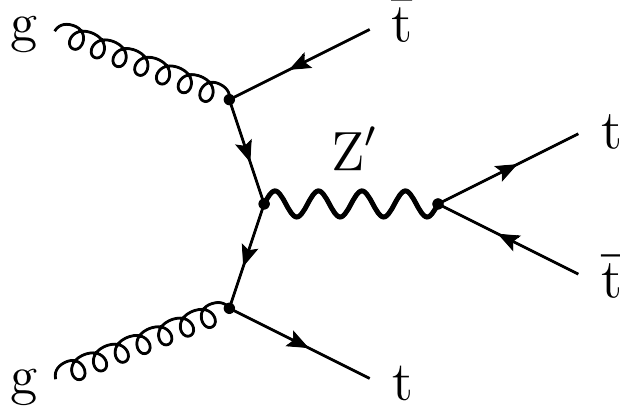

Figure 1.8: Feynman diagrams of associated production of Z' with $t\bar{t}$ at LO.

Other production mechanisms are possible, via mixed QCD and electroweak interactions, resulting in three top quark final states. Moreover, loop-induced production via virtual top quarks is also possible but suppressed in this work by requiring an equal coupling strength for left- and right-handed top quarks, namely $\theta = \pi/4$.

To ensure the validity of Equation 1.40, the target mass range spans from 500 GeV to 4 TeV, and 5%, 10%, 20%, and 50% decay widths are considered. More details are provided in Chapter 7, where the search is presented and motivated by recent complementary results.

Moreover, interference between the Z' signal and the SM four top quarks background, as well as non-resonant Z' contributions, are not considered. While such interference effects can increase the total cross-section for large resonance masses and widths, the resulting kinematic distributions, such as the invariant mass spectrum $m_{t\bar{t}}$), are nearly indistinguishable from the SM prediction, resulting in a much complex discrimination between signal and SM background events. In addition, interference contributions are highly model-dependent, as they depend on the assumed couplings of the Z' to other quarks and gauge bosons.

1.3.2 Two Higgs doublet model and Axion-like particles

In addition to the Higgs sector of the SM, other models, such as type-II Higgs Doublet Model (2HDM) [68, 69], predict the existence of other spin-0 states through the inclusion of another doublet, another singlet, or a combination of the two. The new states of these extensions may include a neutral pseudoscalar a (CP-odd) boson, neutral scalar (CP-even) h and ϕ bosons, where h is the lighter of the two, and a charged Higgs boson $H^{\pm}$. Assuming that the new bosons also interact with fermions via the Yukawa interaction, the coupling between them and the top quark is expected to be large as well. Therefore, the Yukawa Lagrangian after the symmetry breaking assumes

$$\mathcal{L}_{\text{int}}^{\phi} = -g_{\phi t\bar{t}}\frac{m_t}{v}\bar{t}t\phi$$

$$\mathcal{L}_{\text{int}}^{a} = ig_{at\bar{t}}\frac{m_t}{v}\bar{t}\gamma_5 ta, \qquad (1.41)$$

where $g_{\phi t\bar{t}}$ and $g_{at\bar{t}}$ are respectively the coupling constants of the scalar and pseudoscalar mediators to top quarks, v is the vacuum expectation value of the Higgs field, and m_t is the top quark mass.

Axion-like particles (ALPs) represent another compelling class of models in the context of BSM physics, introducing a new singlet pseudoscalar state A. Originally proposed as a solution to the strong CP problem [70, 71], the framework can be extended to address neutrino mass generation, composite Higgs scenarios, and dark matter, among others. In the context of the thesis, only a specific top-philic ALPs model is considered, where the interaction Lagrangian, after spontaneous symmetry breaking, is

$$\mathcal{L}_{\text{int}}^{A} = ic_t^A \frac{m_t}{f_A}\bar{t}\gamma_5 tA, \qquad (1.42)$$

where c_t is the ALP coupling to top quarks and f_A the scale of the effective theory via which the ALP couples to top quarks.

Chapter 2

The CMS experiment

The work presented in this thesis was conducted within the CMS Collaboration at European Organization for Nuclear Research (CERN), and comprises both data analysis of p–p collisions recorded at centre-of-mass energies, $\sqrt{s}$ of 13 TeV and 13.6 TeV during LHC data-taking campaigns, and detector development. In this chapter, the experimental setup is described. In Section 2.1, an overview of the LHC is provided. Section 2.2 describes in detail the CMS apparatus alongside its sub-detector systems. Major emphasis is given to the calorimeter systems, and a brief introduction to calorimetry is also provided.

2.1 The Large Hadron Collider

The LHC is a synchrotron particle accelerator ring with a circumference of 26.7 km, designed to collide protons or heavy ions. It is located at the CERN in Geneva and is the last and largest ring in the complex chain of CERN's accelerators, shown in Figure 2.1. The tunnel is approximately 100 m underground and was constructed between 1998 and 2008 in the existing tunnel of the former Large Electron-Positron Collider. The LHC ring is composed of two beam pipes that can each be filled with up to 2800 bunches, with bunch crossing (BX)s spaced by 25 ns. During Run 1 (2010–2013), the proton beams collided at $\sqrt{s}$ of 7 and 8 TeV, while in Run 2 (2015–2018) the energy was increased to 13 TeV. In the current data-taking period (Run 3), the operational energy is 13.6 TeV, with plans to reach up to 14 TeV during the last phase of operations called HL-LHC phase, described in detail in Chapter 3.

Protons are first obtained by ionizing hydrogen gas with an electric field and then accelerated through a chain of pre-accelerators. The first accelerator is Linac4 [72], a linear accelerator that uses radio-frequency (RF) cavities to accelerate the protons to an energy of 160 MeV. From Linac4, protons are injected into the Proton Synchrotron Booster (PSB) and then into the Proton Synchrotron (PS), reaching energies of 1.4 GeV and 25 GeV, respectively. They are then transferred to the Super Proton Synchrotron (SPS), where they are accelerated up to 450 GeV. From the SPS, the protons are injected into the two beam pipes of the LHC, where they undergo multiple acceleration cycles until the beam energy reaches its operational value. The acceleration is made possible by four groups of radio-frequency cavities, called cryomodules, which operate in a superconducting state. In addition to accelerating the beam, the LHC bends and focuses the

proton bunches using superconducting magnets, which are cooled to 2 K with superfluid helium. More than 1000 dipole magnets bend and guide the beam, with the magnetic field increasing from 0.535 T during injection up to 8.3 T at collision energy. Once the ramp-up is complete, the beam is declared stable, and the protons are focused and brought into collision at four dedicated interaction points along the ring, where the four major *experiments* are located, as visible in Figure 2.1.
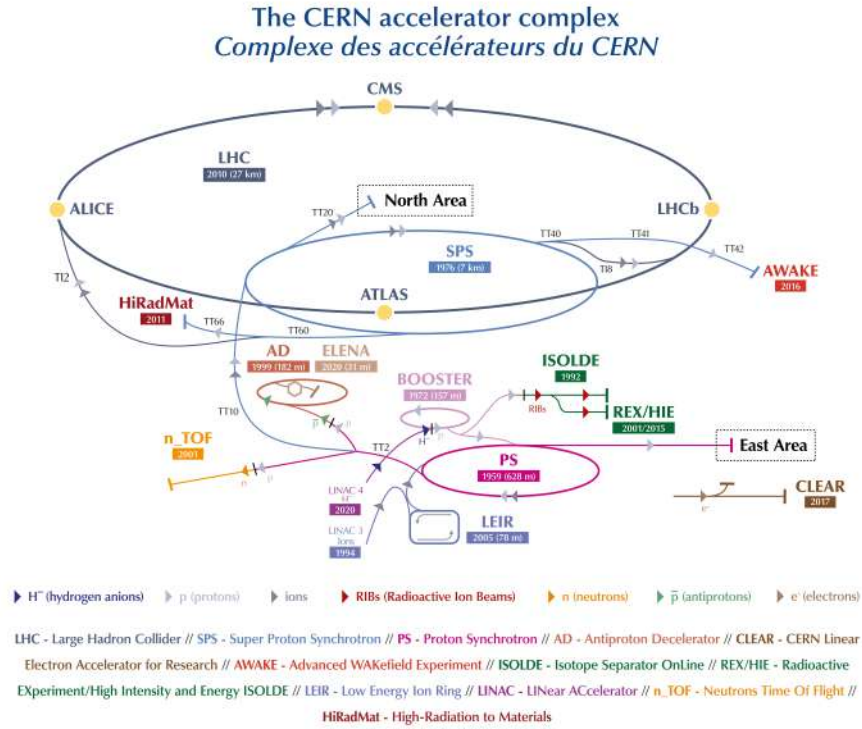

Figure 2.1: Illustration of the CERN accelerator complex [73].

These experiments are: A Large Ion Collider Experiment (ALICE), A Toroidal LHC Apparatus (ATLAS), CMS (Compact Muon Solenoid), and LHCb (LHC beauty). The ATLAS and CMS experiments are multipurpose detectors, designed to discover the Higgs boson, to precision SM measurements and investigate BSM theories. ALICE focuses on studying quark-gluon plasma created in heavy ion collisions, while LHCb examines particles produced in the forward region, focusing on the study of heavy-flavoured mesons and, in particular, b quark physics.

Along with $\sqrt{s}$, another key parameter in collider experiments is the instantaneous luminosity $\mathcal{L}$, which measures the number of particle collisions N per unit time relative to the interaction cross section σ, and is defined as follows

$$L = \frac{1}{\sigma}\frac{dN}{dt}$$

The interaction cross section of p–p collision at 13 and 13.6 TeV is assumed to be 80 mb [74]. The luminosity depends on various LHC parameters, such as the bunch revolution frequency[1] f_r, the number of particles in each bunch

---

[1]In Run 2 operation, f_r was approximately 40 MHz

n, the number of bunches N_b, and the effective collision area transverse to the beam direction, which is assumed to be Gaussian distributed. Assuming that each beam has the same collision area, the luminosity is defined alternatively as

$$L = N_b f_r \frac{n_1 n_2}{4\pi\sigma_x\sigma_y}$$

where and σ_x and σ_y are the beam sizes in x and y direction, transverse to the beam direction[2]. At LHC, each beam is made of about 2800 bunches, separated by 25 ns intervals, and each bunch contains $\mathcal{O}(10^{11})$ of protons. The highest instantaneous luminosity recorded at the LHC is approximately 2.5×10^{34} cm^{-2}s^{-1} during Run 3 operation, exceeding the original design value of 1×10^{34} cm^{-2}s^{-1}. The HL-LHC upgrade aims to reach up to 7.5×10^{34} cm^{-2}s^{-1}.

By integrating the instantaneous luminosity over time, the total delivered luminosity is obtained per unit cross section. The size of a data-taking period is therefore usually measured in integrated luminosity, and the evolution of the total luminosity delivered to CMS during stable beams for p–p collisions at nominal $\sqrt{s}$ is shown in Figure 2.2. In the context of the analysis presented in this thesis, the data recorded by CMS during Run 2 (2016–2018) and Run 3 (2022) are considered, for a total integrated luminosity of 173 fb^{-1}.
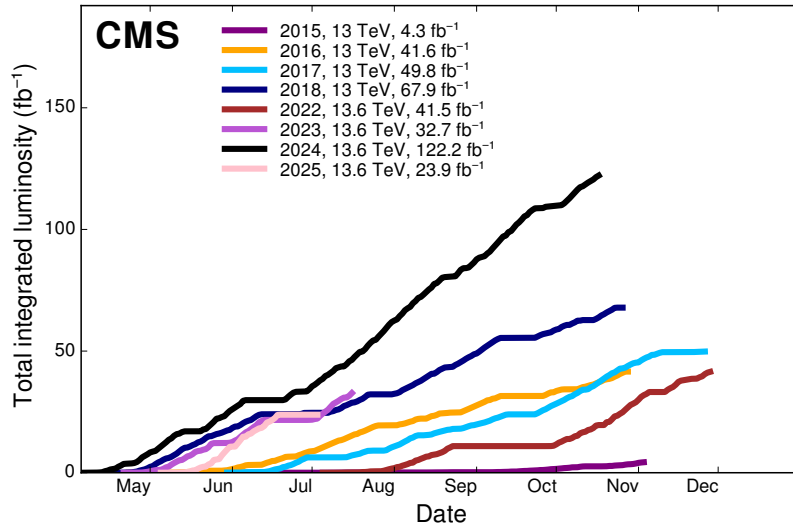
Figure 2.2: Total integrated luminosity versus day delivered to CMS during stable beams for p–p collisions at nominal $\sqrt{s}$ shown for data-taking in 2015 (purple), 2016 (orange), 2017 (light blue), 2018 (navy blue), 2022 (brown), 2023 (light purple), 2024 (dark blue), 2025 (pink) [74].

Multiple p–p collisions occur within each BX, but only the highest-energy interaction is typically used for the physics analysis. The additional interactions are classified as *pileup* (PU) and constitute background collisions that can occur in the same BX (in-time PU) or in previous BXs (out-of-time PU). The average

[2]The widths σ_x and σ_y are about 16 μm

number of PU interactions per BX recorded by CMS was approximately 32 during Run 2 and has reached up to about 55 during Run 3 [74].

2.2 Overview of the CMS detector

The CMS experiment is a multi-purpose detector located at the interaction point 5 of LHC in Cessy, France. The detector has a cylindrical structure with a length of 21.6 m and a diameter of 14.6 m. It comprises several sub-detectors arranged in a central barrel region and two endcap regions, covering a solid angle of nearly 4π. Each system is dedicated to measuring and reconstructing different particles and observables. Comprehensive details can be found in Refs. [75, 76], while an outline relevant to this work is provided below.

The first sub-detector, starting from the interaction point and moving outwards, is the tracking system, which consists of a silicon pixel and strip tracker where the trajectories of charged particles are measured. Surrounding the tracking system are the lead tungstate crystal electromagnetic calorimeter (ECAL) and the brass and scintillator hadron calorimeter (HCAL). These calorimeters are enclosed within[3] the coil of a large superconducting solenoid magnet, which has an internal diameter of 6 m and generates a magnetic field of 3.8 T. The solenoid provides a magnetic field parallel to the beam axis, enabling the measurement of charge and momentum of the particles. Outside the solenoid, the muon detection system is located. It consists of gaseous detectors embedded in the steel flux-return yoke, which guides the magnetic field lines. A schematic overview of the CMS detector is shown in Figure 2.3, and each sub-system is described in detail in the following sections.

2.2.1 Coordinate system

Figure 2.4 shows the conventional three-dimensional coordinate system adopted by the CMS Collaboration. The origin of the coordinate system is centered at the collision point, with the y-axis pointing vertically upward and the x-axis pointing radially inward toward the center of the LHC. Consequently, the z-axis points along the beam direction counterclockwise. Given the symmetrical design of the apparatus, spherical and cylindrical coordinates are also used. The azimuthal angle ϕ is measured from the x-axis in the x–y plane, with the radial coordinate in this plane denoted by r. The polar angle θ is measured from the z-axis.

The three-momentum of particles is described using two components: the longitudinal momentum p_z and the transverse momentum p_T, defined as

$$|\vec{p}_T| = |\vec{p}|\sin\theta = \sqrt{p_x^2 + p_y^2}.$$

Additionally, the pseudorapidity η is often used to describe a particle's angle relative to the z-axis, and is defined as

$$\eta \equiv -\ln\left[\tan\left(\frac{\theta}{2}\right)\right] = \operatorname{arctanh}\left(\frac{p_z}{|\vec{p}|}\right).$$

---

[3]One part of the hadron calorimeter is found outside, as discussed later.
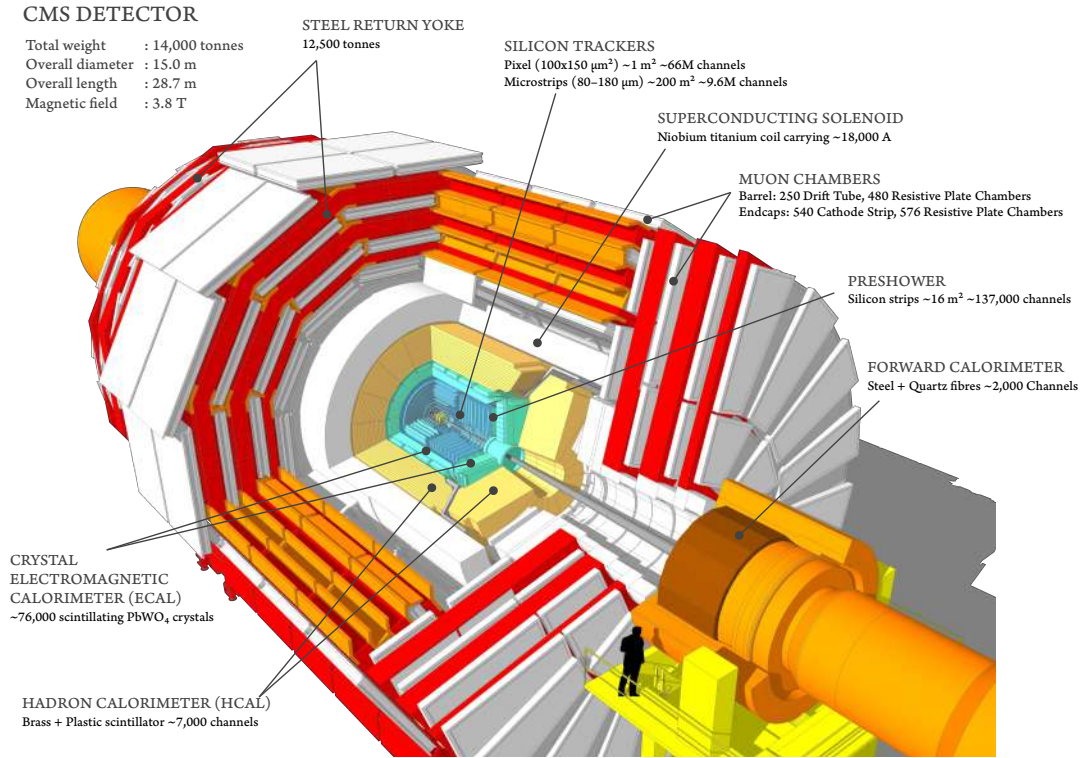
CMS DETECTOR
Total weight   : 14,000 tonnes
Overall diameter : 15.0 m
Overall length   : 28.7 m
Magnetic field   : 3.8 T

STEEL RETURN YOKE
12,500 tonnes

SILICON TRACKERS
Pixel (100x150 μm²) ~1 m² ~66M channels
Microstrips (80–180 μm) ~200 m² ~9.6M channels

SUPERCONDUCTING SOLENOID
Niobium titanium coil carrying ~18,000 A

MUON CHAMBERS
Barrel: 250 Drift Tube, 480 Resistive Plate Chambers
Endcaps: 540 Cathode Strip, 576 Resistive Plate Chambers

PRESHOWER
Silicon strips ~16 m² ~137,000 channels

FORWARD CALORIMETER
Steel + Quartz fibres ~2,000 Channels

CRYSTAL
ELECTROMAGNETIC
CALORIMETER (ECAL)
~76,000 scintillating PbWO₄ crystals

HADRON CALORIMETER (HCAL)
Brass + Plastic scintillator ~7,000 channels

Figure 2.3: Cutaway view of the CMS detector [77].
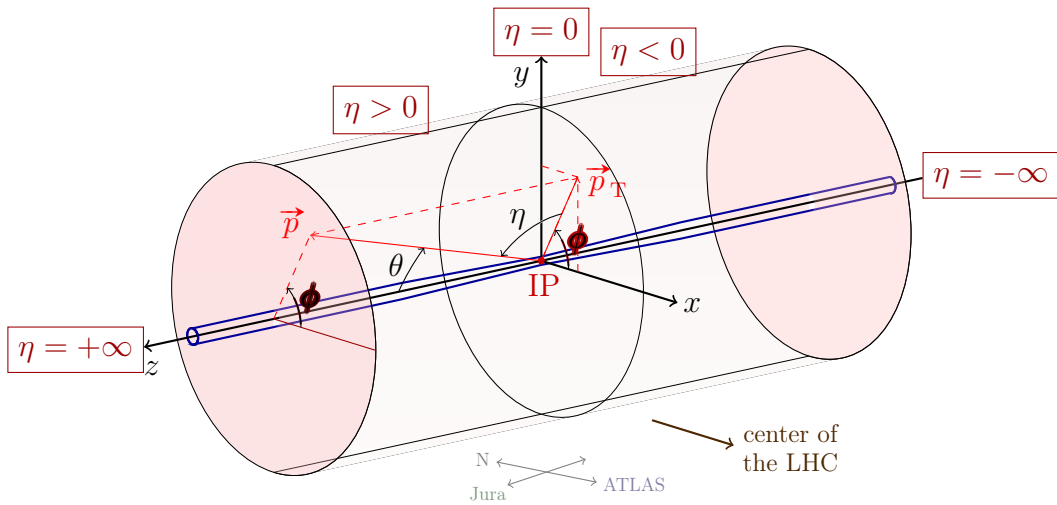
Figure 2.4: The conventional 3D coordinate system at the CMS detector [78].

The region of the detector at high values of $|\eta|$ is commonly referred to as the *forward* region. Particles with high pseudorapidity are therefore described as *forward* particles. In the limit of ultra-relativistic particles, the pseudorapidity converges to the definition of rapidity y,

$$y \equiv \frac{1}{2} \ln \left(\frac{E + p_z}{E - p_z} \right),$$

and differences in rapidity or pseudorapidity are invariant under Lorentz boosts along the z-axis. The angular separation between particles is often measured in the pseudorapidity-azimuth plane using

$$\Delta R \equiv \sqrt{(\Delta \eta)^2 + (\Delta \phi)^2}, \tag{2.1}$$

which is also Lorentz invariant under boosts along the z-axis.

2.2.2 Silicon tracker

The inner tracking system of CMS is designed to provide measurements of the bent trajectories of charged particles emerging from the collisions. It is the first sub-detector moving outwards from the interaction point and has a length of 5.8 m and a diameter of 2.5 m, and it covers a pseudorapidity region of $|\eta| <$ 2.5. It employs silicon detector technology featuring high granularity and fast response, and which is also able to operate in the harsh radiation environment for an expected lifetime of more than 10 years.

The CMS tracker is composed of two sub-systems: a pixel detector with four barrel layers at radii between 4.4 cm and 10.2 cm and a silicon strip tracker with ten barrel detection layers extending outwards to a radius of 1.1 m. Each system is completed by endcaps which consist of two disks in the pixel detector and three plus nine disks in the strip tracker on each side of the barrel. A schematic view of one quadrant of the tracker system is presented in Figure 2.5. With about 200 m^2 of active silicon area, the CMS tracker is the largest silicon tracker ever built [75].
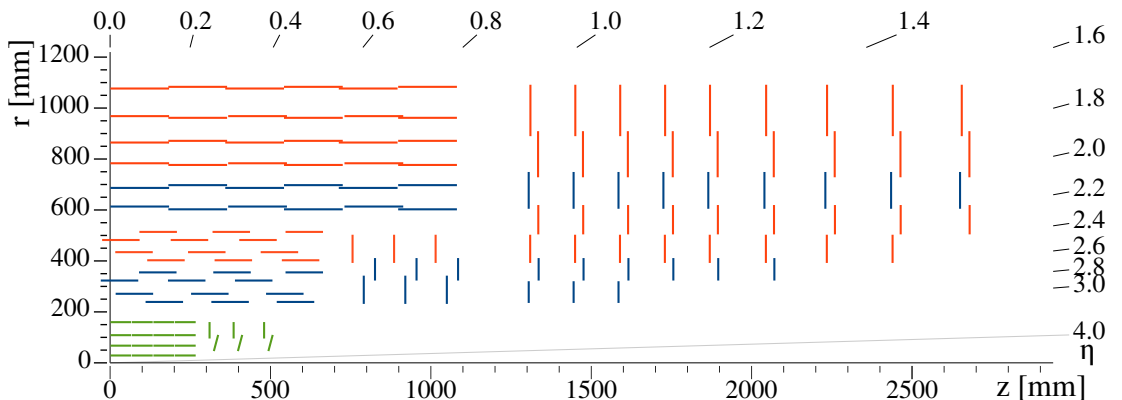
Figure 2.5: Schematic view of one quadrant in the r–z view of the CMS tracker: single-sided and double-sided strip modules are depicted as red and blue segments, respectively. The pixel detector is shown in green [76].

Pixel detector

The first CMS pixel detector design, installed in 2010, consisted of three barrel layers and was operating during Run 1. During Run 2, the instantaneous luminosity delivered by the LHC exceeded the design value, resulting in a pixel detector inefficiency; therefore, an improved version of the detector was installed at the beginning of 2017. The Run 2 detector consists of four barrel layers and an improved version of the electronic readout and cooling system. The basic building block of the detector is a silicon sensor module comprised of a sensor with 160×416 pixels and a pixel size of 100×150 μm^2. In total, 1856 modules are used. To ensure that the inner layer remains fully operational throughout all Run 2, the innermost layer was entirely replaced in 2019.

The two most important parameters to consider for the performance of the pixel detector are the hit efficiency and the pixel spatial resolution, which affect the pattern recognition when reconstructing the track of a charged particle. The average hit efficiency is above 97%, reaching 99% in the forward region. The pixel resolution is measured to be 11.0 μm in the r–ϕ direction and 24.3 μm in the z direction [79].

Strip detector

The silicon strip detector has 9.3 million silicon single-sided p-on-n micro-strips and 198 m^2 of active silicon area distributed over 15,148 modules. The detector is 5 m long and has a diameter of 2.5 m. In the innermost layers of the barrel region, silicon strip sensors with a thickness of 320 μm are used, while in the outermost and endcap regions, strip sensors with a thickness of 500 μm are used. The hit efficiency is about 99.5%, depending on the layer. The single-hit strip resolution is measured to be between 20 and 40 μm, depending on the region and the pitch [80].

2.2.3   Calorimeters

Introduction to calorimetry

The calorimeter systems of the CMS detector are designed to measure the energy of particles as they pass through dense absorber materials, where they are fully absorbed and lose energy by producing cascades of secondary particles, known as *showers*. The characteristics of these showers depend on the incoming particle: electrons and photons generate electromagnetic showers, while hadrons produce hadronic showers involving both electromagnetic and nuclear processes.

At energies above a few tens of MeV, electrons and positrons in most materials lose energy predominantly through bremsstrahlung [6, 81, 82]. In the same energy range, photons interact mainly by producing electron–positron pairs[4]. Electrons, positrons, and photons of sufficiently high energy (typically above 1 GeV, as in LHC p–p collisions) incident on a block of material generate secondary particles through these aforementioned production processes. These secondary particles may, in turn, have sufficient energy to produce other particles through the same

---

[4]At lower energies, the dominant processes are Compton scattering and the photoelectric effect for photons and ionization and excitation for electrons and positrons.

mechanisms, resulting in a shower of particles with progressively decreasing energy. The shower development ceases once the particle energies drop below the *critical energy* [6, 83], where energy loss is dominated by ionization and excitation for electrons and positrons, and by Compton scattering or the photoelectric effect for photons.

The characteristic length scale for electromagnetic showers is the radiation length, X_0, which depends on the characteristics of the material [6, 82],

$$X_0 \simeq \frac{716 \ (\text{g cm}^{-2} A)}{Z(Z+1) \ \ln(287/\sqrt{Z})}, \tag{2.2}$$

where A and Z are the atomic weight and number of the material. The radiation length represents the average distance that an electron needs to travel in a material to reduce via bremsstrahlung $1/e$ of its original energy. Similarly, a photon beam reduces its intensity through pair production to $1/e$, after traveling a distance equal to $7/9 \ X_0$.

The mean longitudinal profile of an electromagnetic shower can be described by a Gamma distribution [82], as a function of the depth in units of radiation length. At the particle energies typical of LHC collisions, electromagnetic calorimeters are relatively compact devices: approximately 95% of the shower energy is contained within a thickness of less than $20 \ X_0$. The transverse development of the shower is characterized by the Molière radius, R_M. A cylinder with radius R_M contains, on average, about 90% of the shower energy, while a radius of 3.5 R_M contains roughly 99% [6]. The Molière radius is related to the material's radiation length X_0 through

$$R_M = X_0 \frac{E_s}{E_c}, \tag{2.3}$$

where $E_s \approx 21$ MeV is a material-independent scale energy, and E_c is the *critical energy* defined by Rossi [83].

The intrinsic energy resolution of an ideal calorimeter, that is, a calorimeter with infinite size and no response deterioration due to instrumental effects, is mainly due to fluctuations of the total track length of the shower. The actual energy resolution of a realistic calorimeter is deteriorated by other contributions, for example, inefficiencies in the signal collection, mechanical non-uniformities, and can be written in a more general way as

$$\left(\frac{\sigma_E}{E}\right)^2 = \left(\frac{S}{\sqrt{E}}\right)^2 + \left(\frac{N}{E}\right)^2 + C^2, \tag{2.4}$$

where S, N, and C are the stochastic, noise, and constant terms [6, 82]. The stochastic term includes the aforementioned shower intrinsic fluctuations. The noise term accounts for the electronic noise of the readout chain, while the constant term accounts for non-uniformities and instrumental effects.

For relativistic charged heavy particles, the mean rate of energy loss per unit length of material is well described by the Bethe–Bloch equation [6], which accounts for inelastic collisions with atomic electrons. The expression can be written as

$$-\left\langle \frac{dE}{dx} \right\rangle = K z^2 \frac{Z}{A} \frac{1}{\beta^2} \left[\frac{1}{2} \ln \left(\frac{2 m_e c^2 \beta^2 \gamma^2 W_{\max}}{I^2} \right) - \beta^2 - \frac{\delta(\beta\gamma)}{2} \right], \qquad (2.5)$$

where $K = 0.307075$ MeV mol^{-1} cm^2, z is the charge of the incident particle, Z and A are the atomic number and mass of the absorber, β and γ are the relativistic factors, m_e is the electron mass, I is the mean excitation energy, $W_{\max}$ is the maximum energy transfer possible in a collision, and δ accounts for density-effect corrections at high energies. This quantity is commonly referred to as the *stopping power*. Its behavior for various particles in different materials is shown in Figure 2.6. The Bethe–Bloch formula is valid in the range $0.1 < \beta\gamma < 1000$, where ionization dominates the energy loss process, and different regimes can be identified within this interval.

At low momenta ($\beta\gamma < 3$), the stopping power decreases with increasing energy, as the cross section for ionization falls with $1/\beta^2$. Around $\beta\gamma \approx 3$, the energy loss reaches a minimum; particles in this region are known as minimum ionising particles (MIP). MIPs are frequently used for detector calibration because their most probable energy loss is well defined and largely material independent. At higher momenta ($3.5 \lesssim \beta\gamma \lesssim 1000$), the energy loss increases slowly, approximately following a logarithmic rise due to relativistic effects and the density correction term. For very high energies ($\beta\gamma > 1000$), radiative processes such as bremsstrahlung, pair production, and photonuclear interactions become dominant, which are characterized by small cross sections, hard spectra, large energy fluctuations, and associated generation of electromagnetic and hadronic showers.

Hadronic calorimetry [6] requires a more detailed description than electromagnetic calorimetry due to the broader variety and complexity of the physical processes involved in shower development and energy deposition. Hadronic showers are initiated by inelastic strong interactions of high-energy hadrons, both charged and neutral, with the atomic nuclei of the absorber material. These interactions produce secondary hadrons and photons, the latter mainly originating from π^0 decays, as well as low-energy neutrons and nuclear fragments. A significant fraction of the primary energy is also released through nuclear processes such as excitation, nucleon evaporation, and spallation, leading to the emission of particles with characteristic energies in the MeV range. While prompt photons from nuclear de-excitations contribute to the measurable signal, recoiling nuclei and low-energy neutrons typically do not. The latter lose kinetic energy through elastic scattering, producing delayed ionization signals on the μs time scale. The energy deposited by these non-detectable components is referred to as invisible energy, and can amount to as much as 40% of the initial hadronic energy, depending on the absorber material and on the energy of the incident particle.

The characteristic length scale for hadronic interactions is the nuclear interaction length λ_I, defined as the mean free path before a hadron undergoes an inelastic collision. It is typically 10 to 30 times larger than the radiation length X_0. The fraction of energy transferred to purely hadronic processes can be parametrized as a power-law function of the incident energy [84, 82], being approximately 0.5 (0.3) for a 100 (1000) GeV incident hadron. Because hadronic interactions are largely charge independent, about one third of the secondary pions produced are neutral (π^0) [82], whose decay photons initiate electromagnetic
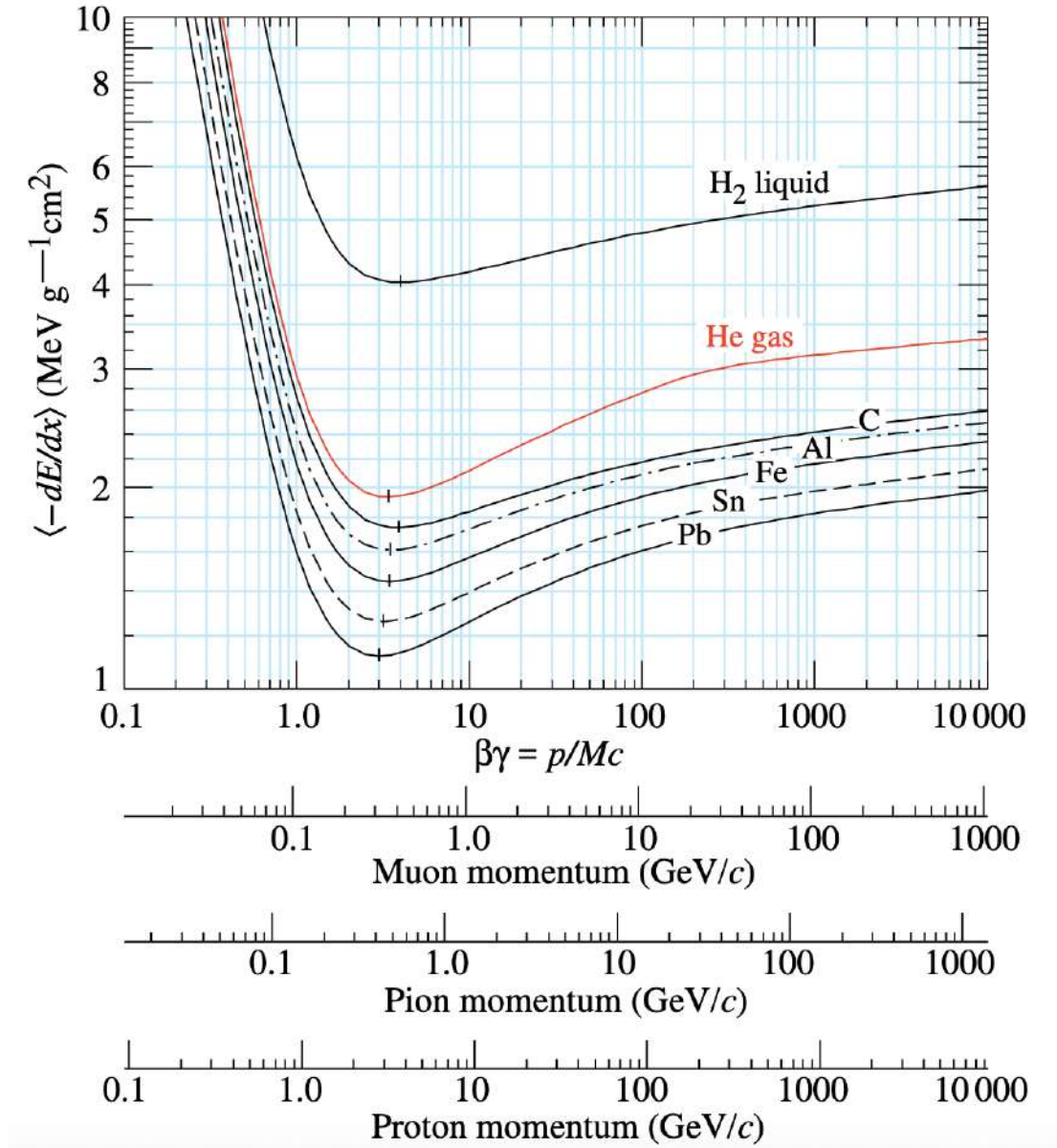
Figure 2.6: Stopping power (Eq. 2.5) times the material density ρ in liquid (bubble chamber) hydrogen, gaseous helium, carbon, aluminum, iron, tin, and lead. Radiative effects, relevant for muons and pions, are not included. These become significant for muons in iron for $\beta\gamma > 1000$, and at lower momenta for muons in higher-Z absorbers [6].

43

subshowers. Capturing this electromagnetic component requires sufficiently fine sampling of the shower. The presence of electromagnetic, hadronic, and invisible components introduces significant event-by-event fluctuations, which directly limit the energy resolution of hadronic calorimeters. Since calorimeters generally have different responses to electromagnetic and hadronic energy depositions, the ratio of these responses, denoted as h/e, is a crucial design parameter, generally smaller than unity [6].

Calorimeters are classified into *sampling* and *homogeneous* calorimeters. Sampling calorimeters consist of alternating layers of an absorber, a dense material used to degrade the energy of the incident particle, and an active medium that provides the detectable signal. Homogeneous calorimeters, on the other hand, are built of only one type of material that performs both the energy degradation and signal generation. To accurately detect both types of showers, the CMS calorimeter system comprises two subsystems: the homogenous electromagnetic calorimeter (ECAL) in the front, and the sampling hadron calorimeter (HCAL) behind.

Electromagnetic calorimeter
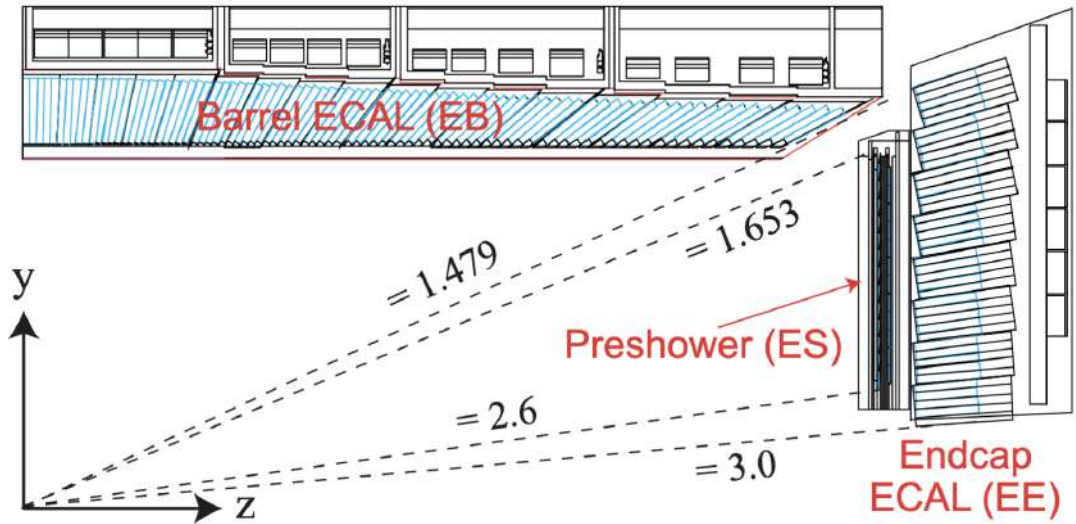
Figure 2.7: Schematic view of one quadrant of the ECAL in the $y - z$ plane [75].

A sketch of the ECAL in the $y - z$ plane is provided in Figure 2.7. The ECAL is placed outside the tracking system and is designed to provide energy and position measurements of photons and electrons. The ECAL is a homogeneous calorimeter consisting of 75,848 lead tungstate ($PbWO_4$) crystals: 61,200 crystals located in the barrel region (EB) and 7,324 in each of the endcaps (EE), providing a pseudorapidity coverage of $|\eta| < 3$. Each lead tungstate crystal has a depth of 23 cm, corresponding to 26 X_0[5]. Given that, for $PbWO_4$, $R_M \approx$ 2.0-2.2 cm [6], the frontal surface of the crystal is chosen to be 2.2×2.2 cm^2. The crystals are arranged in modules, providing a coverage of $\Delta\phi \times \Delta\eta = 0.0175 \times 0.0175$. The scintillation light is detected by silicon avalanche photodiodes (APDs) in the barrel region and vacuum phototriodes (VPTs) in the endcap region.

---

[5]For $PbWO_4$, $X_0 = 0.89$

The depth of the ECAL typically corresponds to approximately $1\ \lambda_I$, meaning that around 70%[6] of all hadronic showers will already begin in the electromagnetic calorimeter. This requires preshower (ES) detectors, which are placed in front of the endcap (EE) detectors, and they consist of silicon sensors interleaved with lead absorber plates, for a total thickness of $3X_0$. They aim to identify two close-by photons from neutral pion decay, allowing for the discrimination of $\pi_0 \to \gamma\gamma$ from γ, and to improve the estimation of the direction of photons.

Given the standard parametrization of the calorimeter energy resolution of Equation 2.4, values of $S = 2.8\%\sqrt{\mathrm{GeV}}$, $N = 0.12$ GeV, and $C = 0.3\%$ [85] were measured with test beam electrons. The scintillation decay time of $PbWO_4$ crystals is of the same order as the LHC bunch-crossing interval: about 80% of the light is emitted within 15 ns [82].

Hadron calorimeter
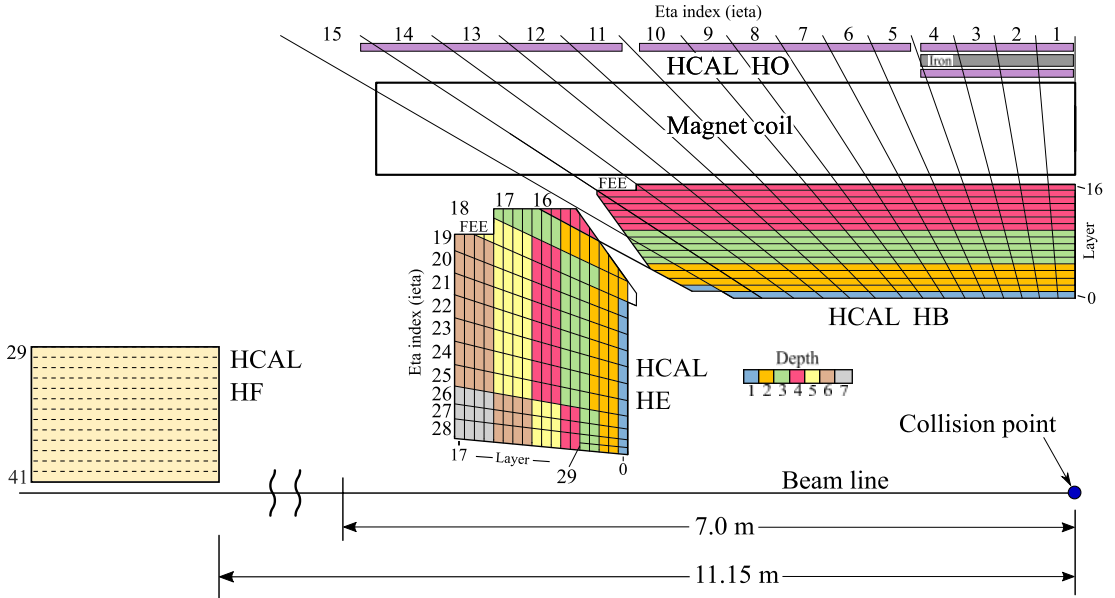
Figure 2.8: Schematic view of the HCAL in the r–η plane at the start of Run 3 operation, showing the positions of its four major components: HB, HE, HO, and HF. The notation *depth* indicates layers that are grouped together [76].

The HCAL is shown schematically in Figure 2.8, and is composed of four major sampling calorimeters sub-detectors: the hadron barrel (HB), hadron endcap (HE), hadron forward (HF), and hadron outer (HO) calorimeters.

The HB and HE cover $|\eta| < 1.392$ and $1.305 < |\eta| < 3.0$, respectively. They are located inside the solenoid magnet and surround the ECAL, and are made of layers of brass plates interleaved with layers of scintillating tiles. The HB consists of 36 identical azimuthal wedges, and the total absorber thickness at $\theta = 90°$ is $5.82\ \lambda_I$. The HB effective thickness increases with θ as $1/\sin\theta$, resulting in 10.6 λ_I at $|\eta| = 1.3$.

The HO provides a measurement of the shower tails in the region $|\eta| < 1.26$. The HF covers $3.0 < |\eta| < 5.2$., and it is a 1.65 m-long sampling calorimeter with steel as absorber and plastic-clad quartz fibers, producing Cherenkov light, with a diameter of 0.6 mm as the active elements for about $10\ \lambda_I$.

45

The HB, HE, and HF underwent major upgrades to replace the originally designed hybrid photodetector (HPD) photodetectors used in Run 1, with the SiPM technology. The motivation was mainly driven by the fact that HPD produced anomalous signals and showed signal degradation. The SiPM technology, which is described in more detail in Section 3.4, has many advantages over the HPD, including higher photon detection efficiency (PDE), higher gain, a larger linear dynamic range, rapid recovery time, better radiation tolerance, and insensitivity to magnetic fields. Moreover, the readout segmentation of the detector increased starting from Run 3, to allow for more accurate damage corrections, reducing the degradation of the resolution.

The energy resolution of the combined ECAL and HCAL systems has been measured in test beams using charged pions to be [86]

$$\frac{\sigma}{E} = \frac{84.7\%}{\sqrt{E}} \oplus 7.6\%$$

where E is in GeV. The HF resolution in test beams is found to be

$$\frac{\sigma}{E} = \frac{280\%}{\sqrt{E}} \oplus 11\%$$

The time resolution for energy deposits in the HB and HE is calculated to be 1.2 ns [86].

The current CMS endcap calorimeter is planned to be replaced by the HGCAL to meet the requirements of the HL-LHC. The work presented in this thesis was carried out in the context of this detector, and its performance results are discussed in detail within the thesis. The description of the upgrade is provided in Chapter 3.

2.2.4 Solenoid magnet

The CMS detector is equipped with a superconducting solenoid magnet that has an inner diameter of 5.9 m and a length of 12.9 m. This magnet encloses the inner tracking system and the calorimeters. The coil consists of four layers of NbTi and generates a uniform magnetic field of 3.8 T and up to 4 T inside the solenoid. This strong field bends the paths of charged particles, enabling precise momentum reconstruction. The magnetic flux is returned through large iron yokes surrounding the magnet, which also serve as support structures for the muon system. In these iron return yokes, the magnetic field ranges from approximately 1.5 T in the inner layers to below 0.5 T in the outermost layers [75].

2.2.5 Muon system

The muon system is the outermost detector of the CMS apparatus, and it is located within the three layers of the return yoke. The muon system comprises four subsystems of gas-ionization detectors: the drift tubes (DTs), the cathode strip chambers (CSCs), the resistive-plate chambers (RPCs), and the gas electron multiplier (GEM) detectors. The system is designed to identify and reconstruct muons, which can pass through the entire CMS detector volume, reaching the detectors without considerable energy loss. Each muon hit position is recorded,
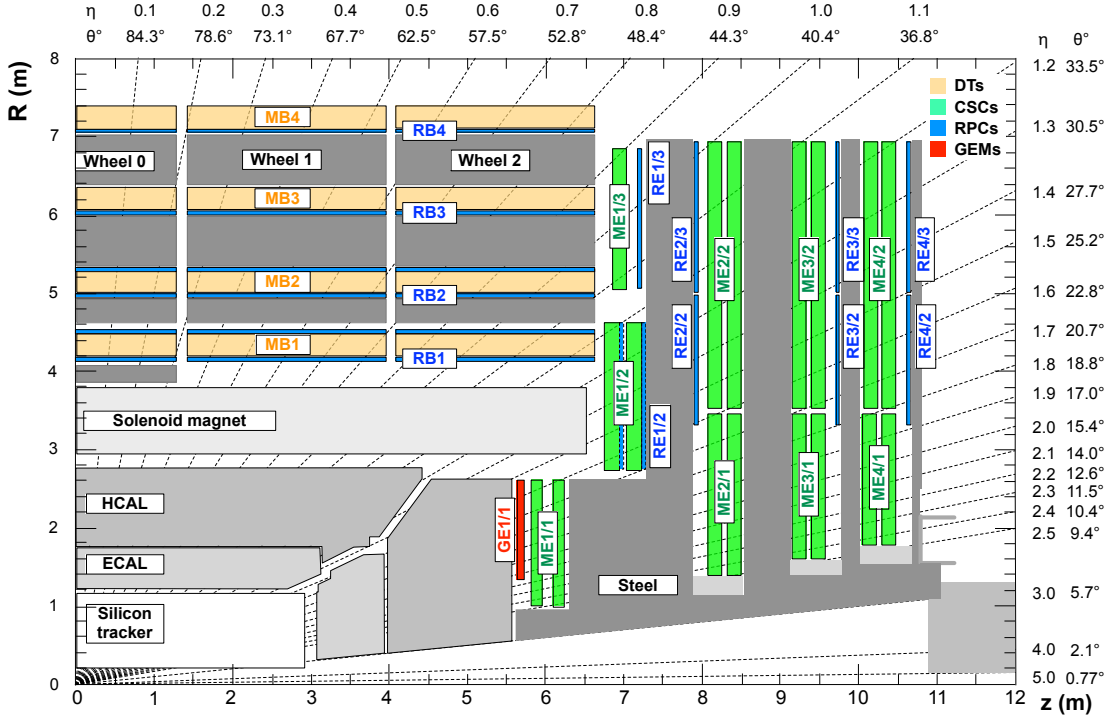
Figure 2.9: Schematic view of the muon system in the r–z plane of a CMS quadrant at the start of Run 3, showing the location of the various muon stations in colors: drift tubes (DTs) with labels MB, cathode strip chambers (CSCs) with labels ME, resistive plate chambers (RPCs) with labels RB and RE, and gas electron multipliers (GEMs) with labels GE. The M denotes muon, B stands for barrel, and E for endcap [76].

and the full muon track is reconstructed by combining hits from multiple detector layers. The return yokes provide a magnetic field of up to ∼2 T, enabling precise momentum measurement. Figure 2.9 shows a schematic view of one quadrant of the muon system in the r–z plane.

The drift tube (DT) system in the barrel covers $|\eta| < 1.2$ and is composed of drift chambers with rectangular cells. They are arranged into four stations, providing spatial measurements, as well as trigger information, in a region where the magnetic field is uniform and the muon rate is low.

The cathode strip chamber (CSC) system in the endcap comprises multiwire proportional chambers having cathode strips with an r–ϕ geometry and covering the region $0.9 < |\eta| < 2.4$. The CSC system provides both trigger and precision position information in a region of higher flux of particles than the barrel regions; therefore, the CSCs are designed to have a faster response (20–30 ns) than the DTs (350–400 ns) [87]. They are arranged in four stations, and the outer ring of CSC chambers in station four (ME4/2) was added at the start of Run 3 operations.

The resistive plate chambers (RPCs) are double-gap chambers operated in avalanche mode, located in both the barrel and endcap regions, and they complement the DTs and CSCs. With a very fast response time (1–2 ns [87]), they can be used to unambiguously identify the BX corresponding to a muon trigger candidate. They are arranged in four stations, and the RE4/2 and RE4/3 were added for Run 3.

The newly installed GE1/1 station is located in front of the inner ring of CSC chambers in the first endcap station and comprises gas electron multiplier

(GEM) chambers. The GEMs have both a fast response (5 ns) and good spatial resolution (100–200 μm) [88], and they augment the CSCs in a region of high particle flux.

Information from each sub-system is used in combination to improve spatial resolution, crucial for precise muon identification and background rejection. The nominal spatial resolution ranges from as low as 50 μm for the CSC chambers to about 1 cm for the RPCs [89]. A good time resolution is also required, since the muon system serves as a trigger and must respond quickly to unambiguously assign a muon trigger candidate to the correct BX. The time resolution is recorded to be lower than 5 ns [89].

2.2.6 Trigger system

As the LHC proton bunches cross at a rate of 40 MHz and each bunch contains $\mathcal{O}(10^{11})$ protons, the resulting proton collision rate is in the range of 10^7–10^9 Hz. Considering an average event size of around 2 MB per collision, the required storage capacity would be approximately 1 PB/s, while the current CERN storage capabilities are only a few tens of PB per year [90]. To address this challenge, the CMS experiment deploys a two-level trigger system to reduce the event rate to a manageable level of a few kHz, selecting events that are interesting from a physics point of view within a very broad research program.

The level-1 (L1) trigger is a hardware-based system that uses information recorded only by the calorimeters and muon detectors. In particular, calorimeter and muon detector data are used to reconstruct trigger primitives, which provide energy and position measurements. This information is used to build muon, hadronic τ, electron/photon objects, and calorimeter energy sums. The global L1 trigger then makes the final decision on whether the full detector data are read out for further filtering in the high-level trigger (HLT), by applying selection criteria on the kinematic quantities of these objects, as well as on timing information. The time required to perform this fast reconstruction and make a readout decision is called the latency, and for the L1 trigger, it is about 4 μs. This includes the time needed to send data to the backend electronics and back to the on-detector electronics. During Run 3, the L1 trigger system reduced the event rate to a maximum of 110 kHz.

The HLT is implemented in software, running on a farm of commercial computers. In 2022, for standard p–p collisions at an average instantaneous luminosity of 1.5×10^{34} cm^{-2}s^{-1}, the average rate of reconstructed physics events written to offline storage was approximately 1.7 kHz. The HLT uses the full event reconstruction to select events relevant for the wide CMS physics program.

A complete sequence of L1 and HLT selection criteria is called a trigger path. After the final HLT decision, the selected dataset is initially stored on disk in raw format and then reprocessed for offline reconstruction. Based on the trigger paths, different classes of datasets are available. The dataset class for dilepton selection, selected by several trigger paths applying requirements on electrons and muons, is used for this thesis and is described in detail in Section 7.2.

Chapter 3

The upgrade of the CMS experiment

Part of the work presented in this thesis contributes to the development and validation of the scintillator section of the new endcap calorimeter of CMS, known as the HGCAL, which will be installed for the HL-LHC. This chapter introduces the broader context of the HL-LHC upgrade in Section 3.1, followed by an overview of the upgraded CMS experiment in Section 3.2. Section 3.3 provides a detailed description of the HGCAL detector, and Section 3.4 focuses specifically on its scintillator section.

3.1 High Luminosity-LHC

The HL-LHC (or Phase 2) project aims to significantly improve the performance of the LHC to increase the potential for discoveries after 2030. The objective is to increase the integrated luminosity by a factor of 10 beyond the design value of LHC, reaching an integrated luminosity of about 3000 fb^{-1} after about 10 years of operation. The current plan of LHC/ HL-LHC is shown in Figure 3.1, while the LHC/ HL-LHC milestones parameters comparison is presented in Table 3.1.

Table 3.1: Comparison of LHC and HL-LHC operating parameters. The prospect column indicates the performance expected when the accelerator operates at its technical limits.

	LHC design	HL-LHC design	HL-LHC prospect
Peak luminosity (10^{34} cm^{-2}s^{-1})	1.0	5.0	7.5
Integrated luminosity (fb^{-1})	300	3000	4000
Number of pile-up events	~ 30	~ 140	~ 200

Motivations for this HL-LHC upgrade arise from the possibilities of addressing some of the fundamental open questions in particle physics, related to the SM and beyond. A major focus will be on the Higgs sector, as the HL-LHC is expected to function as a *Higgs factory*, where over 170 million Higgs bosons will be produced. will allow precise measurements of the Higgs couplings to fermions and bosons, and enable direct tests of yet unmeasured SM predictions, such
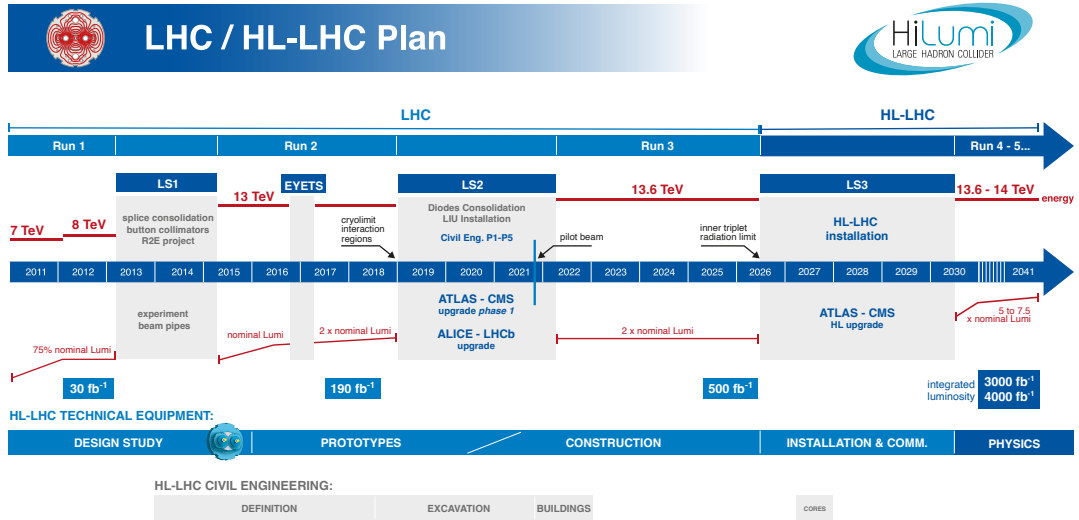
Figure 3.1: An infographic of the LHC and HL-LHC plan, as of January 2025 [91].

as the Higgs self-coupling. Searches for new physics beyond the SM, such as supersymmetry, extra dimensions (e.g., Kaluza-Klein models), and other exotic scenarios, were already tested during Run 2 operation, showing no particular evidence of any of these new particles. At the HL-LHC, searches for BSM physics will benefit from a significantly larger dataset and a higher centre-of-mass energy, enabling sensitivity to rare processes and non-standard signatures, often involving highly boosted or displaced final states and complex topologies. This requires more sophisticated trigger strategies, advanced reconstruction algorithms, and, crucially, upgraded detectors with improved granularity, timing resolution, and radiation hardness.

As visible from Table 3.1, the higher luminosity requirement for HL-LHC operation would increase the number of collisions for BX, reaching 140 collisions per BX. The beam is required to be more intense and more focused, so new equipment is needed. New quadrupole magnets will replace the existing ones in the CMS and ATLAS interaction region: superconductive magnets of Nb_3Sn will be installed to replace the current NbTi magnets. New reinforced machine protections will substitute the current ones to absorb particles that stray from the beam trajectory and might otherwise damage the structures. Two of the current bending magnets will be replaced with two pairs of shorter bending magnets and two collimators that will generate a magnetic field of 11 T, compared with the current 8.3 T, and will thus bend the trajectory of the protons over a shorter distance. For this new challenging scenario, all LHC main experiments will undergo substantial changes and improvements, and details of the CMS upgrades are given in the following sections.

3.2 Overview of the CMS detector upgrade

To sustain performance at the HL-LHC, CMS is being upgraded with sub-detector technologies featuring higher granularity, precision timing, and enhanced

radiation tolerance. This section briefly summarizes those upgrades for all subsystems, excluding the HGCAL, which is detailed in Section 3.3).

Tracker system upgrade

The tracker system will be completely replaced after Run 3 operations due to the substantial radiation damage it will suffer. Moreover, the current pixel detector, as well as the strip detector, cannot cope with the high luminosity and high PU environment of the HL-LHC. To operate at HL-LHC phase, the pixel detector will be equipped with smaller silicon pixels whose area is reduced by a factor of six. The overall granularity, accounting for geometry and readout segmentation, will increase by about a factor of four. The pixel tracker is designed to have seven disks in addition to the three already installed in the z-range between 50 cm and 250 cm, reaching a coverage of up to $|\eta| = 4$ [92].

A completely new system will likewise replace the strip tracker. The strip modules are based on silicon sensors with pitches of approximately 90–180 μm and lengths ranging from 2.4 cm to 5 cm, optimized for high occupancy and radiation tolerance. Two closely-spaced strip sensors are read out simultaneously, forming a p_T-module, providing track identification above ∼2 GeV for L1 trigger seeding.

Overall, the upgraded strip tracker will provide coverage up to $|\eta| \approx 3$, maintain hit resolution comparable to the current tracker under HL-LHC pileup conditions, and enable track information to be incorporated already at the first trigger level.

MIP timing detector

During the HL-LHC, the CMS detector is planned to be equipped with a new detector: the MIP Timing Detector (MTD) [93]. This detector will be capable of measuring the time of arrival of MIPs to assign charged tracks to the correct interaction vertices in BXs, where the expected average is of 140 collisions or more during HL-LHC operation. This exploits the fact that individual interactions within a BX do not occur simultaneously but are distributed in time, with differences of 180–200 ps. The MTD aims to provide additional information for vertex reconstruction by associating tracks with their corresponding times, with a resolution of 30–40 ps. Tracks pointing roughly towards the vertex of interest but arriving at the wrong time can be identified as coming from pileup (PU) interactions rather than from the vertex of interest.

The MTD will provide timing information in the barrel and endcap regions, with a hermetic angular coverage up to a $|\eta| = 3$ and will be located in the region between the tracker and the calorimeters. The barrel region will be equipped with a thin layer of Lutetium Yttrium Orthosilicate crystals doped with Cerium (abbreviated as LYSO:Ce) scintillating crystal with an average thickness of 3 mm, read out by SiPM. Due to the higher radiation levels expected in the endcap, this region will be equipped with silicon low-gain avalanche diodes (LGADs), providing faster timing and higher radiation hardness. The MTD will play a role in new physics searches, for instance, increasing the identification efficiency of delayed particles, the time-of-flight measurement of heavy stable charged particles, amongst other possibilities.

Trigger system upgrade

The trigger latency of the L1 trigger will be increased to 12.5 μs, from the current 3.4 μs, to accommodate front-end buffering required for the L1 tracking seeding. Based on the expected performance of the trigger with track information, the proposed L1-trigger acceptance rate is 500 kHz for beam conditions yielding 140 PU, and 750 kHz for 200 PU [94].

Calorimeters upgrade

The front-end electronics of the barrel calorimeter will be replaced to meet the L1 trigger acceptance rate requirements of HL-LHC, 750 kHz. More details can be found in Reference [95]. The upgrade of the endcap calorimeters is described in detail in Section 3.3.

Muon system upgrade

To cope with the expected L1 rate of up to 750 kHz, the electronics equipped on DT, RPCs, and CSC will be replaced. The region covering $1.5 \leq |\eta| \leq 2.4$, which currently consists of four CSC chambers, will be equipped with additional GEM chambers for good position resolution to improve momentum resolution. This integration will increase the coverage for muon detection to $|\eta| \approx 3$. More details are given in Reference [87].

3.3   The CMS HGCAL project

More than 10 times the luminosity of the LHC design will be collected during HL-LHC, resulting in an increased level of radiation, especially in the forward region. Figure 3.2 shows a simulation study using `FLUKA` [97], indicating the radiation dose accumulated by the CMS detector after 3000 fb^{-1}. The figure shows that the highest absorbed dose is of the order of MGy[1], occurring in the innermost radii of the silicon trackers and in the forward region in the endcaps. This requires the detector in the forward regions to have high radiation tolerance to avoid degrading performance, after 3000 fb^{-1} of integrated luminosity is collected. The requirement for high radiation tolerance alone is not yet met by the current CMS endcap calorimeter, which therefore needs to be replaced.

The HGCAL project has thus been proposed as part of the CMS HL-LHC program, designed to provide five-dimensional information, including three spatial coordinates, time, and energy. In addition, other requirements must be met by the new detector, which can be summarized as follows:

- fine lateral granularity, allowing the separation of nearby showers and the observation of narrow jets;

- fine longitudinal granularity, enabling detailed sampling of the longitudinal development of showers to improve energy resolution, particle identification, and discrimination against PU;

---

[1]A dose of approximately 1 MGy corresponds to a fluence of about 10^{16} neq/cm^2, where the fluence represents the number of 1 MeV neutron-equivalent particles per cm^2.
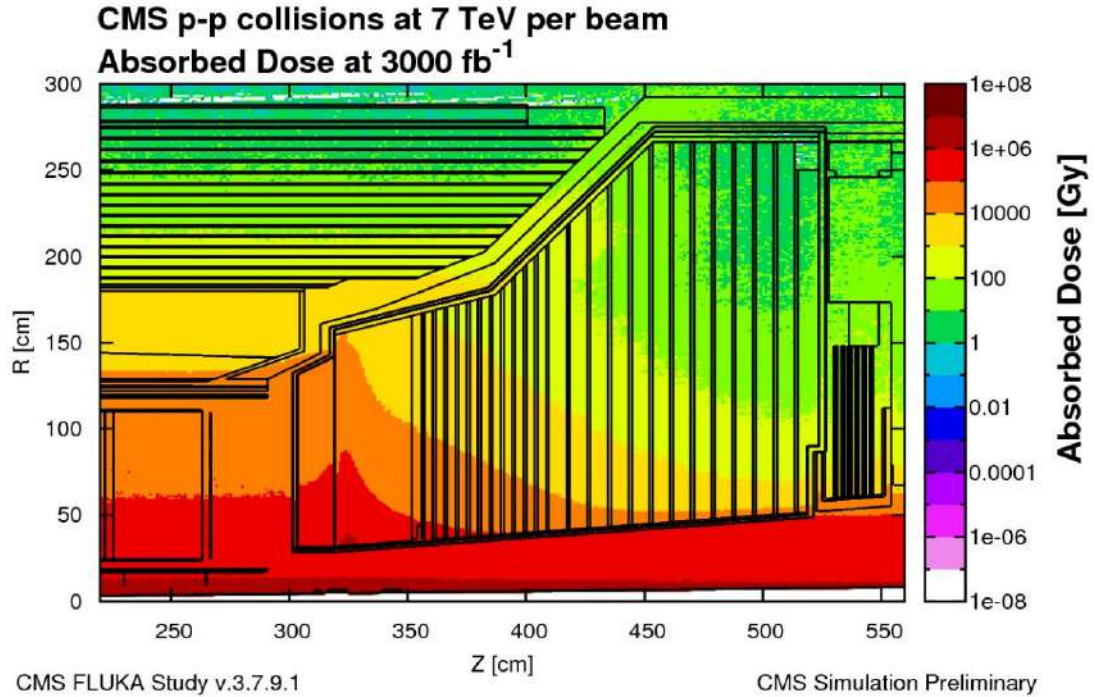
Figure 3.2: The dose of ionizing radiation in the r-z plane, accumulated by one endcap region of CMS, after an integrated luminosity of 3000 fb^{-1}, simulated using the `FLUKA` program [96]. The HGCAL region covers from 300 to 525 cm in the z direction, and from 25 to 275 cm in the r direction.

- precision time measurement, which helps to improve vertex identification and contributes to the L1 trigger decision.

To meet these requirements, the proposed technology combines silicon sensors in the inner, high-radiation region, with plastic scintillator tiles in the outer region, where the maximum expected radiation dose is approximately 3 kGy. Scintillation light is collected by SiPMss, which are cost-effective and insensitive to magnetic fields. The choice of silicon sensors is well motivated by the expertise gained over the years in developing the CMS tracking system, while the scintillator with SiPM design builds on previous experience with highly granular calorimeters, such as those developed by the CAlorimeter for LInear Collider Experiment (CALICE) Collaboration [98] and by the expertise gained during the upgrade of HCAL at the start of Run 3.

Therefore, the HGCAL detector is designed with both silicon- and a scintillator-based sections and is divided into two parts: the Electromagnetic Endcap Calorimeter (CE-E) and the Hadronic Endcap Calorimeter (CE-H). The CE-E consists of 28 sampling layers with a total thickness of 34 cm and a depth of approximately 26 X$_0$ and 1.7 λ. The CE-E section will use hexagonal-shaped silicon sensors as active material. The absorber layer is formed by two 2.1 mm-thick lead planes clad with 0.3 mm stainless steel sheets. The first eight layers of the CE-H will also employ silicon sensors as active material, while the remaining layers in the CE-H combine silicon and scintillator-based detectors, sharing common mechanical and electronics in the so-called *cassettes*. The absorber in the hadronic compartment consists of 12 planes of 35 mm-thick stainless steel plates followed by another 12 stainless steel planes with a thickness of 68 mm, for a total calorimeter thickness

of 10.7 λ. As the HGCAL will be operated at a temperature of $-30\,^\circ$C to mitigate radiation damage in the silicon sensors and reduce leakage currents induced by the high fluences expected at the HL-LHC, the detector volume will be kept under hypoxic conditions (about 3% O_2), with CO_2 used for the cooling system, which will also act as passive material.

A cross-section of the detector in the $y - z$ plane is shown in Figure 3.3. The 2.2 m×2.3 m section comprehends the CE-E in blue, the CE-H in green for the silicon-only part, and in violet for the mixed silicon and scintillator sector. A detailed schematic cross-section of the CE-E and CE-H sections of the HGCAL is shown in Figure 3.4. Each active material component is depicted. The silicon sensors (in blue) are interleaved with layers of copper (in orange) and a printed circuit board (PCB, in green) to form the silicon modules, which are described in detail in the following section. For the CE-H section, the scintillator tiles equipped with SiPMs (in yellow) are also illustrated.
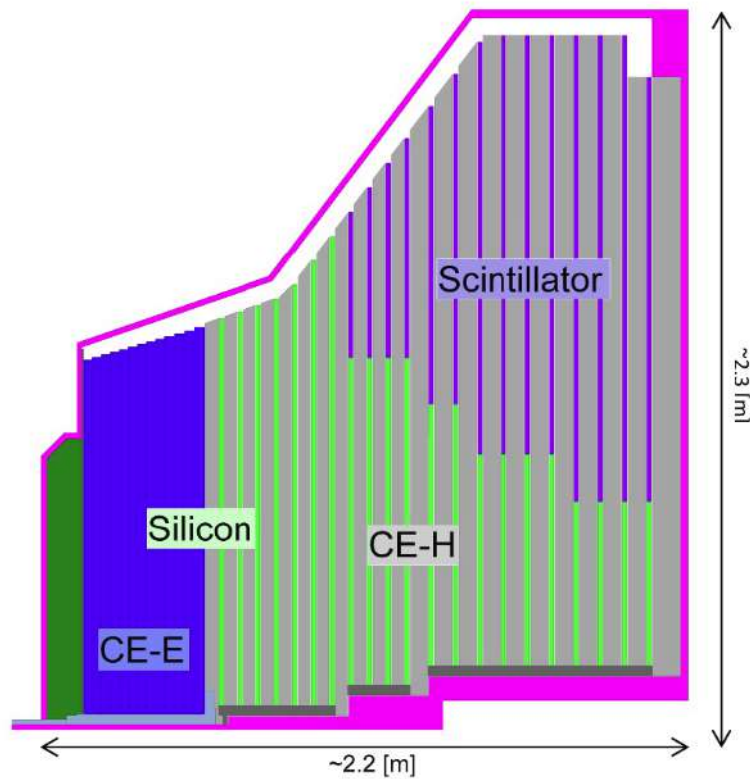
Figure 3.3: Layout of the detector in y–z plane. Different sections of the HGCAL are displayed.

The silicon section of the CMS HGCAL

The HGCAL sensor design draws upon the results from previous studies for the SiW electromagnetic calorimeter developed by the CALICE Collaboration [99], from the research and development of the SiD ECAL [100], and from the HL-LHC pixel tracker (see Section 3.2), as the expected absorbed radiation doses are similar at the end of HL-LHC. The main difference between the tracker and the HGCAL design lies in the area of the pads, which is approximately
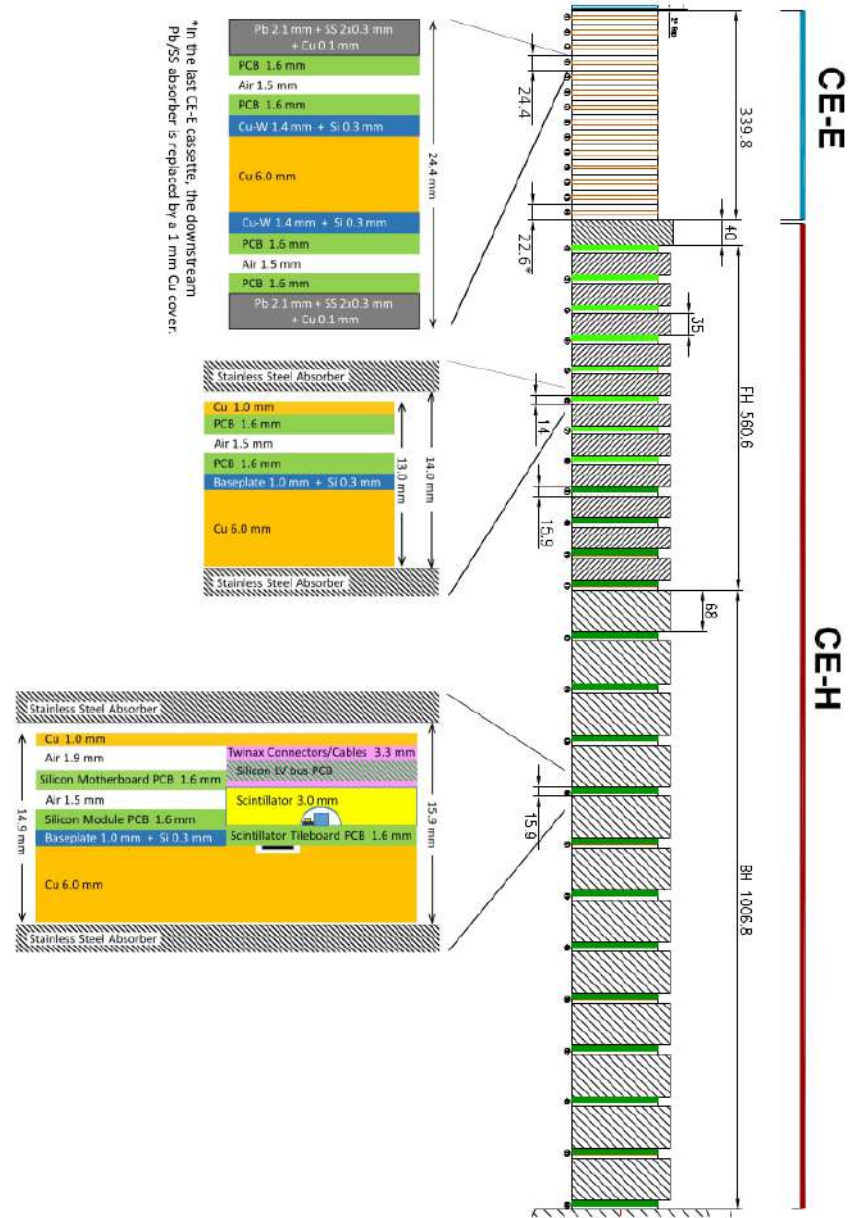
Figure 3.4: Longitudinal structure of the HGCAL. The active material is shown in blue (yellow) for the silicon (scintillator)-based section, as for the Technical Proposal [96].

90 μm^2 for the pixel tracker and around 1 cm^2 for HGCAL. More precisely, the HGCAL silicon sensors will be hexagon-shaped to make more efficient use of the available area of the circular wafers, as compared to square or rectangular sensors, while minimising the ratio of periphery to active surface. The cell area varies from 0.5 cm^2 in regions closer to the beam, where higher granularity is required, to 1.1 cm^2 in regions farther from the beamline. The sensor thickness varies between 120, 200, and 300 μm, increasing with distance from the beamline. The hexagon-shaped sensors are grouped and fabricated on 8-inch wafers, as shown in Figure 3.5. Each silicon sensor is sandwiched with a 1 mm-thick CU/W baseplate, the PCB that carries the front-end electronics to form a silicon module. The baseplate also serves as short radiation-length material.
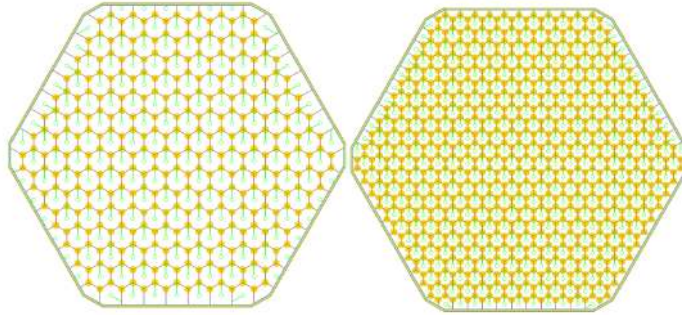
Figure 3.5: Hexagonal 8 inch silicon wafers, with layout of large, 1.18 cm^2, sensor cells (left), and small, 0.52 cm^2, cells (right) [96].

3.4   The scintillator section of the CMS HGCAL

The CE-H section of the HGCAL features a mixed design combining silicon modules and a scintillator-based component, used in regions with relatively low radiation levels (below 3 kGy). In the scintillator section, scintillating tiles serve as the active material and are directly coupled to SiPMs, which detects the emitted light.

Figure 3.6a illustrates the working principle of the SiPM-on-tile technology: when charged particles traverse the scintillator, they lose energy via ionization, producing scintillation photons. These photons are reflected internally and by a foil wrapping and subsequently detected by the underlying SiPM. This technology was pioneered for the Analogue Hadron Calorimeter (AHCAL) and developed by the CALICE Collaboration [98, 101]. As shown in Figure 3.6b, the SiPM is embedded in a small central dimple in the tile, which optimizes optical coupling. Each SiPM comprises thousands of Single-Photon Avalanche Diodes (SPADs), with a typical pitch of ≈ 15 μm. The SPADs are sensitive to single photons, operate in Geiger mode, and are read out in parallel. The total collected charge is proportional to the number of photoelectrons detected across all SPAD cells.

The scintillator section of HGCAL will feature 21 different trapezoidal-shaped scintillator tiles of area ranging from 4 cm^2 to 32 cm^2, depending on the r-distance from the beam axis, and two types of material are considered: polyvinyltoluene-based (PVT) and polystyrene-based (PS). Each tile is wrapped in a layer of 3M Enhanced Specular Reflector (ESR) foil [102] to enhance photon collection. The

(a)Illustration of the working principle of the key elements of the scintillator section of HG-CAL.

(b)Scintillator tiles with central dimple, wrapped and unwrapped, and SiPMs (for the CALICE AHCAL [101]).
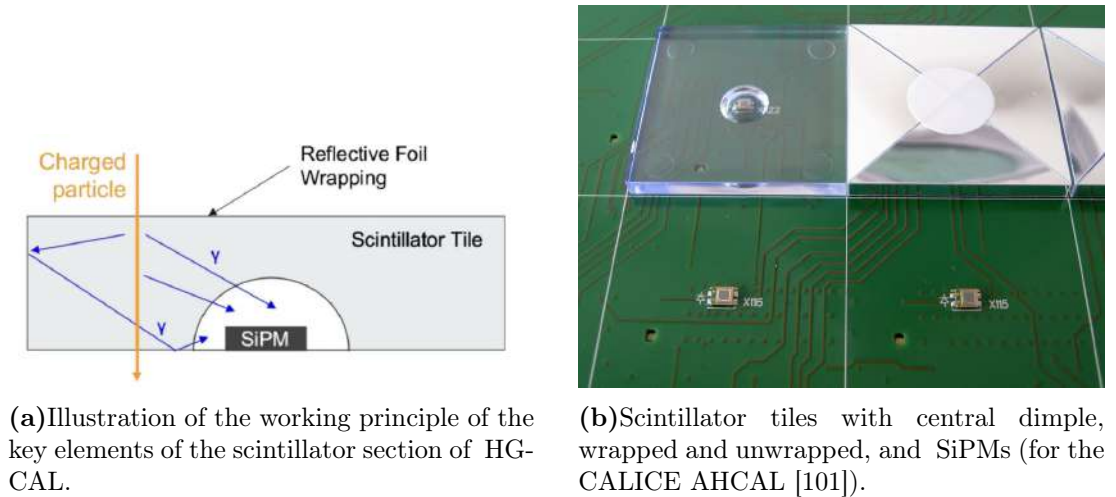
Figure 3.6: Key elements of the scintillator section of HGCAL.

SiPM model used is a custom version of the HDR-2 SiPM (S14160 series [103]), produced by Hamamatsu Photonics K.K. (HPK). To ensure a signal-to-noise ratio greater than 3 for calibration of single MIP, under the radiation levels expected at the end of the lifetime of the detector, the 3×3 cm^2 SiPMs are employed in the innermost region of the scintillator section. The choice of active area is driven by recent studies on the performance degradation of SiPMs after irradiation [104].

Multiple SiPM-on-tile units are grouped into a HGCAL *tilemodule*, which constitutes a complete detection unit composed of the *tileboard*, hosting the SiPMs, the PCB, the readout electronics, including the HGCAL read out chip (HGCROC) [105, 106], and all other onboard electronics, and the attached scintillator tiles. In addition, each SiPM is equipped with an adjacent LED system to enable SiPM calibration, which is also part of the tilemodule. Each module can host between 40 and 144 SiPM-on-tile channels. The module areas range from 15×20 cm^2 to 45×45 cm^2, with eight main geometries (labeled A to K) and 35 variants. Each module covers a $10°$ angular aperture, and up to five modules are placed radially from the beamline. Figure 3.7a and 3.7b show the different module types and their location in the transverse plane of the scintillator section.

3.4.1 The readout electronics of the CMS HGCAL

Signals from up to 72 SiPMs can be read out simultaneously by the front-end HGCROC ASIC at the LHC collision frequency of 40 MHz, placed onto each tileboard. The readout chip measures and digitizes the charge generated in the SiPMs, converting it to analog-to-digital (ADC) or time-over-threshold (ToT) counts, and also provides high-precision measurements of the time of arrival (ToA) of the pulses. A similar chip design and front-end electronics are used for both the silicon and scintillator sections, with minor adaptations to accommodate the large difference in collected charge between the silicon sensors and the SiPMs. Since the charge collected from a SiPM is approximately 0.2 pC/MIP, the signal must be attenuated before reaching the HGCROC, using a current conveyor with a damping factor between 0.025 and 0.375.

There are several requirements the chip must fulfill, given that the detector must measure energy deposits ranging from a single MIP to those produced by
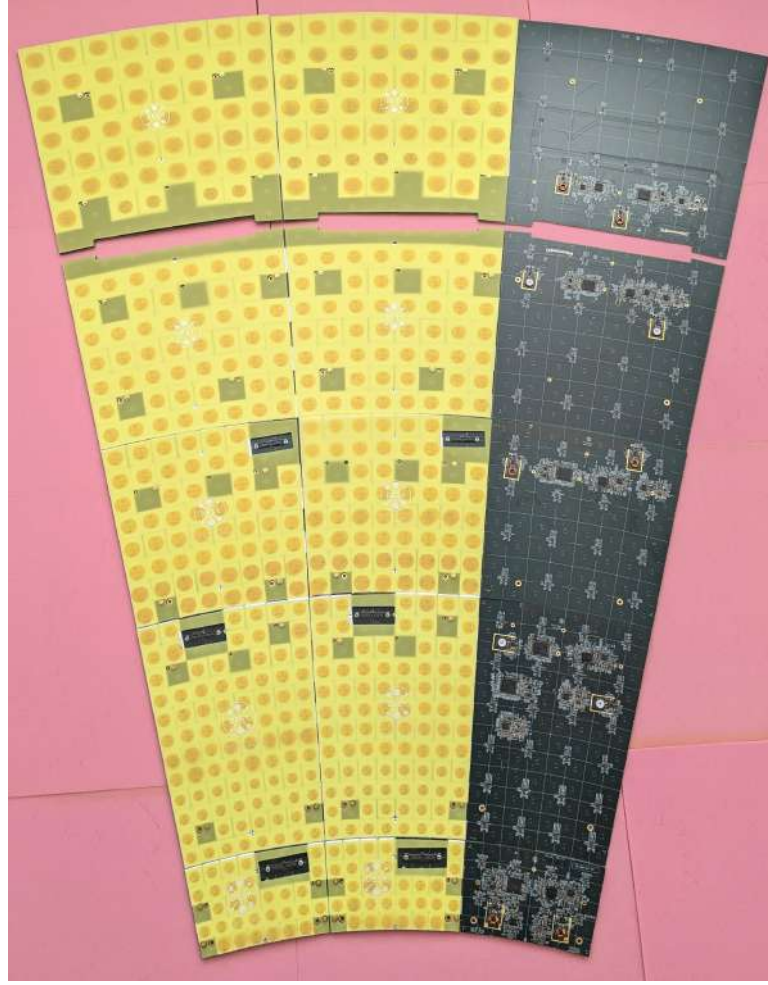
(a)Different module types in three slabs of $10°$ angular aperture. Courtesy of Mathias Reinecke.
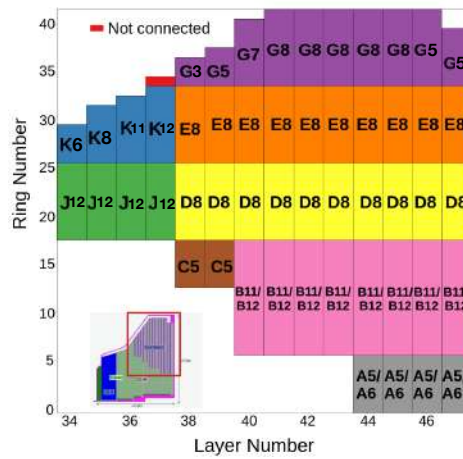
(b)Layout of the tile modules with different geometry. The ring number refers to different scintillator tile areas. Courtesy of Mathias Reinecke.

Figure 3.7: Geometries of tilemodules and their placements in the HGCAL scintillator section.

high-energy electromagnetic and hadronic showers, while also contributing to the L1 trigger system. Therefore, the HGCROC is designed to provide low noise (below 2500 electrons) and a large dynamic range, covering approximately 0.2 fC to 10 pC[2], corresponding to a 16-bit dynamic range.

In addition, the HGCROC needs to provide timing information with a precision of 25 ps, and fast signal shaping, with a peaking time below 20 ns. Moreover, the chip includes a buffering capability of 12.5 μs to meet the latency requirements of the upgraded L1 trigger system, and features a high-speed (up to 1.28 Gb/s) readout link to interface with the front-end and back-end electronics. Finally, given the long operational lifetime of the detector, the chip is designed to operate with a low power budget to maintain performance in a high-radiation environment and to keep the cooling requirements manageable.

The full architecture of the chip is given in the block diagram in Figure 3.8. Each channel consists of a low-noise preamplifier (PA), which adjusts the MIP signal to around 10 ADC counts, and a shaper (SH) for the ADC path, which produces a signal with a more Gaussian-like shape from the SiPM. In the linear regime of the preamplifier and for the low end of the dynamic range, the signal is sent to the 10-bit SAR-ADC. At the high end of the dynamic range, after the preamplifier saturates, the charge is measured by a 12-bit TDC using the time-over-threshold (ToT) technique. The time-of-arrival (ToA) measurements are provided by a fast 10-bit TDC.

The digitized data (ADC, ToT, and ToA) are computed at every BX and stored at 40 MHz in a circular buffer. Specifically, the circular memory stores the ADC or ToT, the ToA, and the ADC value from the previous clock cycle (ADC-1), which is used to identify residual charge from a previous event for calibration purposes and correction in data. Since the ADC and ToT share the same path via multiplexing, ToT data is only stored when the ADC signal exceeds a predefined threshold; otherwise, the ToT information is discarded. When an L1 Accept (L1A) signal is received from the back-end, the data in the buffer is transmitted over two 1.28 Gbps data links, with zero suppression, to the back-end DAQ system. As the chip also contributes to the L1 trigger primitives of CMS, it sums the charge from adjacent channels, either four or nine, and transmits the result through four dedicated 1.28 Gbps links, referred to as the trigger links.

Sampling Time

When the L1A signal is generated by the back-end, it takes a finite amount of time before it reaches the HGCROC, during which the data continues to circulate in the buffer. To accurately reconstruct the event and recover the full charge deposit, it is important to select the correct sample in the buffer. This timing can be adjusted using two HGCROC parameters: the BX offset (or *L1A offset*) and the *phase*. The BX offset accounts for the number of BX that have passed since the L1A was received. The *phase* provides finer timing adjustment within a bunch crossing, with 16 phase steps available between two consecutive BXs. Given the LHC BX frequency of 25 ns, the delay can be accounted for as

---

[2]This range is motivated by the fact that, at the start of operation, a MIP traversing a 120 μm silicon sensor deposits about 1.5 fC, corresponding to 8 ADC bins. At the high end, a 1.5 TeV photon shower may deposit up to 6000 MIPs in a single cell [96].
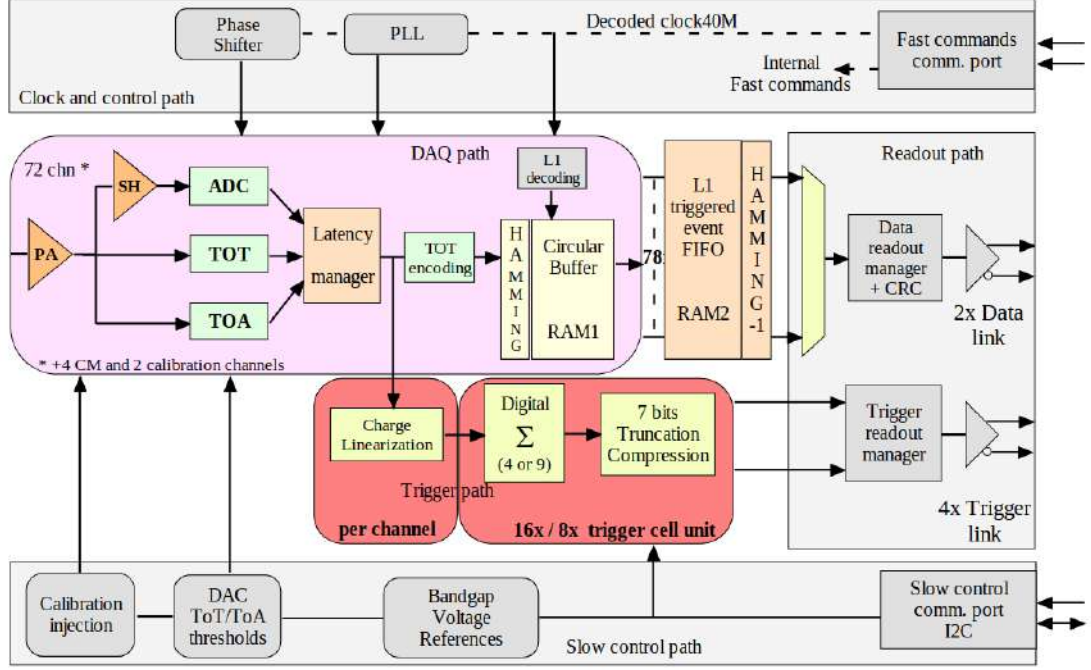
Figure 3.8: HGCROC block diagram with 72 regular channels divided in two paths: data acquisition and trigger [106].

$$\text{Delay [ns]} = \text{L1A offset} \times 25 \text{ ns } + \text{phase} \times \frac{25}{16}\text{ns}, \qquad (3.1)$$

and the ADC, ToT, and ToA are all measured relative to this delay.

Figure 3.9 illustrates how the ADC, ToT, and ToA are defined in relation to the sampling delay for a typical SiPM signal. The ADC is sampled at the peak of the pulse. The ToA is defined as the time from the start of the previous BX to the point where the signal crosses the ToA threshold, measured in TDC units. The ToT is the time difference between when the signal crosses the ToA threshold and when it falls below the ToT threshold. These definitions of L1A offset, phase, and ADC are used in Chapter 4, where the results of the validation of the SiPM-on-tile system are shown.
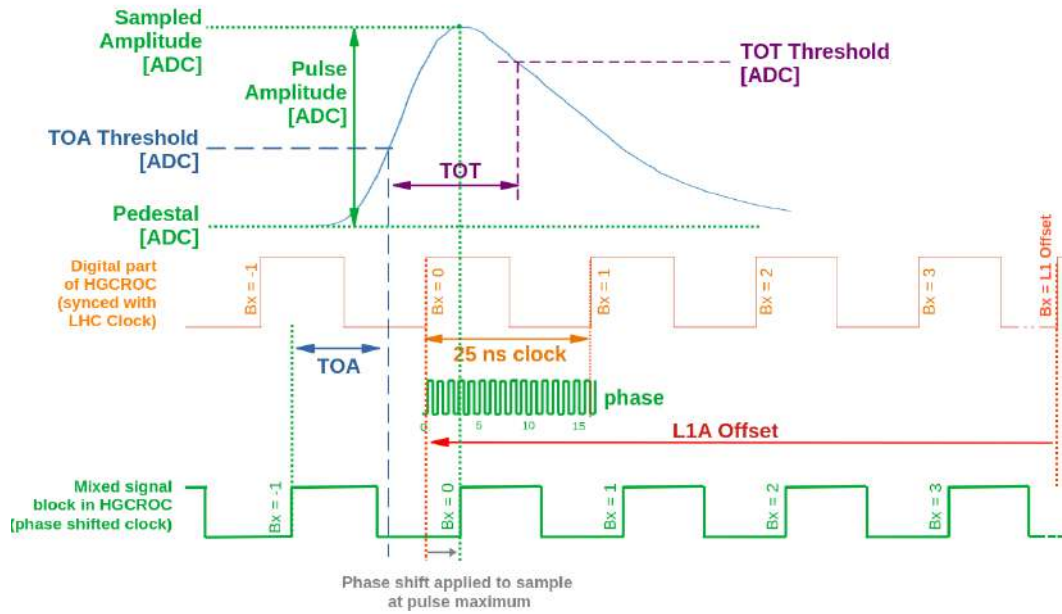
Figure 3.9: Definitions of ADC, ToT, and ToA in relation to the sampling L1A offset and phase for a typical SiPM pulse [104].

Chapter 4

System validation of the scintillator section of the CMS HGCAL

4.1   Introduction and overview

During the R&D phase of the CMS HGCAL, it is essential to assess the quality and validate continuously and with quick feedback the performance of its prototype components. The DESY laboratory in Hamburg is involved in the system design and validation of the scintillator section of HGCAL and serves as a Tileboard Assembly Center (TAC), where detector components, such as bare PCB, tiles and electronic components, are received and assembled on-site: tiles are wrapped with the reflective foil using special machines and then assembled on the PCB, along with the HGCROC and the components described in Section 3.4.

   As part of my thesis work, I contributed to the validation of the system following the assembly process. This included supporting the development of software for data acquisition as well as the framework for analyzing the results. My involvement spanned both laboratory activities and test beam campaigns. The results from test beam campaigns, in particular the May 2024 test beam campaign, are presented in this chapter. All test beams were conducted using either individual tileboards or stacks of tileboards measured separately, since the DAQ system at the time did not yet support simultaneous multi-tileboard readout. Measuring key characteristics of the system, such as the SiPM gain and the light yield of the tiles, is critical for verifying the design and the correct operation, and preparing for the upcoming mass production phase.

   Section 4.2 describes the beam test facility and experimental setup. The SiPM gain measurements are presented in Section 4.3. These studies aim to evaluate the consistency of results across channels and tileboards, assessing the quality of both the electronics and the SiPMs. The light yield results, which are inferred from a combination of test beam results and gain measurements, are discussed in Section 4.4. The goal of these studies is to demonstrate the system's reliability and the consistency of results across different tilemodules, providing validation before the mass production planned for 2025.

   Most of these studies were presented at several workshops and conferences, such as at the European Physical Society Conference on High Energy Physics (EPS-HEP) in Hamburg in 2023 [1]. Additional studies were also undertaken. In

the early stages of my work, I contributed to the development and validation of the
DAQ software and participated in various measurements, including noise studies
and tests on irradiated SiPMs, though these are not included in this thesis. These
results are relevant for assessing the detector lifetime, since radiation reduces the
signal-to-noise ratio; a sufficiently high light yield is required to keep the signal
above the pedestal even after the expected level of radiation at the end of HL-
LHC. I also contributed to the development of the analysis framework used to
evaluate the test beam data.

4.2 Beam tests at the electron beam facility at DESY

Several test beam campaigns have been conducted over the years with different
combinations of SiPMs, scintillator tile types, tileboards, and DAQ systems. The
facility is located in Hamburg at the DESY-II synchrotron accelerator [107], whose
primary role, nowadays, is to provide electrons for the PETRA ring [108], and
offers three different beam lines of electron or positron beams, ranging momenta
with 1-6 GeV/c with an energy spread of 5%. The beam rate of particles ranges
from a few Hz to a few 10 kHz for each beamline. For test beam purposes,
electrons are produced from photon conversions at a fiber target placed in the
beam line. The energy of the resulting electrons is selected with a dipole magnet,
and a collimator further defines both the particle energy spread and the beam
opening. A dipole magnet and a collimator select the desired particles, the energy,
and the opening of the beam, which is of 1 x 1 cm^2 for the results shown in this
thesis. A schematic view of the test beam facility is shown in Figure 4.1.
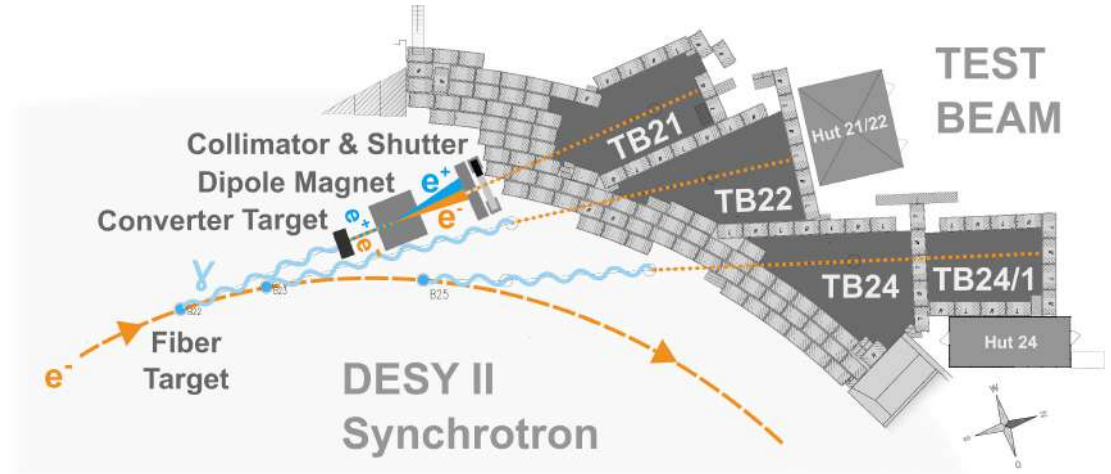
Figure 4.1: Schematic view of the DESY-II synchrotron test beam facility [107].

4.2.1 Test setup

The overall schematic view of the setup of the test beam is shown in Figure
4.2. The tileboard and the DAQ system are attached to a mechanical support,
consisting of an aluminium holder plate placed vertically. Figure 4.3 shows a
tileboard placed onto the aluminium holder, fully equipped with scintillator tiles
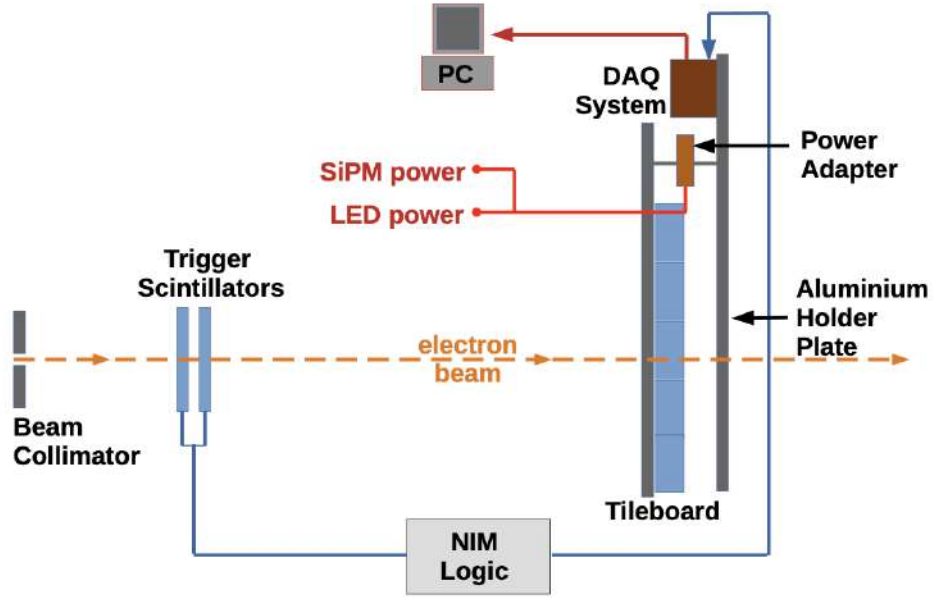
Figure 4.2: Schematic of the setup used during the test beam at the DESY test beam
facility [104].

and the DAQ system. The plate is placed onto a holder frame on a movable stage
perpendicular to the beam line. The aluminium holder plate is covered with a
black cloth to mitigate any light contamination.

Different types of tiles are used during test beams depending on the manu-
facturer's production method, which can be either casting or injection molding.
These types differ in both light yield and production cost. The results presented
in this thesis are based on cast tiles.

The DAQ system used is an FPGA-based (Xilinx Zynq) controller board called
the *TB-Tester*, which was developed by the University of Minnesota (UMN). The
TB-tester provides the fast clock, fast commands, and triggers. It also provides
slow controls, communicating with the GBTSCA ASIC [109], to set configuration
parameters, and with an ALDO chip [110], to set the SiPM supply voltage and
monitors LED bias voltage. It also monitors the temperatures from the eight PT-
1000 platinum temperature sensors attached to the tileboard. The tileboard and
the DAQ system are connected via twinax cables and Samtec QSH connectors.
The system also communicates with an external PC to send configuration data,
to start or stop the data-taking, and to receive prepackaged data event back.

Two scintillator photomultipliers (PMTs) provide the trigger in the beam area
and are connected to the DAQ system after passing a NIM logic. After passing
through a discriminator, the coincidence signals from the two PMTs are sent to
a gate generator that produces a 5 V, 1 μs square pulse (TTL logic), which is
then sent to the DAQ system. The FPGA of the DAQ system then generates
L1A signals to be sent to the HGCROC to trigger the readout, which needs a
time setting to specify which data to receive back.

The impinging electron beam has a selected energy of 3 GeV for all the studies
presented in the thesis. At this energy and considering the 3 mm thickness of

the plastic scintillator, the electrons can be considered as MIP. A photo of the
setup during test beams is shown in Figure 4.3, where the movable stage and the
trigger scintillators are visible.
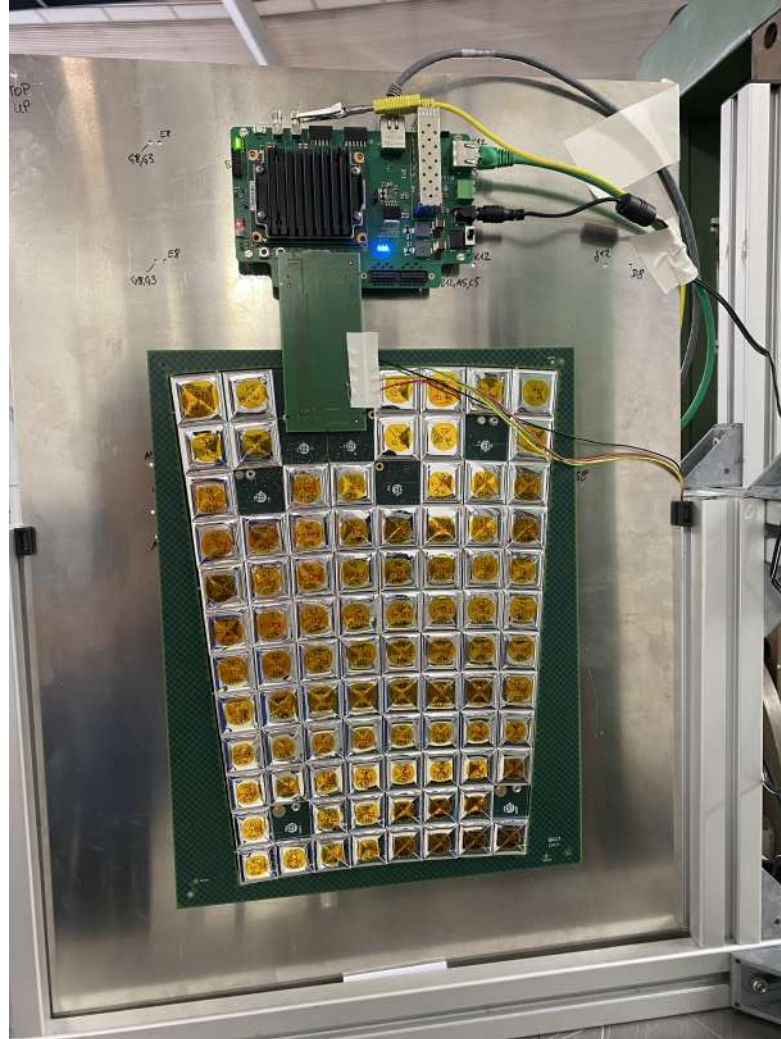
Figure 4.3: A fully-equipped tilemodule placed onto the aluminium plate and the
DAQ system. Courtesy of Jia-Hao Li.

Figure 4.4: Picture of the movable stage and the trigger scintillators used during test beam campaigns. Courtesy of Jia-Hao Li.

4.2.2 Overview of the measurements

Several characteristics of the SiPMs, tiles, and the overall system are measured and presented in this thesis to assess that the components and their assembly meet the required performance expectations and quality standards. The most relevant SiPM properties influencing the measurements are:

- **Breakdown voltage ($V_{\mathbf{br}}$)**: the voltage above which avalanche multiplication occurs;

- **Bias voltage ($V_{\mathbf{bias}}$)**: the reverse voltage applied to operate the SiPM in Geiger mode, which must be greater than V_{br};

- **Overvoltage (OV)**: defined as the difference between the applied V_{bias} and the V_{br}, $OV = V_{\mathrm{bias}} - V_{\mathrm{br}}$, and thus a positive quantity.

The two main quantities measured and presented in this chapter are the SiPM *gain* and the *light yield*, and are defined as follows:

- **SiPM gain**: the factor by which the charge from a single electron–hole pair produced in the photoelectric effect is multiplied during the avalanche process, typically of the order of 10^6 [103]. The gain is a unique characteristic of each SiPM, and is also influenced by test conditions such as temperature, which affects the V_{br} of the SiPM.

- **Light yield** (LY): the number of photons detected by the SiPM produced by an MIP impinging on the scintillator tiles. It is a purely optical parameter depending on the scintillator and SiPM properties and not on the electronics.

4.3 SiPM gain measurements

The low-intensity LED system, described in Section 3.4, is used to determine the SiPM gain. These measurements are taken simultaneously across all channels of a tileboard, with no beam incident on it. As it is a unique characteristic of each SiPM, the measurement is performed for each channel of the tileboard under test and for each setup.

4.3.1 Measurement strategy

Every SiPM in the tileboard is equipped with an LED system, which produces photons in the UV range. The LEDs are activated by the trigger signal readout of the HGCROC, which is triggered by the DAQ system. Single photons are scattered by the scintillator tile and then collected by a few pixels of the SiPM, generating a current pulse which is recorded by the HGCROC and converted to ADC counts. The number of avalanches created in the SiPM is proportional to the number of photons collected and thus the resulting pulse amplitude follows a characteristic multi-peaked spectrum distribution, called Single Photon Spectrum (SPS). In a typical tileboard measurement, each LED fires simultaneously in the corresponding channel. The channel receives 10^4 pulses, and the resulting distribution of ADC counts is analyzed. An example of such a distribution, where the SPS is visible, is shown in Figure 4.5. The first peak corresponds to only noise detection, and it is called *pedestal level*. The $n^{th+1}-$peak in the spectrum reflects the amount of charge produced by collecting n photons.

The SiPM gain represents the multiplication factor of the avalanche; therefore, it can be retrieved by measuring the distance between two consecutive peaks in the SPS. The distance is extracted by fitting the distribution with a sum of Gaussian distributions and measuring the distance between the means of adjacent peaks.

The gain is linearly dependent on the OV and, as the V_{br} is temperature-dependent, the gain is also influenced by temperature. Therefore, the V_{bias} and the temperature are recorded for each data-taking and accounted for later in the analysis. The gain also depends on the size of the SiPM[1].

---

[1]The gain depends primarily on the pixel size rather than on the total SiPM area. Since the pulse shape varies with the SiPM size, larger devices produce slower pulses. The shaping time of the readout chain is optimized to sample the pulse peak and to minimize afterpulsing, and is typically shorter than the full pulse duration. Consequently, only a fraction of the total pulse is integrated, with a smaller fraction for larger SiPMs.
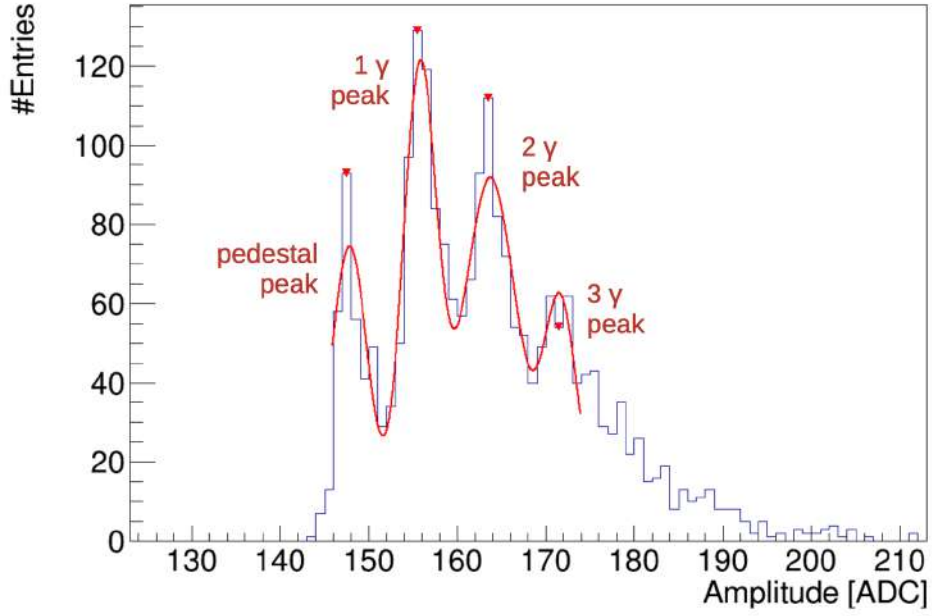
Figure 4.5: Example of a SPS where the pedestal and three photo-electron peaks are visible.

Moreover, various parameters of the setup are to be adjusted to obtain a visible SPS. The two most important are the LED intensity and the sampling time, which is the time when the HGCROC reads the data relative to the LED firing and L1A offset, as described in Section 3.4.1. Since the optimal conditions vary between channels, multiple values of these parameters are scanned during the measurements.

Optimal LED intensity

The light intensity is controlled by the voltage load applied to the LED through a capacitor. The optimal voltage range is between 5.7 V and 6.4 V. If the voltage is too low to produce enough photons, the resulting ADC distributions show the pedestal peak only. On the contrary, if the voltage increases, the light intensity increases, and the photoelectron peaks merge to form a broader spectrum for which the peaks are not visible anymore. The gain measurements are repeated for different LED voltages in 100-mV increments, allowing the SPS to be reconstructed optimally. The optimal setting to produce a visible SPS is channel-dependent due to the slight difference in channel components; therefore, the LED voltage scan is repeated for each channel.

The ADC distributions of the scan of three different LED voltages, i.e., 5700, 5800, and 6000 mV, are shown in Figure 4.6 for one single channel at the same sampling time. While the spectra at 5700 and 5800 mV only show the pedestal (and partially the first photo-electron peak), the setting with 6000 mV results in a well-defined multi-peak structure.
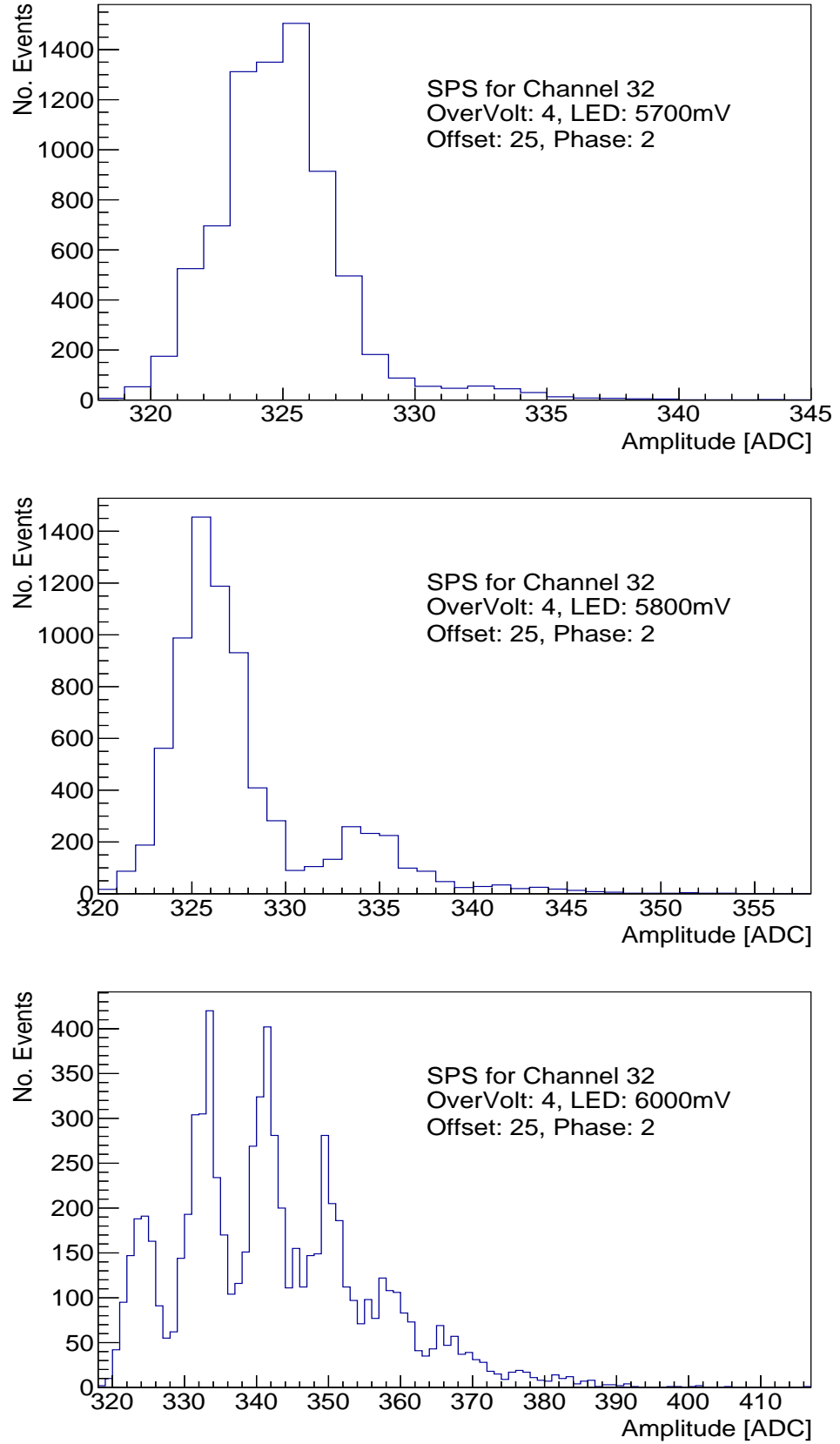
Figure 4.6: Three amplitude distributions of an LED voltage scan. Voltages of 5700, 5800, and 6000 mV are recorded for the same channel with the same settings per LED voltage. The settings with 6000 mV result in a visible SPS.

Optimal sampling time

As described in Section 3.4.1, the sampling time defines when to record data after the readout trigger and L1A offset, and it can be adjusted for each channel by selecting either the specific BX or the precise time window within a BX, controlled by the *phase* parameter of the HGROC. This affects the gain measurement, as the fraction of total charge can be partially collected if the sampling time is not optimal, which corresponds to the highest gain value.

A scan of different sampling times is performed. Figure 4.7 shows the gain measured at different acquisition times for a single channel, highlighting how the gain differs with respect to the choice of the sampling time. The acquisition time is computed as the offset (in BX) multiplied by 16 and added to the phase.
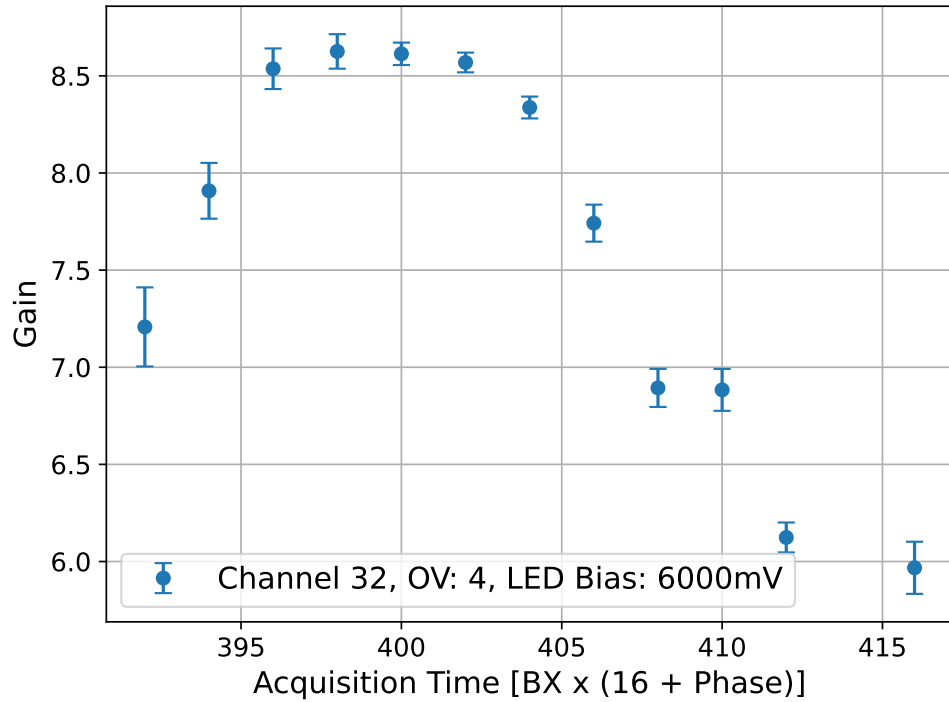
Figure 4.7: The gain measured for different acquisition times.

Differential non-linearity correction

Differential non-linearity (DNL) arises from imperfections in the response of a digital-to-analog converter. Ideally, the transfer function (or step function) from analog to digital shows a uniform staircase characteristic, where each step in the analog input corresponds to an equal increment in the digital output, typically one least significant bit (LSB). In reality, the width of these steps can vary from the ideal 1 LSB, leading to differential non-linearity, which therefore needs to be properly corrected. An example of the ideal and actual response of a 3-bit ADC is shown in Figure 4.8.

The DNL causes the ADC output distribution to deviate from a flat distribution, resulting in a comb-like structure where some ADC bins are more populated than others. It has been observed that every second bin in the ADC scale appears to have systematically more data accumulated with respect to the adjacent bin.
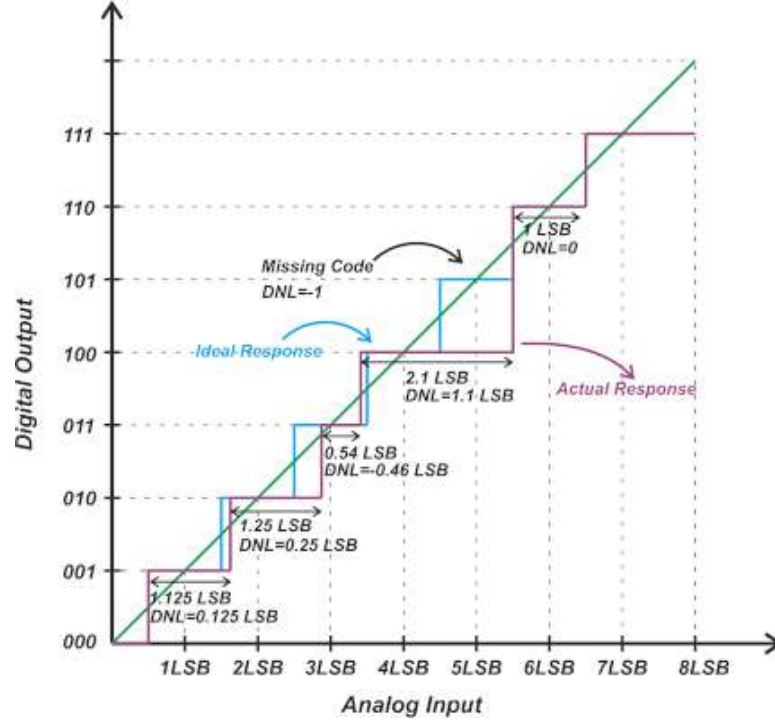
Figure 4.8: An example of the ideal and actual transfer function for a 3-bit ADC [111].

During the gain measurements, the method to mitigate the DNL effect has been to perform three different measurements by shifting the pedestal values and therefore the whole distribution by different ADC counts. Starting from the nominal distribution, the other two measurements have been taken by changing the parameter `trim_inv` of the HGROC, which shifts the distribution by 1 and 2 ADC counts. The datasets from the measurements with modified `trim_inv` settings are aligned to the nominal configuration by shifting their ADC values accordingly, i.e., 1 or 2 counts, and then summed together. Summing the three datasets helps to smooth out the DNL effect in the ADC response.

Figure 4.9 shows the three measurements taken with different `trim_inv` settings for a single channel, along with the summed dataset, which exhibits a smoother distribution. The dataset with `trim_inv` = 0 corresponds to the nominal distribution, while the *Sum with DNL mitigation* histogram shows the result of summing all three aligned distributions.
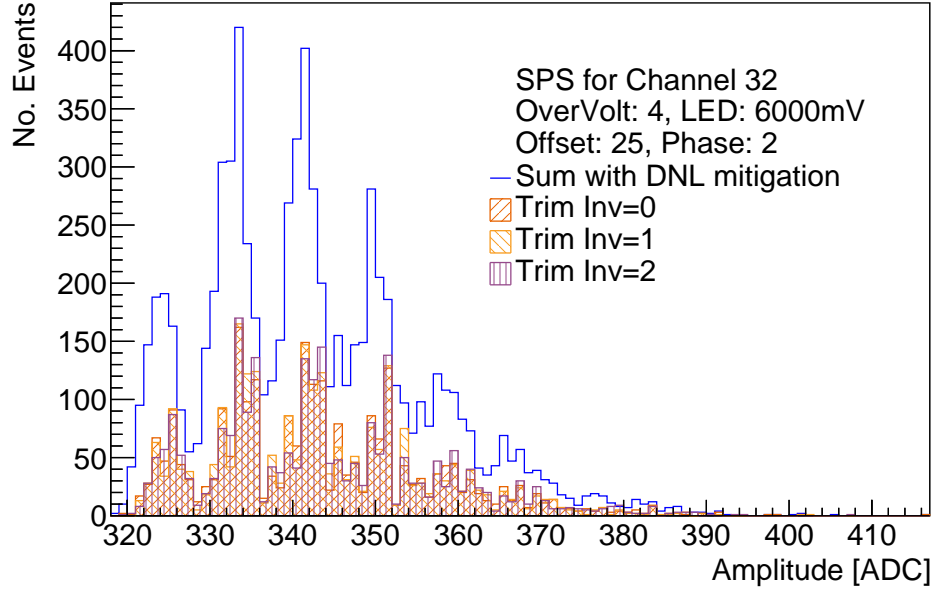
Figure 4.9: An example of the method to mitigate the DNL effect. Three distributions
obtained with different `trim_inv` settings are shown with filled histograms. The sum
of the aligned distributions is shown with a blue line.

4.3.2 Gain value extraction

The extraction of the gain value from the SPS is done using the `ROOT` framework
[112]. The procedure is done in two steps. First, the positions of all peaks in
the distribution are retrieved using the library `TSpectrum` provided by `ROOT`. The
library provides tools for peak searching in one-dimensional spectra, making it
suited for identifying and analyzing the signal peaks. The peak search can be
fine-tuned using various parameters, such as the maximum number of peaks, the
peak width (*sigma*), the resolution, controlling the minimum separation between
two neighboring peaks, and the threshold. Peaks with an amplitude below the
threshold times the highest peak amplitude are discarded. In these studies, the
sigma is set to 1, the resolution value is set to 1 (corresponding to a 3-sigma
distance between peaks), and the threshold is set to 10^{-2}. These parameters
are empirically optimized to achieve the best results for a wide range of SPS
distributions.

Second, a multi-Gaussian fit is performed using the following formula, if at
least two peaks are found:

$$\sum_{i=1}^{N_p} a_i \cdot \exp\left\{ -\frac{1}{2}\left(\frac{x-b_i}{c_i}\right)^2 \right\}, \tag{4.1}$$

where N_p is the total number of peaks fitted [2]. The parameters a_i, b_i, and c_i
are respectively the peak height, the peak position (in ADC), and the standard
deviations of the peaks fitted, and they are initialized with the information re-
trieved with the `TSpectrum` function. The gain is obtained from the fitted spacing

---

[2]In principle, the SPS is modeled as a sum of independent Gaussian distributions, but,
generally, the distance between peaks is forced to be the same, such that $b_i = b_0 + i * G$, where
G is the gain

between consecutive peaks in the ADC spectrum, representing the multiplication factor of the charge corresponding to a single photoelectron.

The uncertainty on the gain represents the one-sigma uncertainty from the fit. The SPS distributions whose χ^2/n.d.f from the fit is larger than 10 are discarded from the analysis. This threshold is chosen as a practical compromise, accounting for the fact that the differential nonlinearity (DNL) of the ADC can distort the peak structure and limit the fit quality. An example of a multi-gaussian fit of an SPS distribution is given in Figure 4.10 for one channel (32) of a D8-type and a specific configuration, i.e., LED bias voltage of 6000mV, BX of 25, and phase of 2.
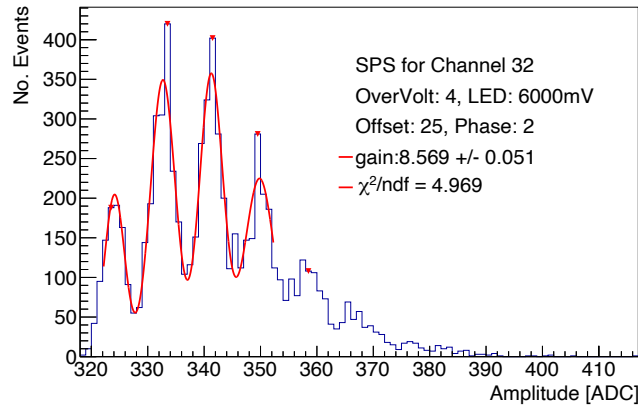
Figure 4.10: An example of a multigaussian fit of an SPS. The peaks found from the `TSpectrum` function are visible as red triangle markers, while four Gaussian distributions are fitted to the histogram. The gain value from the fit and its error, alongside the χ^2/n.d.f, are also shown.

The fitting procedure is done for different sampling times and LED bias voltages for each channel. As already mentioned in Section 4.3.1, the highest gain value is selected if multiple gain values can be extracted for one channel for different sampling times. The gain values obtained for different LED bias voltages are averaged for a single channel, as they are compatible within uncertainties. Therefore, each channel has a single gain value after the measurements.

Figure 4.11 shows the uniformity of the gain measurements across channels of a D8-type tileboard. More than 20% of the channels show a visible SPS that could be successfully fitted, which is sufficient to verify the expected behavior and overall quality of the tileboard. All fitted gain values, except for one channel, lie within a $\pm 5\%$ range around the average gain; all are contained within a $\pm 10\%$ range, which indicates good channel-to-channel uniformity for both the electronics and the SiPMs.
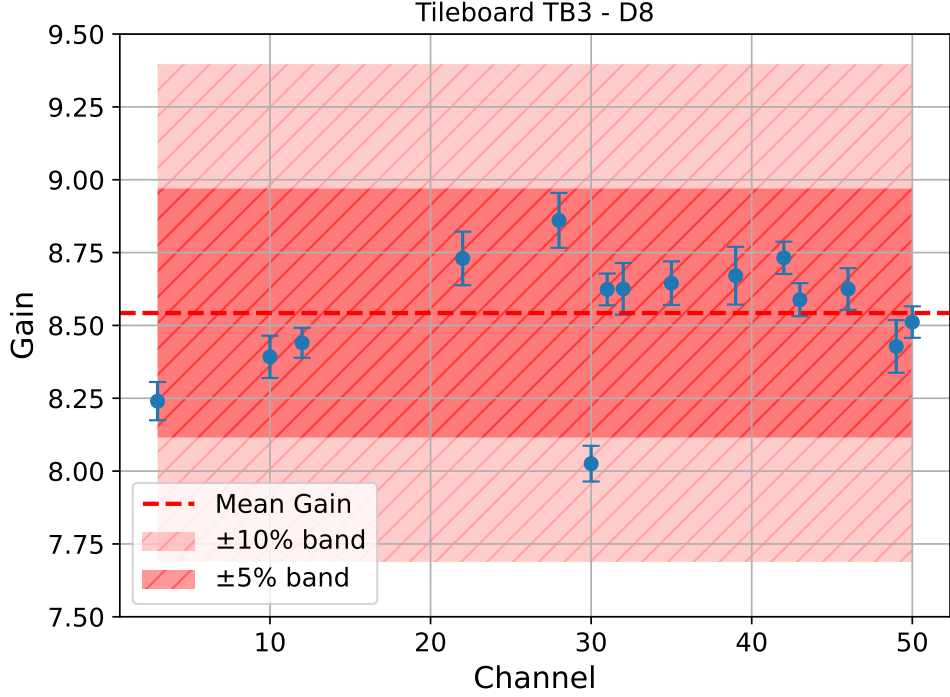
Figure 4.11: The gain uniformity in different channels of a D8-type tileboard. The
mean gain value across the channels is shown as a red dashed line. The $\pm 5\%$ and $\pm 10\%$
uncertainty around the average are also shown.

4.4 Measurements of light yields

4.4.1 Measurement strategy

As the impinging electrons used in the test beam are considered as MIPs, the light
yield can be measured by combining the measurements of the SiPM gain (Section
4.3) and measurements of the most probable charge deposited by a MIP, i.e., the
maximum of the distribution of the MIP deposited charge, which is described in
the following section. The light yield is measured in number of photo-electrons,
and it can therefore be obtained as follows:

$$\text{Light Yield [p.e.]} = \frac{\text{MIP maximum [ADC]}}{\text{SiPM Gain [ADC/p.e.]}} \qquad (4.2)$$

Since both the MIP maximum and the SiPM gain depend on test conditions
such as temperature and V_{bias}, specific corrections are applied to ensure that
both quantities are evaluated under the same conditions.

4.4.2 MIP maximum extraction

As the electrons at the test beam energy release energy to the scintillator tiles
as MIPs, the shape of the generated pulse can be fully reconstructed by the
setup. When an electron impinges on the detector, it produces a signal that can
be modeled using a Landau-Gaussian convolution. By analyzing this spectrum,

74

the value of the MIP maximum can be extracted, as it is the measurement of the most probable charge deposited by a MIP in ADC counts.

The beam frequency is not synchronized with the HGCROC clock, which operates at the LHC BX frequency of 40 MHz, for which the signal will have a fixed phase with respect to the clock. Therefore, during test beams, it is crucial to determine the moment at which the MIP pulse reaches its maximum after the event has been triggered. The HGCROC is highly tunable in time using the L1A offset and the phase (Section 3.4.1): the first, to select the BX to sample; the second, to adjust the clock within that BX. Tuning both parameters ensures that the photoelectron signals are sampled as close as possible to their peak amplitude to ensure that the peak of the incoming pulse is synchronized with the phase-shifted clock.

One of the key features of the test beam DAQ system is the ability to record the time stamps of all the triggered events, namely the time with respect to the clock edge, with a resolution of 0.8 ns. This quantity is referred to as *TrigTime* and is measured with respect to the specific HGCROC digital block after receiving the coincidence trigger signal from the PMTs. This is a special operation mode since the DAQ is not synchronized with the DESY test beam, while at the LHC the timing is set by considering the length from the interaction point.

Different examples of *TrigTime* are shown in the sketch of Figure 4.12. The corresponding ADC sampling points of different generated pulses are visible. Electrons producing pulses such as *Pulse 1* or *Pulse 2* have a small *TrigTime* as they are detected close to the initial digital block, but they are sampled later with respect to the following block. Therefore, the signals are sampled on the falling edge of the pulse. Whereas, signals like *Pulse 5* are sampled too early, thus only the rising edge of the distributions is sampled. The ideal case is represented by signals such as *Pulse 4*, which are sampled precisely at their peak. This alignment ensures optimal timing and charge reconstruction.
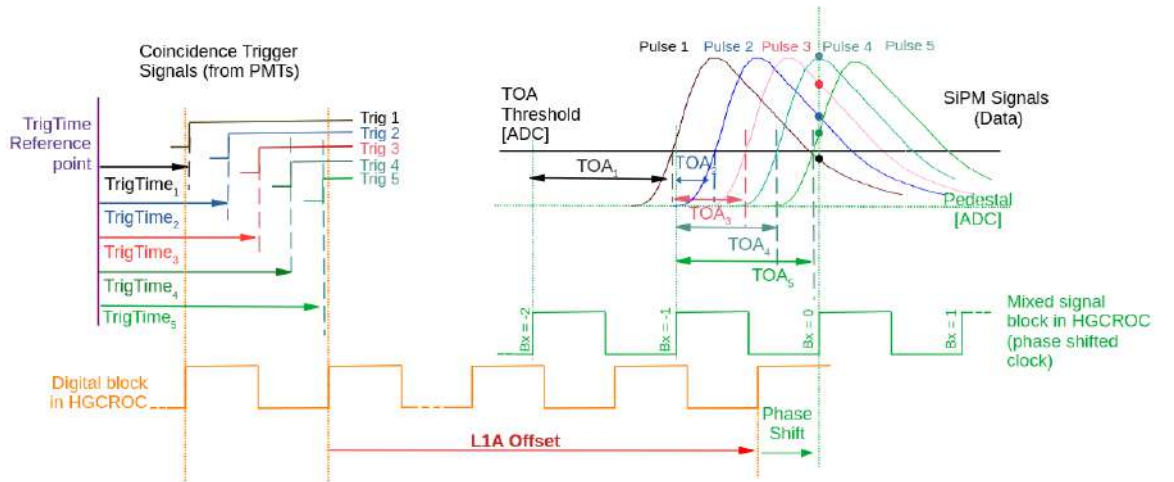
Figure 4.12: Sketch representing different samplings of photo-electron pulses [104].

Figure 4.13 shows the evolution of the signal pulse over three consecutive BX samples, recorded during a test beam campaign. Each sample corresponds to a dataset of 200,000 triggered electron events. The 2D histogram shows the recorded *TrigTime* on the x-axis and the corresponding ADC value on the y-axis,

with the color scale (z-axis) indicating the number of events. The distributions in the first and third samples depict cases where the pulse is sampled too early or too late, respectively, to optimally record the MIP maximum. The second sample contains the MIP maximum, and the *Signal Window* represents a 10-bin range in *TrigTime*, which is used to extract the MIP maximum.
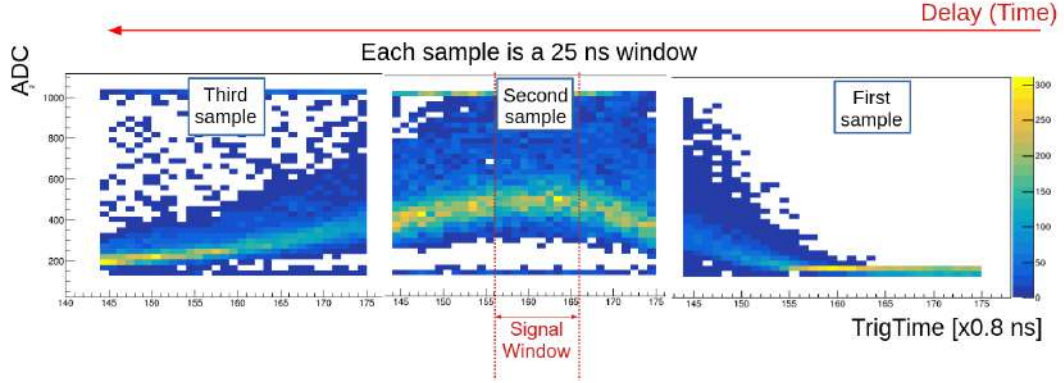
Figure 4.13: 2D distribution of the sampled ADC and *TrigTime* for three consecutive BX in a test beam campaign [104].

The pulse amplitude in ADC of the signal in the 10-bins *TrigTime Signal Window* is presented in Figure 4.14 for one channel. The distribution is fitted with a Landau-Gaussian function to retrieve the distribution maximum, which is extracted as the most probable value. The pedestal peak is visible as a narrow Gaussian-distributed peak at low values of ADC. The fit range is chosen to exclude the pedestal from the fit. The maximum of the fit represents the MIP maximum. For further uses, the maximum of the fit is subtracted by the pedestal value, which is obtained as the median ADC value in a range that contains the pedestal distribution. No DNL mitigation is applied, as the ADC range used for MIP reconstruction is larger than the region typically affected by DNL, and thus the effect does not influence the MIP maximum extraction. However, dips caused by the DNL are still visible, giving the distribution a comb-like shape. The uncertainty of the MIP maximum is derived from the fit parameters, propagating the fit maximum and pedestal position uncertainties.

The measurement is performed for each channel individually, using a movable stage that scans the tiles in the x-y plane perpendicular to the beam axis. Different types of tileboards are considered. The MIP maximum values extracted for different channels in tileboards of the same type, i.e., D8, are shown in Figure 4.15. The signal depends on the tile size and hence the channel, which is the reason why the MIP maximum increases with respect to the channel number.

These results have been obtained during the test beam campaign at DESY in May 2024. Only `TB3_D8_4` and `TB3_D8_10` were fully equipped with SiPM and tiles. A small fraction of channels (less than 1%) exhibited errors during data-taking and are therefore excluded from the figure. Channels 13 to 18 correspond to positions where mechanical pins are located, as visible in Figure 4.3. These channels will be equipped with specifically designed tiles, which were not available during the test beam. The channels of `TB3_D8_3` which exhibit large MIP values were equipped with different types of scintillator tiles.

Since the V_{br} varies between individual SiPMs and tileboards, and the mea-
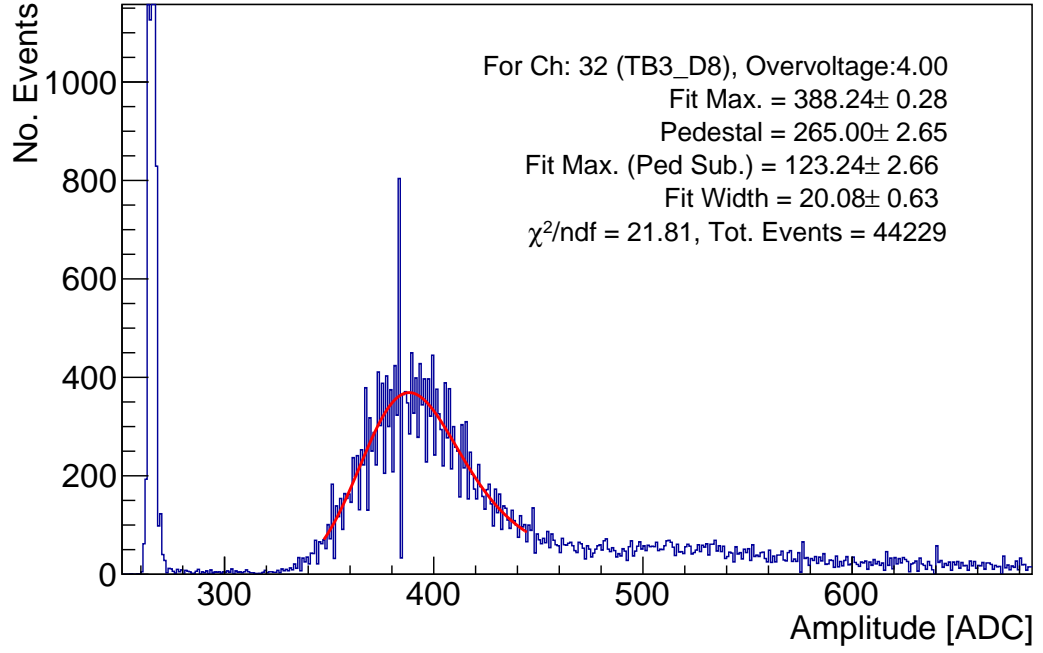
Figure 4.14: The pulse amplitude in ADC of a MIP signal for one channel. The
Landau-Gaussian fit is shown as a red curve. The results of the fit are also shown.
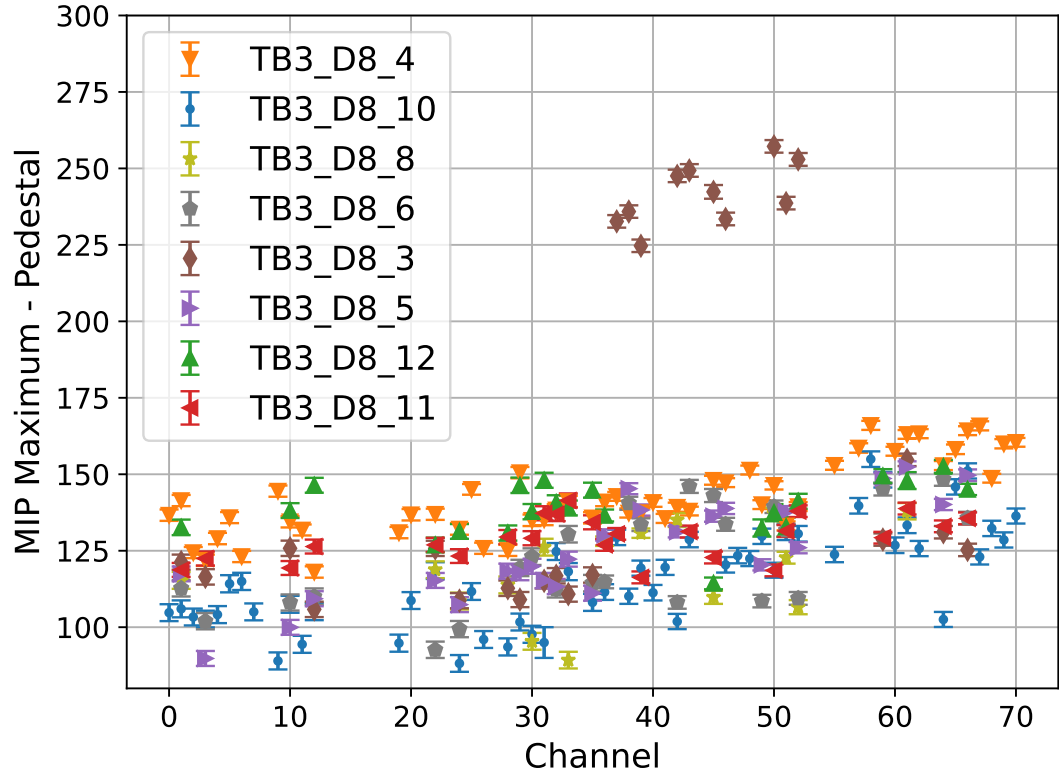
Figure 4.15: MIP maximum minus the pedestal values extracted for different channels
of a D8-type tileboard. Channels of the `TB3_D8_3` tileboard, which exhibit large MIP
values, were equipped with different types of scintillator tiles.

77

surement conditions were not identical, a normalization procedure is applied to account for these differences. First, the actual OV is obtained by calculating the V_{br} at the temperature at which the measurement was taken. As the reference temperature specified by the manufacturer (HPK) is 25°C, and given that the V_{br} increases linearly with temperature, the corrected OV is calculated as

$$OV(T) = V_{\text{bias}} - V_{\text{br}}(25°\text{C}) + (25°\text{C} - T) \cdot 0.0375 \text{ V/K}, \tag{4.3}$$

where V_{bias} is retrieved from the HGCROC, the V_{br} is specified by the manufacturer to 38.04 V[3], and T is the temperature at the time of the measurement, obtained from one of the temperature sensors on the tileboard. The gradient value of 0.0375 V/K is also provided by the manufacturer. Previous studies on the gradient by the HGCAL Collaboration are presented in detail in Ref. [113].

After the correction, the MIP response of each channel has been scaled by the ratio between a fixed OV value (4V) and the corrected OV measured for that channel. The MIP response depends on the number of detected photons, which scales with the photon detection efficiency (PDE)[4] of the SiPM, that increases with OV according to the manufacturer's datasheet [103] as a second-order polynomial curve:

$$\text{PDE} = m_1 \cdot OV^2 + m_2 \cdot OV + c, \tag{4.4}$$

where $m_1 = -0.72 \text{ V}^{-2}$, $m_2 = 10.0 \text{ V}^{-1}$, and $c = 4.41 \text{ V}^{-1}$ are constants determined from the datasheet. The MIP response scaling effectively corrects for variations in the PDE due to temperature and bias differences among channels.

Overall, the results across different tileboards demonstrate good uniformity. The observed trend of higher MIP values for channels with higher indices is consistent with the tileboard layout: these channels are located in the lower part of the board, where the tile areas are smaller. As a result, a higher MIP signal is expected. Lastly, the exact SiPM temperature cannot be retrieved because the tileboard heats non-uniformly through the electronics; therefore, a global value is used. It is then sufficient to keep the correct voltage within 100–200 mV, corresponding to a temperature uncertainty of about 2K.

4.4.3 Light yield evaluation

The light yield can be calculated by combining the MIP and SiPM gain measurements using Equation 4.2. Since both measurements strongly depend on the OV, which depends on the V_{br}, which in turn is temperature-dependent, both must be taken under identical experimental conditions. If this is not the case, appropriate corrections must be applied before calculating the light yield. Note that both measurements are performed using the same HGCROC settings; therefore, no adjustment is needed for those parameters.

---

[3]Hamamatsu provides batches of SiPM with similar V_{br}.

[4]The PDE is the probability of detecting a photon by a SiPM.

Light yield correction

Both the MIP and SiPM gain measurements are corrected by computing the temperature-corrected OV at which the data were taken, using Equation 4.3. Afterwards, the SiPM gain is corrected to OV at which the MIP measurements were taken, given the linear dependence of the gain on the OV. The LY is then measured with Equation 4.2, using the corrected MIP and SiPM gain values.

To compare light yields from different test beams, it is crucial to adjust the measurements to the same conditions, and, in particular, to a fixed OV. The light yield has a proportional dependence on the PDE of the SiPM, which itself changes with the applied OV (Equation 4.4). The same functional form can thus be used to relate the LY to the OV,

$$\text{LY} \propto m_1 \cdot OV^2 + m_2 \cdot OV + c. \tag{4.5}$$

Given a measured light yield at a certain OV, the corresponding light yield at a fixed reference OV can be calculated as:

$$\text{LY}_{\text{ref}} = \text{LY} \cdot \frac{m_1 \cdot OV_{\text{ref}}^2 + m_2 \cdot OV_{\text{ref}} + c}{m_1 \cdot OV^2 + m_2 \cdot OV + c}. \tag{4.6}$$

where, LY_{ref} is the adjusted light yield at the reference overvoltage OV_{ref}, and LY is the originally measured value using Equation 4.2.

Figure 4.16 compares the corrected light yield to the originally measured value for various channels of different D8-type tileboards from the May 2024 DESY test beam campaign. The OV_{ref} is 4V. As shown, the applied correction results in small adjustments, generally within a $\pm15\%$ interval around the measured values. Figure 4.17 shows the distributions of the LY_{ref} for different channels for various D8 tileboards.

The uncertainties on the light yield calculation arise from the propagation of errors from both the MIP peak and gain measurements. These uncertainties are derived from the fits to the Landau-Gaussian distribution (for the MIP peak) and the SPS distribution (for the gain). On average, the relative uncertainty on the gain is around 1%, while that on the MIP peak is approximately 2%. Systematic uncertainties—such as variations in SiPM or scintillator quality, imperfections in tile wrapping, or fluctuations in the applied V_{bias}—are not included in this calculation.

The results shown in Figure 4.16 for `TB3_D8_10` and `TB3_D8_4` deviate slightly from the expected reference point, where $\text{LY}_{\text{ref}} = \text{LY}$, but remain within a 15% variation. This deviation can be attributed to an offset in the V_{bias}, which is read back by the HGCROC, most likely caused by an incorrect DAC calibration. A V_{bias} error of about 0.4–0.5 V, corresponding to the same difference in OV, results in an approximate 10% change in light yield[5]. Another source of deviation arises from a miscalibrated temperature sensor: given the gradient of Equation 4.3, a difference in LY of around 0.4% is expected per K.

---

[5]For typical SiPMs operated at an OV of 3–5 V, the PDE efficiency increases by about 10–20%/V (see Equation 4.4). Hence, a 0.4–0.5 V deviation corresponds to roughly a 10% change in light yield.

No unexpected behavior was observed in the light yield results, and the values are consistent across various channels of different tileboards. Moreover, by converting the light yield measurements to a common reference voltage, the results are made comparable with other measurements obtained under different experimental conditions or in future studies.
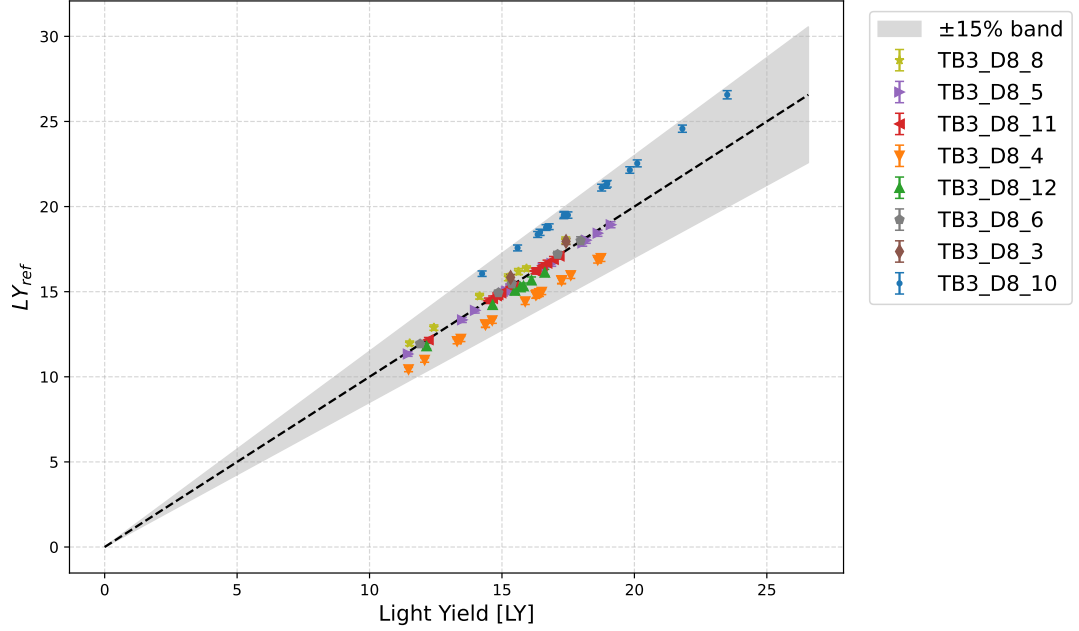
Figure 4.16: Comparison between the measured LY and the LY corrected to the OV_{ref} of 4 V (LY_{ref}) for various D8-type tileboards from the May 2024 DESY test beam campaign. The black dashed line corresponds to the identity $LY_{ref} = LY$, and the grey band indicates a $\pm 15\%$ deviation from this reference.
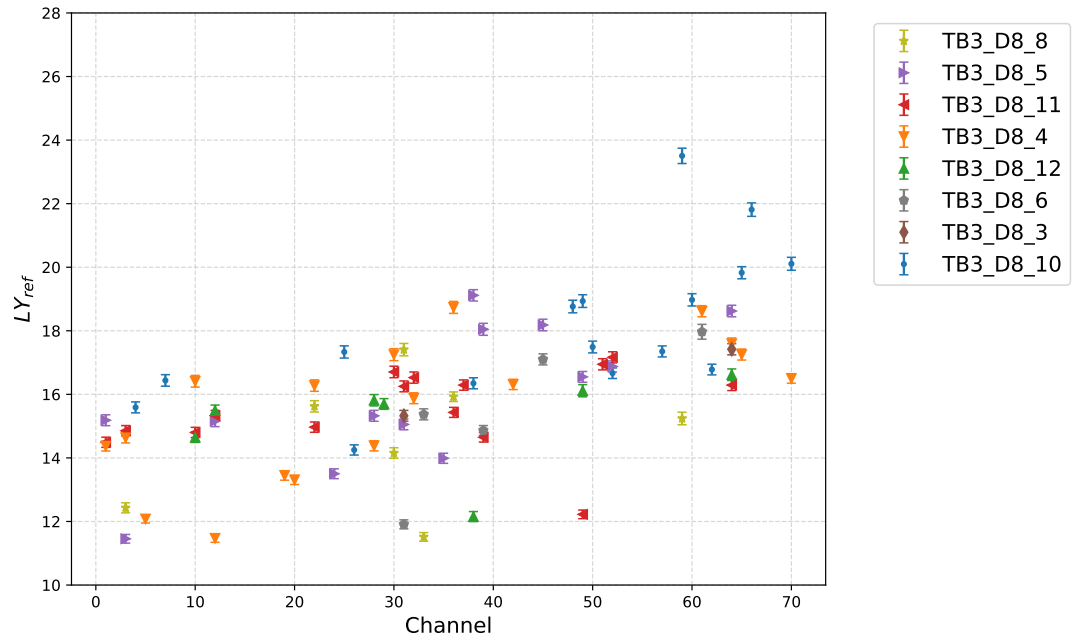
Figure 4.17: The LY_{ref} for various D8-type tileboards for different channels from the
May 2024 DESY test beam campaign.

4.5 Summary and outlook

This chapter presented the validation results of the scintillator section of the CMS HGCAL, based on test beam campaigns conducted at the DESY II facility. These campaigns assessed both the stability and overall performance of the system.

Key parameters and characteristics of the SiPMs, scintillator tiles, and the integrated system were measured or derived. The results showed good agreement with expectations and demonstrated consistent behavior across multiple tileboards, confirming the system's reliability.

The setup included various components that required validation before the planned mass production starting in 2025. The results confirmed that both individual components and the complete system met design expectations, with uniform performance observed across different tileboards.

These results support the current prototype designs, with only minor adjustments—mainly mechanical, such as the use of 9 mm^2 SiPMs and the removal of 2 mm^2 SiPMs, or electronic—anticipated before entering mass production. The DESY laboratories will continue to play a central role in the assembly and validation of final components. Future developments will include measurements involving multiple tileboards and the implementation of a cosmic stand for calibration.

Chapter 5

Physics object reconstruction

The information from the CMS sub-detectors is combined and converted to reconstruct particles resulting from a p–p collision of interest. The snapshot of the collision output is referred to as an *event*. In a single event, multiple objects can be reconstructed and identified in physics analysis, using the readout information of various sub-detectors. The algorithm used for the combination is called *particleFlow* (PF) which is described in detail in Section 5.2.

The PF algorithm combines information from several building blocks. In the tracker system, these include the trajectories of charged particles and the location of the primary interaction vertex, as detailed in Section 5.1. In the calorimeters, dedicated clustering algorithms combine information from ECAL and HCAL cells.

The objects that are reconstructed by the PF algorithm and used in this thesis work are muons (Section 5.3), electrons (Section 5.4), and jets (Section 5.5). Section 5.6 presents the method to identify heavy-flavor quarks, such as b and top quarks. Since tau leptons, photons, and missing transverse energy (used to infer neutrino energy) are not utilized in this thesis, their reconstruction descriptions are not discussed. Further details can be found in Refs. [114, 115, 116].

Some of the results presented below are based on collision data collected during different data-taking periods and at various $\sqrt{s}$. Other results are derived from simulation studies. A detailed description of the Monte Carlo (MC)–based simulation of p–p collisions is provided in Appendix A.

5.1 Track and primary vertex

The reconstruction of charged particle tracks is crucial for both the offline reconstruction and the HLT trigger. Track reconstruction is performed using an iterative procedure consisting of four steps: track seed generation, pattern recognition, ambiguity resolution, and final fitting.

Seed generation begins by selecting either two or four pixel hits that meet the minimum requirements on transverse momentum (p_{T}), as well as transverse d_0 and longitudinal z_0 impact parameters relative to an estimated beam spot or a pixel vertex. The d_0 is defined as the distance of closest approach of a track to the beamline in the transverse $x - y$ plane, while the z_0 is the distance between the point where the track is closest to the beamline and the primary vertex along

the beam axis.

These seeds are then used as input to a pattern-recognition algorithm, which is based on the Kalman filter method [117]. The algorithms extrapolate the seed trajectories outward to the next tracker layers, adding new hits to the trajectory. If multiple compatible hits are found in a layer, the seed trajectory is cloned for each of them. If no hit is found, a "fake" hit is assigned.

Once candidate trajectories are formed, the list of hits per track is fitted using a Kalman Filter (KF)-based helix fit that accounts for material effects and the magnetic field. The fitted tracks must satisfy several quality criteria, including the original seed requirements, the number of fake hits, the χ^2/ndof, and the number of shared hits with other tracks. If two tracks share multiple hits, the one with fewer total hits is discarded. In cases where both tracks have the same number of hits, the one with the higher χ^2/ndof is removed.

During Run 3 data-taking activities, a new recognition pattern algorithm has been employed along with the KF-based algorithm, known as mkFit [118]. This algorithm maximizes parallelization and vectorization in multi-core CPU architectures.

An example of the track build reconstruction efficiency is given in Figure 5.1 for the Kalman Filter and the mkFit algorithms. The efficiency is evaluated in simulation as the fraction of simulated tracks that are matched to at least one reconstructed track [1], averaging more than 90% in the overall distributions.
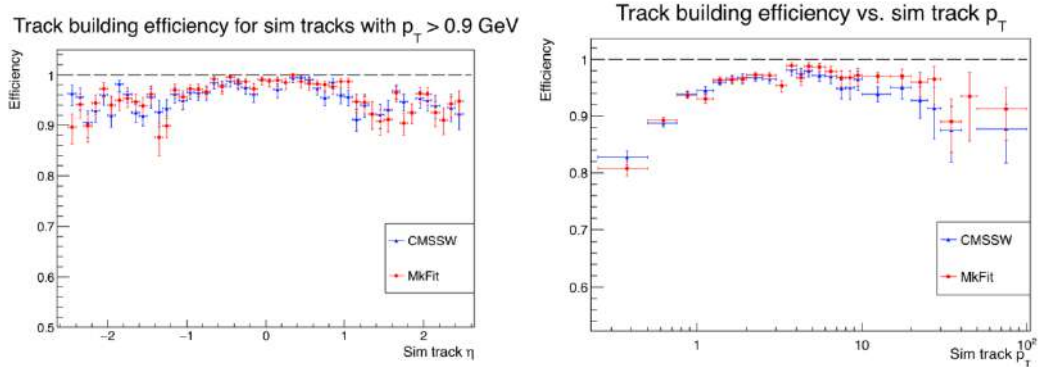
Figure 5.1: Tracking build efficiency in simulation for the Kalman Filter and mkFit algorithms as a function of the simulated η (left) and p_T (right) [118].

Primary vertex reconstruction

In each event, a large number of proton-proton interaction vertices are produced. It is therefore crucial to identify the locations where collisions occurred, known as primary vertices (PV). Vertices are defined as the points of origin for sets of tracks, and their reconstruction involves three main steps: the selection of tracks, the clustering of tracks compatible with a common interaction point, and a fit to determine the vertex position. For each candidate vertex, the sum of the transverse momenta of its associated tracks is calculated, weighted according to their impact parameters with respect to the vertex position. The vertex with the

---

[1]A reconstructed track is considered matched to a simulated track if more than 75% of the reconstructed track hits are shared

highest sum of squared transverse momentum is considered the main (or true) primary vertex.

The primary vertex resolution in y and z is shown in Figure 5.2 as a function of the number of tracks for data collected at $\sqrt{s}$ of 7 TeV for two types of events: jet-enriched and minimum bias. The minimum-bias sample is collected from a set of triggers requiring, for example, minimal selection on the hit in the pixel detectors. The jet-enriched samples are produced by requiring each event to have a reconstructed jet with transverse energy $E_{\mathrm{T}} > 20$ GeV. The resolution is calculated from the distributions in the difference of the fitted vertex positions for a given number of tracks are fitted using a single Gaussian distribution.
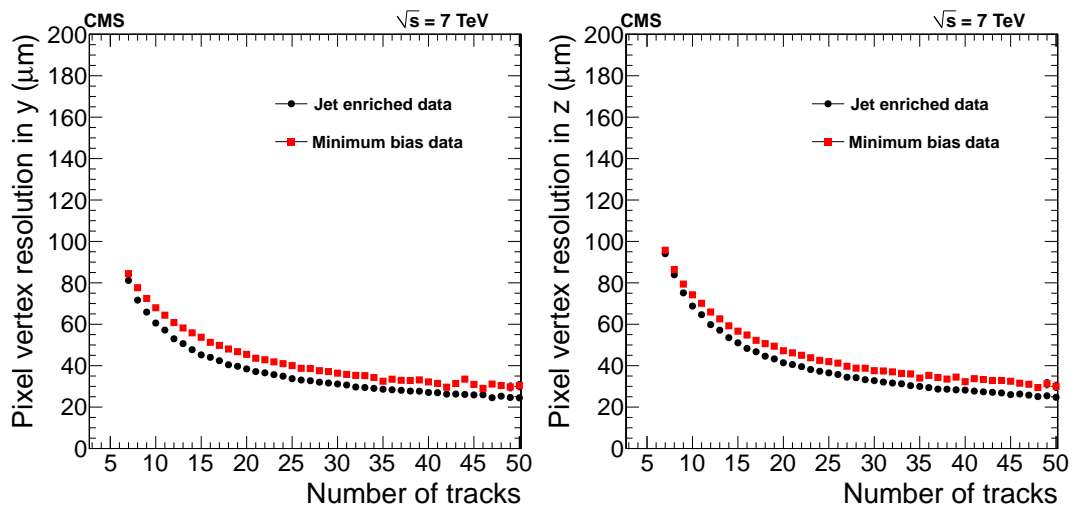
Figure 5.2: Primary-vertex resolution in x (left) and in z (right) as a function of the number of tracks at the fitted vertex, for two kinds of events with different average track p_{T} values [79] .

5.2   Particle Flow

The information from all sub-detectors presented in Section 2.2 is combined to reconstruct global particle candidates such as electrons, muons, photons, neutral hadrons, and charged hadrons. The key element for these object reconstructions is the PF algorithm [119], which aims to improve spatial and energy resolution and particle identification over the single sub-detector reconstruction.

This reconstruction algorithm is based on linking information from the various sub-detectors, including charged particle tracks from the tracking system, calorimeter clusters from the ECAL and HCAL, and tracks from the muon system.

The first candidates to be reconstructed are muons, by extrapolating and linking tracks from the tracker and the muon system. Once identified, the associated tracks and muon system hits are removed from the collections, and their corresponding energy deposits in the ECAL and HCAL are subtracted to avoid double counting in the reconstruction of other particle candidates.

Electron candidates are reconstructed by combining tracks with ECAL clusters, where the trajectories are extended to the expected shower depth of an

electron. After reconstruction, the associated tracks and ECAL clusters are removed from the collections.

Charged hadrons are reconstructed from the remaining tracks and calorimeter clusters. The tracker trajectories are extrapolated to the HCAL cluster up to one interaction length. Neutral hadrons, which do not leave tracks in the tracker, are identified by their energy deposits in the ECAL and HCAL. Photons are reconstructed from ECAL clusters that are not associated with any tracks.

The full description of the reconstruction steps of these objects is given in the following sections. A sketch of the transverse plane of CMS, where the PF candidates are visible, is given in Figure 5.3.

The PF workflow will also be used for object reconstruction during the HL-LHC era, in which most sub-detectors will undergo major upgrades or be replaced, such as the endcap calorimeters, which will be replaced by the HGCAL.
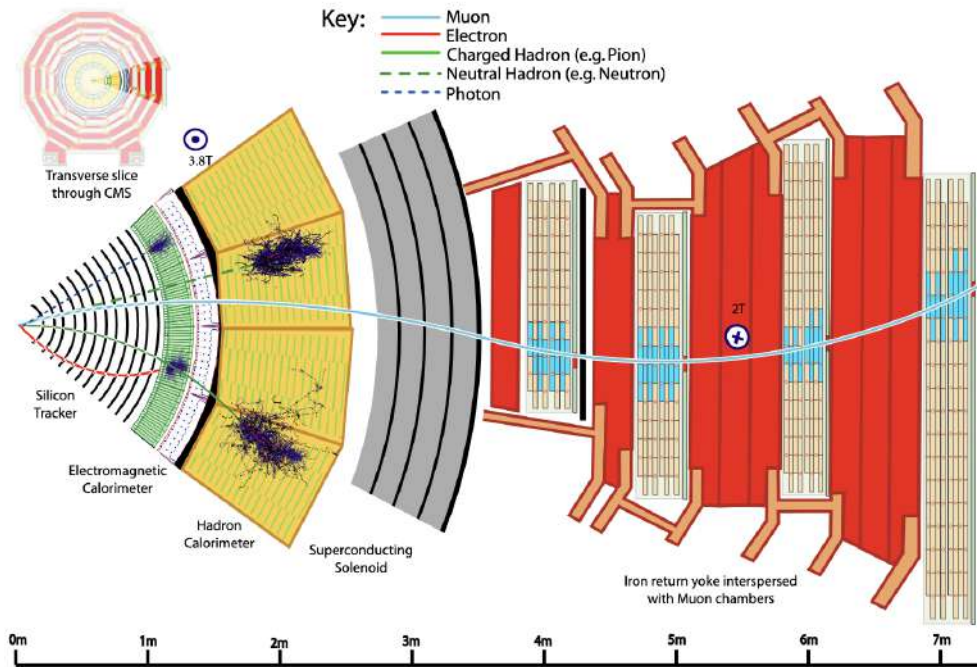
Figure 5.3: Sketch of the characteristics signals from PF candidates in a transverse slice of the CMS detector, from the beam region to the muon detector [119].

5.3 Muons

The building tracks for PF muon candidates are classified in three categories: standalone, tracker, and global tracks. The standalone tracks are reconstructed if the final fit procedure utilizes only seeds and hits recorded in the muon system. Tracker muons are identified if a segment in the inner tracker is extrapolated to the muon system with an $in - out$ approach. Global muons are reconstructed if standalone tracks match tracks in the inner tracker system.

The PF muons are identified from the global and tracker muon tracks. To reject fake muons from hadron showers that are not contained by the HCAL, muon identification criteria are defined based on the purity efficiency and the

misidentification rate. Muon candidates in the analysis described in the thesis are required to fulfill the criteria defined in Table 5.1, which correspond to the medium identification working point with an overall reconstruction efficiency in different η sections of the detectors of 98%.

Table 5.1: Identification requirements and thresholds for a CMS medium working point muon [89].

Requirement	Criterion
Muon type	Tracker or global muon
Inner tracker valid hits	> 5
Pixel hits	≥ 1
Global muon χ^2/dof	< 3
Tracker–standalone χ^2 match	< 12
Valid muon chamber hits (global)	≥ 1
Transverse impact parameter $|d_{xy}|^{\mathrm{a}}$	< 0.2 cm
Longitudinal impact parameter $|d_z|^{\mathrm{a}}$	< 0.5 cm
Primary vertex association	Required

  ^a With respect to the primary vertex.

To increase the purity of muon candidates, isolation criteria are applied in addition to the identification requirements, with the following equation:

$$\frac{1}{p_T^\mu}\left[\sum_{\Delta R < 0.4} p_T^{\mathrm{charged}} + \max\left(0, \sum E_T^{\mathrm{neutral}} + \sum E_T^\gamma - 0.5 \cdot \sum p_T^{\mathrm{PU}}\right)\right] \qquad (5.1)$$

where, p_T^μ is the transverse momentum of the muon, p_T^{charged} is the sum of the transverse momenta of charged hadrons associated with the primary vertex, E_T^{neutral} is the sum of the transverse energies of neutral hadrons, E_T^γ is the sum of the transverse energies of photons, and p_T^{PU} corresponds to the transverse momenta of charged hadrons originating from pileup vertices. The sum is taken over all particles within a cone of radius

$$\Delta R = \sqrt{(\Delta\eta)^2 + (\Delta\phi)^2} < 0.4$$

around the muon candidate. Muon candidates considered in this thesis are required to satisfy that the isolation is less than 0.15.

Figures 5.4 show the reconstruction efficiency for PF muon candidates as a function of the muon p_{T} and η, with ID and isolation requirements, using a tag-and-probe method beginning with tracker tracks as probes. The value of the efficiency is computed by factorizing it into several components, each derived separately, as in the following equation:

$$\varepsilon_{\mathrm{track}} \times \varepsilon_{\mathrm{reco+ID}} \times \varepsilon_{\mathrm{iso}} \times \varepsilon_{\mathrm{trig}} \qquad (5.2)$$
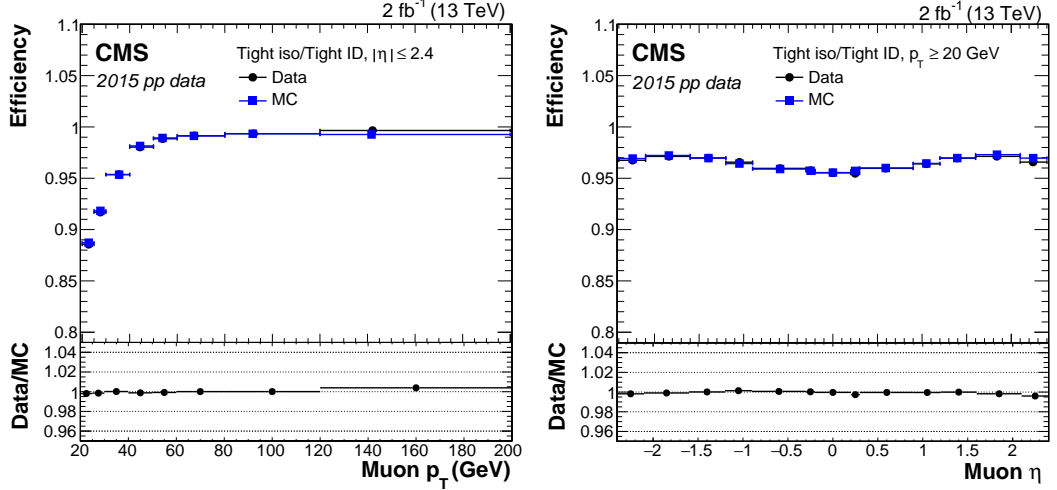
Figure 5.4: Reconstruction efficiency for the tight PF isolation working point on top of the tight ID versus p_T for muons in the acceptance of the muon spectrometer, and (right) versus η for muons with $p_\mathrm{T} > 20$ GeV, for $\sqrt{s}$ of 13 TeV in data (circles), simulation (squares), and the ratio (bottom) [89].

5.4 Electrons

Throughout this thesis, the term *electron* refers to both electrons and positrons. Electron reconstruction is based on linking information from the inner tracker and the ECAL. The main challenge arises from the fact that electrons emit bremsstrahlung photons as they traverse the tracker. These photons often convert into e^+e^- pairs, which can themselves emit additional bremsstrahlung photons, and so on. Therefore, it is crucial to account for these energy losses to ensure an accurate measurement of the electron momentum and to distinguish primary electrons from secondary ones. The energy of the electron and its associated bremsstrahlung photons is collected in *superclusters*, which are aggregations of ECAL clusters reconstructed within a narrow window in η and an extended window in ϕ, centered around the electron's direction.

The PF electron candidate is seeded from a Gaussian-sum filter (GSF) track [119, 120], which is more suited for electrons than the KF used in the iterative track reconstruction algorithm, as it allows for significant energy losses along the trajectory. The GSF-based seed is then linked to an ECAL cluster, provided the cluster has less than three linked tracks.

Electrons are additionally required to satisfy identification criteria. Several identification methods are available, but for this thesis, the MVA-based approach is employed [121]. Up to fourteen variables, such as the amount of energy radiated from the GSF track, the spatial distance between the GSF track extrapolation to the ECAL surface and the position of the ECAL seed cluster, the GSF track χ^2, the number of hits, and others, are combined in a BDT. Relative isolation variables are also included in the training of the MVA.

Figure 5.5 shows the performance of the BDT-based identification, comparing sequential selections with or without isolation requirements used in the training of the BDT. Electron candidates are obtained from DY + jets simulated events. Signal electrons are defined as reconstructed electrons that match generated prompt

electrons within a cone of size $\Delta R = 0.1$. Background electrons are defined as all reconstructed electrons that either match generated nonprompt electrons, i.e., electrons from hard jets. The working point selected for the thesis for electron identification corresponds to an efficiency of 90%, with the isolation requirement. Electrons reconstructed in the transition region between the ECAL barrel and endcap regions, i.e., $1.442 < \eta < 1.566$, are excluded from physics analysis.
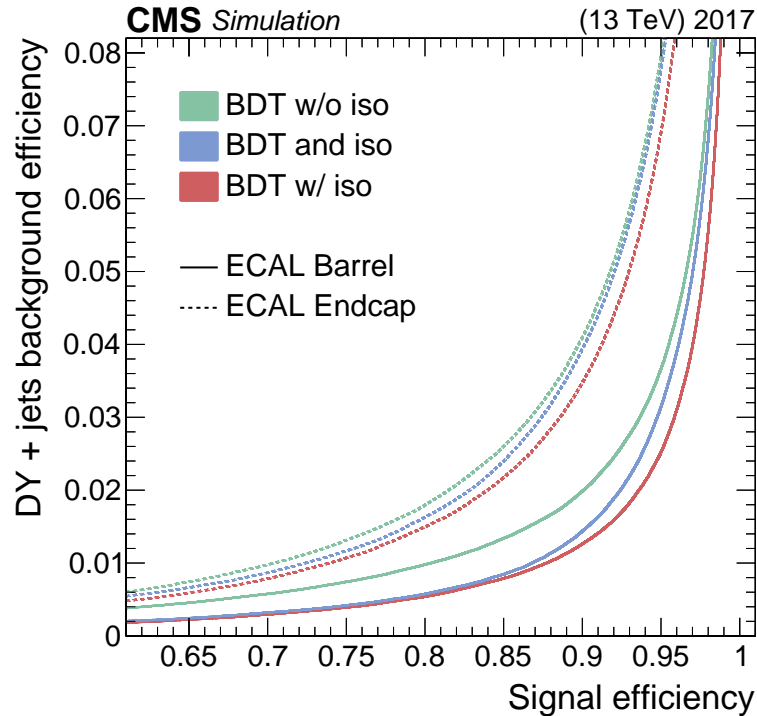
Figure 5.5: Performance of the electron BDT-based identification algorithm with (red) and without (green) the isolation variables, compared to an optimized sequential selection using the BDT without the isolations followed by a selection requirement on the combined isolation (blue) [121].

The same reconstruction technique is employed for isolated photons, but with the requirement of an ECAL cluster with no GSF-based seeded track. After the reconstruction of these objects, the clusters and the track information are removed from the collection.

5.5 Jets

After the removal of reconstructed muons and electrons, the remaining PF objects are used for hadron reconstruction. Deposits in both ECAL and HCAL that are matched to tracks in the inner system are identified as PF candidates for charged hadrons. These are distinguished from non-isolated photons and neutral hadrons, as the former are reconstructed when there are no associated deposits in the HCAL, while the latter are when no seeded track is linked to ECAL and HCAL clusters. Once the PF clusters are formed, they are used in clustering algorithms to reconstruct the collimated particles resulting from parton shower and hadronization of quarks and gluons. The final product is a collimated cluster of particles, called *jets*.

In the CMS Collaboration and for this thesis work, the clustering algorithm used for jets originating from quarks or gluons is the anti-k_T algorithm [122], which is a variation of sequential clustering algorithms, within the FastJet software package [123]. The algorithm used for top quarks identification and reconstruction in this thesis work is the HOTVR, which is also a variation of sequential clustering algorithms and is described in detail in Chapter 6. The main feature of HOTVR jets is the variable jet cone radius, which changes inversely with the p_T of the jet. All these algorithms are infrared and collinear (IRC) safe, as the resulting jet from the algorithm does not change under the emission of infinitely soft particles or collinear splitting of a particle within a jet.

5.5.1 Sequential clustering

The sequential clustering algorithm uses a list of pseudojets (i.e., PF candidates), pairing them iteratively based on their relative distance and their distance with respect to the beam axis until jet objects are formed. Given pseudojets i and j, the distance $d_{i,j}$ between them and the distance between the pseudojet i and the beam axis $d_{i,\mathrm{B}}$ are defined as follows:

$$d_{i,j} = \min\left(p_{\mathrm{T},i}^{2k},\, p_{\mathrm{T},j}^{2k}\right) \frac{\Delta R_{i,j}^2}{R^2}, \tag{5.3}$$

$$d_{i,\mathrm{B}} = p_{\mathrm{T},i}^{2k}, \tag{5.4}$$

where, $\Delta R_{i,j} = \sqrt{(y_i - y_j)^2 + (\phi_i - \phi_j)^2}$ is the distance in the rapidity–azimuth plane between pseudojets i and j, and p_{T} is the transverse momentum of the pseudojet (Equation 2.1). The parameters R and k are specific to the desired algorithm. The anti-k_T algorithm defines $k = -1$, while other algorithms such as the k_T [124] or the Cambridge-Aachen (CA) [125] a defines $k = 1$ or $k = 0$, respectively. In the CMS Collaboration, a value of $R = 0.4$ is used to reconstruct jets originating from gluons, light quarks or b quarks: these are referred to as AK4 jets.

The iterative procedure is as follows: if $d_{i,\mathrm{B}} < d_{i,j}$, the pseudojets i and j are combined by summing their four-momenta to form a new pseudojet. If $d_{i,j} < d_{i,\mathrm{B}}$, the pseudojet i is stored as *jet* and removed from the list of pseudojets. This procedure continues until no pseudojets remain in the list. The order in which the pseudojets are combined depends on the choice of the parameter k: the anti-k_T ($k = -1$) algorithm makes soft particles more likely to cluster with hard particles rather than with other soft particles, resulting in a more circular-shaped jet cone. The k_T ($k = 1$) algorithm clusters soft particles first, resulting in a more irregular shape for the jet, while the C/A ($k = 0$) selects the orders by the geometrical distance only.

The behavior of different algorithms is shown in Figure 5.6, when clustering 10^4 random soft particles in a parton-level event generated with Herwig [126]. The catchment areas around hard for the anti-k_T algorithm for hard jets are all circular with a radius $R = 1$, and only the softer jets have a more complex shape.
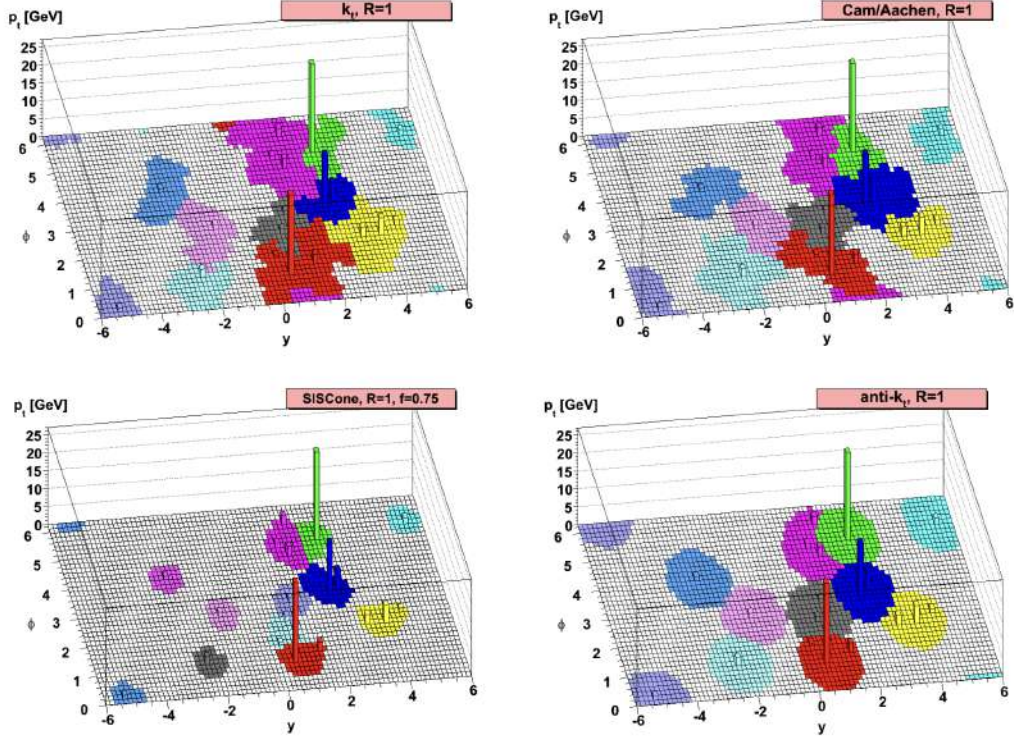
Figure 5.6: Parton-level events clustered by four different sequential clustering algorithms. The catchment areas is visible and shown in different colors for the clustered jets. [122].

5.5.2 Jet substructures

Analyzing jet substructure features can provide information about the origin of the jet, which is essential for jet identification from W bosons, top quarks, and BSM particles. These features are also important discriminators in jet tagging algorithms. The jet substructure variables used in the top-tagging algorithm and relevant for this thesis are presented in the following sections. A more detailed overview of jet substructure techniques can be found in Ref. [127].

Jet mass

While partons can be treated as massless at leading order, jets always acquire mass due to the hadronization effect and the presence of collinear radiation. The invariant mass of a jet is defined as:

$$m_{\text{jet}}^2 = \left(\sum_i P_i \right)^2 \tag{5.5}$$

where P_i is the four-momentum of the jet constituent i. The jet mass reflects the mass of the generating partons. Therefore, it is useful to discriminate jets originating from heavy object,s such as SM bosons and top quarks, from multijet (QCD) events, where the initiating partons are massless and the jet mass arises purely from QCD radiation.

Figure 5.7 shows the jet mass distribution for jets originating from top quarks

and QCD processes, clustered with the anti-k_T algorithm with $R = 0.8$ in $t\bar{t}$ and multijets simulated events. The jets in these studies have been additionally reclustered using the soft-drop method [128]. This aims to systematically remove the soft and collinear radiation to mitigate the effect of PU and to improve the resolution of jet substructure variables, such as the mass. In QCD multijet events, the jet mass distribution peaks at low values due to Sudakov suppression [129]: at leading order, a single massless parton produces a jet with zero mass, and only soft and collinear gluon emissions contribute to its mass. The probability of these emissions being sufficiently hard and wide-angled to generate a large mass is exponentially suppressed by the Sudakov form factor. In contrast, for boosted heavy objects like top quarks or W bosons, the jet mass peaks around the mass of the parent particle because the decay products are typically contained within a single jet.
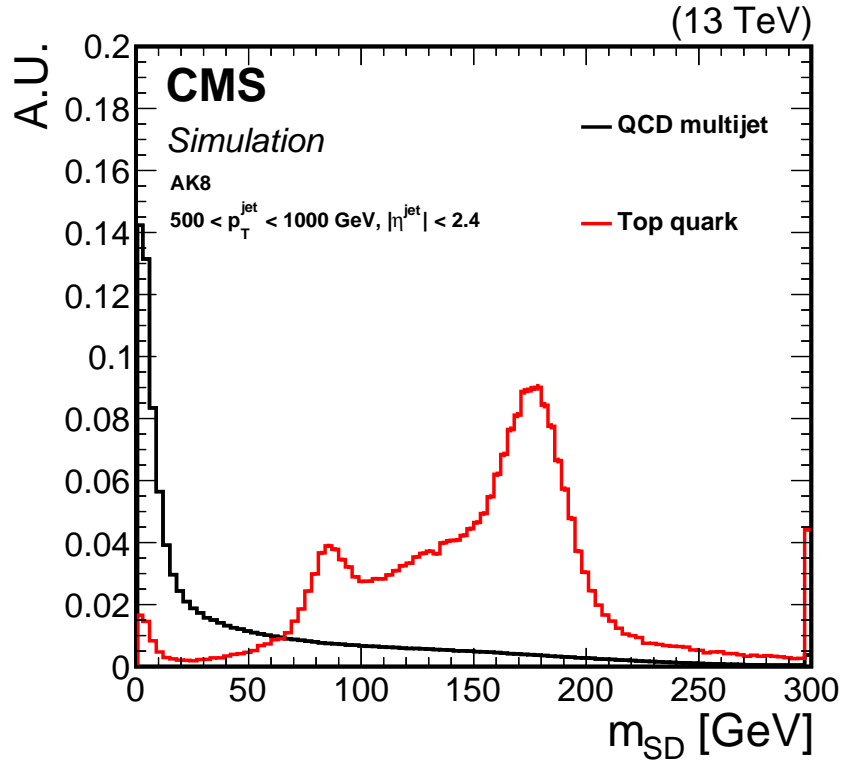
Figure 5.7: Comparison of the jet mass distribution from top quark and QCD origi-nated jets. The fiducial selection on the jets is displayed on the plots [130].

N-subjettiness

Another important discriminating variable is the number of subjets within a jet and the distribution of their energy. Jets originating from the hadronization of gluon or light quarks are expected to have one or two[2] subjets inside the jet, while two-body decay particles, such as those from W, Z, H bosons, usually produce two subjets, and top quarks generally result in three.

---

[2]Due to gluon splitting.

The N-subjettiness variable τ_N quantifies how well the jet can be described as containing N subjets and provides information on how the energy is distributed within the jet. It is defined as follows [131]:

$$\tau_N = \frac{1}{d_0} \sum_i p_{T,i} \min \left[\Delta R_{1,i}, \Delta R_{2,i}, \ldots, \Delta R_{N,i} \right] \tag{5.6}$$

where the index i refers to the number of constituents inside the jet and ΔR to spatial distance between the i constituent and subjets in the $\eta - \phi$ plane. The value of τ_N is close to zero when the jet is compatible with having N subjets. Rather than using the absolute τ_N alone, the ratios between different τ_N values are commonly used as discriminating variables for jet identification. For example, $\tau_{32} = \tau_3/\tau_2$ is used to discriminate jets originating from top quarks from QCD jets. Figure 5.8 shows the τ_{32} distribution for jets originating from top quarks and QCD processes, clustered with the anti-k_T algorithm with $R = 0.8$ in $t\bar{t}$ and multijets simulated events.
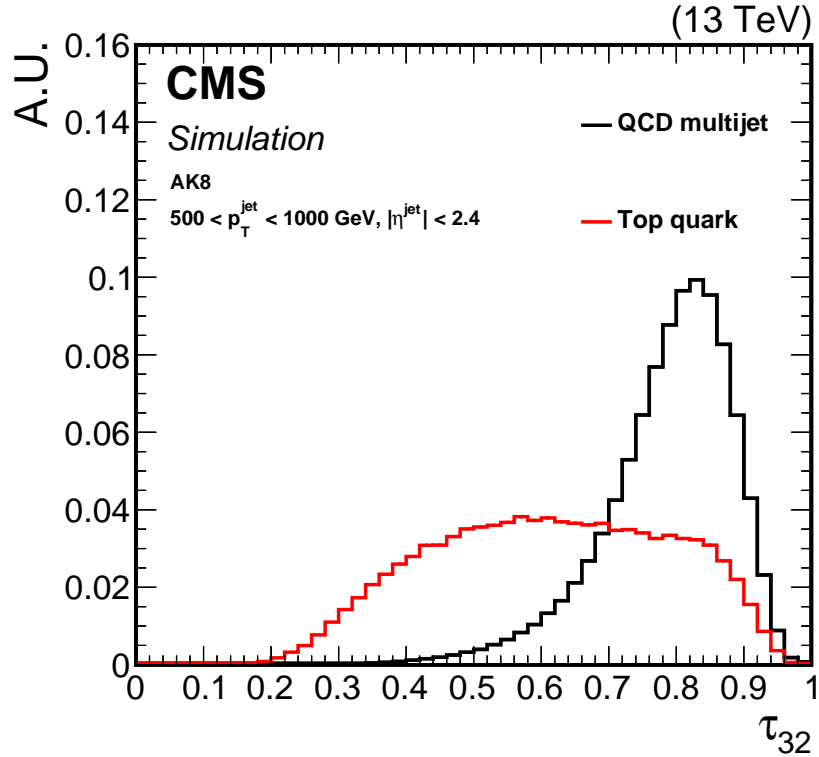
Figure 5.8: Comparison of the τ_{32} distribution from top quark and QCD originated jets. The fiducial selection on the jets is displayed on the plots [130].

5.5.3 Pileup mitigation techniques

To improve the jet identification and the measurements of jet and subjets properties, it is crucial to isolate the products of the primary p–p collisions from contamination due to PU interactions from the same or neighboring bunch crossing. The CMS Collaboration has employed different techniques to mitigate PU effects, such as the Charged-Hadron Subtraction (CHS) [132] method for AK4

jet during Run 2 data-taking and pileup per particle identification (PUPPI) [133] for Run 3 data-taking.

The CHS method removes charged particles from the jet clustering procedure if they are associated with PU vertices, i.e., if the corresponding track was used in the PU vertex fit. Since neutral particles from PU interactions cannot be distinguished in the same way, an additional PU mitigation technique, such as a dedicated PU jet ID or grooming algorithm, is applied to further suppress the residual contamination from neutral PU.

The PUPPI method computes a weight for each particle, from 0 to 1, where particles originating from PU are more likely to have weight values close to zero. Charged particles are treated similarly to the CHS method, where a weight value of 1 is assigned if their tracks are used in the fit for primary vertex reconstruction, or if they are not associated with any vertex but have a distance of closest approach to the primary vertex along the z-axis smaller than 0.3 cm. In all other cases, they receive a weight value of zero.

The weights for neutral particles are derived from a discriminator α_i, which is calculated as follows:

$$\alpha_i = \log \sum_{\substack{j \neq i \\ \Delta R_{ij} < R_0}} \left(\frac{p_{T,j}}{\Delta R_{i,j}} \right)^2 \begin{cases} \text{for } |\eta_i| < 2.5, & \text{j are charged particles from PV} \\ \text{for } |\eta_i| > 2.5, & \text{j are all reconstructed particles} \end{cases}$$

where $\Delta R_{i,j}$ is the distance in the $\eta - \phi$ plane between particles i and j, and R_0 is chosen to be 0.4. If no particles are found within R_0, α_i is set to zero for the i constituent. For other particles in the acceptance region, the α_i is calculated, being large for constituents close to the primary vertex.

This α_i value is then translated into a probability by comparing it to the distribution of α_i values from charged particles associated with PU vertices. The deviation of α_i from the expected mean value is mapped to a weight between 0 and 1, where particles originating from PU are likely to obtain weights closer to zero. The momentum of each PF particle is scaled according to these weights, and particles with weights smaller than 0.01 are entirely removed from the event. In the context of the analysis presented in the thesis, the HOTVR jets are clustered with PUPPI-weighted PF candidates, while AK4 jets with CHS for Run 2 data taking campaigns at $\sqrt{s}$ of 13 TeV, and PUPPI for 2022 campaigns at $\sqrt{s}$ of 13.6 TeV.

5.5.4 Jet energy correction

Corrections are applied to jets to ensure agreement between the true and measured jet energy (jet energy scale, JES) and resolution (jet energy resolution, JER). This jet calibration accounts for the non-uniform response of the detector in p_T and η and is performed in a factorized approach [134, 135].

Corresponding correction factors are applied both in simulation and in data, and are derived using a combination of simulated events and data-driven techniques. The JES corrections, which are used to correct any residual differences in jet energy scale between data and simulation, are computed from measurements of the momentum balance in dijet, Z/γ+jets, and multijet events. The JER is

defined as the spread in p_T response, and it is assumed to be Gaussian. Because the jet response in simulation is usually idealized, JER corrections are applied to simulated jets to match the resolution observed in data.

The AK4 jets used in this thesis are calibrated following the recommendations provided centrally by the CMS Collaboration. As the corrections are stable with respect to the jet size [134], the HOTVR jets are corrected with the same corrections: the HOTVR subjets are firstly corrected and then re-summed to create the final corrected HOTVR.

The response of the HOTVR jet is shown in Figure 5.9 before and after applying the dedicated JEC correction, for $p_\mathrm{T} > 200$ GeV. The response is defined as the average ratio between the reconstructed jet p_T (p_T^{rec}) and the simulated p_T (p_T^{gen}) of the associated particle at generator level. Particles at the generator level are matched to jets by looking at the minimum distance in the $\eta - \phi$ plane for particles located within the jet cone. This procedure is performed in $t\bar{t}$ enriched events.
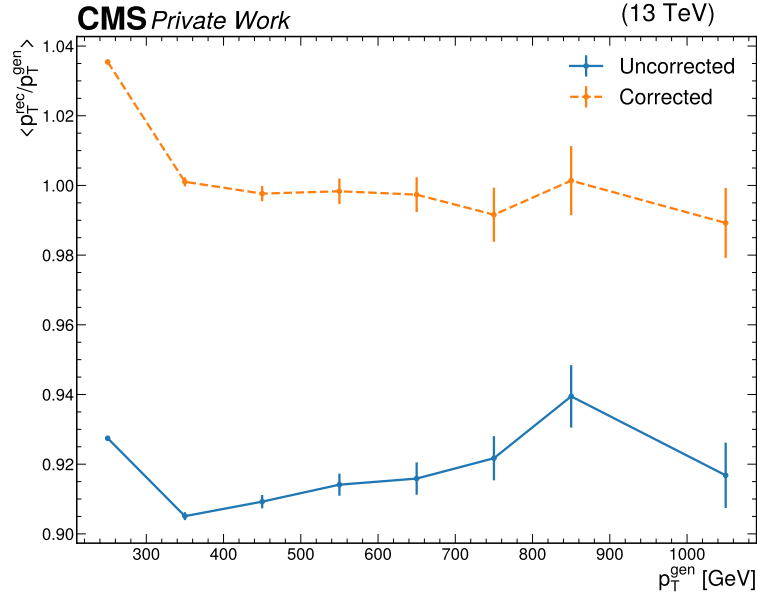
Figure 5.9: HOTVR jet p_T response as a function of simulated jets on generator level p_T^{rec} before (solid blue) and after (dashed orange) jet energy corrections, which are applied to the HOTVR subjets. The p_T response was measured using $t\bar{t}$ simulated events.

5.6 Heavy flavor tagging

A crucial step in CMS analyses, and specifically in the analysis presented in this thesis, is the discrimination of jets originating from top and bottom quarks from those originating from light-flavour quarks. The CMS Collaboration has developed several heavy-flavour tagging algorithms over the years, which exploit the unique properties and signatures of top and b quarks. The identification of b quark jets is discussed in this section. Additionally, a top-tagging algorithm based on machine learning techniques and using fixed wide-angle jets is presented as a

reference. This top-tagging algorithm serves as a comparison to the top-tagging method introduced in Chapter 6, which combines HOTVR variables in a machine learning based algorithm and is the primary approach used in this thesis.

5.6.1 Identification of b quarks

In processes enriched in top quark production, the identification of jets originating from b quarks is essential because top quarks almost always decay to a W boson and a b quark, with a branching ratio of about 99.8% [6]. This is particularly important in the context of this thesis, which focuses on a search in the four-top-quark final state, where the presence of multiple b quark jets is a key signature.

Hadrons produced through the hadronization of b quarks have a lifetime of approximately 1.5 ps; therefore, they can travel a few millimeters before decaying. This results in several tracks that are displaced relative to the PV, which can be used to reconstruct secondary vertices (SV). The displacement of the tracks is measured by their impact parameter, which is the distance between the primary vertex and the tracks at their point of closest approach.

Additionally, due to the larger mass and harder fragmentation of b quarks, their decay products have generally higher p_T than those of light-flavour jets. Moreover, a muon or electron is present in the decay chain with soft p_T on average, which further helps in distinguishing heavy-flavour jets from light-flavour jets [136]. Figure 5.10 is an illustrative sketch of a jet resulting from the decay of a b quark, summarizing all its distinctive properties.
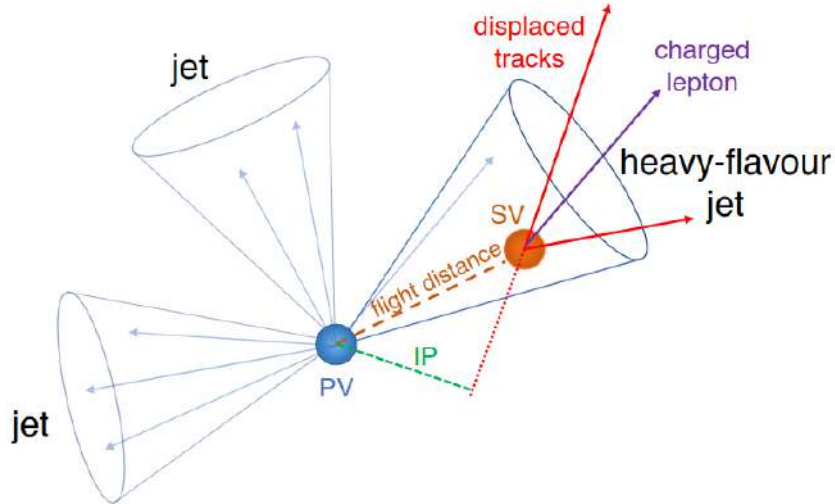
Figure 5.10: Illustration of jet with an SV from the decay of a b hadron, resulting in charged particle tracks displayed with respect to the PV [136].

In the scope of the thesis, the `DeepJet` b-tagging algorithm is employed to identify b jets. The algorithm is trained and tested using a sample of simulated anti-k_T jets with $R = 0.4$ from mixed samples of fully hadronic $t\bar{t}$ and multijet events.

The architecture is based on a convolutional recurrent neural network and uses low-level features from a large number of jet constituents up to 650 input variables, divided into four categories: global variables, charged PF candidate

features, neutral PF candidate features, and SV features associated with the jet. The network outputs six probabilities, each corresponding to whether a jet originates from a b quark, two b quarks, a leptonic b hadron decay, one or more c quarks, a gluon, or a light-flavor quark, respectively. The scores corresponding to the different b jet origins are summed, and different score thresholds (or working points) are defined by the CMS Collaboration, resulting in different tagging efficiency and mistagging rate. In this thesis, the *loose* working point is used, which corresponds to a b-tagging efficiency spanning from 85-92% depending on the year of the data-taking, with a mistagging rate of approximately 10%.

5.6.2   Identification of top quarks with large fixed-radius jets

In the boosted regime[3], top quarks are identified using large fixed radius anti-k_T jets with $R = 0.8$, known as AK8 jets. The tagging algorithm employed for this purpose is ParticleNet [137]. The architecture of the algorithm is based on a customized dynamic graph convolutional neural network (DGCNN) [138] that operates on an unordered set of particles. The novelty of the algorithm is to treat the jet constituents in a very analogous way to the point cloud representation of three-dimensional shapes used in computer vision, where each shape is represented by a set of unordered points in space. This image-based approach has been originally designed specifically for the identification of hadronic decays of highly Lorentz-boosted heavy particles such as the top quark, W, Z, and Higgs boson.

The model takes up to 100 jet constituents with the highest p_T for each jet, and uses seven variables derived from the 4-momentum for each particle as inputs. Some of these variables include kinematic information such as particle energy, p_T differences in azimuthal and pseudorapidity between the particle and jet.

Figure 5.11 shows the performance of the ParticleNet for identifying hadronically decaying top quarks against QCD jets. The p_T range studied is $500 < p_T < 1000$ GeV and the algorithm outperforms the previously used algorithm DeepAK8[4] in terms of lower background rate and higher signal efficiency.

---

[3]$p_T > 600$ GeV

[4]The DeepAK8 algorithm is a multi-class particle identification algorithm [139] for identifying hadronic decays of highly Lorentz-boosted top quarks and W, Z, and Higgs bosons, based on AK8 jets. The algorithm uses a deep one-dimensional convolutional neural network (CNN) to process particle-flow candidates and secondary vertices associated with the jet.
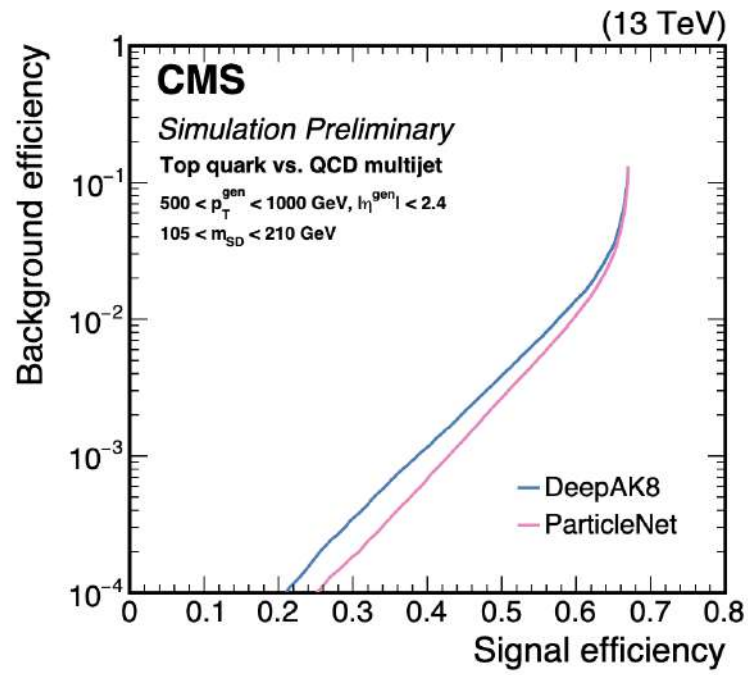
Figure 5.11: Performance of the DeepAK8 and ParticleNet algorithms for identifying hadronically decaying top quarks [140]. The jet mass is corrected using the soft-drop mass procedure described in Section 5.5.2, and its minimum and maximum range values are displayed.

Chapter 6

Hadronic top quark tagger with variable-size jets

6.1 Overview and motivation

Top quarks decay hadronically via the W boson about 60% of the time, making hadronically decaying tops an important object to reconstruct. Their identification is a major challenge in the CMS physics program and is essential for both precision SM measurements and searches for new physics.

Although several reconstruction techniques already exist for tagging jets originating from top quarks, such as the AK8 jets plus particleNet method described in Section 5.6.2, the intermediate kinematic regime ($200 < p_T < 600$ GeV), between the resolved region ($p_T < 200$ GeV) and the boosted region ($p_T > 600$ GeV), remains particularly difficult to handle. The main challenge in this kinematic region is that the decay products of the top quark are not sufficiently collimated, causing them to fall outside the catchment area of the jet. This regime is directly relevant for BSM searches, such as the top-philic Z' search in the four top quarks final state presented in this thesis. For resonance masses below about 1 TeV, the top quark p_T might not reach the fully boosted regime.

To exploit this intermediate region, the HOTVR algorithm has been developed, and is described in detail in Section 6.2. In the context of this thesis, I have developed a new identification algorithm, i.e., tagger, for hadronically decaying top quarks, using features of clustered HOTVR jets, which is presented in Section 6.3. The tagger is built using a BDT algorithm [2], whose implementation details are discussed in the same section. The performance of the model is shown in Section 6.4, while its validation in Z+jets enriched events is presented in Section 6.6, and in the top quarks-enriched region in Section 6.5. Finally, Section 6.7 outlines possible future perspectives for this newly developed tool.

6.2 Sequential clustering with variable radius

The HOTVR algorithm is based on the sequential recombination algorithm described in Section 5.5.1, but it processes the input list of pseudojets using a variable radius (VR) cone size parameter [141]. Therefore, the algorithm uses the same definitions of *distance measures*, d_{ij} and d_{iB}, defined for any sequential-based recombination algorithm in Equation 5.4, with the following modifications,

$$d_{ij} = \min\left(p_{T,i}^{2n},\ p_{T,j}^{2n}\right) \frac{\Delta R_{ij}}{R_{\text{eff}}(p_{T,i})}, \tag{6.1}$$

$$d_{iB} = p_{T,i}^{2n}\, R_{\text{eff}}^2(p_{T,i}), \tag{6.2}$$

$$R_{\text{eff}}(p_T) = \frac{\rho}{p_T}. \tag{6.3}$$

As for the C/A clustering algorithm, $n = 0$ is used. The effective distance parameter R_{eff} scales with $1/p_T$ of the jet and has a minimum and maximum cut-off, namely:

$$R_{\text{eff}} = \begin{cases} R_{\min} & \text{if } \frac{\rho}{p_T} < R_{\min}, \\ R_{\max} & \text{if } \frac{\rho}{p_T} > R_{\max}, \\ \frac{\rho}{p_T} & \text{otherwise}, \end{cases} \tag{6.4}$$

where $R_{\min}$ and $R_{\max}$ are set to 0.1 and 1.5, respectively. The lower bound is set accordingly to the calorimeter granularity, while the upper bound is related to the $|\eta|$ acceptance of the detector.

To avoid the clustering of additional soft radiation into jets, a mass jump condition is included in the sequence [142, 143], which eliminates the need for declustering and grooming steps typically required by other sequential algorithms[1]. The veto is based on the invariant mass of the pseudojets pair of the sequence and prevents the recombination of the pseudojets i and j if the invariant mass m_{ij} is greater than a mass threshold, μ, and if the following condition is met

$$\theta \cdot m_{ij} \geq \max(m_i, m_j), \tag{6.5}$$

where the parameter θ determines the strength of the condition. Given a minimum transverse momentum threshold $p_{T,\text{sub}}$, if the condition 6.5 is fulfilled and transverse momentum of the pair $p_{T,i,j}$ exceeds $p_{T,\text{sub}}$, the pseudojets are combined and stored as subjets of the combined pseudojet.

The parameters of the HOTVR algorithm are summarized in Tab. 6.1, and the default values have been optimized for top quark tagging in p–p collisions [142]. As the HOTVR clustering algorithm is an extension of the sequential clustering algorithms, it inherits infrared and collinear safety by definition.

Table 6.1: Parameters of the HOTVR algorithm. The default values are given for the top-tagging mode [142].

Parameter	Default	Description
$R_{\min}$	0.1	Minimum value of R_{eff}.
$R_{\max}$	1.5	Maximum value of R_{eff}.
ρ	600 GeV	Slope of R_{eff}.
μ	30 GeV	Mass jump threshold.
θ	0.7	Mass jump strength.
$p_{T,\text{sub}}$	30 GeV	Minimum p_T of subjets.

---

[1] For example, the soft drop mass technique presented in Section 5.5.2.

6.2.1 Hadronic top quark tagger with selection-based method

Previous CMS analyses [144, 145] have employed HOTVR jets to identify boosted hadronically decaying top quarks using a selection-based approach based on jet and substructure observables: these observables and their corresponding selections are used to enhance the selection of jets that stem from hadronically decaying top quarks from QCD multijets and are described in Table 6.2. The N_{sub}, m_{jet}, and τ_3/τ_2 follow the same description presented for AK4 and AK8 jets in Section 5.5.2.

The fractional p_{T} $f_{p_{\mathrm{T}}}$, indicates how the transverse momentum of the jet is distributed among its subjets. For a hadronically decaying top quark, the p_{T} is typically shared relatively equally among its three-prong decay products, so $f_{p_{\mathrm{T}}}$ tends to assume values around 0.5 and the distribution is relatively flat. In contrast, QCD jets tend to have an uneven p_{T} distribution among their subjets, with the leading subjet capturing most of the p_{T} of the jet, resulting in higher $f_{p_{\mathrm{T}}}$ values.

The minimum pairwise mass of subjets, $m_{min\,ij}$, is defined as the smallest invariant mass computed from all possible pairs of subjets within a jet, provided the jet has at least three subjets. This variable specifically targets the reconstruction of the W boson decay within top quark jets. As a result, its distribution peaks around the W boson mass for hadronically decaying top quarks, while for QCD jets it tends to peak near zero due to the Sudakov suppression [129].

Figure 6.1 shows the distributions of several variables used in the selection-based method, comparing jets identified as hadronically decaying top quarks to QCD jets. The plots are shown for different selections on N_{sub}.

Table 6.2: Observables used for top-tagging with selection-based approach and their corresponding selections [142].

Variable	Selection	Description
$f_{p_{\mathrm{T}}}$	< 0.8	The p_{T} fraction of the leading subjet with respect to the jet.
N_{sub}	> 2	The number of subjets.
m_{jet}	$\in [140, 220]$ GeV	The jet mass.
$m_{min\,ij}$	> 50 GeV	The minimum pairwise mass of subjets.
τ_3/τ_2	< 0.56	The ratio of the N-subjettiness 3 over 2 [131].
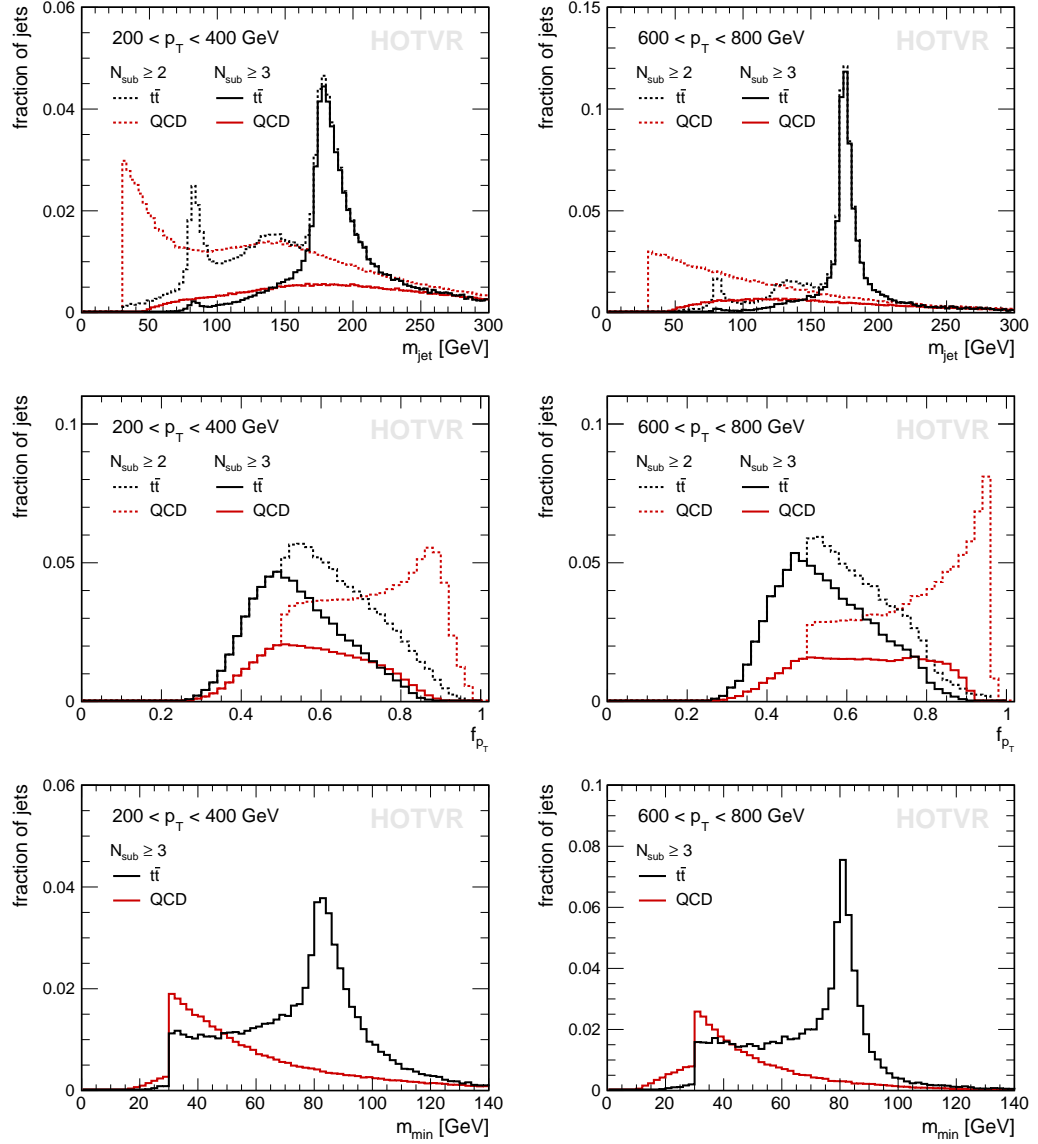
Figure 6.1: The m_{jet}, $f_{p_{\mathrm{T}}}$, and the $m_{min\,ij}$ for two different HOTVR p_{T} ranges: $200 < p_{\mathrm{T}} < 400$ GeV (*left*) and $600 < p_{\mathrm{T}} < 800$ GeV (*right*). The distributions of hadronically decaying top jets are presented in black lines, QCD jets with red lines. The dashed and continuous lines represent jets with N_{sub} greater than or equal than 2 or 3, respectively. Adapted from Ref. [142].

6.3 Hadronic top quark tagger with boosted decision trees

Figure 6.1 shows distinct differences between hadronically decaying top and QCD jets. The latter constitute the main background in the BSM search presented in this thesis, as they originate from light quarks (u, d, and s) and gluons produced in initial- and final-state radiation of SM processes, such as $t\bar{t}$ production.

These differences suggest that the use of a multivariate analysis (MVA) to discriminate these two jet classes could have higher tagging performance than a simple selection-based approach, in terms of background rejection and real top quark tagging efficiency. An MVA method to discriminate hadronically decaying top from QCD jets is thus presented in the subsequent sections and is based on a BDT. The hadronically decaying top and QCD jets are defined with simulation via jet truth-flavors identification, described in detail in Section 6.3.2.

6.3.1 Introduction on boosted decision trees

Classifying the origin of a jet is a common problem typically solved using a supervised machine learning technique, where the jet origin can be predicted based on jet features. The term *supervised* indicates that the desired output classes or labels are defined and known *a priori*, for example, the origin of the jets. In supervised learning, input features are combined with these specified output classes to train a model that predicts the expected outcomes for new, previously unseen data. This model is a mathematical structure that maps new data to the corresponding output labels [146]. The model described in this chapter relies on an ensemble of decision trees that are specifically constructed following the gradient boosting procedure.

Decision trees [147] have been developed with the intent of extending a simple selection-based analysis into a multivariate technique that analyzes events with different selections simultaneously. A decision tree consists of non-leaf nodes, which apply conditions to the input features, and leaf nodes, which contain the final prediction. Binary classification trees assume that there are only two outcomes: the positive (signal) class, generally labeled with 1, and the background class, labeled with 0.

Usually, single decision trees have high variance and limited capacity, whereas ensembles of trees (*decision forests*) are used, which sum the predictions of many trees to achieve better accuracy and robustness. Gradient Boosted Decision Trees (GBDT) [148], [149] are a type of ensemble decision forest where each tree outputs a floating-point value, and the final prediction is obtained by adding the contributions from all trees. A sketch of a tree of this type using jet variables as input features is given in Figure 6.2.

The term *boosted* refers to the process of building the model by sequentially adding trees, each trained to predict the difference between the actual and predicted values from the previous trees. The first decision tree in gradient boosting is called the base learner. Each new tree is added in a way that ensures that the predictions of the model move in the direction of the negative gradient of the loss function, which is the reason for the term *gradient*. For binary classification, the logarithmic loss function is defined as,
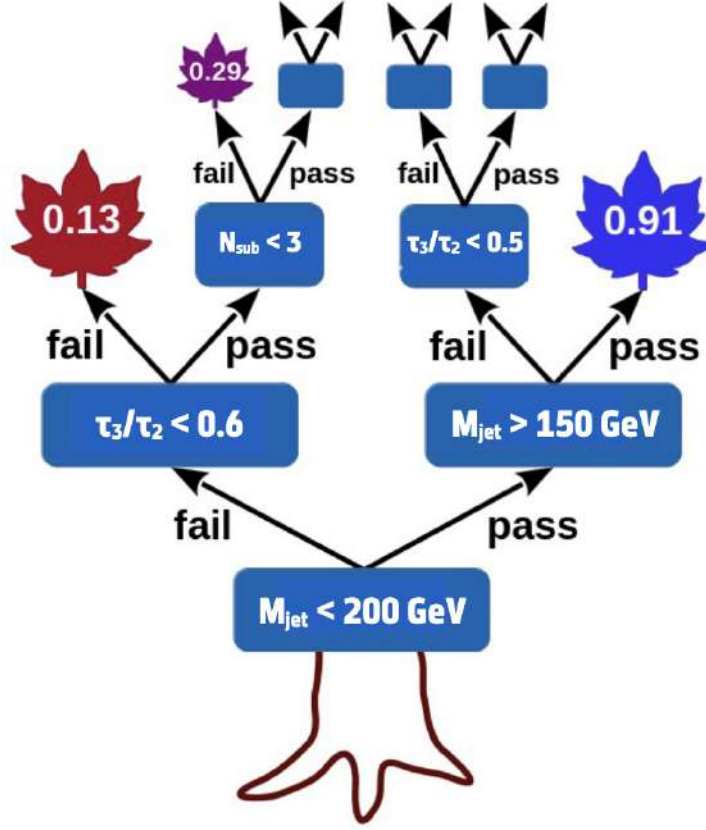
Figure 6.2: Graphical representation of a binary decision tree that uses jet variables to predict the jet origin. Blue rectangles are the non-leaf nodes with their associated splitting criteria; leaves are terminal nodes with their floating-point value. The leaf pass category refers to the jet originating from a top quark decay, while failing from QCD multijets.

$$\text{Log Loss} = -\frac{1}{n}\sum_{i=1}^{n}\left[y_i \log(p_i) + (1 - y_i)\log(1 - p_i)\right], \tag{6.6}$$

where n is the number of observations in the dataset (i.e., the jets), y_i is the actual label (0 or 1) of the i-th observation, and p_i is the predicted probability of the positive (signal) class (class 1) for the i-th observation. The BDT architecture used in the chapter is provided from *XGBoost* [150], which is an optimized distributed gradient boosting library that achieves higher performance with parallelization and efficient memory usage. The output of the *XGBoost* GBDT is a probability, or BDT score, for each candidate of the dataset, indicating the likelihood that the candidate belongs to the positive class. Scores range from $[0, 1]$, where higher values indicate more signal-like candidates.

Various hyperparameters can be adjusted to optimize the performance of the BDT and to prevent *overtraining* (or *overfitting*). Overtraining occurs when a machine learning model learns statistical fluctuations of that particular dataset, resulting in a model that performs very well on the training data but poorly on new data with unseen examples. The most important hyperparameters used and tuned for the development of the classifier in this thesis are defined as follows

- **Number of trees:** it indicates the number of trees in the ensemble. A higher number of trees increases the complexity of the model, but it influences the learning time and decreases the performance with unseen data in case of overfitting.

- **Maximum depth:** it refers to the number of levels or splits that the tree has from the root node to the leaf nodes. A higher number increases the complexity of the model, but it is more likely to cause the model to overfit.

- **Learning Rate:** it represents a weighting factor applied to new trees added to the model during training:

$$F_M(x) = F_{M-1}(x) + \nu \cdot h_M(x),$$

  where $F_M(x)$ is the prediction after M trees, $h_M(x)$ is the output of the M-th tree, and ν is the learning rate with typical values in the range $0 < \nu \leq 1$. A higher learning rate means each tree has a stronger influence on the final prediction, resulting in faster learning but an increased risk of overfitting. Whereas a lower learning rate reduces the impact of each tree, usually requiring a larger number of trees to reach optimal performance

6.3.2 Jet truth-flavor identification

The goal of the top quark tagger presented in this thesis is to distinguish jets originating from hadronically decaying top quarks from those produced by multi-jet processes, in particular from light quarks (u, d, and s) and gluons in $t\bar{t}$ events. These two classes, or jet flavors, can be obtained in MC simulations by geometrically matching jets to generator-level particles. Simulation samples generation is described in detail in Appendix A.

The generator-level matching is done by requiring that the distance in the $\eta - \phi$ space between generator particles and the jet is less than the R_{eff} defined in Equation 6.4, i.e., if the generator particles are found to be inside the HOTVR jet cone. Jets are therefore identified as hadronically decaying top quark jets if they match with hadronic generator top particles and their subsequent decays, i.e., the three quarks from the hadronic decay chain. Jets are classified as QCD jets if they match with gluons or light quarks (u, d, and s) that do not originate from top quarks or their decay products. The jets with generator-level matching with b quarks are not considered in the definition of QCD jets, as their kinematic distributions differ from those of gluon and light quarks.

6.3.3 Training of the binary classifier

The BDT model developed in this chapter classifies jets from hadronically decaying top quarks as the positive (signal) class, while jets from hadronization of light quarks and gluons are classified as the background class, or zero class. The model is trained using the two jet truth-flavors described in Section 6.3.2, which represent the binary classes for the BDT.

Hadronically decaying top jets are selected from simulated samples of $t\bar{t}Z'(Z' \to t\bar{t})$, where the Z' represents the top quark philic resonance presented in the BSM model of Section 1.3.1. Resonance mass values from 500 GeV to 4 TeV are taken

into consideration. This choice ensures that the BDT is trained on a broad p_T spectrum, covering the intermediate region between the resolved and boosted topologies characteristic of low-mass resonances, as well as the fully boosted regime expected for high-mass resonances. The QCD jets are taken from simulated samples of multijet events. The HOTVR jets that fulfill the requirements of Table 6.1 are required to have $p_T > 200$ GeV and $|\eta| < 2.4$. The JES/JER PuPPI corrections described in Section 5.5.4 are applied: the subjets in a given HOTVR jet are calibrated and then re-summed to calculate the corrected HOTVR jet p_T.

The input features of the model are the five variables described in Table 6.2, which are shown for signal and background jets in Figure 6.3 for p–p collisions at $\sqrt{s}$ of 13 TeV.
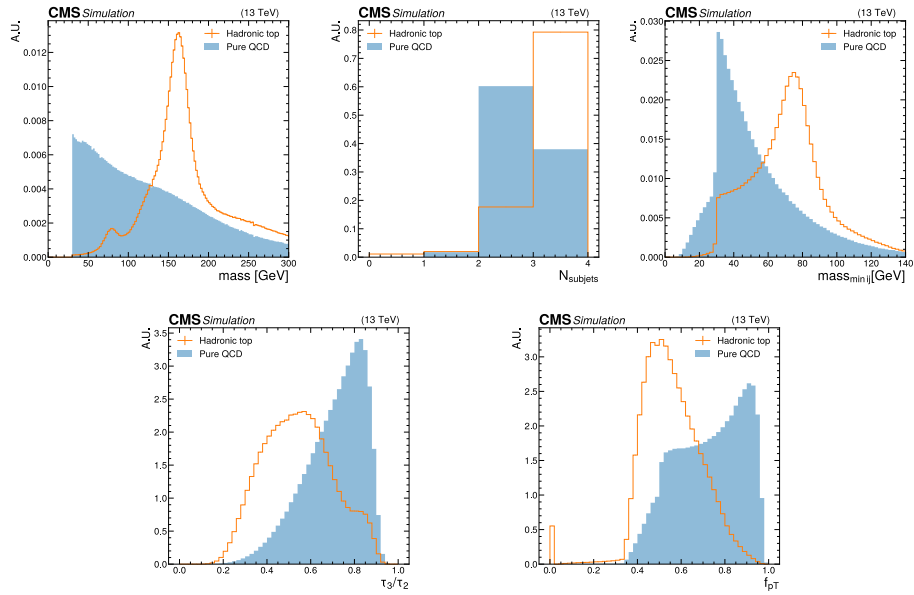
Figure 6.3: Five HOTVR variables, namely the m_{jet}, N_{sub}, $m_{min\ ij}$, f_{p_T}, and τ_3/τ_2. The hadronically decaying top jets distributions are in orange solid lines, while a blue-filled histogram represents the QCD jets. The jets are generated in simulations of p–p collisions at $\sqrt{s}$ of 13 TeV. Signal and background distributions are normalized to the same area [2].

As most of these variables correlate with the jet p_T, a different shape of p_T distributions between the two categories would inevitably affect the training. Therefore, a resampling procedure is required. Considering the p_T distribution of the hadronically decaying top quark jets as the target distribution, the resampling probabilities (weights) are calculated on a bin-by-bin basis as the ratio of the frequency in the target distribution to the frequency in the distribution being resampled. Weights are only calculated for bins where the number of jets is greater than two, and each bin has a width of 10 GeV. Each jet is then resampled if its associated p_T−binned weight is greater than a random number generated uniformly between 0 and 1. If not, the jet is excluded from the resampled set.

The p_T distributions of the hadronic and QCD jets before and after resampling are shown in Figure 6.4. The total jet occurrences of both categories are also depicted. 80% of these resampled jets are used for training the BDT, while 20% are used for testing the performance. Different BDT models were trained independently for each data-taking period to account for variations in detector

conditions and data-taking settings. The input feature distributions are found
to be consistent across data-taking periods, and only minor variations in the
optimal hyperparameter configurations are required to achieve the best tagger
performance for each year.
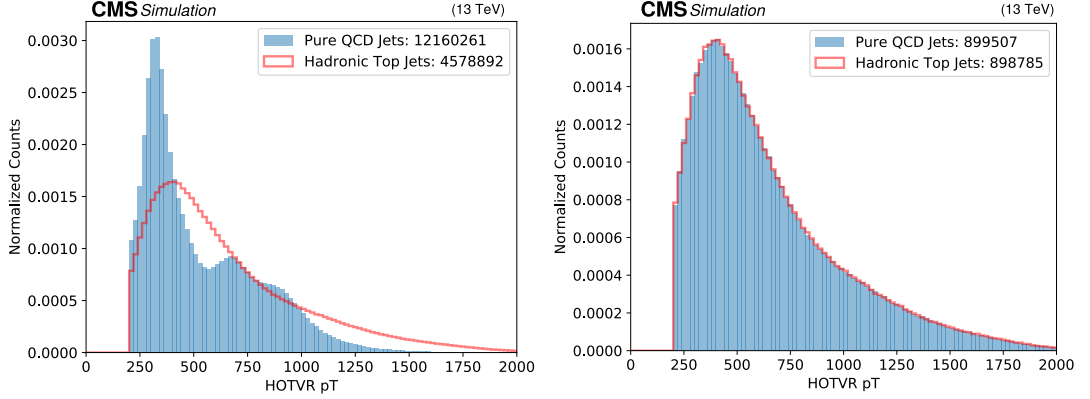
Figure 6.4: Normalized distribution of the HOTVR p_{T} before (left) and after (right)
the resampling procedure. In the legend, the number of jets in the two categories used
in the training [2].

6.3.4 Loss function and feature importances

Tuning the selection of the hyperparameters presented in Section 6.3.1 assures the
best BDT model to guarantee negligible overtraining and the highest Area Under
the ROC Curve (AUC). The overtraining is studied by examining the distribution
of the logarithmic loss (Equation 6.6) for different learning rates and maximum
depth, as a function of the number of trees in the model for both the training and
testing samples. The AUC is calculated as the area under the Receiver Operating
Characteristic (ROC) curve, which maps the true positive rate (or signal efficiency
ε_S) against the false positive rate (or mistag rate ε_B) at various thresholds of the
BDT score. Given a threshold on the BDT score, the signal efficiency ε_S is
defined as the fraction of true signal jets correctly identified by the model over
the total number of signal jets. The ε_B represents the fraction of background jets
which are incorrectly identified as top quark jets, namely whose BDT score is
greater than the threshold. Therefore, the AUC value ranges from 0 to 1, where
1 indicates a perfect model, and 0.5 indicates a model that performs no better
than random guessing.

Figure 6.5 shows the logarithmic loss as a function of the number of trees
for different choices of the maximum depth at a fixed learning rate of 0.05. The
effects of different choices of the parameters are expressed with the AUC values
visible in the figures. The plot on the left represents the choice of parameters
with the highest AUC, i.e., with a maximum depth of 5. The plot in the center

has been obtained with a maximum depth of 1, resulting in a lower AUC, while the one on the right has a maximum depth of 8, showing that the training and testing curve has no overlap.
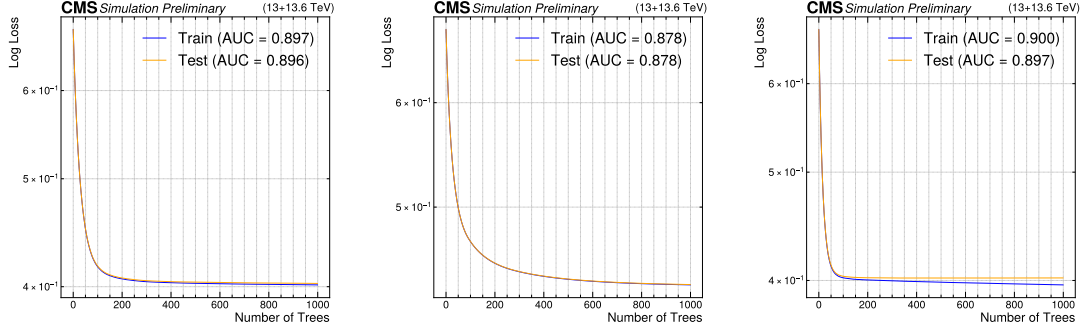
Figure 6.5: Logarithmic loss as a function of the number of trees for different choices of the BDT parameters: maximum depth of values 5 (left), 1 (center), and 8 (right).

To measure the importance of an input feature in the BDT development, the *Gain* is measured as

$$\text{Gain} = \text{logLoss}_{\text{parent}} - (\text{logLoss}_{\text{child1}} + \text{logLoss}_{\text{child2}}) \qquad (6.7)$$

The gain is averaged over all nodes and trees. The higher the gain of a feature, the more important the feature is, as the splitting due to it leads to a significant reduction of the loss function.

In *XGBoost*, feature importance can be measured by summing up the gain for each feature across all nodes where the feature is used. The feature with the highest gain has the biggest impact in the BDT training. The feature importance is shown in Figure 6.6 for the best BDT model, i.e., with 1000 trees, learning rate of 0.05, and maximum depth of 5. The variables are ranked from top to bottom based on their gain values, with the $m_{min\ ij}$ being the most important. However, it is important to note that feature importance may be biased in the presence of correlated features. In such cases, the model tends to favor one variable for splitting, while assigning lower importance to other correlated features.

To assess this effect, a correlation matrix of the input variables is computed, as shown in Figure 6.7. The feature $m_{\min\ ij}$ shows a strong correlation with both N_{sub} ($\rho = 0.80$) and m_{jet} ($\rho = 0.61$). This suggests that the high importance of $m_{\min\ ij}$ may in part reflect the information shared with these other features, and that their lower gain scores should be interpreted accordingly.
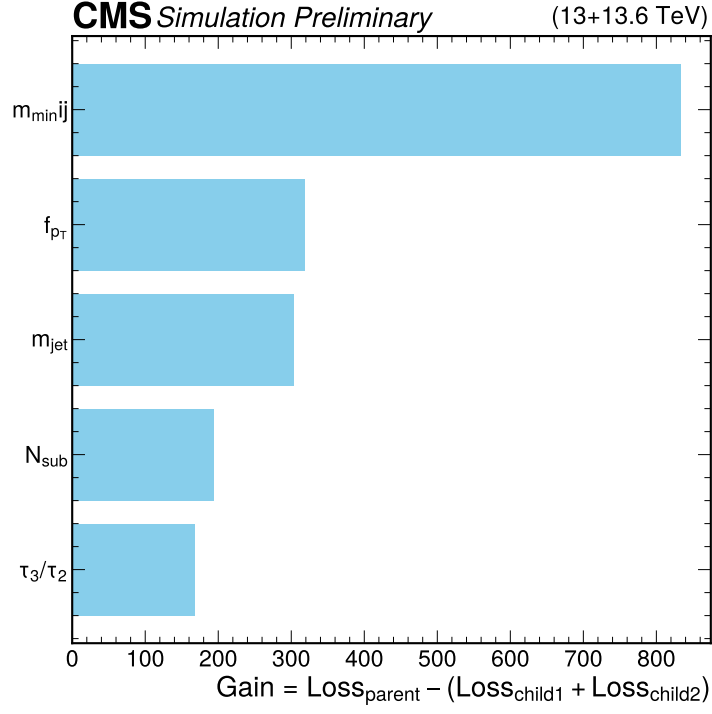
Figure 6.6: The gain of the input features for the training: the variable with the
highest gain is the most important in the training. All the models have been obtained
with the value of 1000 trees, learning rate of 0.05, and maximum depth of 5 [2].
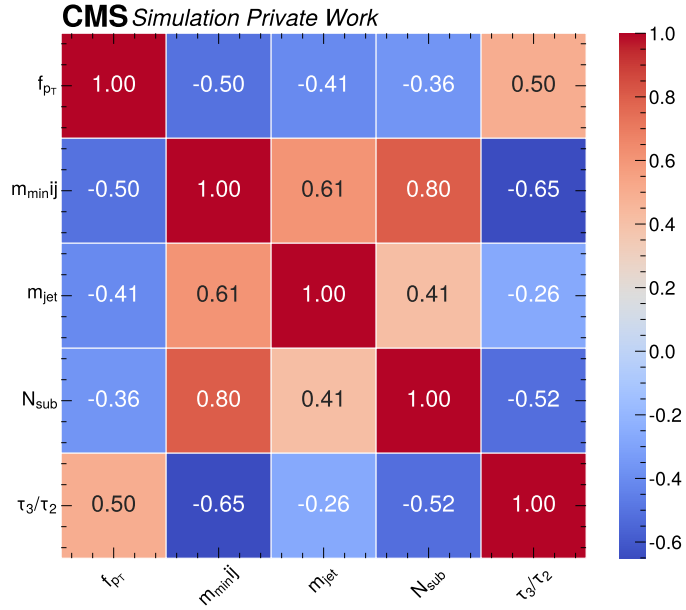
Figure 6.7: Correlation matrix for the five input features.

6.4 Performance of the tagger

The performances of the BDT model are presented for different ranges of jet p_{T}, i.e. $200 < p_{\mathrm{T}} < 400$ GeV, $400 < p_{\mathrm{T}} < 600$ GeV, 600 GeV $< p_{\mathrm{T}}$, and for the inclusive p_{T} spectrum. All the results presented in this section have been obtained by merging simulations of p–p collisions at $\sqrt{s}$ of 13 and 13.6 TeV, as no notable difference in performance is seen depending on the $\sqrt{s}$ [2].

The BDT output score of the jets of the training and testing datasets is shown in Figure 6.8 for the three p_{T} ranges. The distribution of the score for the signal jets is shown as dashed (filled) for the testing (training) datasets. No visible deviation is seen between the test and train distributions, suggesting the robustness of the BDT.

An HOTVR jet is classified as *top-tagged* if its evaluated BDT score exceeds a predefined threshold. In this analysis, a threshold value of 0.5 is used, corresponding to a tagging efficiency of 84.2% and a mistag rate of 21.7%. This *very loose* working point is selected to maximize the sensitivity of the event selection in the search for $t\bar{t}Z'(Z' \to t\bar{t})$, as discussed in Chapter 7.
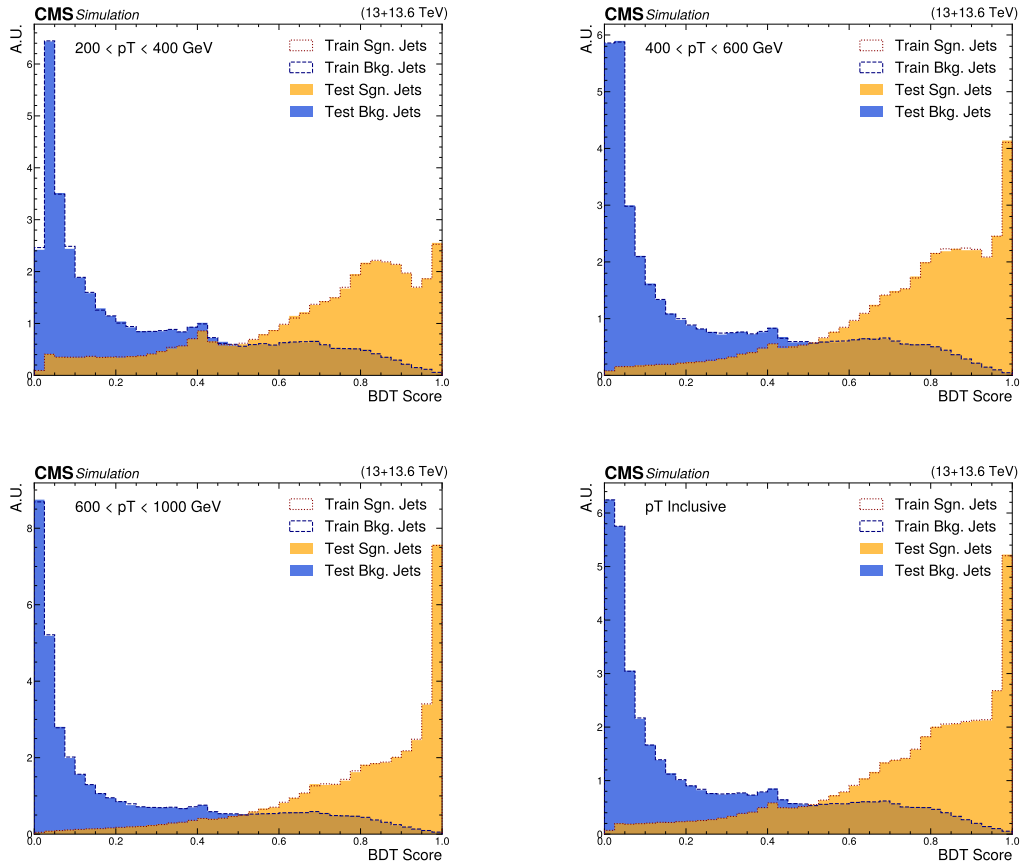
Figure 6.8: BDT score of test (train) of signal and background jets in solid (dashed) lines for different HOTVR p_{T} ranges. The results have been obtained by merging simulations of p–p collisions at $\sqrt{s}$ of 13 and 13.6 TeV. The distributions are normalized to the total number of jets.

To assess the performance of the model, the ROC curves are calculated for the training and testing datasets and shown in Figure 6.9, as the mistag rate

ε_B against the signal efficiency ε_S for different threshold values on the BDT output score. The ROC curve of the train (test) samples is shown as a dashed (continuous) line in the three different HOTVR p_T ranges in blue, orange, and green, respectively. In the figure, the performance of the selection-based method are also shown: applying the selections of Table 6.2 on the jets of the testing sample and calculating the signal and mistag rate using the same approach as for the BDT, the star markers corresponding to the three p_T ranges are obtained and shown in the plot. The figure shows an improvement of more than 10% on the signal efficiency at the same mistag rate when compared to the selection-based approach for each p_T range.
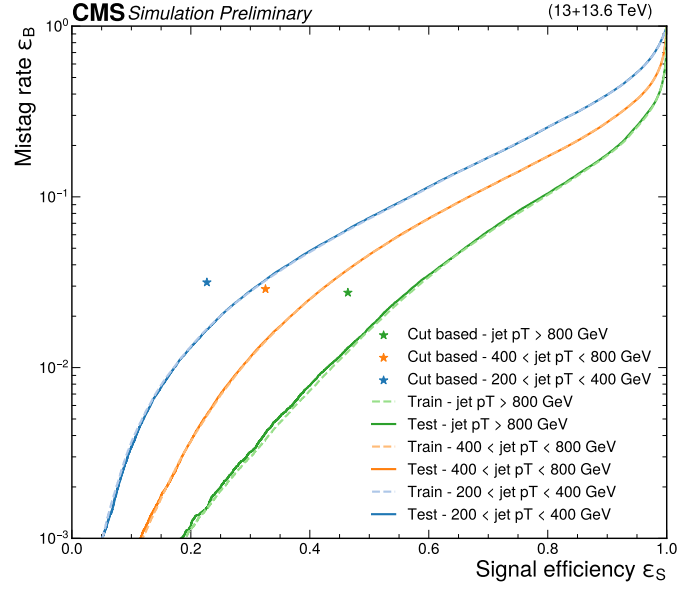
Figure 6.9: ROC curve for training (testing) dataset shown as a dashed (continuous) line in blue, orange, green, respectively for $200 < p_T < 400$ GeV, $400 < p_T < 800$ GeV, 800 GeV$< p_T$. The star markers represent the values obtained using the selection-based approach in the three p_T ranges [2].

6.5 Validation in top quark-enriched region

In this section, the validation of the BDT classifier is presented for jets originating from hadronically decaying top quarks, namely the signal jets used during training. The study is performed using data collected in p–p collisions at $\sqrt{s}$ of 13 TeV (Run 2) and 13.6 TeV (Run 3, 2022). The validation is carried out in a region enriched in semileptonic $t\bar{t} \to \mu + b +$ jets events, which provides a high-purity sample of hadronic top quark decays with well-modelled kinematic properties. This allows for a reliable comparison between data and simulation to verify that the BDT response and tagging performance are accurately described. The region is defined using the following event selections:

- muon event trigger;

- exactly one muon with tight identification requirement (Section 2.2.5);

- no electrons;

- at least two AK4 jets, one of which is tagged as a b quark jet with the medium DeepBTag working point (Section 5.6.1);

- at least one HOTVR jet, with the angular distance $\Delta\phi$ in the transverse plane from the muon to be greater than two;

- reconstructed missing transverse momemtum, p_T^{miss2}, referred to as MET, plus muon p_{T} to be greater than 250 GeV.

In addition, the muon and the b quark jets are required to be in the same hemisphere, i.e. $\Delta\phi(b$ quark jet, muon$) < 2$. For each event, the HOTVR jet with the largest p_{T} is considered.

The hadronically decaying top quark HOTVR jets arise mainly from $t\bar{t}$ events in the semileptonic channel, with smaller contributions from single-top (tW channel), $t\bar{t}W$, and $t\bar{t}Z$ processes. Background jets not originating from top quarks mainly originate from W bosons in $W +$ jets events, due to the selection on p_T^{miss} that targets leptonically decaying W bosons. Another source of background jets is the QCD multijet production.

This region is used to extract the top-tagging scale factor, which corrects the tagging efficiency in simulation to match that observed in data. The scale factor is defined as

$$SF = \frac{\varepsilon_{\mathrm{DATA}}}{\varepsilon_{\mathrm{SIMULATION}}} , \qquad (6.8)$$

where ε denotes the efficiency, i.e. the fraction of events passing the BDT discriminator over the total number of events.

The measurement is performed with a template fit of the HOTVR jet mass distribution in data and simulation. Two categories are defined: events that pass the BDT threshold of 0.5 and events that fail. In the fit, the simulated number of events in the passing category, $N_{\mathrm{pass}}^{\mathrm{MC}}$, is scaled by the factor SF. The yield in

---

$^2 \vec{p}_T^{\,\mathrm{miss}} = -\sum_{i\in\mathrm{PF\ candidates}} \vec{p}_T^{\,i} .$

the failing category is then scaled such that the total number of simulated events remains unchanged,

$$N_{\text{fail}}^{\text{MC}} \longrightarrow N_{\text{fail}}^{\text{MC}} + (1 - SF) \, N_{\text{pass}}^{\text{MC}} \,.$$

Before performing the fit, the distributions are further divided into three jet truth-flavor categories: top quark-, W-, and other-originating HOTVR jets, where the *"other"* is a residual category that includes, for example, b-quark and QCD jets. A separate scale factor is calculated for each category. In the context of this thesis, only the scale factor for the top quark category is determined explicitly, while the scale factors for the other two categories are treated as nuisance parameters in the fit. Furthermore, the fit is performed in five HOTVR jet p_{T} ranges: 200–300, 300–400, 400–480, 480–600, and 600–1200 GeV.

Figure 6.10 shows the BDT output score evaluated on the leading p_{T} HOTVR in the top quark–enriched region for top-tagged HOTVR jets, using data from Run 2 and Run 3 (2022). The simulated prediction is split by the same jet flavor categories used in the scale factor fit, ordered by their yield contributions. The aforementioned top-tagging scale factor is applied to the simulated jets originating from hadronically decaying top quarks. The hatched error bars on the simulated predictions are calculated as the sum in quadrature of the uncertainty from the finite simulation sample size and the systematic uncertainties related to the jet energy corrections, the modelling of the initial and final state radiation for parton shower from `PYTHIA` generator, the reweighting of the pileup profile in simulation, and the top-tagging scale factor uncertainties from the fit. Moreover, the uncertainty on the $t\bar{t}$ cross section is included, from next-to-leading order calculation in QCD (NLO) using `POWHEG` [151, 152, 153]. Moreover, the HOTVR jet mass distribution in the top quark–enriched region for top-tagged HOTVR jets is shown in Figure 6.11, using data from Run 2 and Run 3 (2022). The data-to-simulation agreement is consistent with unity within uncertainties in both distributions for both data-taking periods, indicating that the hadronically decaying top quark jets are well modeled in simulation.
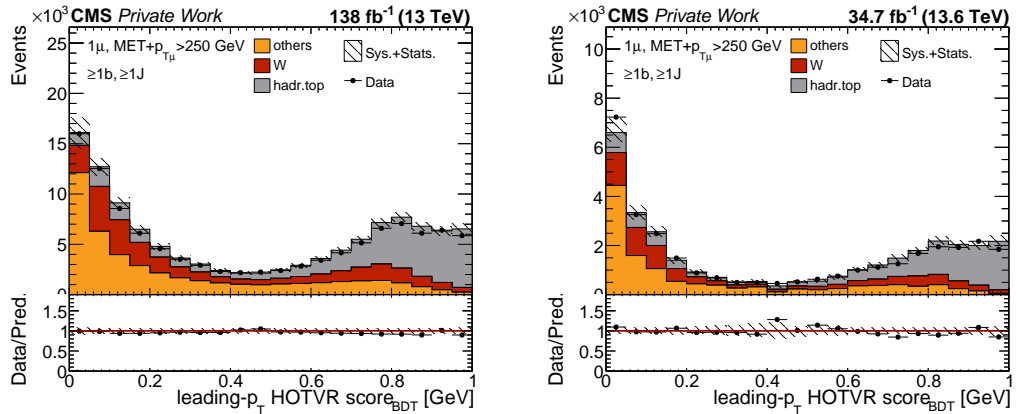
Figure 6.10: Comparison of data (points) and simulated predictions (histograms) for the BDT score of leading-p_{T} HOTVR jet in the top quarks-enriched region for Run 2 (*left*) and Run 3 (2022) (*right*) data campaigns. In the legend, the label *"J"* denotes HOTVR jets.
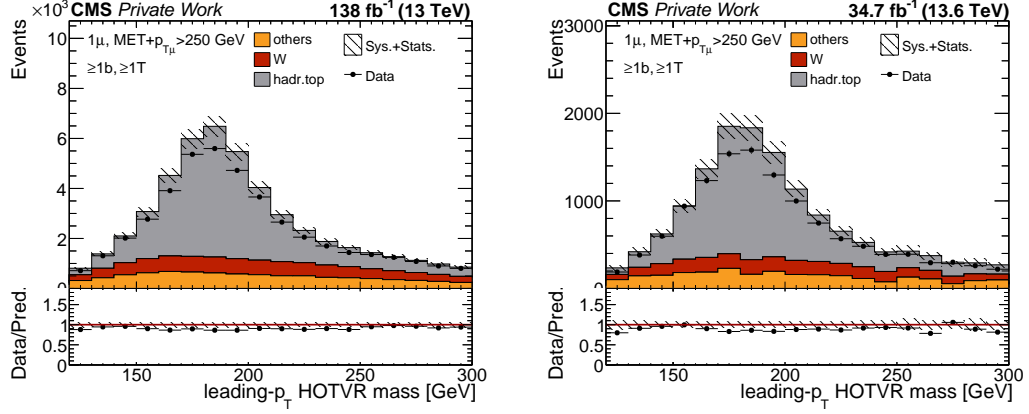
Figure 6.11: Comparison of data (points) and simulated predictions (histograms) for
the leading-p_T HOTVR mass in the top quarks-enriched region for Run 2 (*left*) and
Run 3 (2022) (*right*) data campaigns. The simulation is split by jet truth flavors. In
the legend, the label *"T"* denotes top-tagged HOTVR jets.

6.6 Validation of background jets

To assess the performance of the BDT tagger on data, a validation is performed in
a control region enriched in background jets, using data collected in p–p collisions
at $\sqrt{s}$ of 13 TeV (Run 2) and 13.6 TeV (Run 3). The region is defined to be
enriched in Z+jets events, where additional hadronic activity from QCD radiation
is reconstructed with the HOTVR algorithm. This region provides a clean and
well-understood sample of light-flavour and gluon-initiated jets, allowing for a
validation of the background-jet modelling in simulation and a comparison of
the BDT response between data and simulation. The same control region is
employed in the search for $t\bar{t}Z'(Z' \to t\bar{t})$, presented in Chapter 7, where it serves
as an orthogonal region to the signal regions and is used to validate the modelling
of the background prediction.

The region is obtained using the following event selection:

- double lepton event trigger;

- two leptons with medium identification requirement (Section 5.3 and 5.4),
  same flavor (ee or $\mu\mu$) and opposite charge;

- at least one HOTVR jet.

All the reconstructed objects follow the selection and identification criteria
defined in Chapter 5. The leading (subleading) lepton is required to have p_T
> 25 (15) GeV. The invariant di-lepton mass m_{ll} is required to have values close
to the Z boson mass, i.e. $m_{ll} \in [80, 101]$ GeV. The HOTVR p_T is required to
be greater than 200 GeV, and $|\eta| < 2.4$. The distance in the $\eta - \phi$ plane between
the HOTVR jets and any lepton is greater than R_eff (Equation 6.4), meaning
that leptons found inside the jet cone are vetoed.

After applying the event selection, the jet truth-flavor can be studied using
the criteria detailed in Section 6.3.2. As the main expected background from
simulation is Z+jets, the jets are therefore originated from additional radiation,
namely from multijet QCD processes.

Figure 6.12 shows the different truth-flavors in percentage for the leading p_{T} HOTVR jet in the $\mu\mu$ and the ee channels, respectively. More than 90% of the jets originate from QCD. A small fraction of jets (6%) from b quarks [3] and less than 1% from hadronically decaying top quark. The category *others* contains all the jets which do not fall into the three main categories, e.g., jets originating from hadronically decaying W bosons.
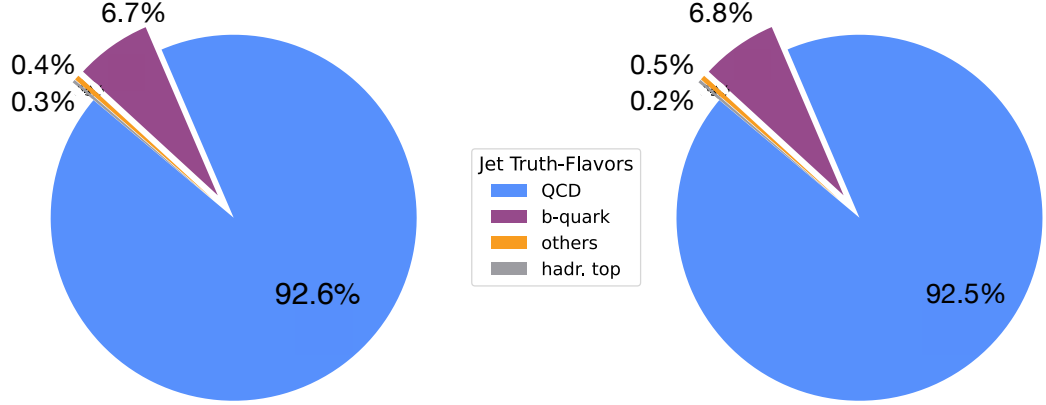
Figure 6.12: Jet truth-flavors in percentage for HOTVR jets in Z+jets enriched events. The ee (*left*) and $\mu\mu$ (*right*) channels are displayed separately.

Before evaluating the performance of the model on data, it is crucial to ensure that the simulated jets accurately represent the observed jets. Therefore, the agreement between data and simulation for the variables used as input features in the BDT training is carefully studied. The comparison between data (points) and simulated predictions (filled histograms) for the five HOTVR variables of Table 6.2 is shown in Figure 6.13 and Figure 6.14 for Run 2 (2017 and 2018) and Run 3 (2022) data campaigns, respectively. The prediction by simulation is split per jet flavour. The lower panel shows the ratio of the yields in data to those predicted in simulations. As no difference is seen in Figure 6.12 from the jet truth-flavors in different dilepton channels, the distributions of ee and $\mu\mu$ channels are summed together. The hatched error bars on the simulated predictions are calculated as the sum in quadrature of the uncertainty from the finite MC sample size and the following sources of systematic uncertainties,

- the jet energy corrections;

- the modelling of the initial and final state radiation for parton shower from PYTHIA generator;

- the reweighting of the pileup profile in simulation.

---

[3] The *b-quark* jet category refers to jets matched to a b quark, independently of whether the b quark originates from a top quark decay or another source.

These systematic uncertainties were included because they lead to the largest bin-by-bin variations in the template shapes.

Overall, the five variables are well modeled by the simulation, with the agreement between simulated samples and data generally close to unity within the uncertainties. However, some deviations are observed for low values in the N_{sub} distribution or for $\tau_3/\tau_2 > 0.8$. As shown in Figure 5.8, the high τ_3/τ_2 region is dominated by multijet processes, and the leading-order Z+jets simulated samples, which constitute the main source of background, may insufficiently model the complexity of multijet radiation.
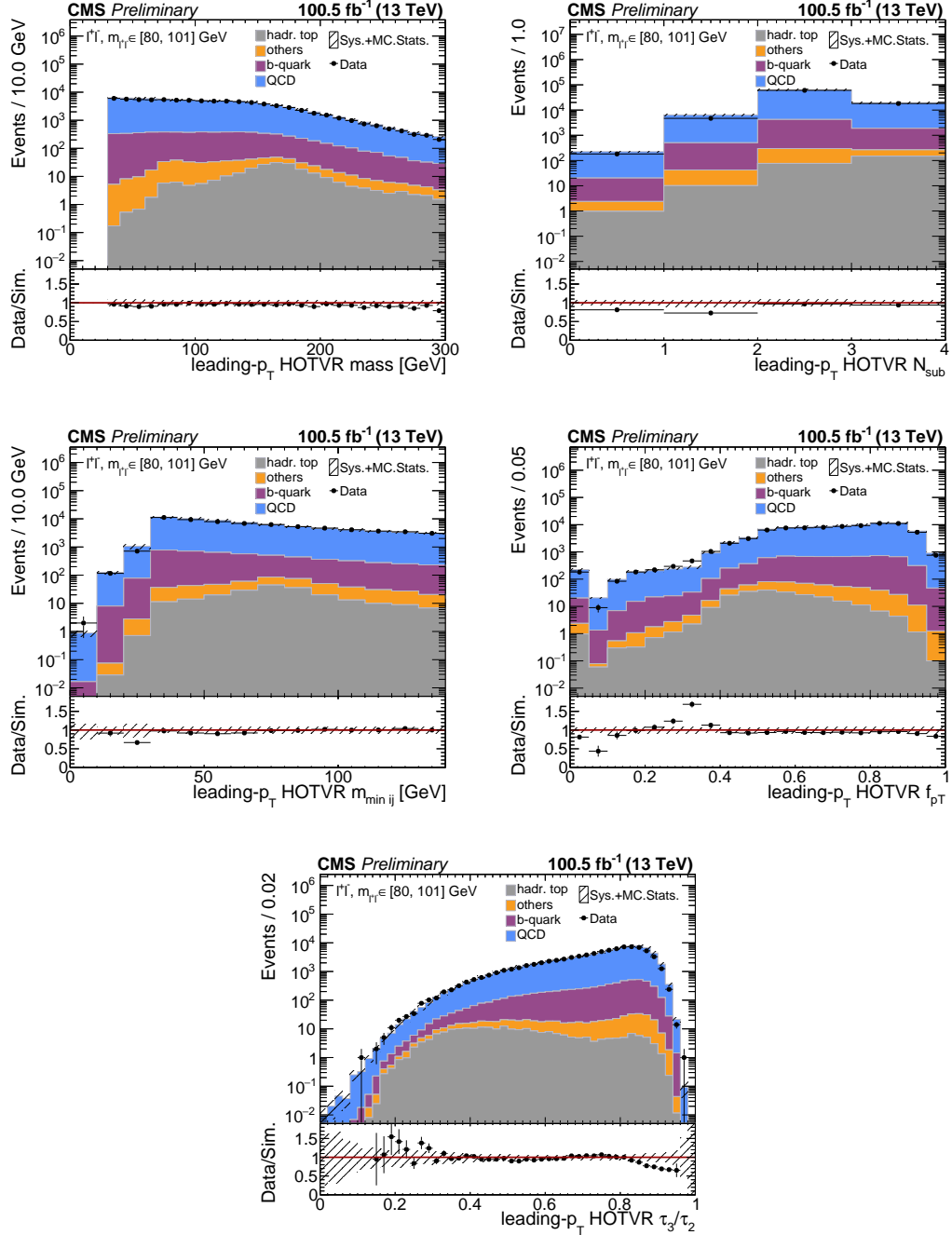
Figure 6.13: Run 2 (2017 and 2018) comparison of data (points) and simulated predictions (histograms) for the five HOTVR variables used in the BDT training [2] in the Z+jets-enriched region.
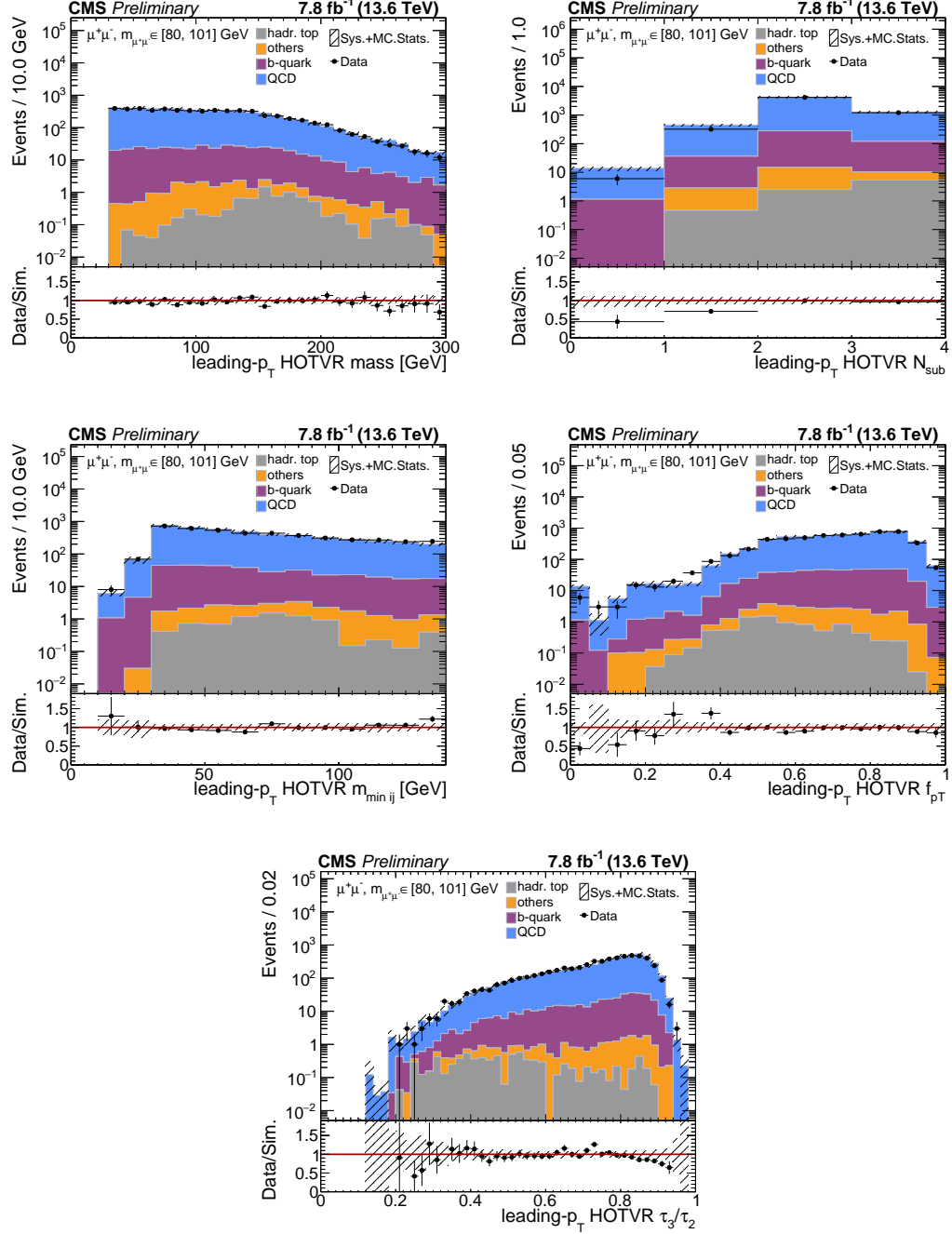
Figure 6.14: Run 3 (2022) comparison of data (points) and simulated predictions (histograms) for the five HOTVR variables used in the BDT training [2] in the Z+jets-enriched region.

Ultimately, the BDT output score evaluated on the leading p_T HOTVR in the Z+jets region is shown in Figure 6.15 for Run 2 (2017 and 2018) and Run 3 (2022) data-taking campaigns. The hatched error bars on simulations are calculated as the sum in quadrature of the uncertainty from the finite MC sample size and the sources of systematic uncertainties aforementioned, i.e., jet energy corrections, initial and final state radiation modelling, and pileup MC reweighting. The data and simulation agreement is close to unity within the uncertainties for both data-taking periods, indicating that the BDT is well described by the prediction from simulation for QCD-originating HOTVR jets.
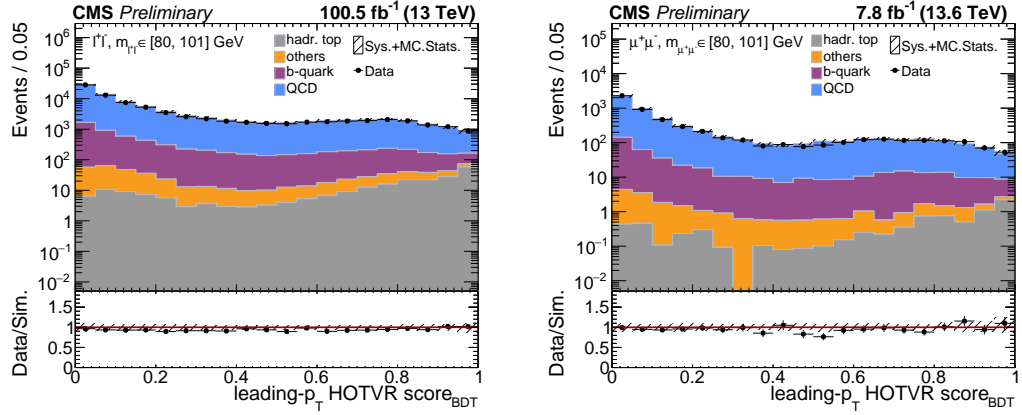
Figure 6.15: Comparison of data (points) and simulated predictions (histograms) for the BDT score of leading-p_T HOTVR jet in the Z+jets-enriched region for Run 2 (2017 and 2018) (*left*) and Run 3 (2022) (*right*) data campaigns.

6.7   Outlook

This chapter introduced a new top-tagging method based on the HOTVR jet algorithm and a BDT. At a fixed mistag rate, the model improves the signal efficiency by more than 10% relative to the selection-based approach used in CMS analyses.

A validation of the modeling of jets originating from hadronically decaying top quarks in a top quark–enriched region shows data-to-simulation agreement close to unity at both $\sqrt{s}$, 13 and 13.6 TeV. Moreover, the modeling of background jets was validated in Z+jets–enriched events. Data and simulation agree within uncertainties for p–p collisions at $\sqrt{s}$ of 13 and 13.6 TeV across all BDT input features and the BDT score. These results are documented in a *Detector Performance Note* [2].

Comparison with AK8+ParticleNet

The HOTVR+ BDT algorithm extends top quark identification to a wider phase space than fixed-radius taggers such as AK8+ParticleNet (see Section 5.6.2), with particular gains for $p_T < 600$ GeV, where the AK8+ParticleNet algorithm is less efficient by construction. This is relevant for searches for top-philic resonances with masses below 1 TeV, where the top quarks are not fully boosted.

To compare the tagging performance of the two algorithms, the reconstruction efficiency ε_S is evaluated in simulated events as

$$\varepsilon_S = \frac{N_S^{\text{tagged}}}{N_S^{\text{total}}}, \tag{6.9}$$

where N_S^{tagged} is the number of reconstructed jets matched to hadronically decaying top quarks (truth-flavor definition in Section 6.3.2) that satisfy the identification criteria of each algorithm, and N_S^{total} is the total number of reconstructed jets matched to hadronically decaying top quarks.

The comparison uses the selection in Section 6.5 and is shown as a function of the p_T of the matched top quark jets for both algorithms in Figure 6.16. The working point for both algorithms corresponds to a signal tagging efficiency of 82%[4]. By design, the HOTVR+ BDT reaches a reconstruction efficiency $> 50\%$ already for $200 < p_T < 400$ GeV and approaches the plateau value of 82% above 500 GeV. It is worth noting that for these working points, the mistagging rate is estimated to be 0.1% for AK8+ParticleNet, compared to 20% for HOTVR+ BDT.

Moreover, the reconstructed jet mass resolution is compared between the two algorithms for simulated hadronically decaying top quark jets with $p_T < 600$ GeV. To increase the purity of the selected top-quark jet samples, the working points of both algorithms are chosen to correspond to a mistag rate of 1%. Following the CMS recommendations, this corresponds to requiring AK8 jets to have a ParticleNet score > 0.58, and HOTVR+ BDT jets to have a score > 0.90.

---

[4]The CMS Collaboration provides fixed working points for the AK8+ParticleNet tagger. For a proper comparison to the HOTVR+ BDT working point in Section 6.4, AK8 jets are required to have a ParticleNet score > 0.97, which corresponds to a signal efficiency of 82%.
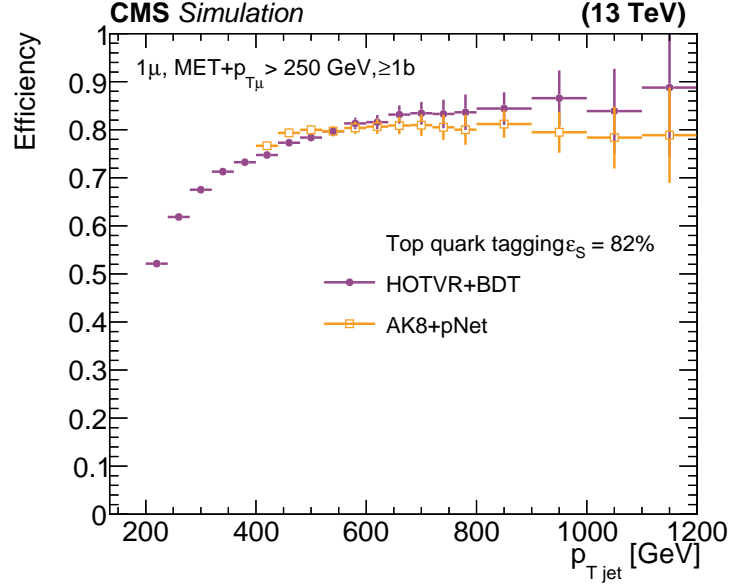
Figure 6.16: The distribution of ε_S as a function of the p_T of true hadronic top
quark jets for a working point corresponding to 80%, for HOTVR+ BDT (violet) and
AK8+ParticleNet (yellow) taggers. The error bars represent the statistical uncertainty
in each specific bin, due to the limited number of simulated events.

Figure 6.17 shows the reconstructed jet mass distributions. The mass resolu-
tion is evaluated as σ/μ, where σ and μ are calculated as standard deviation and
mean from a Gaussian fit[5] in the 140 to 220 GeV mass window. The resulting
resolutions are 7.2% for HOTVR+ BDT and 9.4% for AK8+ParticleNet, show-
ing the improved mass reconstruction with the HOTVR-based tagger in this p_T
range.

---

[5]A Gaussian model is used, as no significant tail structure is visible in the fit window (140–220
GeV). A Crystal Ball fit in the same window results in consistent mean and standard deviation
within uncertainties.
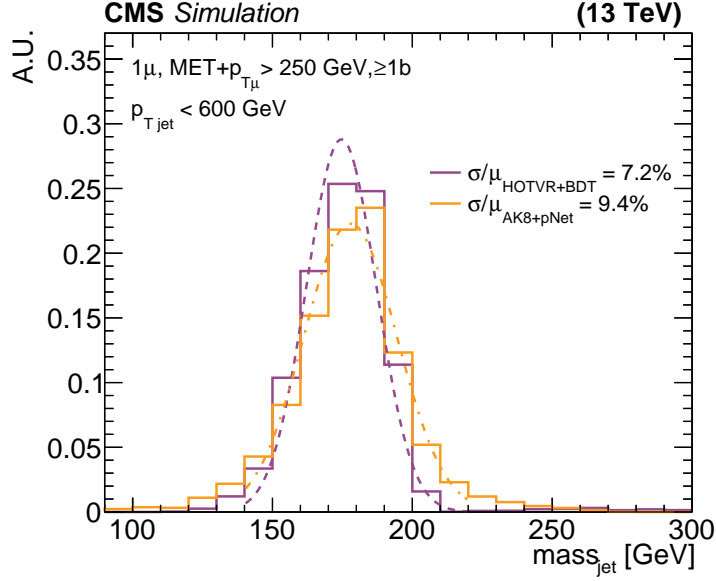
Figure 6.17: The reconstructed jet mass for HOTVR+ BDT jets (purple line) and AK8+particleNet jets (yellow line). From a Gaussian fit, the mass resolution for the two algorithms is shown in percentage. The $\mu \pm \sigma$ values are 174.65±12.50 GeV for HOTVR+ BDT, and 177.85±16.70 GeV for AK8+particleNet. Both distributions are normalized to unity.

Future perspectives

Given the promising performance of HOTVR, a natural next step is to develop a dedicated top quark tagger based on the ParticleNet architecture, which is the state-of-the-art machine learning model used for object tagging in particle physics, trained on HOTVR jets. Such a model could exploit HOTVR features to further improve the tagging efficiency and reduce the mistagging rate, particularly in the low-to-intermediate p_T range, where AK8-based methods are known to lose performance.

Beyond top tagging, the ParticleNet architecture supports multi-class learning, enabling a HOTVR multi-tagger for top, W, and b jets that improves reconstruction efficiency and background rejection, thereby enhancing mass resolution, energy calibration, and uncertainty estimation. Developing and deploying such a model would constitute a comprehensive PhD-scale project for a Run 3 analysis.

Chapter 7

Search for heavy top-philic resonance produced in association with top quarks

This chapter presents the search for a heavy top-philic BSM resonance produced in association with a $t\bar{t}$ pair, based on the theory motivation provided in Chapter 1. The analysis focuses on events where the top quarks from the resonance decay hadronically. It is performed in the opposite-sign dilepton final state to identify leptonically decaying top quarks that do not originate from the resonance. The invariant mass of the resonance is reconstructed from HOTVR jets identified with the hadronic top tagger described in Chapter 6. This represents the first analysis conducted in this channel.

Section 7.1 provides the motivation and the introduction for the analysis. The data and simulated samples used are described in Section 7.2. The event selection and categorization, aimed at enhancing signal sensitivity and reducing background, are detailed in Sections 7.3 and 7.4, respectively. The dominant background arises from multijet (QCD) events that are misidentified as top quark–initiated jets. The data-driven estimation of this background is presented in Section 7.5. Systematic uncertainties are summarized in Section 7.6, followed by the statistical interpretation of the results for various signal hypotheses in Section 7.7.

7.1 Motivation and introduction

The theoretical motivation for the BSM search outlines various signal models predicting vector, pseudoscalar, or scalar heavy resonances. Recent results, both from direct searches and reinterpretations of SM measurements, motivate the search presented in this thesis. As a model-independent analysis targeting an unexplored final state, it provides complementary sensitivity.

Following the recent observation of SM four top quark production by both ATLAS [54] and CMS [53], significant attention has been given to the observed excess, particularly in the dilepton final states. Several ongoing analyses are reinterpreting these results in the context of various BSM scenarios. The analysis presented in this thesis focuses on a different topology and kinematic regime, providing additional sensitivity to new physics effects underlying the observed

excess.

Moreover, in the context of new pseudoscalar resonance scenarios (see Section 1.3.2), this analysis is complementary to recent results at the top quark pair production threshold, where a significant excess of events has been observed [154]. Such an excess could arise either from a color-singlet pseudoscalar quasi-bound toponium state or from a heavy pseudoscalar particle such as a Higgs boson or axion-like particle. Since toponium is not expected to contribute significantly to four-top production, while new heavy pseudoscalars would, this analysis provides help in distinguishing between these interpretations.

Direct searches for top-philic heavy vector Z' resonances in events with four top quarks have been carried out by both the ATLAS [155] and CMS Collaborations, focusing on the single-lepton plus jets final state. This channel is orthogonal to the dilepton final state considered in this thesis. No significant excess over the SM background was observed in these analyses. The resulting observed upper limits by ATLAS on the production cross-section range from 21 fb to 119 fb, depending on the specific model parameters: the former is observed at $m_{Z'}$ of 2.5 TeV with top coupling $c_t = 1$ and chirality $\theta = \pi/2$, while the latter is for 1 TeV with $c_t = 4$ and $\theta = 0$. The analysis excluded a top-philic Z' with mass of 1 TeV, with $c_t = 4$, for $\theta = 0$ and $\theta = \pi/2$.

The search strategy presented in this thesis exploits the fact that, for $m_{Z'} > 1$ TeV, the resonant top quarks are significantly Lorentz-boosted. As a result, their hadronic decay products are highly collimated, allowing each top quark to be reconstructed as a single jet. The novelty of this analysis lies in the reconstruction of $m_{Z'}$ from a pair of jets identified using the HOTVR algorithm and the BDT-based top-tagging method described in Chapter 6. This approach also enables sensitivity to lower-mass scenarios with $m_{Z'} < 1$ TeV using a single reconstruction strategy. The choice of HOTVR is particularly motivated by its variable-radius clustering parameter, which provides top reconstruction across a wide range of momenta and enables a unified strategy sensitive to both high mass and low mass scenarios. This work represents the first application of HOTVR to a four-top search, demonstrating the potential of HOTVR algorithm for future searches. The focus is on final states with leptonically decaying spectator top quarks and a hadronically decaying resonance, as this topology combines the clean dileptonic signature for multijet background suppression with the large signal efficiency achievable in the boosted hadronic channel.

The analysis uses data collected at $\sqrt{s}$ of 13 and 13.6 TeV, which constitutes the first CMS search in this final state at 13.6 TeV. In summary, the analysis complements several existing CMS and ATLAS results and provides a groundwork for future four top quarks searches, as it is the first to use the HOTVR plus BDT top tagger, and to explore this high-energy phase space with the inclusion of 13.6 TeV data.

7.2 Datasets and simulated samples

The analysis uses p–p collision data recorded by the CMS detector at $\sqrt{s} = 13$ TeV (Run 2, 2016–2018) and at $\sqrt{s} = 13.6$ TeV (2022). The integrated luminosity of all datasets is reported in Table 7.1.

The analysis focuses on final states with two leptons, which provides an effi-

Table 7.1: Integrated luminosity of the datasets used in the analysis.

Data-taking period	$\sqrt{s}$ (TeV)	Integrated luminosity [fb^{-1}]
2016 (Run 2)	13	35.9 [156]
2017 (Run 2)	13	41.5 [157]
2018 (Run 2)	13	59.7 [158]
2022 (Run 3)	13.6	34.8 [159]
Total		**173.0**

cient event selection and reduced background contamination. Therefore, datasets collected with double-lepton triggers are used, including events selected by the CMS HLT (see Section 2.2.6) paths based on di-muon, di-electron, or electron–muon trigger conditions initiated at the L1 trigger stage. The p_{T} thresholds for the triggers used in different lepton channels are summarized in Table 7.2. In addition, single-lepton triggers are included to recover efficiency in events where one of the leptons falls below the double-lepton trigger requirements.

Table 7.2: Minimum p_{T} requirements for the double-lepton HLT triggers. In the $e\mu$ channel, two asymmetric threshold combinations are used.

Channel	Lepton p_{T} thresholds [GeV]
ee	leading $e > 23$, subleading $e > 12$
$\mu\mu$	leading $\mu > 17$, subleading $\mu > 8$
$e\mu$	($\mu > 23$, $e > 12$) or ($\mu > 8$, $e > 23$)

Simulated signal samples are produced with MC event generators. Information in terms of setup and configuration of MC generators is given in detail in Appendix A.

The signal samples of heavy Z' vector resonance are generated at leading order (LO) using `MADGRAPH5_aMC@NLOv2.9` [160], and the model described in Ref. [66]. As described in Section 1.3.1, the chirality parameter of $\theta = \pi/4$ is chosen, and the search focuses on the $t\bar{t}Z'$ production mechanism, specifically the associated production of a Z' boson with top quark pairs, under the assumption of a 100% branching fraction for the $Z' \to t\bar{t}$ decay. The mass of the Z' boson is considered in the range from 0.5 to 4 TeV, with simulated samples generated in steps of 250 GeV for masses below 2 TeV and 500 GeV for masses above. Separate sets of samples are produced for Z' boson widths corresponding to 4%, 10%, 20%, and 50% of the boson mass. The signal cross-sections are listed in Tables 7.3, for $\sqrt{s}$ of 13 and 13.6 TeV. All the cross-sections are calculated by `MADGRAPH` at LO. The alternative interpretations involving a scalar ϕ or pseudoscalar a mediator (see Section 1.3), motivated by the 2HDM model [68, 161] or models with a pseudoscalar ALP [70, 71, 162], are also generated using `MADGRAPH5_aMC@NLOv2.6.5` (2016–2018) or v2.9.18 (2022).

Background simulated samples are essential for optimizing the selection to enhance the signal sensitivity and characterizing the dominant processes in each event category. They are also used to optimize the data-driven background estimation, which is discussed in 7.5

The dominant expected background in this analysis is composed of SM $t\bar{t}$ production in the dilepton final state with extra radiation. The $t\bar{t}$+jets events

Table 7.3: $t\bar{t}Z'$ simulated samples and their LO cross-sections for $\sqrt{s}$ of 13 and 13.6 TeV.

$m_{Z'}$ (GeV)	σ [fb] @ 13 TeV	σ [fb] @ 13.6 TeV
500	70	80
750	14	19
1000	4.0	5.0
1250	1.6	1.8
1500	0.54	0.66
1750	0.20	0.26
2000	0.085	0.10
2500	0.016	0.021
3000	0.0033	0.0046
4000	0.00016	0.00021

are simulated using `POWHEG2.0` at next-to-leading order (NLO). The cross-section is corrected to next-to-next-to-leading order (NNLO) in perturbative QCD, including resummation of next-to-next-to-leading-logarithmic (NNLL) soft-gluon contributions [163, 164].

The Z+jets process represents the main background in the control regions, which are used to study the agreement between data and simulation and to validate the background estimation method. The Z+jets samples are generated with `MADGRAPH` at leading order (LO) with four additional jets with MLM matching[1] [165].

Background samples for $t\bar{t}$ production in association with a boson ($t\bar{t}W$, $t\bar{t}Z$), single-top quark production in the s-channel, in association with a Z boson or a pair of W and Z bosons, are simulated at NLO in QCD with `MADGRAPH5_-aMC@NLOv2.6.0`. The single top quark production in the t-channel and in association with a W boson uses `POWHEGv2.0`. The production of $t\bar{t}H$ is obtained using `POWHEGv2.0`. The $t\bar{t}t\bar{t}$ process is simulated at NLO in QCD with the `MADGRAPH5_-aMC@NLOv2.6.5`. Minor backgrounds, such as the production of a dibosons event, are generated using `Pythia 8` at LO, while triple top production is generated using `POWHEG2.0`.

A summary of the background samples used in the analysis is provided in Table 7.4, which includes cross-section values for $\sqrt{s}$ of 13 TeV, along with their corresponding event generators.

All the samples are generated using the proton structure described by the NNPDF3.1 [166] parton distribution function (PDF), detailed in Section 1.1.1. Parton showering (PS) and hadronization are simulated with `Pythia 8` [167], where the parameters for the underlying event description correspond to the CP5 tune [168]. Simulated events are scaled to the integrated luminosity of the recorded data using their theoretical cross-sections.

The simulation of the CMS detector is obtained using GEANT4 [173]. To model the effects of multiple p–p interactions occurring due to PU, additional interactions are overlaid on the primary hard scattering process, with the PU distribution reweighted to match that observed in data.

---

[1]Generated with matrix elements including up to four extra partons. MLM matching pairs these partons to parton–shower jets using a matching scale to avoid double-counting.

Additionally, correction factors are applied to improve the agreement between simulation and data. These factors vary for different reconstructed objects and are year-dependent, due to changes in the experimental conditions across different data-taking periods. The correction factors used in this analysis are described in Chapter 5 and cover lepton identification and isolation, trigger efficiency, jet energy scale and resolution, b-tagging efficiencies and misidentification rates, and the BDT HOTVR top tagger. Uncertainties on these factors are detailed in Section 7.6.

Table 7.4: Background MC samples, their cross-sections, and event generators at $\sqrt{s}$=13 TeV. `Pythia 8` is always used to model the parton shower and the hadronisation.

Category	σ (pb)	Generator
$t\bar{t}$		
$t\bar{t}$, dilepton	88.51 (NNLO)[163, 164]	POWHEG
$t\bar{t}$, ℓ+jets	366.29 (NNLO)[163, 164]	POWHEG
$t\bar{t}V$		
$t\bar{t}W$	0.611 (LO) [169]	MADGRAPH5_aMC@NLO
$t\bar{t}Z$	0.783 (LO) [169]	MADGRAPH5_aMC@NLO
Z+jets (DY)		
Z+jets ($Z \to \ell\ell$), inclusive, $m_{\ell\ell} > 50$ GeV	15910 (LO)	MADGRAPH
Z+jets ($Z \to \ell\ell$), inclusive, $m_{\ell\ell} < 50$ GeV	5343 (LO)	MADGRAPH
Z+jets ($Z \to \ell\ell$), $70 < H_T < 100$ GeV	140.1 (LO)	MADGRAPH
Z+jets ($Z \to \ell\ell$), $100 < H_T < 200$ GeV	140.2 (LO)	MADGRAPH
Z+jets ($Z \to \ell\ell$), $200 < H_T < 400$ GeV	38.39 (LO)	MADGRAPH
Z+jets ($Z \to \ell\ell$), $400 < H_T < 600$ GeV	5.21 (LO)	MADGRAPH
Z+jets ($Z \to \ell\ell$), $600 < H_T < 800$ GeV	1.265 (LO)	MADGRAPH
Z+jets ($Z \to \ell\ell$), $800 < H_T < 1200$ GeV	0.568 (LO)	MADGRAPH
Z+jets ($Z \to \ell\ell$), $1200 < H_T < 2500$ GeV	0.133 (LO)	MADGRAPH
Z+jets ($Z \to \ell\ell$), $2500 < H_T < Inf$ GeV	0.00297 (LO)	MADGRAPH
$t\bar{t}H$		
$t\bar{t}H$, $H \to b\bar{b}$	0.5269 (NLO) [169]	POWHEG
$t\bar{t}H$, $H \nrightarrow b\bar{b}$	0.5638 (NLO) [169]	POWHEG
ST		
single-t (tW), t, leptonic	19.6 (NNLO) [170]	POWHEG
single-t (tW), $\bar{t}$, leptonic	19.6 (NNLO) [170]	POWHEG
single-t (t-chan), $\bar{t}$	80.95 (NNLO) [170]	POWHEG
single-t (t-chan), t	136.02 (NNLO) [170]	POWHEG
single-t (s-chan), leptonic	3.36 (NNLO) [170]	MADGRAPH5_aMC@NLO
single-t (s-chan), hadronic	6.96 (NNLO) [170]	MADGRAPH5_aMC@NLO
SM 4t		
$t\bar{t}t\bar{t}$	0.012 (NLO) [171]	MADGRAPH5_aMC@NLO
$t\bar{t}tX$		
$t\bar{t}tW$	0.00047 (NLO) [172]	MADGRAPH5_aMC@NLO
$t\bar{t}t$+jets	0.0078 (NLO) [172]	MADGRAPH5_aMC@NLO
VV		
WW	110.8 (LO)	Pythia 8
WZ	47.13 (LO)	Pythia 8
ZZ	16.523 (LO)	Pythia 8

7.3   Event selection
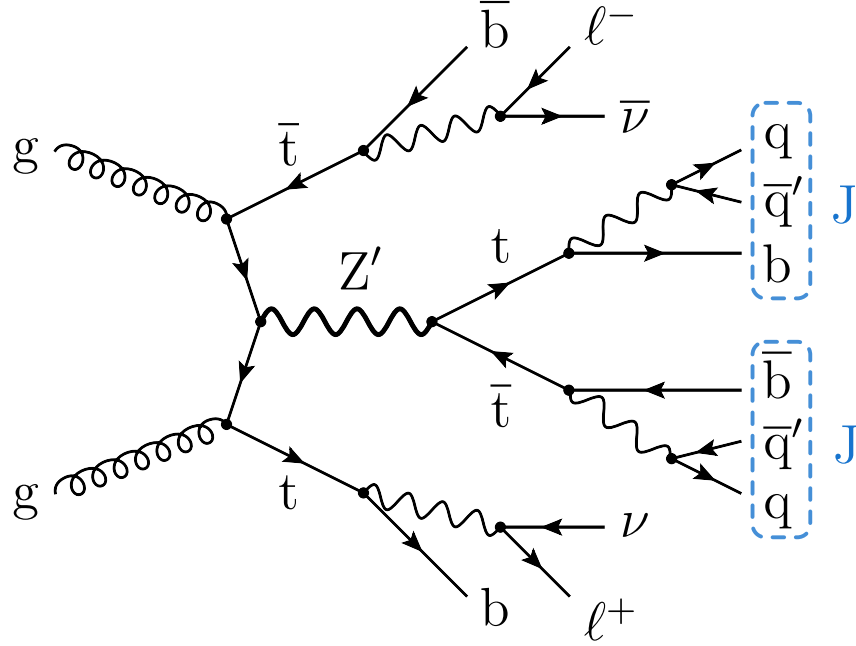
Figure 7.1:   The signal signature targeted in this analysis.   The two hadronically
decaying top quarks from the Z' decay are reconstructed with HOTVR jets, J.

The search focuses on a signal signature defined by a $t\bar{t}$ system originating
from the BSM resonance and decaying hadronically, and two additional top
quarks decaying leptonically, as depicted in Figure 7.1. For the resonant $t\bar{t}$ system
reconstruction, two large radius jets are considered, specifically HOTVR jets,
which are identified as originating from hadronically decaying top quarks using
the BDT-based top tagger method presented in Chapter 6. The simulated mass
points range from 500 GeV to 4 TeV, resulting in a broad distribution of the
p_T of the hadronically decaying top quarks from the resonance, as shown in
Figure 7.2. The peak of the distribution for $m_{Z'}$ of 500 GeV is around 250 GeV,
while at higher masses a double peak appears, originating from events where the
resonance recoils against hard initial-state radiation, leading to an asymmetric
boost of the top and antitop quarks. The HOTVR jets are therefore suited for
identifying top quarks in both the high-p_T (boosted) regime, defined as $p_\mathrm{T} > 600$
GeV, and the intermediate-p_T regime, defined as 200 GeV$<p_\mathrm{T}<$ 600 GeV.

The identification of the additional top quarks is done by requiring two isolated
charged leptons (electrons or muons) in combination with the information on
the number of b quark jets. All the reconstructed objects follow the selection
and identification criteria defined in Chapter 5. Events of interest are therefore
selected, in addition to the double-lepton trigger selection described in Section
7.2, by the following criteria:

- exactly two selected leptons with opposite charge and *medium* identification
  requirement (electron, Section 5.4, or muon, Section 5.3),

- dilepton invariant mass $M_{\ell\ell} \notin [80, 101]$ GeV (only for ee and $\mu\mu$ channels),
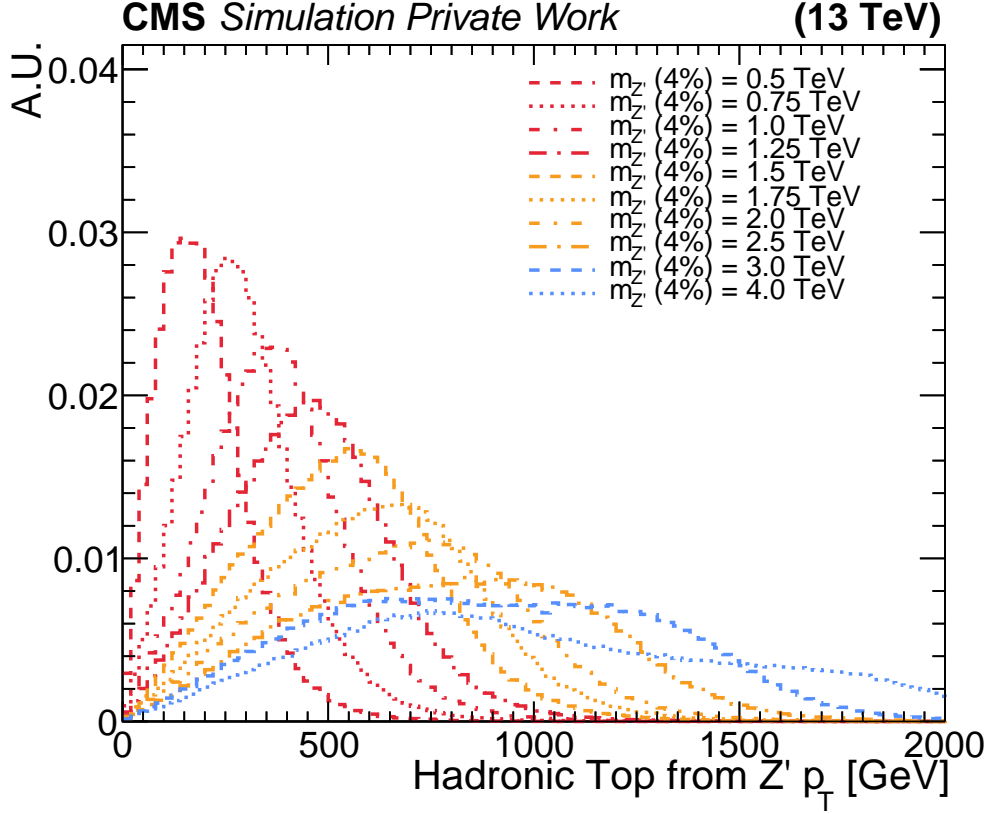
Figure 7.2: The p_{T} of the resonant hadronic top quarks for different $m_{Z'}$. Each
distribution is normalized to unity.

- at least two AK4 jets (Section 5.5),

- at least two HOTVR jets.

These selection criteria are designed to suppress SM background contributions, particularly Z+jets (DY) and pure QCD events, while enhancing signal
sensitivity. Moreover, the p_{T}-leading lepton is required to have $p_{\mathrm{T}} > 25$ GeV,
while the subleading > 15 GeV. Muons are required to have $|\eta| < 2.4$ and to
the tight isolation criteria, described in Section 5.3. Electrons are required to
have $|\eta| < 2.5$. The AK4 jets must have $p_{\mathrm{T}} > 30$ GeV and $|\eta| < 2.4$. Additionally, the AK4 jets are required not to overlap with any leptons, requiring
$\Delta R(\mathrm{AK4}, \ell) > 0.4$, and with any HOTVR, requiring $\Delta R(\mathrm{AK4}, \mathrm{HOTVR}) > R_{\mathrm{eff}}$
(Equation 6.4). AK4 jets with overlap are vetoed in the analysis. The HOTVR
jets are required to have $p_{\mathrm{T}} > 200$ GeV and $|\eta| < 2.4$. The HOTVR jets fulfill
the requirements of Table 6.1.

7.4   Event categorization

Events passing the selection criteria described above are further categorized into
orthogonal regions to enhance signal sensitivity. This categorization is based on
the number of b jets and top-tagged HOTVR jets. The b jets are reconstructed

and identified following the description detailed in Section 5.6.1. The *loose* b-tagging working point is used, and jets are required to have $p_T > 30$ GeV, to suppress pileup and soft b jets from gluon splitting. The *loose* working point is chosen as it yields the highest overall sensitivity of the search compared with the tighter working points. The BDT defined in Section 6.3 is used to identify top-tagged HOTVR jets. A score threshold of 0.5 is used, corresponding to the working point that maximizes the median sensitivity, averaged over the targeted mass range. The resulting tagging efficiency and mistag rate for this working point are 84.2% and 21.7%, respectively.

The signal sensitivity is evaluated using the Punzi sensitivity metric [174]. The choice of the Punzi metric over the $S/\sqrt{B}$ metric is motivated by the very low signal yields expected in the four-top final state. In addition, the metric is independent of the signal cross-section, unlike $S/\sqrt{B}$, and it remains meaningful in the low-count scenario, where Gaussian approximations fail. It is defined as

$$\frac{\varepsilon_{cut}}{a/2 + \sqrt{B}} \tag{7.1}$$

where ε_{cut} is the fraction of signal events that pass a selection criterion and B is the number of expected simulated background events after the selection. The a parameter is the number of sigmas corresponding to one-sided Gaussian tests at a significance α: the choice of a is set to be equal to three for the following results. This value is chosen as it corresponds to optimizing for a 3-σ evidence sensitivity, and is standard practice in searches for rare processes.

Figure 7.3 shows the 2D distribution of the punzi sensitivity for signal of $m_{Z'} = 1, 2, 3$ TeV, after the event selection described in Section 7.3, and resulting from different cuts on the exact number of b jets ($N_{\text{b-loose}} \notin$ HOTVR) and top-tagged HOTVR jets ($N_{\text{top-tagged HOTVR}}$). The punzi sensitivity is shown on the z-axis. The ε_{cut} is calculated considering the number of signal events remaining from the specific choice of a cut in this 2D plane, i.e., the number of b jets and top-tagged HOTVR jets, divided by all the signal events after the pre-selection criteria. The punzi distribution is calculated considering all lepton channels. The punzi sensitivity is scaled by 100 for plotting purposes.

As shown in the figures, the highest punzi sensitivity is achieved when requiring at least one b jet and at least two top-tagged HOTVR jets. Based on this, two orthogonal signal regions, **SR1b2T** and **SR2b2T**, are defined, as summarized in Table 7.5.

Table 7.5: Definition of signal regions.

	$N_{\text{b-loose}} \notin$ HOTVR	$N_{\text{top-tagged HOTVR}}$
SR2b2T	≥ 2	≥ 2
SR1b2T	$= 1$	≥ 2

The number of expected signal and background events and the Punzi sensitivity for the subsequent selection criteria, which form the two signal regions, are given in the cutflow plots in Figure 7.4, 7.5. The figures show the step-by-step predicted events after applying each selection cut of **SR2b2T** and **SR1b2T** respectively, for each lepton channel ($e\mu$, ee, $\mu\mu$). The cut flow plots show the
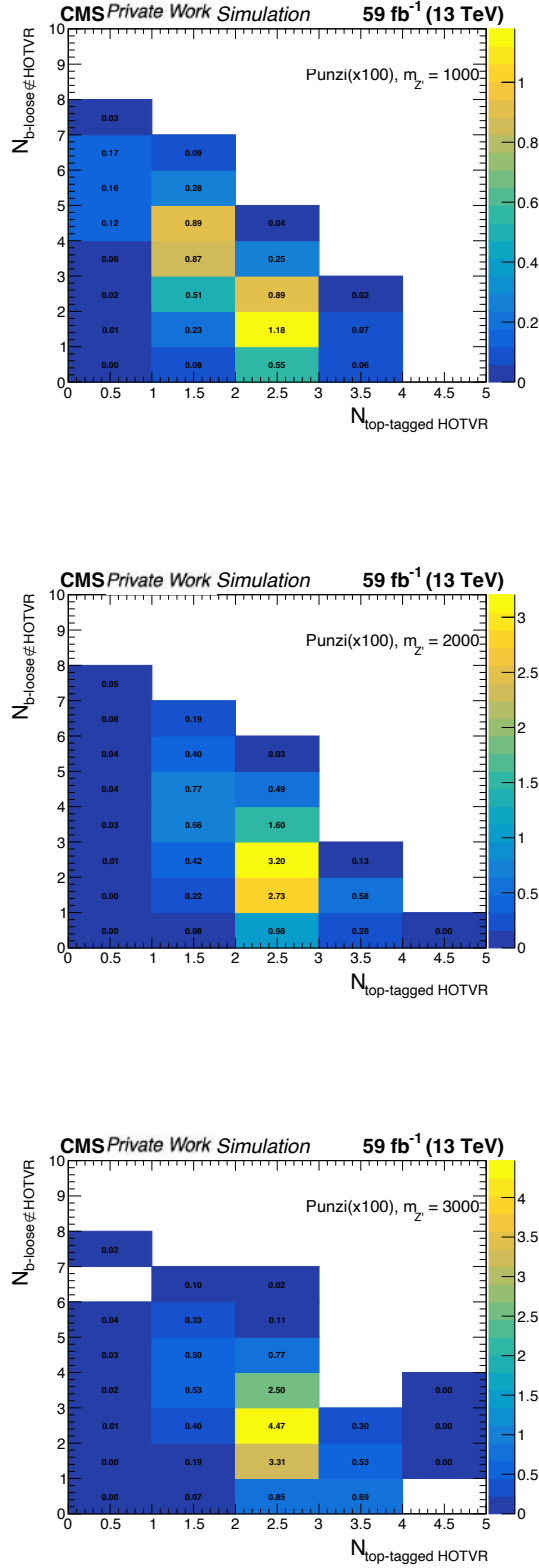
Figure 7.3: Punzi sensitivity for signal of $M_{Z'} = 1, 2, 3$ TeV after the selection described in Section 7.3, and calculated for different selections on the number of b jets (y-axis) and top-tagged HOTVR (x-axis). These results show simulated data from 2018 data-taking, as an example of the full analysis.

simulated background contributions as stacked plots and the signal contributions
of $M_{Z'}$ equal to 750, 1250, and 2000 GeV. The AK4 jets are referred to as j,
whereas HOTVR jets are referred to as J. The T stands for the number of
top-tagged HOTVR jets. The lower box shows the trend of the punzi sensitivity
for each cut and it is calculated using the Equation 7.1, where the fraction of
signal events in each bin is calculated relative to the previous bin.
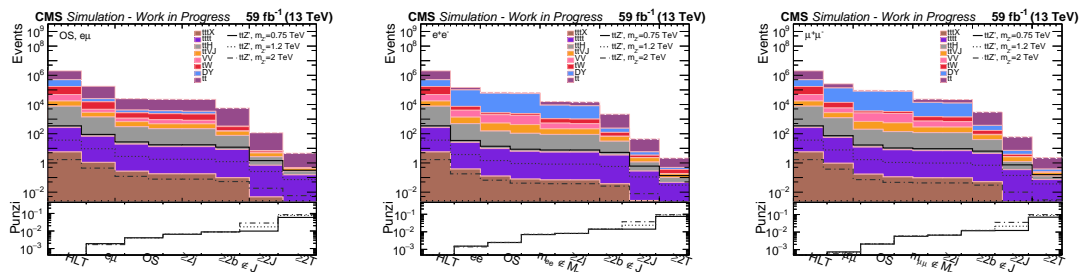
Figure 7.4: Cut flow plots resulting from the selection results of **SR2b2T**. Three
signal samples are shown. These results show simulated data from 2018 data-taking, as
an example for the full analysis.
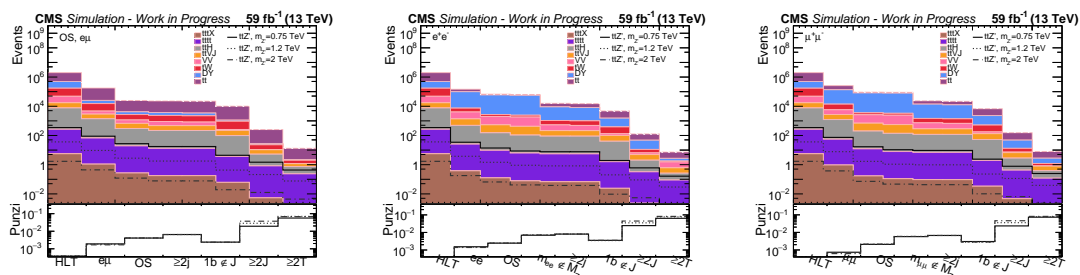
Figure 7.5: Cut flow plots resulting from the selection results of **SR1b2T**. Three
signal samples are shown. These results show simulated data from 2018 data-taking, as
an example for the full analysis

Jet flavors in signal regions

As mentioned in Section 7.2, the primary expected background contribution in
both signal regions arises from $t\bar{t}$ events. In events selected in the two opposite
final states, the HOTVR jets are typically produced from the hadronization of
light quarks or gluons radiated from the initial state and are thus incorrectly
tagged as originating from top quarks.

To fully understand the various generated origins of background HOTVR jets
in signal regions, a dedicated study on jet truth flavors is performed in simula-
tion. The flavors are assigned to HOTVR using simulated background samples
in signal regions, by matching jets to generator-level particles (gen-particle). This
matching is performed by requiring $\Delta R(\text{HOTVR}, \text{gen-particle}) < R_{\text{eff}}$. The cat-
egories are defined hierarchically as,

- **Hadronic top:** a hadronically decaying generator-level top quark and all of
  its decay products are contained within the jet. This definition is consistent
  with the one used for training the BDT HOTVR top tagger (Section 6.3).

- **Hadronic W:** both hadronic decay products of a W boson are contained in the jet.

- **q from W:** exactly one hadronic W decay product is found in the jet, without a b quark.

- **q (from W) + b:** a hadronic W decay product and a b quark are both present, but the full top decay is not contained.

- **b-quark:** the jet contains a generator-level b quark but does not fulfill the criteria above.

- **QCD:** the jet contains only light quarks or gluons and none of the conditions above are satisfied.

- **Others:** jets that do not fall into any of these categories, e.g. those matched to hadronic τ decays or to partially contained multi-particle topologies.

The categories *q from W* and *q (from W) + b* together account for less than 1% of jets. The different jet origins, or *flavors*, are shown in percentage in the bar chart in Figure 7.6 for the leading-p_T HOTVR jet, for the two signal regions, for the combination of ee and $\mu\mu$ lepton channels, and the $e\mu$ channel. No difference is seen for the subleading-p_T jet; therefore, it is not shown.

As shown in the chart, the *QCD* flavor constitutes more than 75% of all jets in both signal regions. The second most frequent flavor is the *b-quark*, representing about 15% of all jets. Genuine *hadronic top* jets make up roughly 4% of the total.
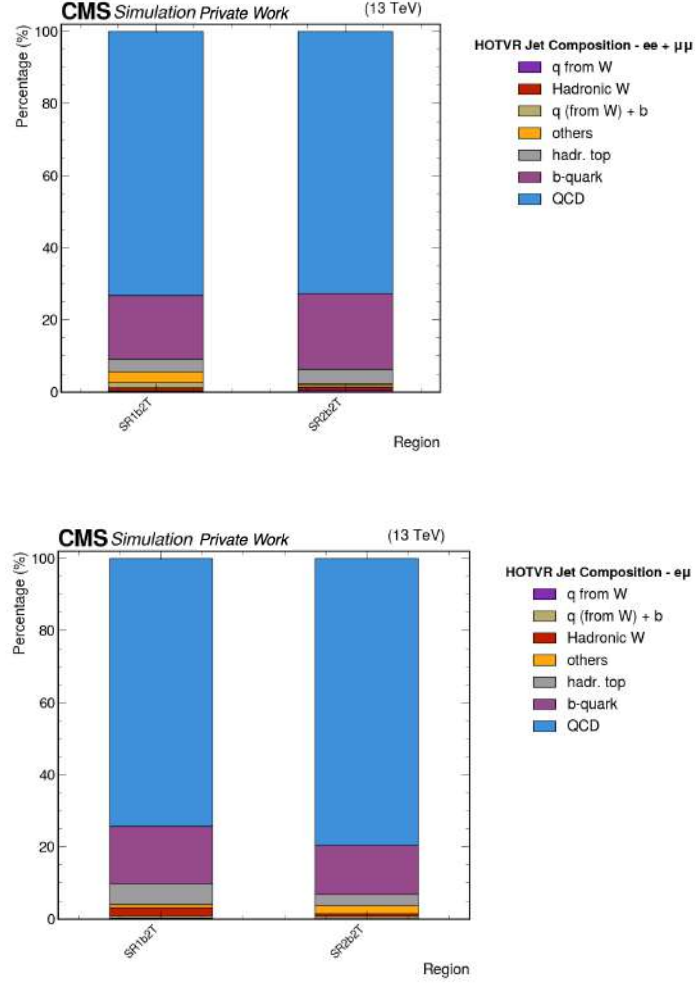
Figure 7.6: Jet flavor composition in **SR2b2T** and **SR1b2T** for the leading-p_T HOTVR jet, for the combination of ee and $\mu\mu$ lepton channels (top), and the $e\mu$ channel (bottom).

7.4.1 Definition of control regions

It is useful to define regions with an overall topology and jet flavor composition similar to those of the signal regions. This allows for investigating and assessing how well HOTVR jets are modeled in the simulation compared to data, specifically in regions similar to the signal regions but depleted of the actual signal. As the main origin of high-momentum jets in signal regions is from QCD processes in events with a dilepton signature, the target processes for constructing the control regions are DY processes, which also contain two leptons, and can be accompanied by HOTVR jets from ISR. Moreover, the control regions are used to assess the agreement between the data and simulation, and to validate the background estimation method, which is described in Section 7.5. These regions are signal-depleted, with the expected signal yield being less than 0.5% of the total expected background.

Therefore, the regions can be defined by selecting events enriched in Z+jets events with the following criteria

- double-lepton and single-lepton triggers (as defined in Section 7.2),

- exactly two selected leptons (electron or muon) with the same requirements of the signal regions selections (see Section 7.4),

- dilepton invariant mass in the range $M_{\ell\ell} \in [80, 101]$ GeV,

- at least two HOTVR jets.

These are almost the same requirements as the event selection described in Section 7.3, except for the inverted dilepton invariant mass range requirement and the multiplicity on AK4 jets. No requirements on AK4 jets multiplicity are made to ensure more statistics in these regions. These selections ensure similar topology and kinematics to the signal-region requirements. The orthogonality is obtained by inverting the $M_{\ell\ell}$ requirement. As the selection criteria are designed to have a region enriched in Z+jets events, only the ee and $\mu\mu$ channels are considered. In addition to these baseline criteria, three regions can be defined with the additional requirements of exactly zero (**CR2J0T**), one (**CR2J1T**), and at least two top-tagged (**CR2J2T**) HOTVR jets, respectively.

The percentage of different jet flavors is shown in Figure 7.7 for the different control regions and for the leading-p_{T} HOTVR jets. As shown in the figures, the QCD flavor dominates in all control regions, resulting in a flavor composition closely matching that of the signal regions. The contribution from genuine hadronically decaying top quarks becomes non-negligible (4-5% of the total) in **CR2J2T**, where the hadronic top jets primarily originate from $t\bar{t}Z$ samples.

Figure 7.8 and 7.13 show the distributions in simulation and data of the invariant mass of the HOTVR dijets system (M_{JJ}) in these control regions for $\sqrt{s}$ of 13 and 13.6 TeV and for both dilepton channels of control regions. The same variable is used for the statistical inference in the signal regions presented in Section 7.7. The binning is chosen to match the distribution shown in the signal regions, ensuring that no bins are empty. The data are shown in black markers, while the simulated background is shown in the stacked histograms. The simulated samples reflect the nomenclature defined in 7.4, where the $t\bar{t}H$ and $t\bar{t}V$ categories are grouped together in $t\bar{t}X$, and $t\bar{t}tX$ and $4t$ in $3t + 4t$.
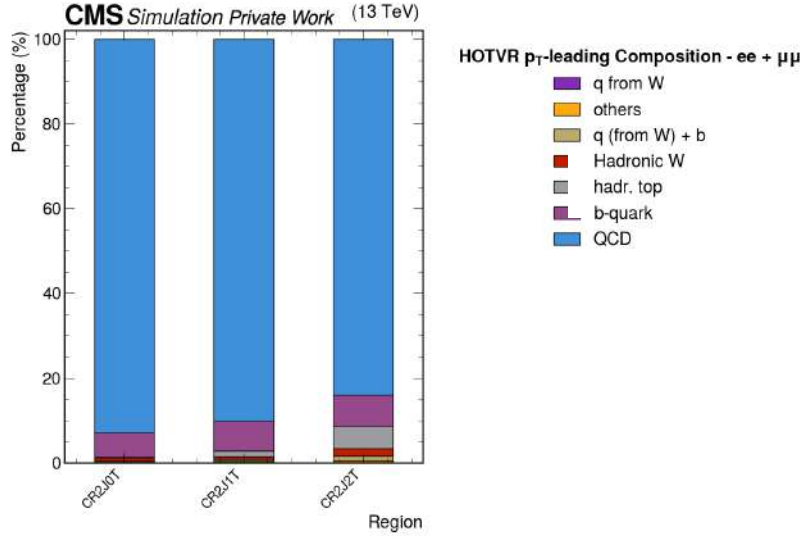
Figure 7.7: Jet flavor composition in **CR2J0T CR2J1T** and **CR2J2T** for the leading-p_T HOTVR jet. The lepton channels (ee and $\mu\mu$) are merged.

The M_{JJ} distribution shows good agreement between data and simulation in both normalization and shape. Across all lepton channels and years, the data-to-simulation ratio is compatible with unity within the associated uncertainties, with deviations observed in a few bins. These deviations appear randomly across channels and years, with no systematic trend or shape trend observed. This behavior suggests that the problem is due to statistical fluctuations rather than modeling. Finally, the variables in these regions are used for validating the background estimation method, described in the following section.
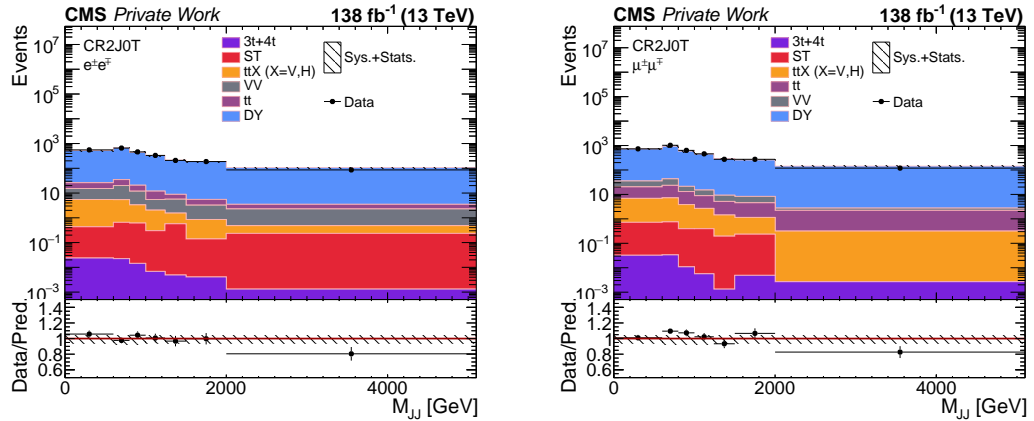
Figure 7.8: Distributions of the M_{JJ} in the ee (left) and $\mu\mu$ (right) channels in **CR2J0T** for $\sqrt{s}$ of 13 TeV with Run 2 data.

136
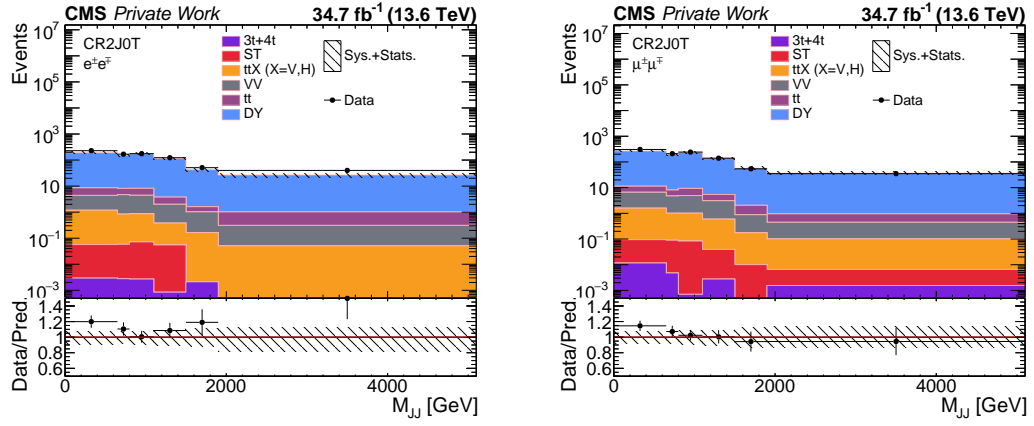
Figure 7.9: Distributions of the M_{JJ} in the ee (left) and $\mu\mu$ (right) channels in **CR2J0T** for $\sqrt{s}$ of 13.6 TeV.
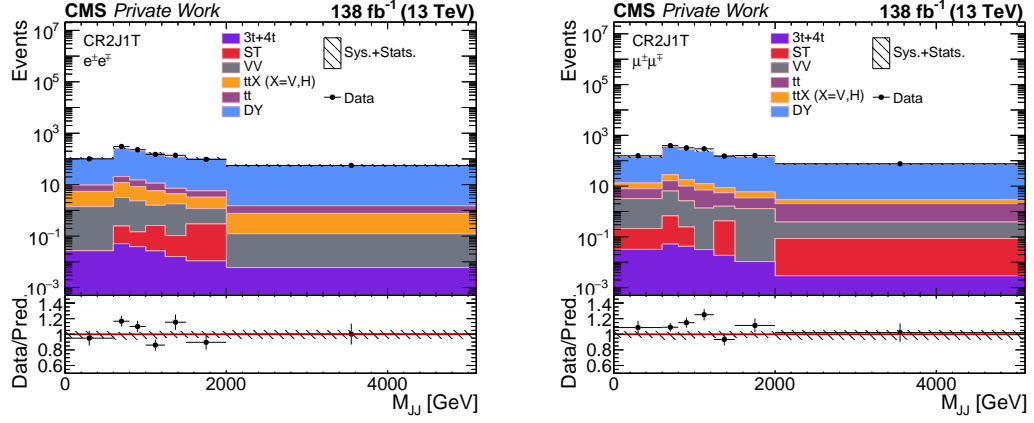
Figure 7.10: Distributions of the M_{JJ} in the ee (left) and $\mu\mu$ (right) channels in **CR2J1T** for $\sqrt{s}$ of 13 TeV.
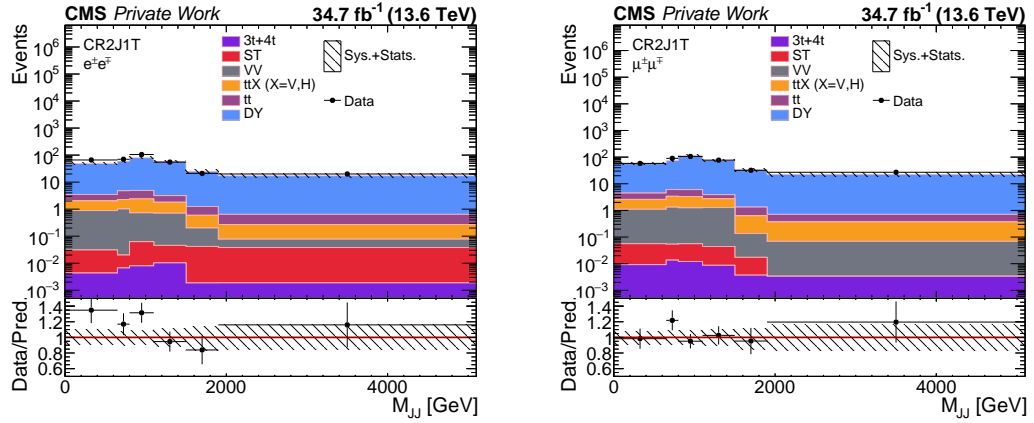
Figure 7.11: Distributions of the M_{JJ} in the ee (left) and $\mu\mu$ (right) channels in **CR2J1T** for $\sqrt{s}$ of 13.6 TeV.
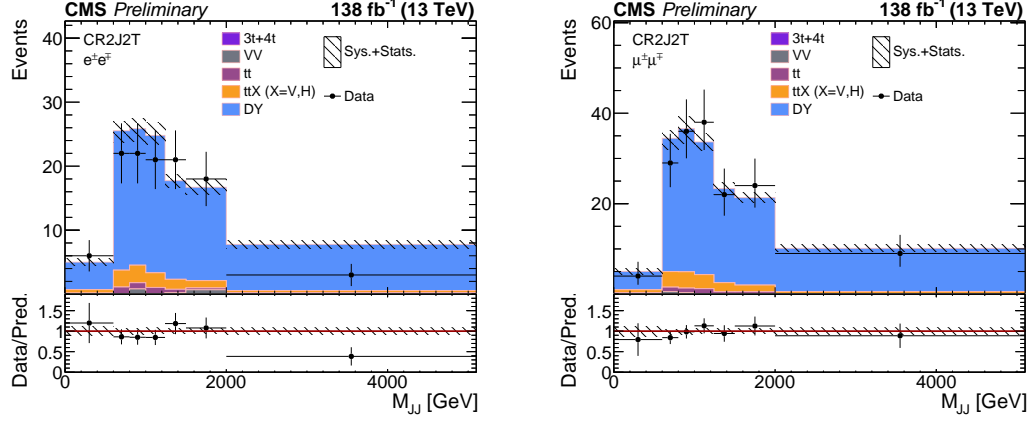
Figure 7.12: Distributions of the M_{JJ} in the ee (left) and $\mu\mu$ (right) channels in **CR2J2T** for $\sqrt{s}$ of 13 TeV.
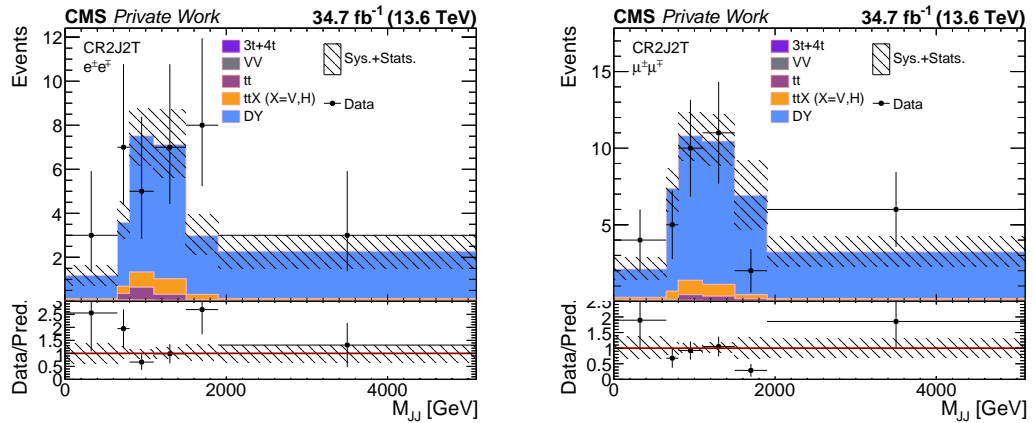
Figure 7.13: Distributions of the M_{JJ} in the ee (left) and $\mu\mu$ (right) channels in **CR2J2T** for $\sqrt{s}$ of 13.6 TeV.

7.5   Background estimation

As detailed in Section 7.4, the main source of background HOTVR jets in the signal regions is QCD, primarily ($> 80\%$) from $t\bar{t}$+jets events where these extra jets are misidentified as top quarks. A data-driven method is therefore developed to estimate the M_{JJ} distribution in regions where these jets are misidentified as top quarks. The infographic in Figure 7.14 summarizes the background estimation method.
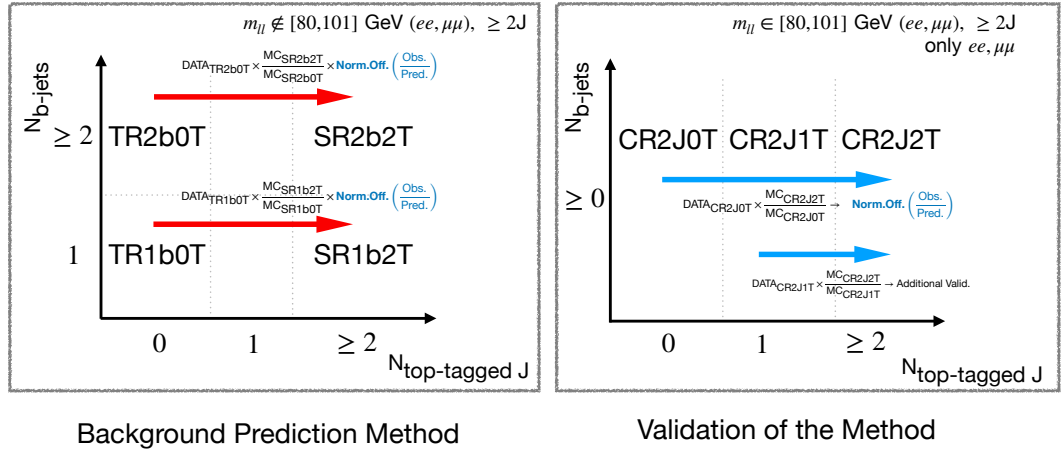
Figure 7.14: Overview of the background estimation method.

The method uses reweighted data events with no top-tagged HOTVR jets. The non-tagged distributions are used to predict the tagged distributions using a reweighting factor, or transfer factor, that is calculated in bins of M_{JJ} using simulated samples as the ratio of events with two top-tagged HOTVR, namely the signal regions, to those with no top-tagged jets. Events with no top-tagged jets requirements define transfer regions (**TRXb2T**, where X denotes the number of b jets), and they are constructed to be orthogonal to signal regions and signal-depleted.

Validation is performed in control regions by predicting the M_{JJ} shape in **CR2J2T** using **CR2J0T** as the transfer region. The predicted shapes reproduce the observed distributions within uncertainties. A residual normalization difference is observed to be 10-15%, depending on the lepton channel and eras, and calculated in the following section. This offset arises from differences between data and simulation in the correlation of the top-tagging probabilities of the two HOTVR jets. The factor k_{CR} is then applied to the signal-region prediction, and its uncertainty is propagated, as detailed in Section 7.5.1. The summary of the regions used for validating and applying the background estimation method is shown in Table 7.6.

The contribution of genuine hadronic top quarks is non-negligible in signal regions, as already shown in Figure 7.6. Therefore, to ensure that the method

Table 7.6: Definition of the regions used in different procedures of the background estimation, along with the selection criteria and details about them. HOTVR jets are labelled as J, top-tagged HOTVR as T, and leptons as ℓ.

Region	Selection Criteria	Description
CR2J2T	$2\ell^\dagger + \geq 2\mathrm{J} + \geq 2\mathrm{T}$	Region where M_{JJ} is estimated in the validation test of the method.
CR2J0T	$2\ell^\dagger + \geq 2\mathrm{J} + 0\mathrm{T}$	Transfer region used in the validation test of the method.
CR2J1T	$2\ell^\dagger + \geq 2\mathrm{J} + 1\mathrm{T}$	Transfer region for an additional cross-check of the method.
SRXb2T	$2\ell^* + \geq Xb + \geq 2\mathrm{J} + \geq 2\mathrm{T}$	Signal regions. The **X** assumes 2 or 1.
TRXb0T	$2\ell^* + \geq Xb + \geq 2\mathrm{J} + 0\mathrm{T}$	Transfer regions used in the method. The **X** can be either 2 or 1.

$\dagger\ ee,\ \mu\mu$ with $m_{\ell\ell} \in [80, 101]$ GeV,
$ee,\ \mu\mu$ ($m_{\ell\ell} \notin [80, 101]$ GeV) and $e\mu$.

predicts only the contribution from misidentified hadronic top quarks, the contamination from genuine hadronic top quarks is evaluated and treated separately. Specifically, the contribution from genuine hadronic top quarks is estimated directly using simulated samples. This contribution is subtracted from the data distribution in the transfer regions and excluded when computing the transfer factor, and added back as a simulated background to the predicted backgrounds in the signal regions.

7.5.1 Validation of the method in control regions

The validation test of the method aims to estimate the M_{JJ} distribution in **CR2J2T** using region **CR2J0T** as the transfer region. The M_{JJ} distribution in both regions is presented in Section 7.4.1, along with the data and simulated samples distributions. The transfer factor is calculated as the ratio of the M_{JJ} distribution in **CR2J2T** over the distribution in **CR2J0T** using simulated samples. The contribution of genuine hadronic top, as visible in Figure 7.7, is estimated from simulation (in $t\bar{t}$ and ttV events) for the transfer and estimation region and subtracted from the data in the transfer region and before computing the transfer factor. The subtraction of genuine hadronic top contributions changes the normalization of the transfer factor by about 10% compared to the case without subtraction.

Figures 7.15-7.16 show the comparison between the observed data M_{JJ} distribution with black markers in **CR2J2T** and the estimated distribution from the method using **CR2J0T** as transfer region with red markers for $\sqrt{s}$ of 13 and 13.6 TeV, in the ee and $\mu\mu$ lepton channels. The genuine hadronic top quark contribution is also displayed. The uncertainties on the estimation include contributions from the Poisson statistical uncertainties of the data in the transfer region **CR2J0T**, as well as the uncertainties on simulated samples used to derive the transfer factor. The full list of uncertainties is detailed in Section 7.6.

The lower panel shows the ratio bin-by-bin of the observed data to the estimation. The estimated distribution correctly models the observed distribution

shape, which validates the estimation method. Additionally, a normalization off-set is observed and treated as follows. The ratio plots are fitted with a constant function (0th-order polynomial), resulting in fitted values of

- 0.87 ± 0.10 for the *ee* channel and 0.94 ± 0.09 for the $\mu\mu$ channel at $\sqrt{s}$ of 13 TeV,

- 0.92 ± 0.23 for the *ee* channel and 0.66 ± 0.15 for the $\mu\mu$ channel at $\sqrt{s}$ of 13.6 TeV;

These *normalization offsets*, which reflect discrepancies in the overall normalization between the observed data and the estimation, are treated as additional scale factors in the signal region estimation. Their uncertainties are propagated and considered as systematic uncertainties in the final results.
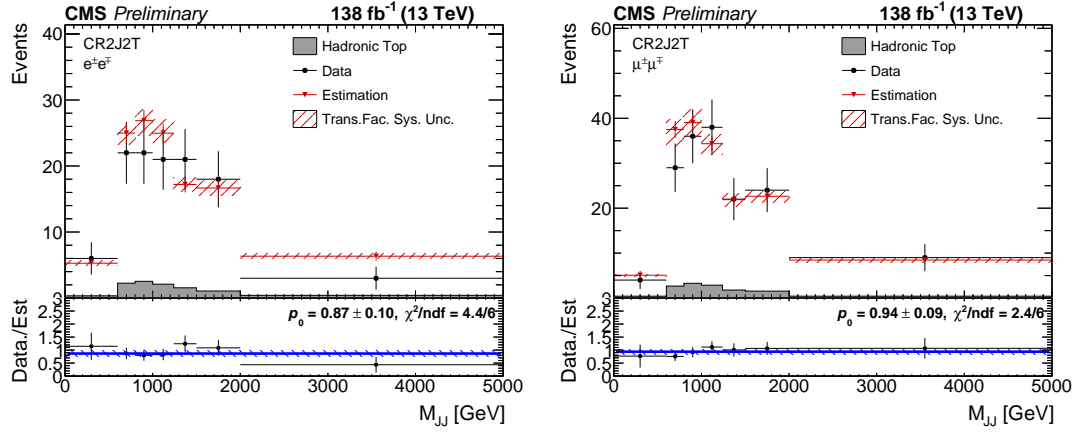
Figure 7.15: The comparison plots between the observation and the estimation in **CR2J2T** using **CR2J0T** as transfer region for the two lepton channels, *ee* (left) and $\mu\mu$ (right), at $\sqrt{s}$ of 13 TeV.
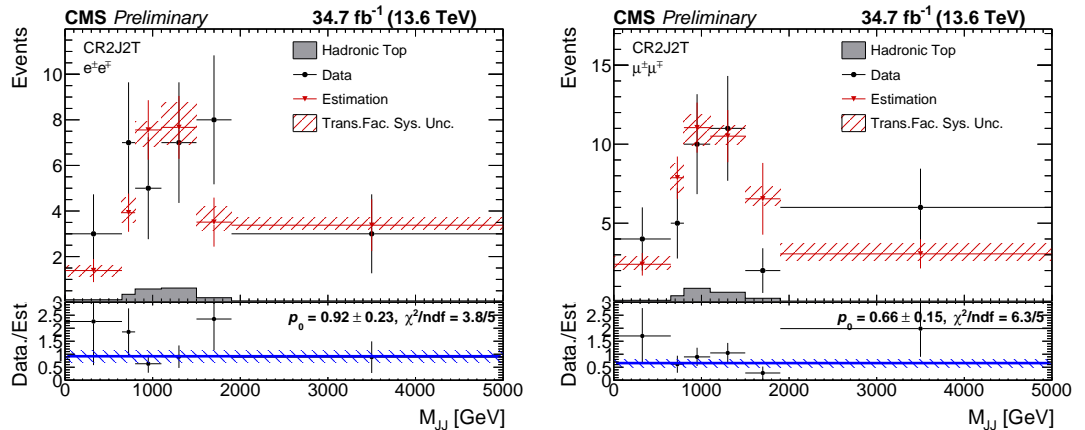
Figure 7.16: The comparison plots between the observation and the estimation in **CR2J2T** using **CR2J0T** as transfer region for the two lepton channels, *ee* (left) and $\mu\mu$ (right), at $\sqrt{s}$ of 13.6 TeV.

7.5.2   Estimation in signal regions

The estimated M_{JJ} distributions in **SR2b2T** and **SR1b2T** are obtained by
reweighting data from the transfer regions, **TR2b0T** and **TR1b0T**, which are
selected by requiring no top-tagged HOTVR jets. The reweighting transfer
factors calculated from a bin-by-bin ratio of the M_{JJ} distributions in **SR2b2T**
and **SR1b2T** to those in **TR2b0T** and **TR1b0T**, separately. The normalization
offsets resulting from the fit obtained in Section 7.5.1 for the validation in control
regions are multiplied as a scale factor to the distributions. For the $e\mu$ channels,
the weighted average of the normalization offset between the ee and $\mu\mu$ channels
is deployed. Additionally, the genuine hadronic contribution in all regions is
evaluated and subtracted from the simulation.

Figures 7.17-7.18 show the estimated distribution for $\sqrt{s}$ of 13 and 13.6 TeV,
for each lepton channel and region separately. These distributions are used as the
expected background contributions in the statistical calculations and the deriva-
tion of cross-section limits for different mass points and signal models, detailed
in Section 7.7. The hadronic top contribution is also shown as a filled histogram.
The templates of three signal samples are also displayed: $m_{Z'}$ of 500 GeV and
$\Gamma/m_{Z'} = 4\%$, $m_{Z'}$ of 3 TeV and $\Gamma/m_{Z'} = 4\%$, 50%.

SR2b2T - $e\mu$ **SR2b2T - ee**   **SR2b2T - $\mu\mu$**

SR1b2T - $e\mu$ **SR1b2T - ee**   **SR1b2T - $\mu\mu$**
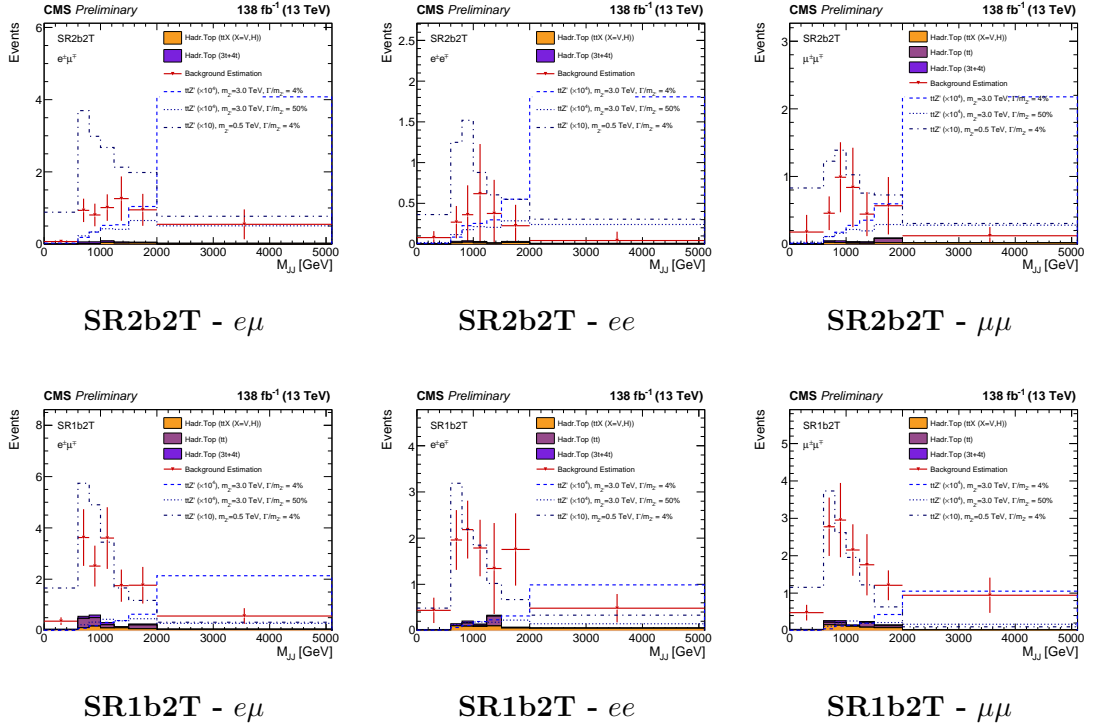
Figure 7.17: The estimated M_{JJ} distributions in signal regions for $\sqrt{s}$ of 13 TeV data
campaigns, using $t\bar{t}Z'(Z' \to t\bar{t})$ signal model of masses = 500, 3000 GeV.
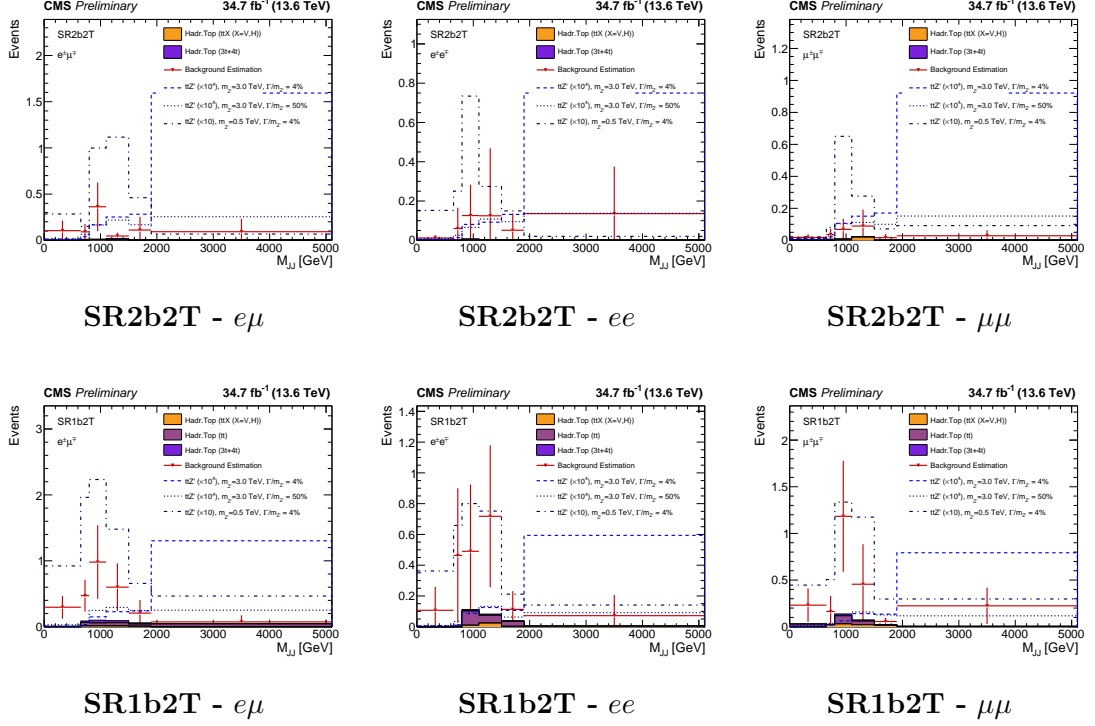
Figure 7.18: The estimated M_{JJ} distributions in signal regions for $\sqrt{s}$ of 13.6 TeV data campaigns, using $t\bar{t}Z'(Z' \to t\bar{t}$) signal model of masses = 500, 3000 GeV.

7.6 Systematic uncertainties

Several systematic uncertainties are considered in the analysis, affecting both the shape and normalization of the templates used to calculate the cross-section limit and the statistical interpretation. These uncertainties are incorporated into the analysis through nuisance parameters that change the expected event yields and are independent across all M_{JJ} bins in signal regions and data-taking periods, where applicable. The table 7.7 summarizes all the sources of systematic errors and the correlations between years of data-taking. The uncertainties are grouped into three categories: background estimation, experimental, and theoretical uncertainties.

7.6.1 Background estimation uncertainties

The uncertainties related to the data-driven background estimation are listed as follows

- the statistical uncertainties of data in transfer regions,

- the statistical uncertainties of the simulated samples propagated into the transfer factor,

- the theory and experimental uncertainties affecting the simulated samples in the transfer factor,

- the normalization offset derived from the validation of the method in control regions,

Table 7.7: Systematic uncertainties grouped by category. Type: rate (R) or rate
and shape (S). Corr.: correlated between years of the same era, Part. corr.: partially
correlated between years of the same era, Uncorr.: uncorrelated between years of the
same era.

Source	Type	Correlation	Samples
Background estimation uncertainties			
Norm. offset (**CR2J0T→CR2J2T**)	R	Uncorr.	Bkg. est.
Jet flavor composition difference	R	Corr.	Bkg. est.
Experimental uncertainties			
Pileup	S	Corr.	Simulation
b-tagging	S	Part. corr.	Simulation
Lepton ID, isolation, trigger	S	Corr.	Simulation
Jet energy scale/resolution	S	Uncorr.	Simulation
Top tagger (BDT)	S	Uncorr.	Simulation
Trigger Prefiring	S	Uncorr.	Simulation
Luminosity	R	Corr.	Simulation
Simulation stat. uncertainty	S	Uncorr.	Simulation
Theoretical uncertainties			
QCD Scale ($\mu_{\mathrm{R}}/\mu_{\mathrm{F}}$)	S	Corr.	Simulation
PDF shape	S	Corr.	Simulation
PS scale ISR*/FSR†	S*, R†	Corr.	Simulation

- the jet flavors composition difference.

As detailed in section 7.5, the statistical uncertainties from the transfer regions, as well as the statistical uncertainties of the simulated samples, are propagated to the final template. Both are treated as uncorrelated between lepton channels, signal regions, and M_{JJ} distribution bins. The theory and experimental uncertainties from the transfer factor calculation are considered as shape uncertainties, and they are considered correlated between lepton channels and signal regions.

The uncertainties from the normalization offset are computed and provided in section 7.5.1 for $\sqrt{s}$ of 13 and 13.6 TeV. As they are computed per lepton channel, they are treated as uncorrelated across lepton channels and correlated across signal regions. The normalization offset for the $e\mu$ channel is treated as correlated across ee and $\mu\mu$, as it is calculated as the weighted average of them.

To account for potential differences in the background estimation arising from differences in jet flavor composition across signal regions and lepton categories, a dedicated study has been performed and illustrated briefly as follows. As shown in Figure 7.6, HOTVR jets in the signal regions mainly originate from either b quarks or QCD. Since the transfer factor may depend on the jet flavor, the background estimation is re-evaluated specifically for the b quark-flavored jets and compared to the inclusive estimation. The relative difference in normalization (40-60%, depending on the regions and lepton categories), calculated as the ratio between the b quark-specific and inclusive estimations, is interpreted as a

normalization systematic uncertainty.

7.6.2 Experimental uncertainties

The experimental uncertainties are treated as follows

Pileup: the uncertainty on the modeling of the PU profile in simulation is calculated by varying the inelastic p–p cross-section by $\pm 4.6\%$ from its nominal value.

b-tagging: Differences in the b-tagging efficiency between data and simulation are accounted for by data-to-simulation scale factors. The uncertainties are split into efficiencies for b, c, and light jets [175].

Lepton ID, isolation, trigger: uncertainties in the lepton reconstruction, identification, and trigger efficiencies are accounted for by varying p_{T} and η-dependent normalisation factors, derived from data-to-simulation ratios, within their uncertainties.

Jet energy scale/resolution: the jet energy scale (JES) and jet energy resolution (JER) corrections are varied within their uncertainties to determine their effect on the shapes of the final distributions, as described in Section 5.5. The JEC and JER are varied simultaneously for AK4 and HOTVR jets, therefore the uncertainties on the two different jet types are considered totally correlated.

Top tagger (BDT): as presented in section 6.3, the uncertainties on the top-tagging scale factor are applied only on genuine hadronic top jets.

Trigger prefiring: the term refers to L1 timing miscalibration that causes energy deposits in the preceding bunch crossing to satisfy the trigger. This leads to a self-veto of the true event of interest. It affects mostly the ECAL region, and it is modeled in simulation with an event weight that reduces the expected yield to account for data losses. The associated uncertainty is taken from data to simulation studies of the prefiring rate and propagated as a correlated normalization across the signal regions.

Luminosity: this uncertainty is rate-only and affects all simulation-based processes. The overall uncertainty for Run 2 is 1.6% [176], while for 2022 data it is 1.4% [177], as determined from luminometer calibrations and van der Meer scans. A more detailed treatment of the luminosity correlations and era-dependent effects is available within CMS, but it has a negligible impact given that the analysis is statistically dominated.

7.6.3 Theoretical uncertainties

Theoretical uncertainties refer to uncertainties arising from the modelling of the physics processes in simulation, such as scale variations, parton shower modelling, and parton distribution functions. They are treated as follows:

μ_R/μ_F scales: the renormalization and the factorization scale defined in Section 1.2 are useful to correct high-order effects in perturbation theory. The associated uncertainties are calculated by varying these scales up and down by a factor of two, both independently and simultaneously, providing an estimate of the size of missing higher-order corrections. The bin-by-bin maximum (minimum) difference with respect to the nominal value is taken as up (down) variation and propagated to the final templates. This systematic uncertainty is treated as fully correlated across the years. These scale weights are normalized with respect to the sum of the weights in the full phase space for each process. The normalization ensures that the variations reflect only shape differences in the final distributions, leaving the overall normalization, i.e., the cross-section, unchanged. The inclusive uncertainty on the cross-section of the processes is instead accounted for separately as a rate parameter.

PDF shape: the uncertainty from the choice of PDFs is estimated by calculating the signal and background estimations in each bin of the final distribution using sets of varied PDF replicas, i.e. NNPDF3.1 NNLO PDF set, described in Section 1.1.1.

PS scale ISR/FSR: the scales (ISR, FSR) in the parton shower simulation are varied by factors of 0.5 and 2 independently to assess the impact of the choice of α_S. Both uncertainties are treated as correlated across the years. The ISR variations are propagated to the final distributions. For the FSR variations, due to limited MC statistics, the variations result in unstable, effectively one-sided shifts in certain bins. Smoothing was attempted for other uncertainties, but no reliable shape information could be recovered. Therefore, the FSR variations are treated as normalization uncertainties, using the larger of the differences between the integrals of the upwards and downwards variations compared to the nominal.

Uncertainties resulting from the finite size of the simulated samples are accounted for using the Barlow–Beeston method [178]. The total uncertainty is found to be dominated by the statistical uncertainties on data in the signal regions. The largest systematic uncertainties can be attributed to the background estimation, with the main sources being the statistical uncertainty of the data in the transfer regions and the uncertainty accounting for differences in the jet flavour composition.

7.7 Statistical interpretation

The estimated background and expected signal M_{JJ} distributions in signal regions and lepton channels are used as the basis for the statistical interpretation. Figures 7.17-7.18 show the estimated background and an example of the expected signal distributions of Z' model of $m_{Z'}$ of 500 GeV and 3 TeV, for different signal regions and lepton channels at $\sqrt{s}$ of 13 and 13.6 TeV. To determine the final background estimation and constrain the uncertainties, a simultaneous binned maximum likelihood template fit of the M_{JJ} distributions in all signal regions is performed. The fit is carried out on an *Asimov* dataset, a representative

dataset constructed from the expected event yields under the background-only
(or signal-plus-background) hypothesis, where the observed data are set equal to
the expected values from background estimation.

Systematic uncertainties described in Section 7.6 are incorporated as nuisance
parameters in the fit. Normalization (or *Rate*) uncertainties are treated with log-
normal priors, while shape uncertainties in the distributions are modeled with
Gaussian priors [179]. Statistical uncertainties in each bin are handled using a
simplified Barlow-Beeston method [178], introducing one nuisance parameter per
bin with a Gaussian prior to account for the statistical uncertainty of the bin. If
the bin has fewer than 10 counts, a Poissonian prior is used.

To evaluate the expected sensitivity to the signal hypothesis, a simultaneous
fit of the signal-plus-background model is performed, treating the signal strength
parameter r as an unconstrained parameter. The expected exclusion limits on the
signal strength are then derived using an Asimov dataset and computed under the
background-only hypothesis, using the asymptotic likelihood ratio test statistic
within the CLs method as implemented in the Combine framework [180]. The
CL_s method is a modified frequentist approach widely adopted in particle physics
searches. It is based on the profile likelihood ratio,

$$q_r = -2\ln\left(\frac{\mathcal{L}(r,\hat{\theta}_r)}{\mathcal{L}(\hat{r},\hat{\theta})}\right),$$ (7.2)

where r is the signal strength under test and θ denotes the nuisance parameters
describing systematic uncertainties. The denominator contains the maximum
likelihood estimate, while the numerator sets the signal strength to the value
under test and maximizes with respect to the nuisance parameters.

From the distributions of q_r under the background-only and signal-plus-background
hypotheses, the corresponding p-values, p_b and p_{s+b}, are defined as the probabil-
ities of obtaining a value of q_r at least as large as the observed one under each
hypothesis. The modified confidence level is then defined as

$$CL_s = \frac{p_{s+b}}{1 - p_b},$$ (7.3)

and a signal strength r is excluded at 95% confidence level if $CL_s < 0.05$.

Upper limits on the Z' resonance signal strength decaying to a pair of top
quarks are calculated at 95% confidence level using the asymptotic approximation
of the profile likelihood test statistic [181]. In this approach, the distribution of
the test statistic under the signal and background hypotheses is approximated
using asymptotic formulae derived from Wilks theorem [182] [2].

The expected upper limits are presented in Figure 7.19 as a function of res-
onance masses for various widths. Since two different collision energies are com-
bined, the limits are first calculated relative to the theoretical cross sections at the
respective energies, then scaled to the production cross-sections times branching
fraction at 13 TeV to allow easier comparison with results at a single energy.

The theory curve in blue corresponds to the LO predicted production cross-
section times branching ratio at $\sqrt{s} = 13$ TeV. For each width scenario, the
couplings are chosen such that the branching ratio to $t\bar{t}$ is close to 100%. In
accordance with Equation 1.40, both the Z' production cross-section and the

---

[2]Although these approximations may fail in the small-sample limit, the results have also
been cross-checked with pseudo-experiments (*toys*), yielding consistent results.

width $\Gamma(Z' \to t\bar{t})$ scale with c_t^2. Consequently, the theoretical predictions for widths of 10%, 20%, and 50% are obtained by rescaling the 4% reference by factors of 10/4, 20/4, and 50/4, respectively.

The experimental limits are obtained from the upper limits on the signal strength r by multiplying the excluded values of r by the predicted cross-section. The dashed line shows the median expected limit under the background-only hypothesis. The green and yellow bands around the median correspond to the 1σ (68%) and 2σ (95%) uncertainty intervals, which quantify the ranges of statistical fluctuations expected in the absence of a signal.

The expected limits are found to be consistently above the theoretical prediction for $\Gamma(Z' \to t\bar{t})$ of 4%, indicating that the benchmark Z' model cannot be excluded in the tested mass range with the current collected data. The results for $\Gamma(Z' \to t\bar{t})$ of 4% are compared with the search in the single lepton plus jets final state by CMS (blue) and ATLAS (red) [155], yielding comparable results which can increase the sensitivity of the search if combined. For broader resonance, mass exclusion limits on the Z' mass are set by comparing the upper cross-section limit with the theoretical cross-section. The expected mass exclusion limits are found to be 500 GeV for a 10% width resonance, 820 GeV for a 20% width, and up to 1000 GeV for a 50% width.
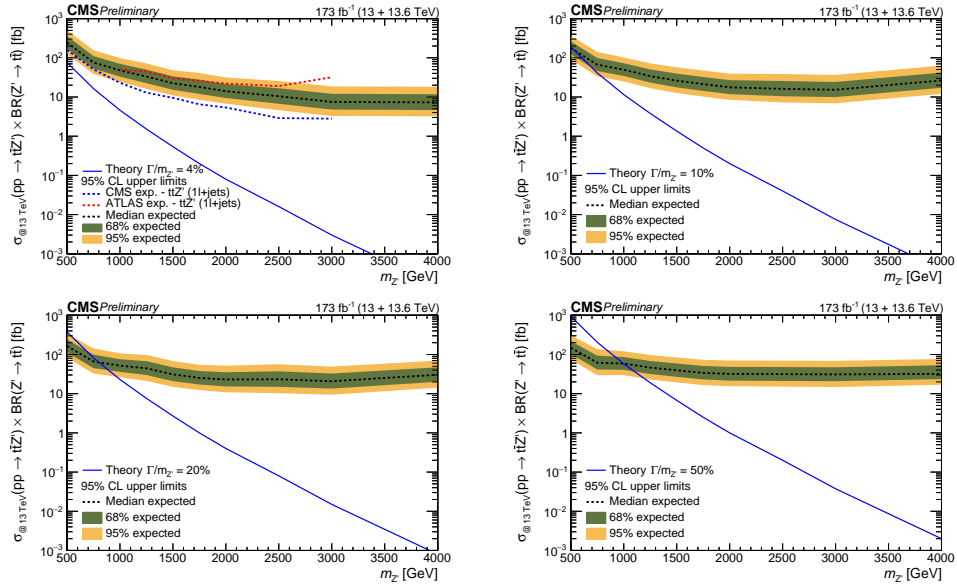
Figure 7.19: Expected upper limits at 95% CL on the $t\bar{t}Z'$ production cross-section times branching fraction at 13 TeV as a function of $m_{Z'}$ for various relative decay widths $\Gamma/m_{Z'}$ as indicated in the legends.

Figure 7.20 displays the impact plots of the nuisance parameters on the fitted signal strength parameter, obtained from the signal-plus-background fit using the Asimov dataset. The figure shows the results for a Z' mass point of 500 GeV, for which the expected signal strength is 2.5. The left panel shows the pulls of the nuisance parameters, θ, defined as the differences between their post-fit and pre-fit values normalized by the pre-fit uncertainty. Since the fit is performed on an Asimov dataset, which corresponds exactly to the model expectation without statistical fluctuations, the fitted nuisance parameters are expected to remain close to their nominal values, resulting in pulls centered at zero with unit width.

The right panel illustrates the change in the fitted signal strength r when each
nuisance parameter is varied by $\pm 1\sigma$ of its post-fit uncertainty: the red (left) bars
correspond to an upward variation, while the blue (right) bars correspond to a
downward variation.

As detailed in Section 7.6, the dominant uncertainty originates from the lim-
ited statistics in the signal regions. Figure 7.20 shows that the systematic sources
with the largest impacts on r arise from the modeling of FSR, the QCD scale vari-
ations (μ_F and μ_R), and the background estimation, in particular the jet flavor
differences between QCD- and b-initiated jets.
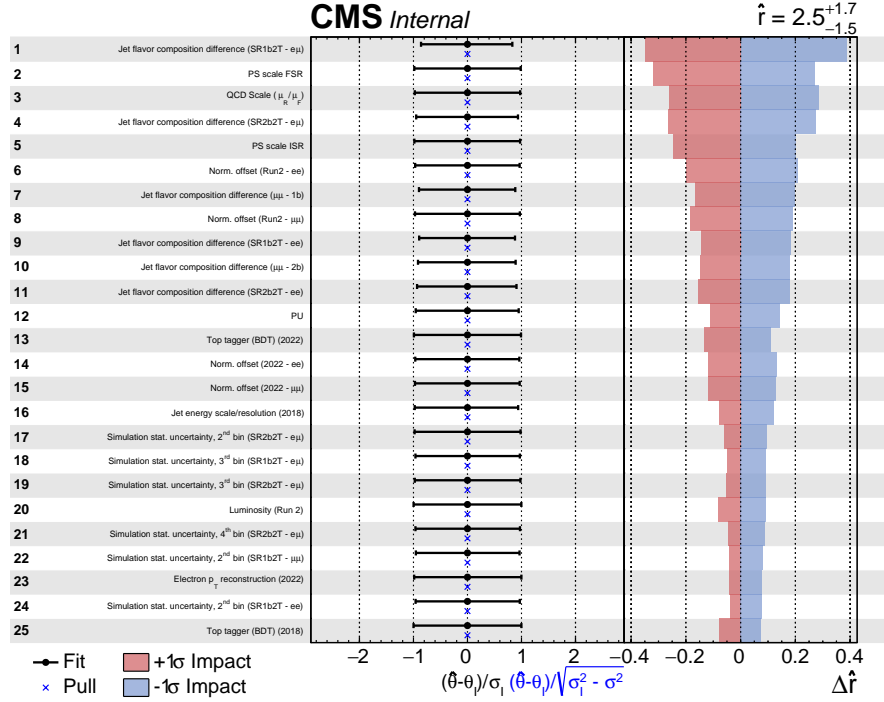
Figure 7.20: Pulls and impacts using $t\bar{t}Z'$ signal mass equal to 500 GeV and using an
Asimov dataset.

Interpretation with 2HDM and ALPS models

The results of the analysis are also interpreted in the context of the production
of a pseudoscalar a and scalar ϕ resonance, described in Section 1.3.2, by fitting
the signal plus background hypothesis. Therefore, upper limits on the a and ϕ
resonances signal strength decaying to a pair of top quarks at 95% confidence
level (CL) are shown in Figures 7.21 and 7.22, respectively. Limits on the cross-
section production of a or ϕ produced in association with $t\bar{t}$ for masses of 500
GeV and resonance width of 50% are set. These represent the first results for the
search for these signal models in this final state.
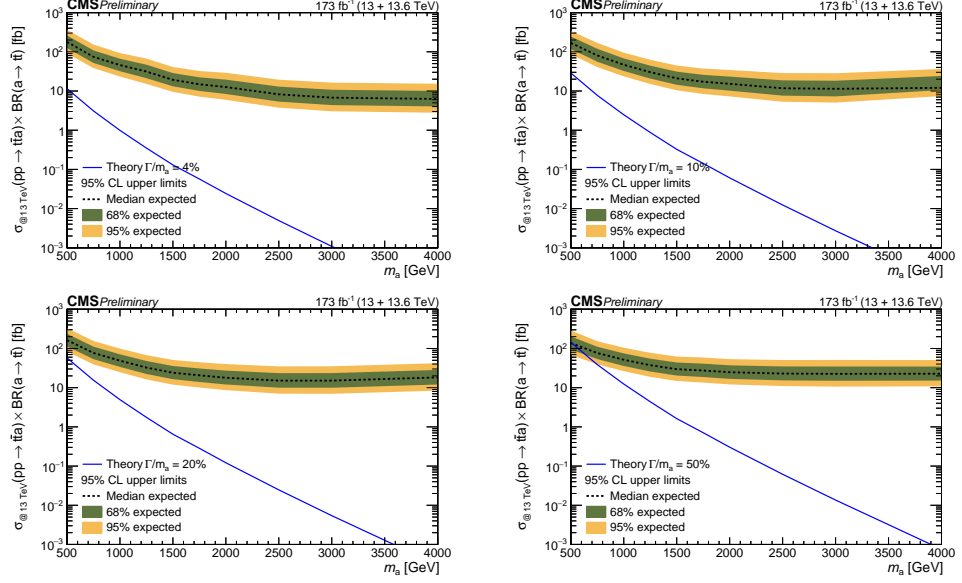
Figure 7.21: Expected upper limits at 95% CL on the $t\bar{t}a$ production cross-section
times branching fraction at 13 TeV as a function of m_a for various relative decay widths
Γ/m_a as indicated in the legends.
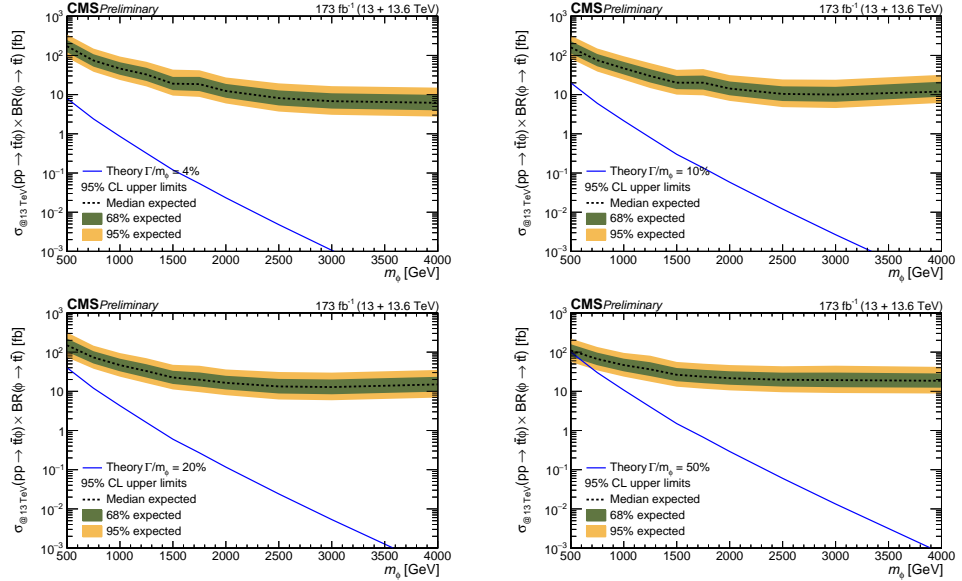
Figure 7.22: Expected upper limits at 95% CL on the $t\bar{t}\phi$ production cross-section
times branching fraction at 13 TeV as a function of m_a for various relative decay widths
Γ/m_ϕ as indicated in the legends.

7.8   Discussion and outlook

This analysis constitutes the first BSM search in this channel and the first to
incorporate data at $\sqrt{s}$ of 13.6 TeV in this signature. Moreover, it is the first
analysis to use HOTVR jets in combination with the BDT-based tagger presented
in Chapter 6 to reconstruct the resonant top quark system.

Using the heavy top-philic vector Z' resonance as a benchmark model, exclu-
sion $m_{Z'}$ mass limits are found to be 500 GeV for a 10% width resonance, 820

GeV for a 20%, and up to 1000 GeV for a 50% width. Further interpretations
are provided in the context of extended Higgs sectors and models with axion-like
particles, with the obtained upper limits representing the first results from the
CMS Collaboration for this signature. Exclusion mass limits on the cross-section
production of a or ϕ produced in association with $t\bar{t}$ for masses of 500 GeV and
resonance width of 50% are set.

Given the high-energy phase space of the search and the low number of events
after the event selection, the analysis is largely limited by the statistical uncer-
tainty in the signal regions. Furthermore, the cross-section of the four-top-quark
signature increases more rapidly than that of the dominant $t\bar{t}$ background with
increasing $\sqrt{s}$, due to the behavior of the parton distribution functions. The
analysis is therefore expected to benefit substantially from the additional data
collected during the final years of Run 3 (2023–2025) and from the HL-LHC
phase. Moreover, additional gains in sensitivity can be obtained from studying
the fully hadronic final state, which has the larger branching ratio.

Run 3 and HL-LHC projection

The expected results of Section 7.7 can be projected to a total integrated lumi-
nosity of about 360 fb^{-1}, corresponding to the combined dataset from Run 2 and
the full Run 3. Assuming identical detector performance and scaling the 2022
data campaign templates to the full Run 3 integrated luminosity, the projected
exclusion limits on the $t\bar{t}Z'$ production signal strength are shown in Figure 7.23.
The expected mass reach extends up to 700 GeV for a resonance with a 10%
width, 1000 GeV for a 20% width, and up to 1200 GeV for a 50% width, corre-
sponding to an improvement in signal strength of roughly a factor of 1.2–1.9, i.e.
a 20–40% reduction in the expected limits across the explored mass range.
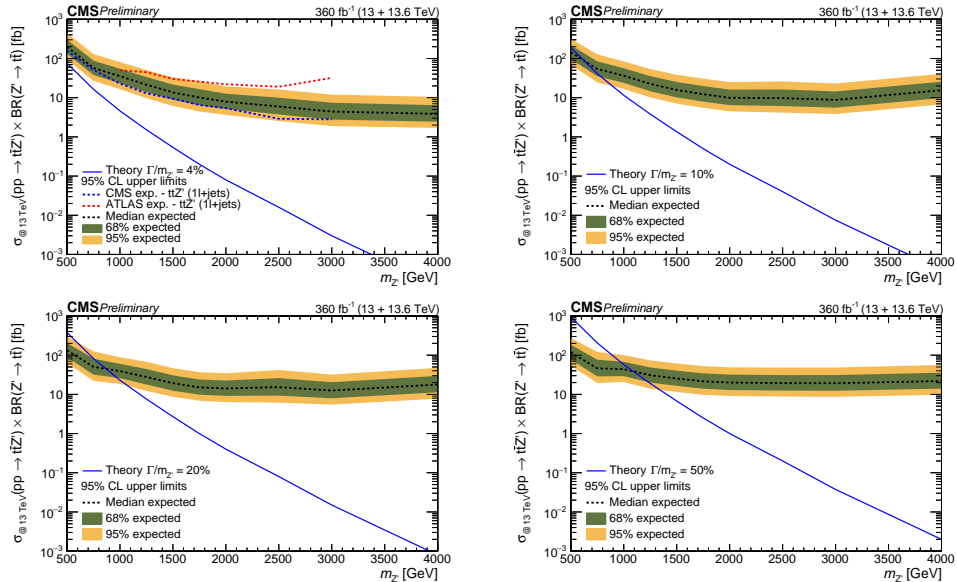
Figure 7.23: Expected upper limits at 95% CL after scaling to the full Run 3 lu-
minosity on the $t\bar{t}Z'$ production cross-section times branching fraction at 13 TeV as a
function of $m_{Z'}$ for various relative decay widths $\Gamma/m_{Z'}$ as indicated in the legends.

For the HL-LHC phase, the envisaged integrated luminosity is approximately
3000 fb^{-1} at $\sqrt{s} = 14$ TeV, yielding over an order of magnitude more data than

the full Run 2 and 3 combined. A rough projection of the $t\bar{t}Z'$ search sensitivity can be obtained by scaling the expected upper limit to 3000 fb^{-1}. When scaled, the expected upper limits on the signal strength improve by roughly a factor of 3–5 across the explored mass range, resulting in 65-80% reduction in the expected limit values[3]. This corresponds to expected upper mass limits of approximately 500 GeV, 900 GeV, 1100 GeV, and up to 1300 GeV for resonance widths of 4%, 10%, 20%, and 50%, respectively. This estimate assumes that detector performance and analysis techniques remain unchanged. In practice, the search is expected to benefit even further from the higher collision energy and upgraded detector technologies at the HL-LHC, such as the HGCAL, which will play a central role in heavy-flavor object reconstruction, as well as from improved top quark tagging techniques.

---

[3]Scaling from 170 fb^{-1} to 3 ab^{-1} (a factor 20 in luminosity) gives an expected sensitivity gain of $\sqrt{20} \approx 4.5$.

Chapter 8

Conclusions

The thesis work covers a diverse range of topics, from detector development to a search for new physics, where a new hadronic top quark tagger based on variable-radius jets and a BDT model is employed.

Part of the thesis work related to the detector development focused on the system validation of the scintillator section of the CMS HGCAL upgrade, which is based on SiPM-on-tile technology. The system consists of *tilemodules*, each comprising up to 94 scintillator tiles wrapped in reflective foil and coupled to SiPMs, together with onboard and readout electronics, namely the HGCROC chips. The primary objectives of the system validation were to assess the performance of the tilemodules and to measure key properties such as the SiPM gain and light yield. These measurements were conducted at the DESY-II test beam facility using a 3 GeV electron beam to determine the most probable charge deposition. Results from different SiPM-on-tile and tilemodules confirmed that the components met the required performance specifications. These results, together with additional validation studies not included in this thesis work, established the quality and reliability of both the individual and assembled components of the tilemodules, providing the groundwork for the production phase of the detector, which began in 2024. The final assembly of the detector will follow these and additional quality control tests with the components of the production phase, with the installation in the CMS cavern scheduled for 2027.

The part of the thesis devoted to the physics search presents the development of a new hadronic top quark tagger, based on the variable-radius jet clustering algorithm HOTVR and a BDT-based tagger. This method is employed for the first time in a physics analysis at the LHC. The variable-radius feature of HOTVR enables efficient identification of jets from boosted hadronic top quark decays over a wide range of momenta. The BDT model is trained to distinguish top quark-initiated jets from those originating from QCD processes, using samples from several data-taking years. Its performance is evaluated in terms of tagging efficiency and mass reconstruction resolution. The validation of the BDT in data is performed in both top-enriched and QCD-enriched event regions at $\sqrt{s}$ of 13 and 13.6 TeV, confirming the accurate modeling of these jet classes in simulation.

The HOTVR combined with the BDT-based hadronic top tagger is used in the search for a top-philic heavy resonance produced in association with a $t\bar{t}$ pair, as presented in this thesis. The analysis relies on p–p collision data recorded by the CMS detector at $\sqrt{s}$ of 13 and 13.6 TeV, corresponding to a total integrated luminosity of 173 fb^{-1}. The study focuses on the opposite-sign dilepton final

state, which targets the leptonic decays of the non-resonant top quarks, while the top quarks originating from the resonance are identified using the HOTVR plus BDT-based hadronic top tagger. A benchmark signal model of the production of a heavy vector top-philic resonance Z' in association with $t\bar{t}$, $t\bar{t}Z'(Z' \to t\bar{t})$, is employed with simulation, for $m_{Z'}$ ranging 500 GeV to 4 TeV, with 5%, 10%, 20%, and 50% resonance decay width. Additionally, signal models including a new neutral pseudoscalar, a, and a scalar, ϕ, are also tested. The background arises mainly from QCD multijets misidentified as top quark jets in $t\bar{t}$ dilepton events, and it is estimated with a data-driven background method. Expected exclusion limits are set on the Z' benchmark models, excluding the vector-like scenarios of 500 GeV for a 10% width resonance, 820 GeV for a 20% width, and up to 1000 GeV for a 50% width. Expected mass limit of 500 GeV is set for the $t\bar{t}a$ and $t\bar{t}\phi$ cross-section production for 50% width resonances. These results represent the first search in this final state and the first top-philic resonance search in the four-top final state using Run 3 data. The analysis is currently under final review by the CMS Collaboration and is planned to be statistically combined with the single-lepton plus jets analysis channel. Including the remaining Run 3 data will further improve the expected signal strength by up to a factor 2, with an extrapolation to the expected integrated luminosity at the end of the HL-LHC phase yielding the expected signal strength by up to a factor 5.

Bibliography

[1]   Gabriele Milella. "An overview of the CMS High Granularity Calorimeter". In: *Proceedings of The European Physical Society Conference on High Energy Physics — PoS(EPS-HEP2023)*. Vol. 449. 2023, p. 523. DOI: `10.22323/1.449.0523`.

[2]   "Hadronic top quark tagging with variable-sized jets for the CMS experiment". In: (2024). URL: `https://cds.cern.ch/record/2902861`.

[3]   G. Aad et al. (ATLAS Collaboration). "Observation of a New Particle in the Search for the Standard Model Higgs Boson with the ATLAS Detector at the LHC". In: *Physics Letters B* 716 (2012), pp. 1–29. DOI: `10.1016/j.physletb.2012.08.020`.

[4]   S. Chatrchyan et al. (CMS Collaboration). "Observation of a New Boson at a Mass of 125 GeV with the CMS Experiment at the LHC". In: *Physics Letters B* 716 (2012), pp. 30–61. DOI: `10.1016/j.physletb.2012.08.021`.

[5]   Gordon Kane. *Modern Elementary Particle Physics: Explaining and Extending the Standard Model*. 2nd Revised. Includes recent Higgs boson and top quark discoveries. Cambridge University Press, 2017. ISBN: 978-1-107-16508-3.

[6]   R.L. Workman et al. (Particle Data Group). "Review of Particle Physics". In: *Prog. Theor. Exp. Phys.* 2024.8 (2024), p. 083C01. DOI: `10.1093/ptep/ptae083`.

[7]   Michael E. Peskin and Daniel V. Schroeder. *An Introduction to Quantum Field Theory*. See Chapter 20: Spontaneous Symmetry Breaking and the Higgs Mechanism. Westview Press, 1995. ISBN: 978-0-201-50397-5.

[8]   Otto Nachtmann. *Elementary Particle Physics: Concepts and Phenomena*. Vol. Volume 7. Theoretical and Mathematical Physics. English translation of German lectures held at Universität Heidelberg. Springer-Verlag Berlin Heidelberg, 1990. ISBN: 978-3-540-51647-7. DOI: `10.1007/978-3-642-61281-7`.

[9]   *The Standard Model*. `https://tikz.net/sm_particles/`.

[10]   Christian Wüthrich and Nick Huggett. "Quantum Gravity". In: *The Stanford Encyclopedia of Philosophy*. Ed. by Edward N. Zalta. Spring 2020. Metaphysics Research Lab, Stanford University. URL: `https://plato.stanford.edu/archives/spr2020/entries/quantum-gravity/`.

[11]   Assaf Shomer. *A pedagogical explanation for the non-renormalizability of gravity*. arXiv:0709.3555 [hep-th]. 2007. arXiv: `0709.3555 [hep-th]`. URL: `https://arxiv.org/abs/0709.3555`.

[12]   Peter W. Higgs. "Broken Symmetries and the Masses of Gauge Bosons". In: *Physical Review Letters* 13 (1964), pp. 508–509. DOI: `10.1103/PhysRevLett.13.508`.

[13]   J. J. Thomson. "Cathode Rays". In: *The London, Edinburgh, and Dublin Philosophical Magazine and Journal of Science* 44 (1897), pp. 293–316. DOI: `10.1080/14786449708621070`.

[14]   C. D. Anderson and S. H. Neddermeyer. "Note on the Nature of Cosmic-Ray Particles". In: *Physical Review* 50 (1936), pp. 263–265. DOI: `10.1103/PhysRev.50.263`.

[15]   C. L. Cowan et al. "Detection of the Free Neutrino: A Confirmation". In: *Science* 124 (1956), pp. 103–104. DOI: `10.1126/science.124.3212.103`.

[16]   G. Danby et al. "Observation of High-Energy Neutrino Reactions and the Existence of Two Kinds of Neutrinos". In: *Physical Review Letters* 9 (1962), pp. 36–44. DOI: `10.1103/PhysRevLett.9.36`.

[17]   M. L. Perl et al. "Evidence for Anomalous Lepton Production in e^+-e^- Annihilation". In: *Physical Review Letters* 35 (1975), pp. 1489–1492. DOI: `10.1103/PhysRevLett.35.1489`.

[18]   K. Kodama et al. (DONuT Collaboration). "Observation of Tau Neutrino Interactions". In: *Physics Letters B* 504 (2001), pp. 218–224. DOI: `10.1016/S0370-2693(01)00307-0`.

[19]   M. Gell-Mann. "A Schematic Model of Baryons and Mesons". In: *Physics Letters* 8 (1964), pp. 214–215. DOI: `10.1016/S0031-9163(64)92001-3`.

[20]   E. D. Bloom et al. "High-Energy Inelastic e–p Scattering at $6°$ and $10°$". In: *Physical Review Letters* 23 (1969), pp. 930–934. DOI: `10.1103/PhysRevLett.23.930`.

[21]   J. J. Aubert et al. "Experimental Observation of a Heavy Particle J". In: *Physical Review Letters* 33 (1974), pp. 1404–1406. DOI: `10.1103/PhysRevLett.33.1404`.

[22]   J.-E. Augustin et al. "Discovery of a Narrow Resonance in e^+e^- Annihilation". In: *Physical Review Letters* 33 (1974), pp. 1406–1408. DOI: `10.1103/PhysRevLett.33.1406`.

[23]   S. W. Herb et al. "Observation of a Dimuon Resonance at 9.5 GeV in 400-GeV Proton-Nucleus Collisions". In: *Physical Review Letters* 39 (1977), pp. 252–255. DOI: `10.1103/PhysRevLett.39.252`.

[24]   F. Abe et al. (CDF Collaboration). "Observation of Top Quark Production in $\bar{p}p$ Collisions". In: *Physical Review Letters* 74 (1995), pp. 2626–2631. DOI: `10.1103/PhysRevLett.74.2626`.

[25]   S. Abachi et al. (D0 Collaboration). "Observation of the Top Quark". In: *Physical Review Letters* 74 (1995), pp. 2632–2637. DOI: `10.1103/PhysRevLett.74.2632`.

[26]   A. Einstein. "Über einen die Erzeugung und Verwandlung des Lichtes betreffenden heuristischen Gesichtspunkt". In: *Annalen der Physik* 322 (1905), pp. 132–148. DOI: `10.1002/andp.19053220607`.

[27] G. Arnison et al. (UA1 Collaboration). "Experimental Observation of Isolated Large Transverse Energy Electrons with Associated Missing Energy at $\sqrt{s} = 540$ GeV". In: *Physics Letters B* 122 (1983), pp. 103–116. DOI: `10.1016/0370-2693(83)91177-2`.

[28] P. Bagnaia et al. (UA2 Collaboration). "Evidence for $Z^0 \rightarrow e^+e^-$ at the CERN $\bar{p}p$ Collider". In: *Physics Letters B* 122 (1983), pp. 476–485. DOI: `10.1016/0370-2693(83)91605-2`.

[29] D. P. Barber et al. (TASSO Collaboration). "Discovery of Three-Jet Events and Evidence for Gluon Bremsstrahlung in e^+e^- Annihilations". In: *Physics Letters B* 86 (1979), pp. 243–249. DOI: `10.1016/0370-2693(79)90832-0`.

[30] Emmy Noether. "Invariante Variationsprobleme". In: *Nachrichten von der Gesellschaft der Wissenschaften zu Göttingen, Mathematisch-Physikalische Klasse* (1918), pp. 235–257. URL: `https://eudml.org/doc/59024`.

[31] V. E. Barnes et al. "Observation of a Possible Δ^{++} Particle". In: *Physical Review Letters* 12 (1964), pp. 204–206. DOI: `10.1103/PhysRevLett.12.204`.

[32] O. W. Greenberg. "Spin and Unitary-Spin Independence in a Paraquark Model of Baryons and Mesons". In: *Physical Review Letters* 13 (1964), pp. 598–602. DOI: `10.1103/PhysRevLett.13.598`.

[33] M. Y. Han and Y. Nambu. "Three-Triplet Model with Double SU(3) Symmetry". In: *Physical Review* 139.4B (1965), B1006–B1010. DOI: `10.1103/PhysRev.139.B1006`.

[34] H. David Politzer. "Reliable Perturbative Results for Strong Interactions?" In: *Physical Review Letters* 30 (1973), pp. 1346–1349. DOI: `10.1103/PhysRevLett.30.1346`.

[35] E. Eichten et al. "The Spectrum of Charmonium". In: *Physical Review Letters* 34.6 (1975), pp. 369–372. DOI: `10.1103/PhysRevLett.34.369`.

[36] Steven Weinberg. "A Model of Leptons". In: *Physical Review Letters* 19 (1967), pp. 1264–1266. DOI: `10.1103/PhysRevLett.19.1264`.

[37] Abdus Salam. "Weak and Electromagnetic Interactions". In: *Elementary Particle Theory: Relativistic Groups and Analyticity*. Ed. by N. Svartholm. Vol. 8. Proceedings of the Nobel Symposium. Stockholm: Almqvist and Wiksell, 1968, pp. 367–377.

[38] Sheldon L. Glashow. "Partial Symmetries of Weak Interactions". In: *Nuclear Physics* 22 (1961), pp. 579–588. DOI: `10.1016/0029-5582(61)90469-2`.

[39] C. S. Wu et al. "Experimental Test of Parity Conservation in Beta Decay". In: *Physical Review* 105 (1957), pp. 1413–1415. DOI: `10.1103/PhysRev.105.1413`.

[40] F. Englert and R. Brout. "Broken Symmetry and the Mass of Gauge Vector Mesons". In: *Physical Review Letters* 13 (1964), pp. 321–323. DOI: `10.1103/PhysRevLett.13.321`.

[41] S. Schael et al. "Precision electroweak measurements on the Z resonance". In: *Phys. Rept.* 427 (2006), pp. 257–454. DOI: `10.1016/j.physrep.2005.12.006`. arXiv: `hep-ex/0509008`.

[42] S. Schael et al. "Electroweak Measurements in Electron-Positron Collisions at W-Boson-Pair Energies at LEP". In: *Phys. Rept.* 532 (2013), pp. 119–244. DOI: 10.1016/j.physrep.2013.07.004. arXiv: 1302.3415 [hep-ex].

[43] ATLAS Collaboration and CMS Collaboration. "Combined Measurement of the Higgs Boson Mass in pp Collisions at $\sqrt{s} = 7$ and 8 TeV with the ATLAS and CMS Experiments". In: *Physical Review Letters* 114 (2015). Updated world average $m_H = 125.25 \pm 0.17$ GeV., p. 191803. DOI: 10.1103/PhysRevLett.114.191803.

[44] Makoto Kobayashi and Toshihide Maskawa. "CP-Violation in the Renormalizable Theory of Weak Interaction". In: *Progress of Theoretical Physics* 49.2 (1973), pp. 652–657. DOI: 10.1143/PTP.49.652.

[45] Nicola Cabibbo. "Unitary Symmetry and Leptonic Decays". In: *Physical Review Letters* 10.12 (1963), pp. 531–533. DOI: 10.1103/PhysRevLett.10.531.

[46] James D. Bjorken. "Asymptotic Sum Rules at Infinite Momentum". In: *Physical Review* 179.5 (1969), pp. 1547–1553. DOI: 10.1103/PhysRev.179.1547.

[47] Guido Altarelli and G. Parisi. "Asymptotic Freedom in Parton Language". In: *Nucl. Phys. B* 126 (1977), pp. 298–318. DOI: 10.1016/0550-3213(77)90384-4.

[48] Yuri L. Dokshitzer. "Calculation of the Structure Functions for Deep Inelastic Scattering and e+ e- Annihilation by Perturbation Theory in Quantum Chromodynamics". In: *Sov. Phys. JETP* 46 (1977). [Zh. Eksp. Teor. Fiz. 73 (1977) 1216], pp. 641–653.

[49] V. N. Gribov and L. N. Lipatov. "Deep inelastic e p scattering in perturbation theory". In: *Sov. J. Nucl. Phys.* 15 (1972). [Yad. Fiz. 15 (1972) 781], pp. 438–450.

[50] Richard D. Ball et al. "Parton distributions from high-precision collider data". In: *Eur. Phys. J. C* 77 (2017), p. 663. DOI: 10.1140/epjc/s10052-017-5199-5. arXiv: 1706.00428 [hep-ph].

[51] Andy Buckley et al. "LHAPDF6: parton density access in the LHC precision era". In: *Eur. Phys. J. C* 75 (2015), p. 132. DOI: 10.1140/epjc/s10052-015-3318-8. arXiv: 1412.7420 [hep-ph].

[52] M. Czakon, P. Fiedler, and A. Mitov. "Total Top-Quark Pair-Production Cross Section at Hadron Colliders Through $O(\alpha_S^4)$". In: *Physical Review Letters* 110.25 (2013), p. 252004. DOI: 10.1103/PhysRevLett.110.252004.

[53] CMS Collaboration. "Observation of four top quark production in proton-proton collisions at $\sqrt{s}$ 13 TeV". In: *Physics Letters B* 847 (Dec. 2023), p. 138290. ISSN: 0370-2693. DOI: 10.1016/j.physletb.2023.138290. URL: http://dx.doi.org/10.1016/j.physletb.2023.138290.

[54] ATLAS Collaboration. "Observation of four-top-quark production in the multilepton final state with the ATLAS detector". In: *The European Physical Journal C* 83.6 (June 2023). ISSN: 1434-6052. DOI: 10.1140/epjc/s10052-023-11573-0. URL: http://dx.doi.org/10.1140/epjc/s10052-023-11573-0.

[55] Claus Kiefer. *Quantum Gravity*. 3rd ed. Oxford University Press, 2012.

[56] Planck Collaboration. "Planck 2018 results. VI. Cosmological parameters". In: *Astronomy & Astrophysics* 641 (2020), A6. DOI: 10.1051/0004-6361/201833910. arXiv: 1807.06209.

[57] Y. Fukuda et al. "Evidence for oscillation of atmospheric neutrinos". In: *Physical Review Letters* 81 (1998), pp. 1562–1567. DOI: 10.1103/PhysRevLett.81.1562. arXiv: hep-ex/9807003.

[58] Q. R. Ahmad et al. "Direct evidence for neutrino flavor transformation from neutral-current interactions in the Sudbury Neutrino Observatory". In: *Physical Review Letters* 89 (2002), p. 011301. DOI: 10.1103/PhysRevLett.89.011301. arXiv: nucl-ex/0204008.

[59] Vera C. Rubin and W. Kent Ford. "Rotation of the Andromeda Nebula from a Spectroscopic Survey of Emission Regions". In: *Astrophysical Journal* 159 (1970), pp. 379–403. DOI: 10.1086/150317.

[60] Fritz Zwicky. "Die Rotverschiebung von extragalaktischen Nebeln". In: *Helvetica Physica Acta* 6 (1933), pp. 110–127.

[61] Jihn E. Kim and Gianpaolo Carosi. "Axions and the Strong CP Problem". In: *Rev. Mod. Phys.* 82 (2010), pp. 557–602. DOI: 10.1103/RevModPhys.82.557.

[62] Lisa Randall and Raman Sundrum. "Large Mass Hierarchy from a Small Extra Dimension". In: *Physical Review Letters* 83.17 (Oct. 1999), pp. 3370–3373. ISSN: 1079-7114. DOI: 10.1103/physrevlett.83.3370. URL: http://dx.doi.org/10.1103/PhysRevLett.83.3370.

[63] Ben Lillie, Jing Shu, and Tim M. P. Tait. "Kaluza-Klein gluons as a diagnostic of warped models". In: *Physical Review D* 76.11 (Dec. 2007). ISSN: 1550-2368. DOI: 10.1103/physrevd.76.115016. URL: http://dx.doi.org/10.1103/PhysRevD.76.115016.

[64] Yoshio Koide. *Composite Model of Quarks and Leptons*. 2021. arXiv: 2106.02464 [hep-ph]. URL: https://arxiv.org/abs/2106.02464.

[65] Brando Bellazzini, Csaba Csáki, and Javi Serra. "Composite Higgses". In: *The European Physical Journal C* 74.5 (May 2014). ISSN: 1434-6052. DOI: 10.1140/epjc/s10052-014-2766-x. URL: http://dx.doi.org/10.1140/epjc/s10052-014-2766-x.

[66] Jeong Han Kim et al. "Probing TeV scale top-philic resonances with boosted top-tagging at the high luminosity LHC". In: *Phys. Rev. D* 94 (3 Aug. 2016), p. 035023. DOI: 10.1103/PhysRevD.94.035023. URL: https://link.aps.org/doi/10.1103/PhysRevD.94.035023.

[67] Nicolas Greiner et al. "Model-independent production of a top-philic resonance at the LHC". In: *Journal of High Energy Physics* 2015.4 (Apr. 2015). ISSN: 1029-8479. DOI: `10.1007/jhep04(2015)029`. URL: `http://dx.doi.org/10.1007/JHEP04(2015)029`.

[68] G. C. Branco et al. "Theory and phenomenology of two-Higgs-doublet models". In: *Phys. Rept.* 516 (2012), p. 1. DOI: `10.1016/j.physrep.2012.02.002`. arXiv: `1106.0034 [hep-ph]`.

[69] Margarete Mühlleitner et al. "Phenomenological comparison of models with extended Higgs sectors". In: *Journal of High Energy Physics* 2017.8 (2017), p. 132. ISSN: 1029-8479. DOI: `10.1007/JHEP08(2017)132`. URL: `https://doi.org/10.1007/JHEP08(2017)132`.

[70] R. D. Peccei and Helen R. Quinn. "CP Conservation in the Presence of Pseudoparticles". In: *Phys. Rev. Lett.* 38 (25 June 1977), p. 1440. DOI: `10.1103/PhysRevLett.38.1440`. URL: `https://link.aps.org/doi/10.1103/PhysRevLett.38.1440`.

[71] R. D. Peccei and Helen R. Quinn. "Constraints imposed by CP conservation in the presence of pseudoparticles". In: *Phys. Rev. D* 16 (6 Sept. 1977), p. 1791. DOI: `10.1103/PhysRevD.16.1791`. URL: `https://link.aps.org/doi/10.1103/PhysRevD.16.1791`.

[72] Maurizio Vretenar et al. *Linac4 design report*. Vol. 6. CERN Yellow Reports: Monographs. Geneva: CERN, 2020. DOI: `10.23731/CYRM-2020-006`. URL: `https://cds.cern.ch/record/2736208`.

[73] Esma Mobs. "The CERN accelerator complex in 2019. Complexe des accélérateurs du CERN en 2019". In: (2019). General Photo. URL: `https://cds.cern.ch/record/2684277`.

[74] *Public CMS Luminosity Information*. `https://twiki.cern.ch/twiki/bin/view/CMSPublic/LumiPublicResults#Summary_proton_proton_collisions`.

[75] "The CMS experiment at the CERN LHC". In: *Journal of Instrumentation* 3.08 (Aug. 2008), S08004. DOI: `10.1088/1748-0221/3/08/S08004`. URL: `https://dx.doi.org/10.1088/1748-0221/3/08/S08004`.

[76] CMS Collaboration. "Development of the CMS detector for the CERN LHC Run 3". In: *Journal of Instrumentation* 19.05 (May 2024), P05064. ISSN: 1748-0221. DOI: `10.1088/1748-0221/19/05/p05064`. URL: `http://dx.doi.org/10.1088/1748-0221/19/05/P05064`.

[77] Tai Sakuma. "Cutaway diagrams of CMS detector". In: (2019). URL: `https://cds.cern.ch/record/2665537`.

[78] *CMS coordinate system*. `https://tikz.net/axis3d_cms/`.

[79] The CMS Collaboration. "Description and performance of track and primary-vertex reconstruction with the CMS tracker". In: *Journal of Instrumentation* 9.10 (Oct. 2014), P10009–P10009. ISSN: 1748-0221. DOI: `10.1088/1748-0221/9/10/p10009`. URL: `http://dx.doi.org/10.1088/1748-0221/9/10/P10009`.

[80] The CMS Collaboration. "Operation and performance of the CMS silicon strip tracker with proton-proton collisions at the CERN LHC". In: *Journal of Instrumentation* 20.08 (). ISSN: 1748-0221. DOI: `10.1088/1748-0221/20/08/p08027`. URL: `http://dx.doi.org/10.1088/1748-0221/20/08/P08027`.

[81] H. Messel and D. F. Crawford. *Electron–Photon Shower Distribution Function: Tables for Lead, Copper and Air Absorbers*. Oxford: Pergamon Press, 1970, p. 1512. ISBN: 0-08-013374-6.

[82] C. W. Fabjan and F. Gianotti. "Calorimetry for particle physics". In: *Landolt-Börnstein - Group I Elementary Particles, Nuclei and Atoms*. Ed. by C. W. Fabjan and H. Schopper. Vol. 21B. Springer, 2003, pp. 1–108. DOI: `10.1007/b12114`. URL: `https://doi.org/10.1007/b12114`.

[83] Bruno Rossi. *High-Energy Particles*. 3rd ed. Englewood Cliffs, NJ: Prentice-Hall, 1952, p. 569.

[84] D. E. Groom. "A simplistic view of hadron calorimetry". In: *Proceedings of the 7th International Conference on Calorimetry in High Energy Physics (CALOR 97), Tucson, Arizona*. Ed. by E. Chen et al. World Scientific, 1998, pp. 507–514.

[85] CMS Collaboration. "Energy calibration and resolution of the CMS electromagnetic calorimeter in pp collisions at $\sqrt{(s)} = 7$ TeV". In: *Journal of Instrumentation* 8.09 (Sept. 2013), P09009. DOI: `10.1088/1748-0221/8/09/P09009`. URL: `https://doi.org/10.1088/1748-0221/8/09/P09009`.

[86] CMS Collaboration. *The CMS hadron calorimeter project: Technical Design Report*. Tech. rep. CERN-LHCC-97-031, CMS-TDR-2. CERN, 1997. URL: `https://cds.cern.ch/record/357153`.

[87] *The Phase-2 Upgrade of the CMS Muon Detectors*. Tech. rep. This is the final version, approved by the LHCC. Geneva: CERN, 2017. DOI: `10.17181/CERN.5T9S.VPMI`. URL: `https://cds.cern.ch/record/2283189`.

[88] *CMS Technical Design Report for the Muon Endcap GEM Upgrade*. Tech. rep. CERN-LHCC-2015-012, CMS-TDR-013. CERN, 2015. URL: `https://cds.cern.ch/record/2021453`.

[89] CMS Collaboration. "Performance of the CMS muon detector and muon reconstruction with proton-proton collisions at $\sqrt{s}=13$ TeV". In: *Journal of Instrumentation* 13.06 (June 2018), P06015. DOI: `10.1088/1748-0221/13/06/P06015`. URL: `https://dx.doi.org/10.1088/1748-0221/13/06/P06015`.

[90] *LHC Computing Grid: Technical Design Report*. Tech. rep. CERN-LHCC-2005-024, LCG-TDR-001. CERN, 2005. URL: `https://cds.cern.ch/record/840543`.

[91] *The HL-LHC project*. `https://hilumilhc.web.cern.ch/content/hl-lhc-project`.

[92] *The Phase-2 Upgrade of the CMS Tracker*. Tech. rep. Geneva: CERN, 2017. DOI: `10.17181/CERN.QZ28.FLHW`. URL: `https://cds.cern.ch/record/2272264`.

[93]   Collaboration CMS. *A MIP Timing Detector for the CMS Phase-2 Upgrade*. Tech. rep. Geneva: CERN, 2019. URL: https://cds.cern.ch/record/2667167.

[94]   *The Phase-2 Upgrade of the CMS Level-1 Trigger*. Tech. rep. Final version. Geneva: CERN, 2020. URL: https://cds.cern.ch/record/2714892.

[95]   *The Phase-2 Upgrade of the CMS Barrel Calorimeters*. Tech. rep. This is the final version, approved by the LHCC. Geneva: CERN, 2017. URL: https://cds.cern.ch/record/2283187.

[96]   *The Phase-2 Upgrade of the CMS Endcap Calorimeter*. Tech. rep. Geneva: CERN, 2017. DOI: 10.17181/CERN.IV8M.1JY2. URL: https://cds.cern.ch/record/2293646.

[97]   F. Ballarini et al. "The FLUKA code: Overview and new developments". In: *EPJ Nuclear Sciences & Technologies* 10 (2024), p. 25. DOI: 10.1140/epjn/s40436-023-00450-y.

[98]   The CALICE collaboration et al. "Construction and commissioning of the CALICE analog hadron calorimeter prototype". In: *Journal of Instrumentation* 5.05 (May 2010), P05004–P05004. ISSN: 1748-0221. DOI: 10.1088/1748-0221/5/05/p05004. URL: http://dx.doi.org/10.1088/1748-0221/5/05/P05004.

[99]   D. Breton et al. "CALICE SiW ECAL—Development and performance of a highly compact digital readout system". In: *Journal of Instrumentation* 15.05 (May 2020), pp. C05074–C05074. ISSN: 1748-0221. DOI: 10.1088/1748-0221/15/05/c05074. URL: http://dx.doi.org/10.1088/1748-0221/15/05/C05074.

[100] J. E. Brau, M. Breidenbach, and Y. Fujii. "The silicon detector (SiD) and linear collider detector \& in Asia and North America". In: *4th ECFA / DESY Workshop on Physics and Detectors for a 90-GeV to 800-GeV Linear e+ e- Collider*. Mar. 2004, pp. 95–106.

[101] Felix Sefkow and Frank Simon. "A highly granular SiPM-on-tile calorimeter prototype". In: *Journal of Physics: Conference Series* 1162 (Jan. 2019), p. 012012. ISSN: 1742-6596. DOI: 10.1088/1742-6596/1162/1/012012. URL: http://dx.doi.org/10.1088/1742-6596/1162/1/012012.

[102] *3M Science. Applied To Life.* https://www.3m.com/3M/en_US/p/.

[103] *Hamamatsu Photonics K.K. MPPC S14160-976x series specification sheet, 2022.* https://www.hamamatsu.com/content/dam/hamamatsu-photonics/sites/documents/99_SALES_LIBRARY/ssd/s14160_s14161_series_kapd1064e.pdf.

[104] Malinda De Silva. "SiPM-on-Tile Modules for the CMS High Granularity Calorimeter". Dissertation, Heidelberg University, 2023. Dissertation. Heidelberg University, 2023, p. 196. URL: https://bib-pubdb1.desy.de/record/622771.

[105] J D González-Martínez. "H2GCROC: Design and performance of a dedicated very front-end ASIC for SiPM readout of the CMS High Granularity Calorimeter". In: *Nucl. Instrum. Methods Phys. Res., A* 1047 (2023), p. 167863. DOI: `10.1016/j.nima.2022.167863`. URL: `https://cds.cern.ch/record/2843769`.

[106] F. Bouyjou et al. "HGCROC3: the front-end readout ASIC for the CMS High Granularity Calorimeter". In: *JINST*. Vol. 17. 03. Online Conference, France, Sept. 2021, p. C03015. DOI: `10.1088/1748-0221/17/03/C03015`. URL: `https://hal.science/hal-03610231`.

[107] R. Diener et al. "The DESY II test beam facility". In: *Nuclear Instruments and Methods in Physics Research Section A: Accelerators, Spectrometers, Detectors and Associated Equipment* 922 (2019), pp. 265–286. ISSN: 0168-9002. DOI: `https://doi.org/10.1016/j.nima.2018.11.133`. URL: `https://www.sciencedirect.com/science/article/pii/S0168900218317868`.

[108] *PETRA III*. URL: `https://www.desy.de/forschung/anlagen__projekte/petra_iii/index_ger.html`.

[109] A. Caratelli et al. "The GBT-SCA, a radiation tolerant ASIC for detector control and monitoring applications in HEP experiments". In: *Journal of Instrumentation* 10.03 (Mar. 2015), p. C03034. DOI: `10.1088/1748-0221/10/03/C03034`. URL: `https://dx.doi.org/10.1088/1748-0221/10/03/C03034`.

[110] P. Carniti et al. "ALDO: A radiation-tolerant, low-noise, adjustable low drop-out linear regulator in 0.35μm CMOS technology". In: *Nuclear Instruments and Methods in Physics Research Section A: Accelerators, Spectrometers, Detectors and Associated Equipment* 824 (2016). Frontier Detectors for Frontier Physics: Proceedings of the 13th Pisa Meeting on Advanced Detectors, pp. 258–259. ISSN: 0168-9002. DOI: `https://doi.org/10.1016/j.nima.2015.10.054`. URL: `https://www.sciencedirect.com/science/article/pii/S0168900215012668`.

[111] Steve Arar. *Understanding ADC Differential Nonlinearity (DNL) Error*. `https://www.allaboutcircuits.com/technical-articles/understanding-analog-to-digital-converter-differential-nonlinearity-dnl-error/`. Accessed: 2024-08-16.

[112] *ROOT Data Analysis Framework*. `https://root.cern/`.

[113] Arjan Heering et al. *Endcap Calorimeter: SiPM Production Readiness Review*. 2022. URL: `https://indico.cern.ch/event/1227228/contributions/5163765/attachments/2563671/4419615/Endcap%20Calorimeter%20-%20PRR%20for%20SiPMs%20v4.pdf` (visited on 05/04/2025).

[114] CMS Collaboration. "Performance of reconstruction and identification of τ leptons decaying to hadrons and $\nu\tau$ in pp collisions at $\sqrt{s}$=13 TeV". In: *Journal of Instrumentation* 13.10 (2021). ISSN: 1748-0221. DOI: `10.1088/1748-0221/13/10/p10005`. URL: `http://dx.doi.org/10.1088/1748-0221/13/10/P10005`.

[115] CMS Collaboration. "Electron and photon reconstruction and identification with the CMS experiment at the CERN LHC". In: *Journal of Instrumentation* 16.05 (May 2021), P05014. ISSN: 1748-0221. DOI: `10.1088/1748-0221/16/05/p05014`. URL: `http://dx.doi.org/10.1088/1748-0221/16/05/P05014`.

[116] The CMS collaboration. "Performance of the CMS missing transverse momentum reconstruction in pp data at $\sqrt{s} = 8$ TeV". In: *Journal of Instrumentation* 10.02 (Feb. 2015), P02006–P02006. ISSN: 1748-0221. DOI: `10.1088/1748-0221/10/02/p02006`. URL: `http://dx.doi.org/10.1088/1748-0221/10/02/P02006`.

[117] R. Frühwirth. "Application of Kalman filtering to track and vertex fitting". In: *Nuclear Instruments and Methods in Physics Research Section A: Accelerators, Spectrometers, Detectors and Associated Equipment* 262.2 (1987), pp. 444–450. ISSN: 0168-9002. DOI: `https://doi.org/10.1016/0168-9002(87)90887-4`. URL: `https://www.sciencedirect.com/science/article/pii/0168900287908874`.

[118] S. Lantz et al. "Speeding up particle track reconstruction using a parallel Kalman filter algorithm". In: *Journal of Instrumentation* 15.09 (Sept. 2020), P09030. DOI: `10.1088/1748-0221/15/09/P09030`. URL: `https://dx.doi.org/10.1088/1748-0221/15/09/P09030`.

[119] The CMS Collaboration. "Particle-flow reconstruction and global event description with the CMS detector". In: *Journal of Instrumentation* 12.10 (Oct. 2017), P10003. DOI: `10.1088/1748-0221/12/10/P10003`. URL: `https://dx.doi.org/10.1088/1748-0221/12/10/P10003`.

[120] W Adam et al. "Reconstruction of electrons with the Gaussian-sum filter in the CMS tracker at the LHC". In: *Journal of Physics G: Nuclear and Particle Physics* 31.9 (July 2005), N9–N20. ISSN: 1361-6471. DOI: `10.1088/0954-3899/31/9/n01`. URL: `http://dx.doi.org/10.1088/0954-3899/31/9/N01`.

[121] CMS Collaboration. "Electron and photon reconstruction and identification with the CMS experiment at the CERN LHC". In: *Journal of Instrumentation* 16.05 (2021). ISSN: 1748-0221. DOI: `10.1088/1748-0221/16/05/p05014`. URL: `http://dx.doi.org/10.1088/1748-0221/16/05/P05014`.

[122] Matteo Cacciari, Gavin P. Salam, and Gregory Soyez. "The anti-kt jet clustering algorithm". In: *Journal of High Energy Physics* 2008.04 (Apr. 2008), p. 063. DOI: `10.1088/1126-6708/2008/04/063`. URL: `https://dx.doi.org/10.1088/1126-6708/2008/04/063`.

[123] Matteo Cacciari, Gavin P. Salam, and Gregory Soyez. "FastJet user manual". In: *The European Physical Journal C* 72.3 (2012), p. 1896. ISSN: 1434-6052. DOI: `10.1140/epjc/s10052-012-1896-2`. URL: `https://doi.org/10.1140/epjc/s10052-012-1896-2`.

[124] Stephen D. Ellis and Davison E. Soper. "Successive combination jet algorithm for hadron collisions". In: *Physical Review D* 48.7 (Oct. 1993), pp. 3160–3166. ISSN: 0556-2821. DOI: `10.1103/physrevd.48.3160`. URL: `http://dx.doi.org/10.1103/PhysRevD.48.3160`.

[125] Yu.L Dokshitzer et al. "Better jet clustering algorithms". In: *Journal of High Energy Physics* 1997.08 (Aug. 1997), pp. 001–001. ISSN: 1029-8479. DOI: 10.1088/1126-6708/1997/08/001. URL: http://dx.doi.org/10.1088/1126-6708/1997/08/001.

[126] G Corcella et al. *HERWIG 6.5 Release Note*. 2005. arXiv: hep-ph/0210213 [hep-ph]. URL: https://arxiv.org/abs/hep-ph/0210213.

[127] Roman Kogler. *Advances in Jet Substructure at the LHC: Algorithms, Measurements and Searches for New Physical Phenomena*. Vol. 284. Springer, May 2021. ISBN: 978-3-030-72857-1, 978-3-030-72858-8. DOI: 10.1007/978-3-030-72858-8.

[128] Andrew J. Larkoski et al. "Soft drop". In: *Journal of High Energy Physics* 2014.5 (May 2014). ISSN: 1029-8479. DOI: 10.1007/jhep05(2014)146. URL: http://dx.doi.org/10.1007/JHEP05(2014)146.

[129] Yacine Mehtar-Tani and Konrad Tywoniuk. "Sudakov suppression of jets in QCD media". In: *Physical Review D* 98.5 (Sept. 2018). ISSN: 2470-0029. DOI: 10.1103/physrevd.98.051501. URL: http://dx.doi.org/10.1103/PhysRevD.98.051501.

[130] The CMS Collaboration. "Identification of heavy, energetic, hadronically decaying particles using machine-learning techniques". In: *Journal of Instrumentation* 15.06 (June 2020), P06005. DOI: 10.1088/1748-0221/15/06/P06005. URL: https://dx.doi.org/10.1088/1748-0221/15/06/P06005.

[131] Jesse Thaler and Ken Van Tilburg. "Identifying boosted objects with N-subjettiness". In: *Journal of High Energy Physics* 2011.3 (Mar. 2011). ISSN: 1029-8479. DOI: 10.1007/jhep03(2011)015. URL: http://dx.doi.org/10.1007/JHEP03(2011)015.

[132] *Pileup Removal Algorithms*. Tech. rep. Geneva: CERN, 2014. URL: http://cds.cern.ch/record/1751454.

[133] Daniele Bertolini et al. "Pileup Per Particle Identification". In: *JHEP* 10 (2014), p. 059. ISSN: 1029-8479. DOI: 10.1007/JHEP10(2014)059. URL: https://doi.org/10.1007/JHEP10(2014)059.

[134] CMS Collaboration. "Jet energy scale and resolution in the CMS experiment in pp collisions at 8 TeV". In: *Journal of Instrumentation* 12.02 (Feb. 2017), P02014. DOI: 10.1088/1748-0221/12/02/P02014. URL: https://dx.doi.org/10.1088/1748-0221/12/02/P02014.

[135] "Jet energy scale and resolution performance with 13 TeV data collected by CMS in 2016-2018". In: (2020). URL: https://cds.cern.ch/record/2715872.

[136] CMS Collaboration. "Identification of heavy-flavour jets with the CMS detector in pp collisions at 13 TeV". In: *Journal of Instrumentation* 13.05 (May 2018), P05011. DOI: 10.1088/1748-0221/13/05/P05011. URL: https://dx.doi.org/10.1088/1748-0221/13/05/P05011.

[137] Huilin Qu and Loukas Gouskos. "Jet tagging via particle clouds". In: *Phys. Rev. D* 101 (5 Mar. 2020), p. 056019. DOI: `10.1103/PhysRevD.101.056019`. URL: `https://link.aps.org/doi/10.1103/PhysRevD.101.056019`.

[138] Yue Wang et al. "Dynamic Graph CNN for Learning on Point Clouds". In: *ACM Trans. Graph.* 38.5 (Oct. 2019). ISSN: 0730-0301. DOI: `10.1145/3326362`. URL: `https://doi.org/10.1145/3326362`.

[139] *Machine learning-based identification of highly Lorentz-boosted hadronically decaying particles at the CMS experiment.* Tech. rep. Geneva: CERN, 2019. URL: `https://cds.cern.ch/record/2683870`.

[140] "Identification of highly Lorentz-boosted heavy particles using graph neural networks and new mass decorrelation techniques". In: (2020). URL: `https://cds.cern.ch/record/2707946`.

[141] David Krohn, Jesse Thaler, and Lian-Tao Wang. "Jets with variable R". In: *Journal of High Energy Physics* 2009.06 (June 2009), pp. 059–059. ISSN: 1029-8479. DOI: `10.1088/1126-6708/2009/06/059`. URL: `http://dx.doi.org/10.1088/1126-6708/2009/06/059`.

[142] T. Lapsien, R. Kogler, and J. Haller. "A new tagger for hadronically decaying heavy particles at the LHC". In: *The European Physical Journal C* 76.11 (Nov. 2016). ISSN: 1434-6052. DOI: `10.1140/epjc/s10052-016-4443-8`. URL: `http://dx.doi.org/10.1140/epjc/s10052-016-4443-8`.

[143] Martin Stoll. "Vetoed jet clustering: the mass-jump algorithm". In: *Journal of High Energy Physics* 2015.4 (Apr. 2015). ISSN: 1029-8479. DOI: `10.1007/jhep04(2015)111`. URL: `http://dx.doi.org/10.1007/JHEP04(2015)111`.

[144] CMS Collaboration. "Search for a heavy resonance decaying into a top quark and a W boson in the lepton+jets final state at $\sqrt{s}$ = 13 TeV". In: *Journal of High Energy Physics* 2022.4 (Apr. 2022). ISSN: 1029-8479. DOI: `10.1007/jhep04(2022)048`. URL: `http://dx.doi.org/10.1007/JHEP04(2022)048`.

[145] CMS Collaboration. "Machine Learning Techniques for JetMET Data Certification of the CMS Detector". In: (2023). URL: `https://cds.cern.ch/record/2860924`.

[146] *Deep Learning Book.* `https://www.deeplearningbook.org/contents/ml.html`.

[147] Leo Breiman et al. *Classification and Regression Trees.* 1st. Chapman and Hall/CRC, 1984. DOI: `10.1201/978131513947`.

[148] Yann Coadou. "Boosted Decision Trees". In: *Artificial Intelligence for High Energy Physics.* WORLD SCIENTIFIC, Feb. 2022, pp. 9–58. ISBN: 9789811234033. DOI: `10.1142/9789811234033_0002`. URL: `http://dx.doi.org/10.1142/9789811234033_0002`.

[149] Google Developers. *Introduction to Gradient Boosted Decision Trees.* `https://developers.google.com/machine-learning/decision-forests/intro-to-gbdt`. Accessed: 2024-08-16. 2024.

[150]   *XGboost Documentation.* https://xgboost.readthedocs.io/en/stable/.

[151]   Paolo Nason. "A New method for combining NLO QCD with shower Monte Carlo algorithms". In: *JHEP* 11 (2004), p. 040. DOI: 10.1088/1126-6708/2004/11/040. arXiv: hep-ph/0409146.

[152]   Stefano Frixione, Paolo Nason, and Carlo Oleari. "Matching NLO QCD computations with Parton Shower simulations: the POWHEG method". In: *JHEP* 11 (2007), p. 070. DOI: 10.1088/1126-6708/2007/11/070. arXiv: 0709.2092 [hep-ph].

[153]   Simone Alioli et al. "A general framework for implementing NLO calculations in shower Monte Carlo programs: the POWHEG BOX". In: *JHEP* 06 (2010), p. 043. DOI: 10.1007/JHEP06(2010)043. arXiv: 1002.2581 [hep-ph].

[154]   CMS Collaboration. *Observation of a pseudoscalar excess at the top quark pair production threshold.* 2025. arXiv: 2503.22382 [hep-ex]. URL: https://arxiv.org/abs/2503.22382.

[155]   ATLAS Collaboration. "Search for top-philic heavy resonances in pp collisions at $\sqrt{s}$ 13 TeV with the ATLAS detector". In: *The European Physical Journal C* 84.2 (Feb. 2024). ISSN: 1434-6052. DOI: 10.1140/epjc/s10052-023-12318-9. URL: http://dx.doi.org/10.1140/epjc/s10052-023-12318-9.

[156]   *CMS Luminosity Measurements for the 2016 Data Taking Period.* Tech. rep. Geneva: CERN, 2017. URL: https://cds.cern.ch/record/2257069.

[157]   *CMS luminosity measurement for the 2017 data-taking period at $\sqrt{s} =$ 13 TeV.* Tech. rep. Geneva: CERN, 2018. URL: https://cds.cern.ch/record/2621960.

[158]   *CMS luminosity measurement for the 2018 data-taking period at $\sqrt{s} =$ 13 TeV.* Tech. rep. Geneva: CERN, 2019. URL: https://cds.cern.ch/record/2676164.

[159]   *Luminosity measurement in proton-proton collisions at* 13.6 TeV *in 2022 at CMS.* Tech. rep. Geneva: CERN, 2024. URL: https://cds.cern.ch/record/2890833.

[160]   J. Alwall et al. "The automated computation of tree-level and next-to-leading order differential cross sections, and their matching to parton shower simulations". In: *Journal of High Energy Physics* 2014.7 (July 2014). ISSN: 1029-8479. DOI: 10.1007/jhep07(2014)079. URL: http://dx.doi.org/10.1007/JHEP07(2014)079.

[161]   T. D. Lee. "A Theory of Spontaneous T Violation". In: *Phys. Rev. D* 8 (4 Aug. 1973), p. 1226. DOI: 10.1103/PhysRevD.8.1226. URL: https://link.aps.org/doi/10.1103/PhysRevD.8.1226.

[162]   Simone Blasi et al. "Top-philic ALP phenomenology at the LHC: the elusive mass-window". In: *JHEP* 06 (2024), p. 077. DOI: 10.1007/JHEP06(2024)077. arXiv: 2311.16048 [hep-ph].

[163]   Michał Czakon and Alexander Mitov. "Top++: A program for the cal-
         culation of the top-pair cross-section at hadron colliders". In: *Computer
         Physics Communications* 185.11 (2014), pp. 2930–2938. ISSN: 0010-4655.
         DOI: `https://doi.org/10.1016/j.cpc.2014.06.021`. URL: `https://
         www.sciencedirect.com/science/article/pii/S0010465514002264`.

[164]   Michal Czakon and Alexander Mitov. "NNLO corrections to top pair
         production at hadron colliders: the quark-gluon reaction". In: *Journal of
         High Energy Physics* 2013.1 (Jan. 2013). ISSN: 1029-8479. DOI: `10.1007/
         jhep01(2013)080`. URL: `http://dx.doi.org/10.1007/JHEP01(2013)
         080`.

[165]   Johan Alwall et al. "Comparative study of various algorithms for the merg-
         ing of parton showers and matrix elements in hadronic collisions". In: *Eur.
         Phys. J. C* 53 (2008), pp. 473–500. DOI: `10.1140/epjc/s10052-007-
         0490-5`. arXiv: `0706.2569 [hep-ph]`.

[166]   Richard D. Ball et al. "Parton distributions from high-precision collider
         data: NNPDF Collaboration". In: *The European Physical Journal C* 77.10
         (Oct. 2017). ISSN: 1434-6052. DOI: `10.1140/epjc/s10052-017-5199-5`.
         URL: `http://dx.doi.org/10.1140/epjc/s10052-017-5199-5`.

[167]   Torbjörn Sjöstrand et al. "An introduction to PYTHIA 8.2". In: *Computer
         Physics Communications* 191 (June 2015), pp. 159–177. ISSN: 0010-4655.
         DOI: `10.1016/j.cpc.2015.01.024`. URL: `http://dx.doi.org/10.1016/
         j.cpc.2015.01.024`.

[168]   "Extraction and validation of a new set of CMS pythia8 tunes from underlying-
         event measurements". In: *The European Physical Journal C* 80.1 (Jan.
         2020). ISSN: 1434-6052. DOI: `10.1140/epjc/s10052-019-7499-4`. URL:
         `http://dx.doi.org/10.1140/epjc/s10052-019-7499-4`.

[169]   *Summary table of samples produced for the 1 Billion campaign, with 25ns
         bunch-crossing.* arXiv: `hep-ph/0210213 [hep-ph]`. URL: `https://twiki.
         cern.ch/twiki/bin/viewauth/CMS/SummaryTable1G25ns#ttH%20`.

[170]   *Predictions at NNLO of single top-quark production cross-sections.* `https:
         //twiki.cern.ch/twiki/bin/view/LHCPhysics/SingleTopNNLORef`.

[171]   Rikkert Frederix, Davide Pagani, and Marco Zaro. "Large NLO corrections
         in $t\bar{t}W^{\pm}$ and $t\bar{t}t\bar{t}$ hadroproduction from supposedly subleading EW con-
         tributions". In: *JHEP* 02 (2018), p. 031. DOI: `10.1007/JHEP02(2018)031`.
         arXiv: `1711.02116 [hep-ph]`.

[172]   Gauthier Durieux. *Triple top-quark production at NLO in QCD.* Version v1.0.
         Feb. 2023. DOI: `10.5281/zenodo.7682519`. URL: `https://doi.org/10.
         5281/zenodo.7682519`.

[173]   S. Agostinelli et al. "Geant4—a simulation toolkit". In: *Nuclear Instru-
         ments and Methods in Physics Research Section A: Accelerators, Spec-
         trometers, Detectors and Associated Equipment* 506.3 (2003), pp. 250–
         303. ISSN: 0168-9002. DOI: `https://doi.org/10.1016/S0168-9002(03)
         01368-8`. URL: `https://www.sciencedirect.com/science/article/
         pii/S0168900203013688`.

[174] Giovanni Punzi. *Sensitivity of searches for new signals and its optimization.* 2003. arXiv: `physics/0308063` [`physics.data-an`]. URL: `https://arxiv.org/abs/physics/0308063`.

[175] "Identification of heavy-flavour jets with the CMS detector in pp collisions at 13 TeV". In: *Journal of Instrumentation* 13.05 (). ISSN: 1748-0221. DOI: `10.1088/1748-0221/13/05/p05011`. URL: `http://dx.doi.org/10.1088/1748-0221/13/05/P05011`.

[176] CMS Collaboration. "Precision luminosity measurement in proton–proton collisions at $\sqrt{s} = 13\,\text{TeV}$ in 2015 and 2016 at CMS". In: *The European Physical Journal C* 81.9 (2021), p. 800. DOI: `10.1140/epjc/s10052-021-09538-2`. URL: `https://doi.org/10.1140/epjc/s10052-021-09538-2`.

[177] *Luminosity measurement in proton-proton collisions at 13.6TeV in 2022 at CMS.* `https://cds.cern.ch/record/2890833`.

[178] Roger Barlow and Christine Beeston. "Fitting using finite Monte Carlo samples". In: *Computer Physics Communications* 77.2 (1993), pp. 219–228. ISSN: 0010-4655. DOI: `https://doi.org/10.1016/0010-4655(93)90005-W`. URL: `https://www.sciencedirect.com/science/article/pii/001046559390005W`.

[179] J.S. Conway. "Incorporating Nuisance Parameters in Likelihoods for Multisource Spectra". In: (2011). Comments: Presented at PHYSTAT 2011, CERN, Geneva, Switzerland, January 2011, to be published in a CERN Yellow Report, pp. 115–120. DOI: `10.5170/CERN-2011-006.115`. arXiv: `1103.0354`. URL: `https://cds.cern.ch/record/1333496`.

[180] "The CMS Statistical Analysis and Combination Tool: Combine". In: *Computing and Software for Big Science* 8.1 (). ISSN: 2510-2044. DOI: `10.1007/s41781-024-00121-4`. URL: `http://dx.doi.org/10.1007/s41781-024-00121-4`.

[181] Glen Cowan et al. "Asymptotic formulae for likelihood-based tests of new physics". In: *The European Physical Journal C* 71.2 (Feb. 2011), p. 1554. ISSN: 1434-6052. DOI: `10.1140/epjc/s10052-011-1554-0`. URL: `https://doi.org/10.1140/epjc/s10052-011-1554-0`.

[182] S. S. Wilks. "The Large-Sample Distribution of the Likelihood Ratio for Testing Composite Hypotheses". In: *Annals of Mathematical Statistics* 9.1 (1938), pp. 60–62. DOI: `10.1214/aoms/1177732360`.

[183] *cmssw - GitHub.* `https://github.com/cms-sw/cmssw`.

[184] Stefan Höche. *Introduction to parton-shower event generators.* 2015. arXiv: `1411.4085` [`hep-ph`]. URL: `https://arxiv.org/abs/1411.4085`.

[185] Andrea Banfi et al. "A POWHEG generator for deep inelastic scattering". In: *Journal of High Energy Physics* 2024.2 (Feb. 2024). ISSN: 1029-8479. DOI: `10.1007/jhep02(2024)023`. URL: `http://dx.doi.org/10.1007/JHEP02(2024)023`.

Appendix A

Simulation of p-p interactions

Various results in this thesis rely on MC simulated samples for different purposes: measuring the properties of physics objects, evaluating detector performance, comparing experimental data to SM expectations, and simulating BSM scenarios. The analyses presented use numerous samples provided by the CMS Collaboration. In particular, for the development of the top quark tagger based on HOTVR (Chapter 6), I modified the central CMS software framework (`CMSSW` [183]) to include HOTVR-specific variables. For the search for a heavy vector top-philic BSM resonance (Chapter 7), I contributed to the generation of dedicated signal samples in Collaboration with the analysis team. These samples are now available to the entire Collaboration.

The steps to generate simulated samples are four: generation, simulation, digitisation, and reconstruction. Given the multi-particle scenario and the high-dimensional phase of the processes, the MC-based integration is the most feasible approach. The hard scattering between partons in the colliding bunches, along with the production of outgoing particles, is modeled in the generation step. The trajectories of these particles through the detector are simulated in the simulation step. The detector response is emulated during the digitisation step. Finally, the reconstruction step applies the same algorithms described in Chapter 5 to build physics objects, closely mimicking those in real data.

Simulations of specific physics processes are produced to enable precise and accurate modeling of particular background or signal samples, and to optimize storage of the resulting samples. Samples are generated either inclusively or with specific final states. Each event in the simulated samples is weighted by the product of the process cross section and the target luminosity, divided by the total number of generated events. The cross section values used for signal and background processes at $\sqrt{s}$ of 13 and 13.6 TeV are listed in Tables 7.3, 7.4.

The chain of the generator steps includes

- the hard scattering,

- the parton shower from outgoing partons,

- the parton-to-hadron transition,

- the underlying event resulting from secondary collisions.

and it is summarized in Figure A.1.
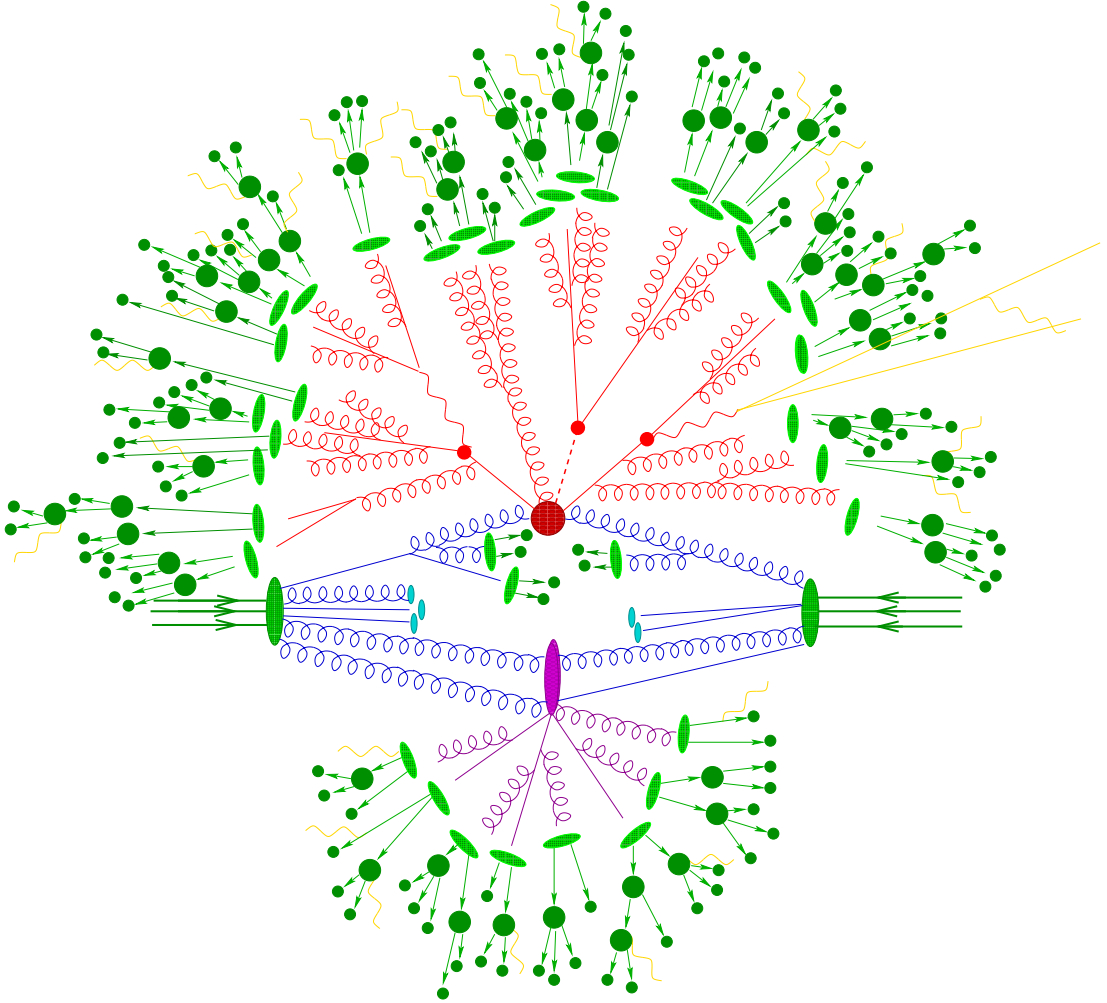
Figure A.1: Sketch of a hadron-hadron collision as simulated by a Monte-Carlo event generator. The red blob in the center represents the hard collision, surrounded by a tree-like structure representing Bremsstrahlung as simulated by parton showers. The purple blob indicates a secondary hard scattering event. Parton-to-hadron transitions are represented by light green blobs, dark green blobs indicate hadron decays, while yellow lines signal soft photon radiation. [184].

Different event generators are employed depending on the required precision and the specific stage of the simulation. The hard scattering process is typically calculated at leading order (LO) or next-to-leading order (NLO) in perturbative QCD. For instance, the `MADGRAPH` generator computes matrix elements at LO, allowing for the inclusion of multiple additional partons in the final state. Its extension, `MADGRAPH_aMC@NLO`, supports both LO and NLO calculations and enables matching to parton shower simulations. This generator is used to produce the BSM signal samples of $t\bar{t}Z'$ at LO accuracy, as described in Section 7.2. Other generators, such as `POWHEG`[185], generate the hardest emission first at NLO accuracy, before interfacing with parton shower programs. This approach avoids double-counting between the matrix element and the parton shower. `POWHEG` is used for producing NLO samples of $t\bar{t}$, single top, and $t\bar{t}H$ processes, as presented in Section 7.2. All these generators rely on parton distribution functions (PDFs), such as the NNPDF3.1 set [166], which encode the momentum distributions of the incoming partons inside the proton.

Parton showering is performed with the `PYTHIA` generator [167], which simulates soft and collinear QCD radiation, final-state radiation, fragmentation, and hadronization. It also models the underlying event and beam remnants. To consistently combine matrix-element and parton showers, matching and merging schemes are applied. These ensure smooth transitions between the hard matrix-element emissions and the soft parton shower. The MLM scheme is used for LO samples in `MADGRAPH`, while the FxFx method is employed for NLO samples in `MADGRAPH_aMC@NLO` [160].

All generated events undergo a full simulation of the CMS detector response using `GEANT4` [173], followed by the standard event reconstruction chain applied to collision data.

List of Figures

List of Tables

Acronyms

OV Overvoltage.

V_{bias} Bias voltage.

V_{br} Breakdown voltage.

ATLAS A Toroidal LHC Apparatus.

BDT Boosted Decision Tree.

BSM Beyond Standard Model.

BX bunch crossing.

CERN European Organization for Nuclear Research.

CMS Compact Muon Solenoid.

ECAL lead tungstate crystal electromagnetic calorimeter.

EWK electroweak.

HCAL brass and scintillator hadron calorimeter.

HGCAL High Granularity Calorimeter.

HGCROC HGCAL read out chip.

HL-LHC High-Lumi-LHC.

HLT high-level trigger.

HOTVR Heavy Object Tagger with Variable Radius.

LHC Large Hadron Collider.

MC Monte Carlo.

MIP minimum ionising particles.

p–p proton-proton.

PU *pileup*.

QCD Quantum Chromo Dynamics.

SiPM silicon photomultiplier.

SM Standard Model.

Acknowledgments

As I write this final part of my thesis from the comfortable couch in my office, I would like to take a moment to thank the many people who accompanied and supported me throughout this journey.

I would like to begin by expressing my sincere gratitude to Prof. Dr. Freya Blekman. I am truly honored to have been part of her research group and deeply thankful for the opportunity she has given me. From the job interview on a hot August day in Italy to every one-to-one meeting, I will always remember our insightful and exciting conversations, where you challenged my knowledge and understanding and helped me grow as a researcher.

I also thank Dr. Katja Krüger for agreeing to be my second supervisor and thesis evaluator, and for providing insightful comments and suggestions that improved the quality of my work.

A major thank you goes to Dominic and Matthias. You have been incredibly helpful throughout the development of the analysis, from writing code to drafting both the article and the thesis. Thank you so much for all your comments and suggestions. Working with you has always been easy, productive, and enjoyable.

Many thanks to the whole search group at DESY, Jeremy, Lovisa, Juliette, Mykyta, Soham, and especially Kuan Yu-Lin and Andreas Hinzmann, who supported the analysis development. Your suggestions were always precise and invaluable.

I also thank the entire FTX-HGCAL group at DESY with whom I worked: Daria, Antoine, Ji-Hao, and Mathias. We shared long test-beam shifts filled with fun and lots of food. A special thanks to Malinda: your thesis became an inspiring textbook for me.

A gigantic thank you goes to the people who shared the office with me and who now hold a special place in my heart. Starting with Benno, who has been there since day one. He turned out to be the best match to my personality that I could have ever imagined. Not surprisingly, he has become one of my closest friends. Then my dear friend Alexi, who unfortunately left DESY too soon. The triumvirate we formed with Benno was probably the peak of fun I have ever had in a work environment. You helped me get through the toughest days of my PhD. Then came Lucia and Shahzad: you two lovely people made the working days pass easily and made the office the coziest in all of DESY. As my buddy Tupac once said, "Keep your head up": you are going to make it, and it is going to be awesome. Thanks also to David and Lukas for the support.

Special thanks to Simone, who always made me question how little I know about physics and how bad I am at swimming.

Many thanks to all the people I met during my PhD years at DESY (especially Beatriz, Michele, Federica, and Mikel). Each one of you enriched me with

knowledge, culture, and respect, and for that I will always be grateful. You made me feel part of a community.

Although they did not directly contribute to this thesis work, I want to thank my precious family. My mum and dad always believed in me, showing unconditional love and interest in my research. My brother and Janu have always supported me, especially when dealing with all sorts of bureaucratic struggles.

Big thanks to everyone I lived with during my PhD: Finn, Lea, Lotte, Frank, Marco, Sean, Chris, Jojo, and Ruben. Coming home to you after stressful days made everything easier and always felt like home.

Last but certainly not least, thank you to all my friends in Hamburg, Bari, and around the world for the emotional support you gave me. A special mention to Paola and Angela, who were in some way also helpful for this work and with whom I would have loved to collaborate directly. And finally, a very special mention to Bobby and Sonia.